2009

Linerless Eutectic Al-Si Engine Wear: Microstructural Evolution

Benjamin Slattery
University of Windsor

Linerless Eutectic Al-Si Engine Wear:

Microstructural Evolution

by

Benjamin E. Slattery

A Thesis

Submitted to the Faculty of Graduate Studies

through Materials Engineering

in Partial Fulfillment of the Requirements for

the Degree of Master of Applied Science at the

University of Windsor

Windsor, Ontario, Canada

2009

Linerless Eutectic Al-Si Engine Wear:

Microstructural Evolution

by

Benjamin E. Slattery

APPROVED BY:

_____
Dr. J. Johrendt
Department of Mechanical, Automotive, & Materials Engineering

_____
Dr. A.T. Alpas
Department of Mechanical, Automotive, & Materials Engineering

_____
Dr. A. Edrisy, Advisor
Department of Mechanical, Automotive, & Materials Engineering

_____
Dr. H. Hu, Chair of Defense
Department of Mechanical, Automotive, and Materials Engineering

18 September 2009

DECLARATION OF CO-AUTHORSHIP/PREVIOUS PUBLICATIONS

I hereby declare that this thesis incorporates material that is the result of a joint research undertaken in collaboration with Dr. T. Perry from the Materials and Processes Laboratory of General Motors Research and Development Center under the supervision of Dr. A. Edrisy. The research collaboration is covered in Chapters 3, 4, and 5 of the thesis.

I am aware of the University of Windsor Senate Policy on Authorship and I certify that I have properly acknowledged the contributions of other researchers to my thesis, and have obtained permission from each of the co-authors to include the above materials in my thesis.

I certify that, with the above qualification, this thesis, and the research to which it refers, is the product of my own work.

This thesis includes two original papers that have been previously published/submitted for publication in peer reviewed journals, as follows:

1. B.E. Slattery, T. Perry, A. Edrisy, Microstructural evolution of a eutectic Al-Si engine subjected to severe running conditions, Materials Science & Engineering: A, 2009. 512(1-2): p. 76-81 doi:10.1016/j.msea.2009.01.025
2. B.E. Slattery, T. Perry, and A. Edrisy, Investigation of wear induced surface and subsurface deformation in a linerless Al-Si engine, under GM approval for submission to Wear: An International Journal on the Science and Technology of Friction, Lubrication and Wear; August. 2009: p. 1-29.

I certify that I have obtained permission from the copyright owners to include the above published materials in my thesis. I certify that the above material describes work completed during my registration as a graduate student at the University of Windsor.

I declare that, to the best my knowledge, my thesis does not infringe upon anyone's copyright nor violate any proprietary rights and that any ideas, techniques, quotations, or any other material from the work of other people included in my thesis, published or otherwise, are fully acknowledged in accordance with the standard

referencing practices. Furthermore, to the extent that I have included copyrighted material that surpasses the bounds of fair dealing within the meaning of the Canada Copyright Act, I certify that I have obtained permission from the copyright owners to include such materials in my thesis.

I declare that this is a true copy of my thesis, including any final revisions, as approved by my thesis committee and the Graduate Studies office, and that this thesis has not been submitted for a higher degree to any other University or Institution.

ABSTRACT

The wear mechanisms of novel linerless eutectic Al-Si engines subjected to extensive dynamometer testing have been thoroughly investigated using an array of surface and subsurface techniques to elucidate the effects of alloying, surface preparation, and temperature on the overall wear progression of linerless Al-Si engines.

The efforts of this research have revealed that the long term wear resistance of linerless eutectic Al-Si engine bores is derived from the combined effects of oil deposits, silicon exposure, and the formation of reduced grain structures in the aluminum-matrix. Under this criterion, silicon particles maintained exposure at an equilibrium height of ~0.4 to 0.6 μm. Amorphous structured oil deposits, abundant on the worn surface, were shown to fill/protect uneven areas on the aluminum-matrix. The evolution of the bore microstructure is explained in terms of fragmentation of silicon particles and subsequent "polishing" of the entire worn surface caused by sliding contact with the rings.

To my mother, Aurora

for always placing her family above all else

ACKNOWLEDGEMENTS

Table of Contents

NOMENCLATURE

Abbreviations

AES	auger electron microscopy
AFM	atomic force microscopy
AW	antiwear
BDC	bottom dead center
BHN	Brinell hardness number
BRR	bottom ring reversal
BS	backscattered
CB	cell blocks
CE	chemically etched
CGI	compact graphitic iron
Cu:MR:HT	Copper alloyed : Mechanical reduced : Hot tested
DAS	dendrite arm spacing
DDWs	dense dislocation walls
DLC	diamond-like carbon
EDM	electrical discharge machine
EDS	energy dispersive spectroscopy
EHL	elastohydrodynamic lubrication
EP	extreme pressure
EPMA	electron probe micro-analyzer
f.c.c.	face center cubic
FIB	focused ion beam
HR-TEM	high resolution transmission electron microscopy
IC	internal combustion
LEDS	low energy dislocation structures
MBs	micro bands

MM	mischmetal
MML	mechanically mixed layer
MR	mechanically reduced/stripped
MW	mild wear
Ni:CE:CS	Nickel alloyed : chemically etched : Cold scuff
Ni:CE:HT	Nickel alloyed : chemically etched : Hot tested
Ni:MR:HT	Nickel alloyed : Mechanical reduced : Hot tested
RC	relaxed constraints
RNT	radionuclide technique
SAD	selected area diffraction
SDAS	secondary dendrite arm spacing
SEM	scanning electron microscopy
SI	spark ignition
SiC	silicon carbide
Si-I	diamond cubic silicon
Si-XII	amorphous rhombohedral silicon
SOI	site of interest
SPC	pancake-shaped cells
SRP	silicon -rich particles
STEM	scanning transmission electron microscopy
SW	severe wear
TDC	top dead center
TEM	transmission electron microscopy
TRR	top ring reversal
UFG	ultra fine grain
UMW	ultra-mild wear
VI	viscosity index

XPS	X-ray photoelectron spectroscopy
ZDDP	zinc dialkyl-dithiophosphate

Symbols

a	contact area radius
A	real/true area of contact
d	separation distance
d	grain size diameter
$d\gamma/dt$	shear strain rate
E	elastic modulus
F	frictional force
F_{adh}	frictional force due to adhesion
F_{def}	force due to deformation
f_i	material properties
F_{max}	maximum tangential force
H	indentation hardness
H	bulk hardness
h_{min}	minimum film thickness
h_o	outlet film thickness
K	wear coefficient
L	length of plate
l_c	width of particle
p	normal stress
P	normal load
P	hydrostatic pressure
r	radius
R	radius of sphere

$\dot{R}$	rate of void growth
R_a	average roughness
R_f	silicon exposure
s	junction shear strength
s	sliding distance
t	particle elevation height
T_b	average bulk hardness
t_c	critical thickness
T_m	melting temperature
T_o	initial temperature
U	velocity
v	Poisson's ratio
V	sliding velocity
W	normal load
W	rate of sliding wear
w	volume loss
W_i	wear rate
Y	uniaxial yield stress
Z	asperity height
ε	strain
η	viscosity
θ^*	root mean squared surface roughness
μ	coefficient of friction
ρ	fluid density
$\rho^\perp$	dislocation density
σ_y	yield stress
τ	shear stress

LIST OF FIGURES

Chapter 2

Chapter 3

Chapter 4

LIST OF TABLES

1   INTRODUCTION

1.1   Background and Objective of Research

In a global attempt to minimize harmful exhaust emissions, reduce fuel consumption and increase the efficiency of the automobile, replacement of heavy cast iron components with lightweight cast aluminum alloys is a simple yet cost effective method [1]. In general, lightweight materials fall short when replacing components subjected to continual wear such as bearings, pistons, and cylinder liners due to their lack of wear resistance. Consequently, significant improvements in wear resistance have been achieved by alloying aluminum with high fractions of silicon, typically 10-25 wt.% [2-6]. As a result, laboratory wear testing [7-15], engine testing [16-18], and modification [2, 19] of aluminum-silicon alloys has been the main focus of many studies in an attempt to improve the wear behavior and understand and the effects of microstructure, composition, lubrication, and surface preparation; the latter of ,which has been thought to play a significant role with regard to linerless aluminum-silicon engine bores.

Since the focus of this work is based on the wear mechanisms of eutectic Al-Si alloys it is appropriate to summarize the work thus far by other researchers. Under dry sliding laboratory conditions, Riahi et al. [20] has examined the scuffing resistances of etched eutectic Al-Si alloys with varying particle morphologies (high aspect ratio—needle-like, low aspect ratio—spherical). They have determined that the onset of scuffing was dependent upon the etching time, and that a microstructure with a lower aspect ratio increased scuffing resistance. Moreover, over-etching resulted in a weak Al/Si interface, due to excessive dissolution of the matrix surrounding the silicon particles; thus leading to premature particle removal, three-body abrasion, direct metal-to-metal contact, and scuffing. Recently, Chen et al. [21-23] has performed lubricated pin-on-disc studies which have shown that the wear resistance of etched Al-Si alloys are dependent upon parameters influencing the resistance of silicon particles sinking into the aluminum matrix during loading, as well as the formation of amorphous oil residue layers. They

concluded that increasing the silicon particle size, lowering the aspect ratio, and improving matrix hardness would increase the load carrying capacity of the alloys, and in turn the overall wear resistance under ultra-mild conditions.

Complimentary to laboratory studies, monolithic aluminum silicon engines have been developed and were first introduced to the auto industry with the production of the Vega 2300 [24-26]. However, excessive tool wear and an unreliable casting processes limited its marketability as a result of the silicon particles being large and blocky (hypereutectic). Currently, other alloys and techniques such as Alusil™, Silitec™, and Lokasil™ dominate the monolithic engine market [26-29]. Literature based on wear testing and characterization of linerless Al-Si engines is scarce due to the difficulties associated with measuring the low wear rates and isolating parameters that are dependent upon the combustion process [16, 30].

Of the few available linerless Al-Si engine studies, Kurita et al. [17] has examined hypereutectic DiASil engine bores after dynamometer testing. They have shown that the monolithic Al-Si engine provided superior cooling and oil consumption compared to the engine with cast iron sleeves. Their results have suggested that cylinder wear proceeds initially by abrasive wear which decreases the silicon exposure height until elastohydrodynamic lubrication (EHL) is established at an equilibrium Si exposure of 0.15 μm; here, the EHL conditions terminate excessive wear providing long term engine endurance. Through dynamometer engine testing of an etched Alusil™ cylinder, Dienwiebel et al. [16] has shown that after running-in silicon particles, which initially protruded from the aluminum matrix, exhibited no exposure height. Instead, wear resistance was maintained by the formation of a chemically modified near-surface matrix. However, the authors suggested that silicon exposure was important in order to initially direct the energy input into the silicon particles and protect the nascent aluminum until running-in was complete.

Currently, monolithic Al-Si engines are commonly produced with high concentrations of silicon in order to increase hardness and minimize cylinder wear. This leads to costly processing techniques which limits these engines to only premium

vehicles. Consequently, more affordable eutectic aluminum-silicon engines, as in the present study, are in development and will incorporate cheaper casting and surface preparation techniques. Therefore, in order to understand the wear mechanisms associated with eutectic Al-Si engine bores the present study will encompass detailed microstructural investigations before and after rigorous dynamometer testing. Identifying and understanding wear in linerless Al-Si engines are crucial steps towards the future development of lightweight wear resistant engines which will provide a cheap yet robust solution to cast iron liners.

1.2　Organization of Thesis

This thesis is organized into six chapters, each of which is described as follows:

Chapter 1 introduces the basic background related to this research as well as the overall objective and organization of the thesis.

Chapter 2 begins with introducing the basics of tribology including the wear mechanisms typically observed in metals. Focus is then allocated towards the wear of Al-Si alloys in both dry and lubricated conditions; followed by relevant literature based on the wear mechanisms, microstructural changes, and potential production of linerless Al-Si engines currently on the market.

Chapter 3 encompasses the materials and experimental procedures used to characterize the wear of multiple linerless engines. This chapter elaborates on the different types of alloying elements, dynamometer tests, cylinder surface finish, and methodology used to accurately examine the engine bores mechanically, microstructurally, and chemically.

Chapter 4 describes, in detail, the results obtained from the worn and unworn regions of four different engine bores. This chapter includes materials characterization information obtained by a number of different techniques that range from simple optical microscopy to sophisticated nano-indentation and high resolution transmission electron microscopy.

Chapter 5 describes and identifies the wear mechanisms of each engine with reference to the previous chapter. The effect of alloying, surface preparation, and temperature are addressed with regards to the microstructural evolution of the engine bore.

Chapter 6 presents the conclusions resulting from this research, followed by suggestions towards future development and research of linerless eutectic Al-Si engines.

2   LITERATURE SURVEY

2.1   General Introduction

In contrast to old well established engineering subjects such as thermodynamics, plasticity, and mechanics, tribology is relatively a new field of science that has yet to be perfected [31]. The term "tribology" can be defined as "the science and technology of interacting surfaces in relative motion and all practices related thereto [32]." In other words, it is related to friction, wear, and lubrication.

Tribology has been in existence throughout history and began when early civilizations developed bearings and low friction surfaces. In fact, "tribology" originated from the Greek word "tribos" meaning rubbing or sliding [31]. The cost of tribological deficiencies to any economy is substantial because essentially every mechanical device in operation will produce large energy and material losses during its lifetime. For example, in the early 18th century it was suggested by Jacobs Rowe that the number of horses required for carriages in the United Kingdom could be halved by the application of a rolling element bearing; resulting in savings of one million pounds per annum at that time [33]. In more contemporary times by reducing tribological deficiencies in cars alone, the U.S. economy can save approximately 18.6% of the total annual energy consumed by cars, or equivalent to $14.3 billion USD per year. At a larger scale, it has been approximated that one-third of the world's energy resources is required to overcome friction in one shape or another [31].

By effective lubrication, wear and friction can be drastically reduced. In short, the concept of tribology portrays that friction and wear can be best controlled by a thin layer or film of material separating the contacting bodies. The film can either be solid, liquid, or gas and can be generated as a result of the wear process or added to the system intentionally. Unfortunately many mechanical systems often suffer from inadequate film availability, thus leading to excessive wear and/or catastrophic failure. To prevent these types of occurrences, tribological problems must be resolved by identifying the appropriate approach and methodology needed for the specific situation [32]. When

solving wear problems often the biggest challenge is that of anticipating the type(s) of wear the components will be subjected to. Although material can only be removed from a solid by three ways (i.e. physical separation of atoms from the surface, chemical dissolution, or by melting) it is still difficult to determine the type of wear and mechanisms involved [34]. In order to understand how friction and wear can be controlled in a given system (e.g. engine cylinder), it is imperative to differentiate between the different types of wear modes, processes, and mechanisms; and have a basic understanding of how materials interact during contact and their dependence upon surface features (i.e. roughness, protruding second phase particles), microstructure (i.e. precipitates, grain size), and processing techniques.

2.2   Surface Topography

No matter how smooth or flat a solid surface is it will always be uneven when studied on a fine scale. Even truly smooth surfaces (i.e. mica) will have surface irregularities due to the size of atoms and molecules present within the material [35]. Irregularities much larger than atomic dimensions are present in even the most highly polished engineering materials. Therefore, many methods (i.e. electron microscopy, optical microscopy, stylus profilometry, etc.) have been exploited to study surface topographies. A prime example would be engine cylinders; in this tribosystem a specific surface finish is required to maintain effective oil retention via grooves or pockets in the surface, as well as, limit point pressure loading (see §2.7.4.2).

2.2.1   Measurement of Surface Topography

When topographies of delicate surfaces need to be obtained optical interferometers are typically employed. Optical interferometers operate on the basis of beams of light that distort with changing topography. They can reach extremely small resolutions but are limited to the depth of focus of the instrument. Therefore, optical interferometry is employed for very fine surfaces, while stylus profilometry is used for coarse surfaces [35].

2.2.2 Surface Roughness

The term roughness refers to the minute scale irregularities of a surface. Typically the average roughness R_a, is used to describe surface roughness. It is the mean deviation of the surface height from a line (mean line) through the profile which equally separates the areas above and below it (Figure 2-1); it is described by the following equation [35].

$$R_q = 1 / L \int_0^L | y(x) | \, dx \ldots\ldots(2-1)$$
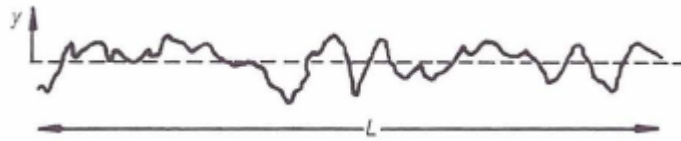
Figure 2-1 Example of a surface profile [35].

Referring to (Equation 2-1), L is the overall length of the profile, y is the surface height above the mean line at a distance x from the origin.

2.2.3 Contact Between Surfaces

As two smooth and parallel surfaces are brought slowly together initial contact will take place at high points called asperities. Asperities are the real areas of contact (see Figure 2-2); therefore they support the normal load, are responsible for any frictional forces generated, and influence the electrical contact resistance. For the sake of modeling asperities they are considered to be blunt, shallow, and smooth spherical protuberances [35-37].
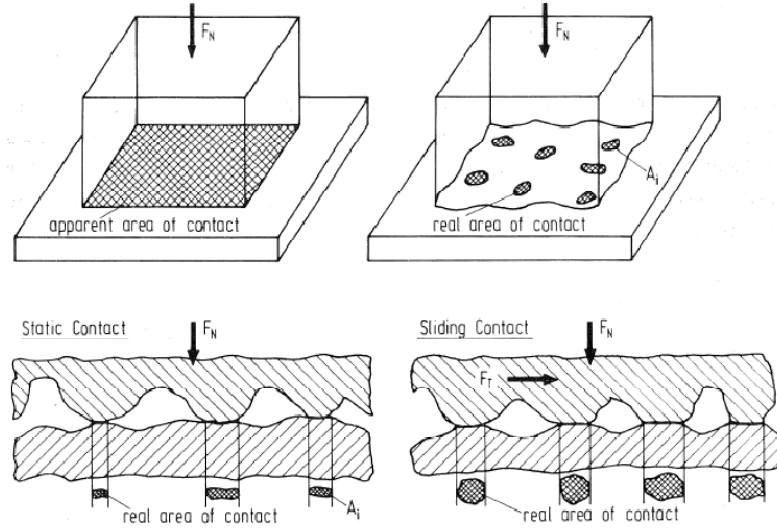
Figure 2-2 Apparent and real areas of contact [36].

2.2.4　Elastic Deformation of a Single Asperity

According to Hertz [38], a circular contact area of radius (*a*), is made when a sphere of an elastic material is compressed with a normal load (*w*) against a plane. The contact radius can be expressed as:

$$a = (\frac{3wr}{4E})^{1/3} ......(2-2)$$

$$\frac{1}{E} = \frac{1-v_1^2}{E_1} + \frac{1-v_2^2}{E_2} ......(2-3)$$

where *r* is the radius of the sphere, and *E* is the elastic modulus of the sphere and plane system represented in Equation 2-3. The area of contact between the sphere and plane will be πa^2. Referring to (Equation 2-3), E_1 and E_2 are Young's moduli, and v_1 and v_2 are Poisson's ratios for the sphere and plane materials [35].

During purely elastic deformation the area of contact is proportional to $w^{2/3}$. The mean pressure or normal stress is $w\pi a^2$. The stress distribution over the contact area is not uniform. A maximum stress of 3/2 the mean pressure occurs at the center and falls to zero at the edge of the contact area [35].

2.2.5   Plastic Deformation of a Single Asperity

Plastic deformation will occur either in the sphere or plane, depending on hardness, as the load is increased [35]. Assuming the sphere is a rigid indenter, the maximum shear stress occurs at a depth of $0.47a$ (where a is the contact area radius) beneath the indenter, according to Hertz. When the yield criteria is reached (i.e. *Y/2*, where Y is the uniaxial yield stress of the softer material), plastic flow initiates. Assuming a Poisson's ratio of approximately 0.3, plastic deformation will initiate at a mean contact pressure of $1.1Y$ [35].

By further increasing the load, the plastic deformation zone extends to the surface of the plane [35]. At this stage the mean pressure has risen to $3Y$ and remains nearly constant for subsequent increases in load. Once full plasticity has been met, the mean contact pressure will be independent of the load and the constant proportionality between the yield stress and this pressure becomes the basis for indentation hardness testing. Indentation hardness is the measure of the mean indentation pressure during fully plastic deformation. For the case of a rigid plane and soft sphere similar results are obtained [35].

2.2.6   Multiple Asperities In Contact

In reality, as the normal load is increased the contact area of individual asperities increases as well as the number of asperities making contact; because of this the average area of contact per asperity remains constant and the increase in load is caused by the increasing number of contacting asperities [35]. To analyze multiple asperities Greenwood and Williamson [39] assumed that asperities are spherical, of the same radius (r), and deform elastically under load according to Hertz's equations (see. Equation 2-2 and Equation 2-3). An asperity can support a load if the asperity has a height (z) (taken from a lower reference plane within the rough surface) which is greater than the separation distance (d), between the smooth surface and the reference plane (Figure 2-3). The load (w), that an asperity can support is described by Hertz's theory and expressed as:

$$w = \frac{4}{3} Er^{1/2}(z-d)^{3/2} \dots\dots(2-4)$$
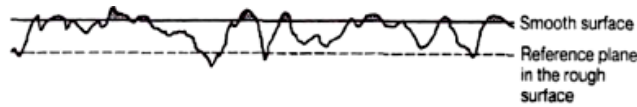
Figure 2-3 Model for contact between a rough surface and smooth rigid plane [39].

2.3   Friction and Wear

The field of tribology is so broadly spaced over science and technology that the terminology of basic concepts sometimes lack consistency [32]. To understand tribology concise definitions of friction and wear are necessary. According to the ASTM G-40 Standard wear is defined as "damage to a solid surface, generally involving progressive loss of material, due to relative motion between that surface and a contacting substance or substances"; and friction force is defined as "the resisting force tangential to the interface between two bodies when, under the action of an external force, one body moves or tends to move relative to the other [40]." In broad terms, friction is the resistance of one body moving over another in either a sliding or rolling motion. For both ideal sliding and rolling, a tangential frictional force (F), acting on one of the bodies, is always required for motion. The coefficient of friction (μ) is the ratio between the frictional force and normal load (W) expressed in the following equation:

$$\mu = \frac{F}{W} \dots\dots(2-5)$$

2.3.1   Theories of Friction

The laws of sliding friction established by Amontons and Leonardo da Vinci state that the frictional force is proportional to the normal load, frictional force is independent of the nominal contact area, and the frictional force is independent of the sliding velocity [41]. These laws are approximately valid and many attempts have been made to explain these laws without great success [42].

Early investigators such as Coulomb and Amontons predicted that the major source of frictional forces resulted from the interaction of plastically or elastically

deforming asperities. Coulomb's model assumed that wedge shaped asperities caused two surfaces to move apart when under sliding motion. However, his model did not incorporate net energy dissipation and hence no frictional force should be observed. A complete model of friction must contain a mechanism of energy dissipation such as plastic deformation in metals or the viscoelastic behavior in polymers [43].

2.3.1.1 Adhesion and Deformation Forces

Bowden and Tabor studied sliding friction and concluded that frictional forces originate from two sources, an adhesion force and a deformation force [37]. The adhesion force arises from the attractive forces at contacting asperities. The deformation force is the force needed for hard asperities to plough though the softer surface.

Typically, strong adhesion occurs between clean ductile materials; because strong interfacial bonds across asperities can take place [43]. Adhesion between two metals is usually not significant due to oxide layers weakening adhesion and elastic strains around asperities creating high enough stresses to break asperity junctions. Assuming that the real area of contact (A) is linearly proportional to the applied load (W) and initial asperity contacts are essentially plastic, the contribution of the adhesive force to the coefficient of friction is therefore represented as follows:

$$\mu_{adh} = \frac{F_{adh}}{W} = \frac{As}{AH} \approx \frac{s}{H}......(2-6)$$

where F_{adh} is the frictional force due to adhesion, s is the junction shear strength of the weaker material, and H is the indentation hardness of the weaker material [43].

The deformation force of hard asperities ploughing through a softer material can be modeled by a rigid conical asperity with a semi-angle α siding through a plastically deforming surface with indentation hardness (H) (Figure 2-4) [43]. The deformation term will contribute to the coefficient of friction by an amount μ_{def} seen in Equation 2-7 ; where F_{def} is the force due to deformation and W the normal load. Values obtained for the coefficient of friction by Equation 2-6 and Equation 2-7 do not match up with experimental values of μ. This discrepancy arises because the above equations do not incorporate the effects of junction growth (§2.3.1.3) and work hardening (§2.3.1.2).

$$\mu_{def} = \frac{F_{def}}{W} = (\frac{2}{\pi}) \cot \alpha ......(2-7)$$
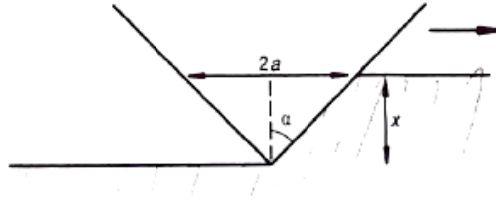
Figure 2-4 Model for the deformation component of friction, in which a conical asperity of semi-angle α indents and slides through the surface of a plastically deforming material [43].

2.3.1.2 Work Hardening

The previous model assumed that the material had a constant flow stress. In reality, a variable flow stress is present due to strain hardening (see §2.5). The junctions will work harden, this tends to raise the shear strength (s) compared to the indentation hardness (H). The increase in shear strength results in an increase in μ_{adh} and an increase in the overall coefficient of friction [43].

2.3.1.3 Junction Growth

The true area of contact relies both on the normal load (W) and the tangential forces of the system [43]. As seen from Figure 2-5, a normal stress p_0 subjects an element into uniaxial compression, which is assumed to be at the point of yielding because plastic asperity contact is presumed. When a tangential force (F) is added to the system an additional shear stress (τ) is exerted on the element. For the element to remain at the point of yielding the normal stress is reduced to p_1. This is accomplished by an increase in the true area of contact also known as junction growth. Therefore, the true area of contact (A) will increase with increasing tangential force, along with the coefficient of friction [43].

Junction growth can occur until the entire specimen area is in contact [43]. However, junction growth is limited by weak interfacial films and the ductility of the materials involved. If a weak interfacial film is present the maximum tangential force F_{max} will be limited by the shear strength of the film. Therefore, minimal junction growth is a result of weak interfacial films [43]. Here, the frictional force (F) is determined by

the shear strength of the film (τ_i), while the normal load (W) is determined by the plastic flow stress of the bulk asperity. This leads to an equation where $\tau_i \ll \tau_0$ shown below:

$$\mu = \frac{F}{W} = \frac{\tau_i}{p_0} \ldots (2-8)$$

where p_0 is the normal stress. Therefore friction can be drastically reduced by introducing a film of material with low shear strength between two surfaces. This is the main principle behind lubricants and is essential for the optimal operation of any reciprocating engine [43].
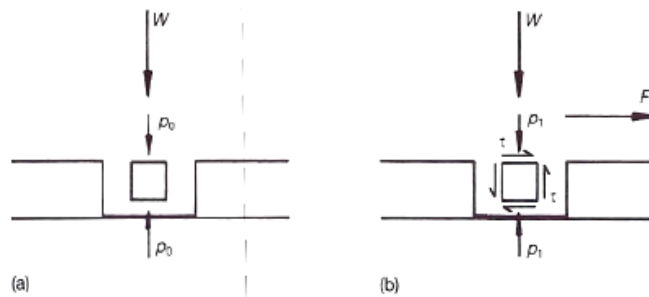
Figure 2-5 Stresses acting on an element within an idealized asperity pressed against a counterface (a) with no tangential force, and (b) with tangential force applied [43].

2.3.2   Friction of Metals

2.3.2.1   Clean Metals in High Vacuum

Regardless of material type, the precise value of the coefficient of friction will depend on the experimental conditions at which it was measured as well as material properties. Clean metals subject to high vacuum conditions experience strong adhesion and high coefficients of friction. This is caused by strong metallic bonds forming at the interface. The high vacuum prevents any interfacial contamination; therefore junction growth is only limited by the ductility of the asperities [43].

2.3.2.2   Self-Mated Metals In Air

All metals, with the exception of gold, oxidize when exposed to air. The presence of oxide films during the dry sliding behavior of metals almost always reduces the coefficient of friction when compared to the sliding of the bare metal counterparts. When surfaces are separated by oxide layers the coefficient of friction is essentially being

measured between the oxide films. Oxide layers have low shear strengths and low ductility, this limits junction growth and lowers μ. Once the oxide layer is removed (i.e. oxide layer penetration at high loads) metal-to-metal contact takes place and a rise in μ is typically observed. With an increase in μ considerable surface damage transpires along with increased wear rates [43].

2.3.2.3 Dissimilar Metals and Alloys

Typically, alloys tend to have lower coefficients of friction when compared to their pure components. Dissimilar metals and alloys (i.e. carbon steel) can have stratified oxide structures due to their multiple constituents. This can result in lower values of μ occurring at high loads. The high loads penetrate the top oxide layer, exposing the next oxide layer which exhibits a lower μ than the first. Constituents can also segregate to the contacting surfaces (i.e. aluminum segregation in steel) causing oxide layers to form from these minor constituents [43].

2.3.2.4 Effect of Temperature

The rate of oxidation, mechanical properties, and phase transformations of metals can all be affected with a change in temperature [43]. In general, the rate of oxidation increases with increasing temperature. This permits the formation of a thick oxide layer which further reduces the friction (see § 2.3.3.3).

In face-centered cubic metals high temperatures bring about high values of μ because the work hardening rate reduces with increasing temperature. Body-centered cubic metals exhibit a brittle to ductile transformation with increasing temperature, hence raising μ. Hexagonal close-packed metals have no change in μ as their mechanical properties do not change significantly with temperature [43].

Phase transformations greatly influence the mechanical properties of metals, which results in significant changes in friction [43]. As the transition from solid to liquid is approached the strength of the material is drastically reduced, and creep and thermal diffusion can set in. The onset of melting results in an increase in ductility and adhesion at points of contact; this effectively increases the friction. Melting occurs when the

dissipation of frictional work is high enough to provide sufficient local heating. Once one of the sliding surfaces melts a molten layer is formed at the contact interface. This layer loses its shear strength, resulting in a loss of friction. The coefficient of friction now depends on the viscous forces of this layer (i.e. hydrodynamic lubrication; see § 2.6.3) [43].

2.3.3 Classification of Wear

Wear has been classified by a number of different ways [31, 32, 36, 44-56] based on categories such as surface features, deterioration mechanisms, material type, and even the number of bodies in the contact zone.

For clarity, wear terms will be divided into a hierarchy of three specific terms: wear mechanism, wear process, and wear mode [32, 36]. A wear mechanism is the lowest on the hierarchy and it involves basic atomic and molecular interactions such as atomic diffusion, surface chemical reactions, film formation, adhesion, dislocation interaction, etc.

The second level on the hierarchy is the wear process which incorporates a combination of two or more wear mechanisms to initiate a wear damage process. For example, the process of crack initiation which involves the mechanisms of crystallographic defect generation, interaction of defects (i.e. dislocations), the formation of highly defected regions to produce microvoids, and eventually the amalgamation of microvoids to nucleate microcracks near the worn surface. Processes operate to produce observable wear modes and thus, a wear mode is a unique combination of basic wear processes. Essentially a wear mode is the manifestation of wear processes [32]. The most commonly observed modes of wear are as follows: abrasive wear, cavitation, chemical and oxidative wear, erosion, fretting, impact wear, and sliding wear [32].

2.3.3.1 Abrasive Wear

Abrasive wear is defined as wear due to hard particles or hard protuberances forced against and moving along a solid surface [40]. It can occur as a wear mode or wear process since it can represent the dominant wear mode on a surface, or be one of

multiple processes contributing to sliding wear (see § 2.3.3.7.). Abrasive wear typically operates by the cutting or plowing of a surface by particles of equal or greater hardness. These particles can be embedded within the counterface (i.e. two-body abrasion) or loose within the contact zone (i.e. three-body abrasion) [32, 44, 45, 47, 57]. The abrasive particles may aid material removal by microcutting, accelerated fatigue by repeated plowing, pullout of individual grains, or microfracture [31]. Abrasion can also be classified based on the severity of the surface damage such as low-stress grinding abrasion (scratching), high-stress grinding abrasion, and gouging abrasion [32, 47].

2.3.3.2   Cavitation

Cavitation is defined as the formation and collapse, within a liquid, of cavities or bubbles that contain vapor or gas or both [40]. Cavitation wear typically occurs in tribosystems of rapidly moving fluids or solid surfaces moving through a body of fluid. Cavitation arises due to localized reduction of the pressure within a fluid when the fluid collides rapidly with a solid. As the pressure decreases bubbles of vapor form, grow, and then collapse generating minute pressure spikes that act as micro-jet that eventually accumulate damage in the form of cavities or pits in the solid surface [31, 32, 54, 58].

2.3.3.3   Chemical and Oxidative Wear

Chemical reactions will occur on wearing surfaces to some degree in almost any environment. The degree of chemical reaction will influence the observable wear and frictional behavior of the tribosystem. Corrosive wear can be defined as wear in which chemical or electrochemical reaction with the environment is significant [40, 54]. Beneficial surface chemical reactions that typically prevent adhesive wear can lead to corrosive wear if left unchecked. When a material is corroded to generate a surface film during sliding contact four processes may take place: i) a durable lubricating film which prevents subsequent corrosion and wear can develop; ii) a weak film that is quickly removed during sliding may form but lead to high wear rates and coefficients of friction due to the destruction of the film; iii) surface films may be worn and a galvanic couple between the remaining films and the underlying substrate may facilitate rapid corrosion; and iv) the corrosion and wear processes may act independently [31].

16

Oxidative wear occurs when metals are worn in the presence of air or oxygen under unlubricated conditions [31]. It has been determined that when load and sliding speeds are significant enough to substantially increase the frictional contact temperature, wear debris will change from metallic to metallic oxides. When thick oxide films are present on the worn surfaces "mild wear" (see §2.9.2) is dominant and when these oxides are absent or removed "severe wear" (see §2.9.2), a form of adhesive wear, prevails [31, 32, 36, 54, 59]. In the case of mild wear, the oxide films prevent direct metal-to-metal contact and are typically supported by the strain-hardened substrate layers generated by plastic deformation. Oxidative wear is similar to corrosive wear except for the fact that metallic oxides tend to combine with the worn metal and form layers of mixed oxide and metal [31]. Figure 2-6 illustrates the process of oxidative wear.
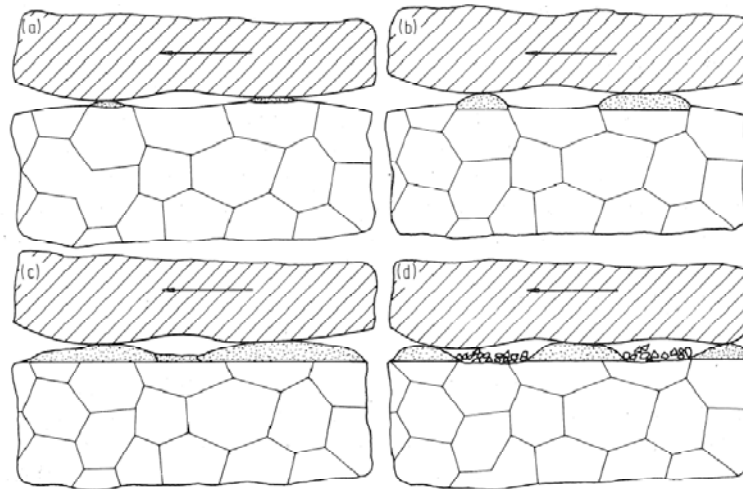
Figure 2-6 Wear by tribochemical reaction: (a) formation by oxide islands, (b) and (c) growth of oxide islands and (d) destruction of primary load-bearing oxide plateaus and formation of new ones [36]

2.3.3.4 Erosion

Erosion is defined as the progressive loss of original material from a solid surface due to mechanical interaction between that surface and a fluid, a multicomponent fluid, or impinging liquid or solid particles [40]. Erosion itself may be considered a subset of impact of wear. There are a number of wear mechanisms with which erosion can thrive as the dominant mode of wear; however, most forms of erosion will occur when relatively small particles (5 to 500 μm) impact a given surface [31].

The erosion of a solid body can occur by its interaction with an impinging stream of solids, liquids, gasses or a combination of these [36]. Particle erosion, cavitation erosion, spark erosion, and fluid erosion are the four most common erosive wear mechanisms [60]. Erosion mechanisms are largely controlled by the following factors [32]:

- velocity of the impinging stream
- angle of incidence of the impinging stream
- mass of impacting particles
- chemical reactivity of the impinging stream
- temperature of the worn surface and impinging stream
- concentration of solid material within the impinging stream
- size, shape, and hardness of particles within the impinging stream

2.3.3.5 Fretting Wear

Fretting wear can be defined as a phenomena taking place between two surfaces having oscillatory motion of small amplitude usually less than 25 μm occurring over a large number of cycles [31, 32]. Even with amplitudes on the order of 1 μm (i.e. mechanical fastenings, vibrating machinery, between strands of wire rope…etc) fretting wear can prevail. The three fretting regimes are stick, partial slip, and gross slip [31]. When the fretting contact operates under stick conditions no damage occurs. Under the partial slip regime the contact is susceptible to crack development leading to fretting fatigue. Lastly, in the gross slip regime damage by wear will occur by plastic or elastic mechanisms. The wear debris produced during fretting is often retained within the contact due to the small amplitudes of motion. With time, the accumulating wear debris may gradually separate the two surfaces leading to accelerated wear by abrasion. Other factors such as temperature, corrosion, and delamination can also accelerate fretting [31, 32, 61].

2.3.3.6 Impact Wear

Impact wear may be defined as the loss and/or displacement of surface material resulting from the mechanical interaction and collision of two or more solid bodies [32].

A classic example of impact wear occurs when a hammer strikes a surface. Impact wear is associated with elastic and plastic deformation when the impact energy is high combined with the release of wear debris caused by crack initiation. It has been demonstrated that the impact wear of metals involves three distinct damage zones: i) the undeformed base metal; ii) a region of plastic deformation and refinement; and iii) a highly deformed "compositional mix" region just beneath the contact surface [32]. Surprisingly, the thickness of these damage zones remains unaffected even after increasing the impact load by a factor of ten. In general, the impact of a surface rarely remains normal to a surface, some form of transverse direction typically arises during an impact [31, 32]. This transverse motion leads to a sliding component of wear and will be discussed in the following section.

2.3.3.7 Sliding Wear

Sliding wear is amongst the most complex and thoroughly researched modes of wear [49, 53, 62-67]; however, no universally acceptable, accurately predictive models for sliding wear have been developed. Sliding wear is characterized by the relative motion between two smooth solid surfaces under contact loading, where surface damage does not promote deep grooving or penetration by asperities or foreign particles [36]. Essentially, there is potential for sliding wear whenever relative motion between two contacting solid bodies occurs [65]. Historically, adhesive wear was used synonymously with sliding wear, but far more than just adhesion occurs during sliding wear. It may take place under lubricated or unlubricated conditions and often involves other modes of wear in addition to those unique to sliding. Chemical reactions, abrasion, fatigue, aspects of impact, and adhesion can all operate in tandem with sliding depending on the tribosystem and material couple [32]. Figure 2-7 illustrates some of the possible mechanisms of sliding wear.

For most metals the extent of sliding wear can be expressed in terms of the mild and severe wear regimes [62]. In general, mild wear is associated with low loads and composed of $0.01\mu m$ to $0.1\mu m$ sized oxide wear debris. Conversely, severe wear is associated with high loads, producing large metallic debris ranging from $20\mu m$ to $200\mu m$

in size that tend to flake away or transfer to the counterface due to the high shear strains and cyclic loads. The transition from mild to severe wear will occur when the formation of oxide/tribological layers equals the exposure of fresh metal [62]. Relatively simple test rigs such as pin-on-disk, block-on-ring, and reciprocating tribometers are just a few examples with which some of the variables of sliding wear can be isolated and studied. Aside from material properties, the severity of sliding wear for a given material will depend on the nominal pressure, distance slid, sliding velocity, simulation time, linear dimensions, and environment temperature. These variables of wear are independent, as changes in one can often induce a transition from one wear mechanism to another throughout the life of a single test. Subsequently, it is difficult to relate experimental simulations to practical applications [62].

In terms of real world usefulness the "zero-wear" model by R. Bayer is amongst the most successful [32, 68]. This model is based on two regimes: one with no measurable wear loss, and one in which there is. According to Bayer, when the change in surface roughness is less than one-half the original peak-to-valley surface roughness the zero-wear criteria is maintained. In addition, wear can be controlled by limiting the maximum Hertzian shear stress τ_{max}, in the region of contact. Bayer concludes that the maximum shear stress for a given sliding distance will depend on the type of lubrication and the sliding material's tendency for transfer [32, 68].

The "Archard wear law" is the most widely adopted theory and model for sliding wear. After hundreds of unlubricated wear experiments with numerous material couples Archard and Hirst developed the following relationship [56]:

$$W = \frac{w}{s} = \frac{KP}{H} \ldots (2-9)$$

which states that the rate of sliding wear W, at a constant sliding speed is equal to the volume lost w, per sliding distance s. Archard also related the linear wear rate to the applied normal load P, bulk hardness of the material (H), and the dimensionless wear coefficient (K) that is always less than unity and is heavily dependent upon the wear environment. In other words, a change in K denotes a change in surface conditions.

Based on the assumption of plastic deformation of asperities, Archard and Hirst concluded that once equilibrium surface conditions have been met the wear rate will be proportional to the applied load; and independent of the apparent area of contact regardless of the mechanism of wear. The Archard equation is linear; and hence tribological effects, such as frictional heating and work hardening, encountered in common engineering situations are not accounted for. In summary, the Archard equation must be used with caution, as it does not provide variables which deal with changing wear rates often found during running-in and sliding wear transitions [32, 45, 56, 62].

One way to account for changing wear rates is to divide the wear curve into various stages and calculate the wear coefficients valid for each interval or to construct wear mechanism maps. The first wear mechanism map was developed by Lim and Ashby [59, 69]; these diagrams summarize wear behavior by identifying areas corresponding to dominant mechanisms of wear (i.e. seizure, melt, oxidation, and delamination). A typical wear mechanism map will illustrate wear rates and regimes over a wide range of loads and sliding velocities. It is imperative to understand that wear maps are only as good as the models and data used to construct them. These maps can be constructed in two ways. The empirical method of map creation involves plotting experimental data and identifying the dominant wear mechanisms for each point. The second method uses physical modeling by means of equations that describe each dominant mechanism of wear. This method contains constants that are not absolute. Therefore, calibration of these equations with empirical data is essential. Lim and Ashby have brought about two important statements [59]:

> "..research has tended to focus on the details of a single mechanism, not on the relationship between mechanisms."

> "So many mechanisms are involved in describing wear that there is no hope of constructing a universal diagram which describes all materials, or even all metals."

With the above statements in mind, it is clear that identifying wear mechanisms during sliding wear can be a difficult and sometimes impossible task. From one tribosystem to another the dominant factors controlling sliding wear will vary; and hence, each situation will require its own analysis in order to determine the dominant wear

21

behavior at any given time [32]. Only by first understanding the basic factors that influence wear can one hope to identify the mechanism at work.
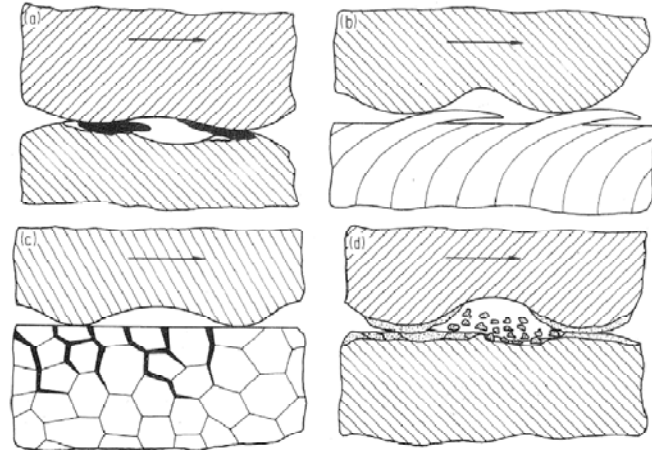
Figure 2-7 Mechanisms of wear during sliding contact: (a) adhesive junctions, material transfer and grooving, (b) surface fatigue due to repeated plastic deformation on ductile solids, (c) surface fatigue results in cracking on brittle solids and (d) tribochemical reaction and cracking of reaction films [36]

2.4 Factors that Influence Wear Rates

As previously mentioned, the volume lost from a surface per unit sliding distance is defined as the wear rate W_i (m³/m). The wear rate is a function of the normal force P, sliding velocity v, initial temperature T_o, and the material properties f_i (thermal, mechanical, chemical) for a given sliding geometry [31, 59]. This relationship can be represented as follows:

$$W_i = f_i(P, v, T_0, thermal, mechanical, chemical)......(2-10)$$

Often, load is considered the dominant factor governing the rate of wear. Archard and Hirst experimentally tested the influence of load on numerous materials and developed the famous Archard wear equation previously elucidated in section 2.3.3.7. They determined that under constant velocities and surface conditions the wear rate will be proportional to the applied load, and independent of the apparent area of contact [56].

It is clear from previous sections describing wear modes that the wear rate of real engineering applications will depend, not solely the load but, on a number of other factors which can be interrelated. For example, when studying the effect of velocity on

sliding wear, allied effects of frictional heating and tribochemical surface activation such as oxidation can transpire. In fact, increasing the velocity of an unlubricated metal sliding system may even produce a film of liquid metal [59]. The increase in velocity limits the cooling time between asperity contact intervals, thus generating high flash temperatures [70, 71], and providing melt lubrication which will lower the coefficient of friction. The environment in which a specific tribosystem is situated will also influence wear rates. Environmental factors found in many real life applications such as humidity, along with dust and dirt will obviously influence a material's response to wear. Furthermore, use of lubrication, be it solid, liquid, or gas will also influence wear. Material related properties such as the use of alloying elements, the addition of large incoherent ceramic particulates, or the amount of defects can all potentially influence the life of a tribosystem. Even the orientation of a tribosystem (i.e. vertical---allowing debris to fall, or horizontal---allowing debris to be ground, deformed, and agglomerated) will have an effect on wear [32]. In the following sections important parameters (i.e. lubrication, surface preparation, alloying…etc), used to promote the low wear rates associated with modern day internal combustion engines, will be discussed in detail and related to the linerless aluminum-silicon engine.

2.5   Fundamentals of Deformation and Structural Evolution

After the start of sliding contact between unworn solid surfaces, significant changes in temperature, friction, and wear rate are frequently observed and are known as the process of running-in. These brief fluctuations are sometimes ignored and assumed to be the normal course of operation. However, it is advantageous to make use of these fluctuations to improve the performance of components such as gears, bearings, brakes, and cylinders by making certain that running-in is executed in an optimal manner.

Many studies involving sliding friction and the wear of materials, whether the tribosystem is lubricated or not, ignore the initial transient running-in stage and focus mainly on the steady state conditions. By disregarding the importance of the running-in process, important clues to the evolution of collective processes that operate during the long term wear behavior are overlooked.

Abbott and Firestone [72] are one of the first to address the importance of running-in, which came about during their studies of bearing contact in 1933. They stated that:

> "When two newly machined surfaces are placed together, they touch only on the peaks of the highest irregularities, and the actual contact area is very small. If surfaces are 'run-in' under load, or otherwise fitted, the projecting irregularities are gradually removed and the actual area of contact is increased. At first the wear is quite rapid, but it decreases as the contact area increases [72, 73]."

Unquestionably, Abbott and Firestone sparked the notion of running-in by observing changes in microtopography; however, they overlooked the changes in the materials directly adjacent to the sliding surfaces. For engineering surfaces to precisely fit together (i.e. piston/cylinder---where tolerances for pressure tightness are essential), elastic and in most cases plastic deformation of the asperities is compulsory. Throughout the deformation process changes in crystallographic orientation as well as the state of work hardening typically arise. Therefore, amidst running-in not only do the surface features change (i.e. texture, roughness, and shape) but so does the substructure and micromechanical properties [30, 73-76]. Figure 2-8 gives an overall example of some of the microscopic and atomic differences between a metal's bulk structure and near worn surface. Several authors have investigated deformation and its structures [36, 63, 67, 75-88], subsurface zones [49, 78, 89-94], and tribolayers/mechanical mixed layers (MML) [52, 90, 93, 95] in response to the sliding wear of metals. The following subsections will cover the fundamental aspects of plastic deformation, deformation microstructures, and the structural evolution of ductile materials.
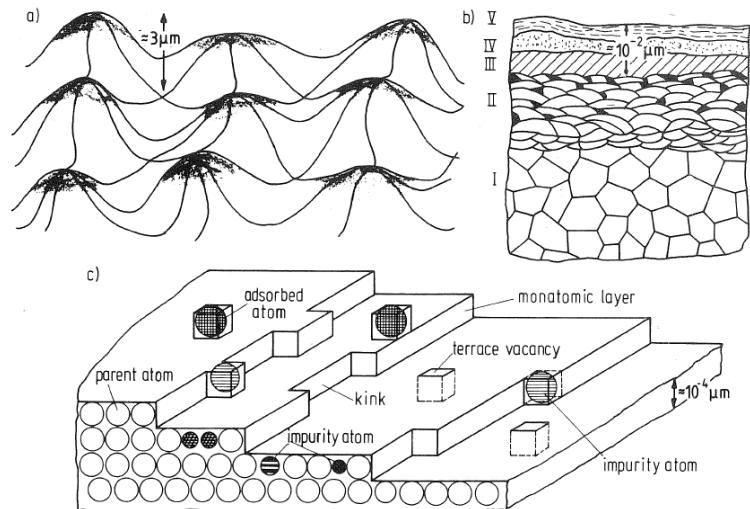
Figure 2-8 Topography and structure of surfaces of metals: (a) surface topography on a microscopic scale, (b) cross-section of the transition of a metal to its environment. (I) bulk microstructure, (II) defect or worked layer, (III) reaction layer, (IV) adsorption layer and (V) contamination layer. (c) surface topography on an atomic scale [36]

2.5.1 Plastic Deformation

The microstructural changes which take place during cold deformation are significant in the aspects of deformation mechanisms and mechanical properties. Additionally, recovery and recrystallization are influenced by deformation microstructures.

2.5.1.1 Macroscopic Strain Accommodation

The microstructural evolution of polycrystalline materials during plastic deformation involves macroscopic and microscopic strain accommodation processes. Macroscopic strain accommodation has been explained by a number of deformation models. Of these, the Taylor theory suggests that all grains in a polycrystalline experience the same homogeneous strain as the bulk material and that, homogeneous slip occurs when simultaneous slip of at least five independent slip systems takes place. Modifications to Taylor's theory, specifically the relaxed constraints (RC) model, suggest that heterogeneous plastic interactions between grains accounts for part of the mechanical continuity but, the majority of slip is still homogeneous. Regardless, the type of model and the number of slip systems will influence the development of deformation and flow stress behavior [96, 97].

25

2.5.1.2 Polycrystalline Deformation

During plastic deformation the slip pattern and number of slip systems is of great significance. The non-uniformity of slip is a key characteristic of the deformation pattern. A number of surface observations show that few slip systems operate in individual parts of grains; this may not necessarily represent the bulk behavior [97]. Nonetheless, it is suggested that the number of slip systems operating in individual parts of a grain is fewer than suggested by the Taylor model. With fewer slip systems the flow stress is reduced due to a decrease in intersecting jogs. Therefore, the stress required for further deformation at a given strain is lowered. A reduction in slip systems is energetically favorable, but the number of slip systems cannot be too low because strain accommodation will be difficult and the build-up of cell walls as LEDS is dependent upon slip systems [97].

As polycrystals with a reduced number of slip systems deform, grains may subdivide into volume elements [97]. These volume elements may deform as a group similar to the Taylor model. However, since the number of slip systems in each volume is reduced dislocation boundaries will be generated (see Figure 2-9). With increasing strain, further subdivision of grains transpires. In general, for individual volume elements to be formed as a result of reduced slip systems, it must be apparent that differences in the number of slip systems varies across a grain and that, the number of operating slip systems varies with grain orientation, grain size, and deformation mode [97].

a dislocation structure; *b* slip line pattern
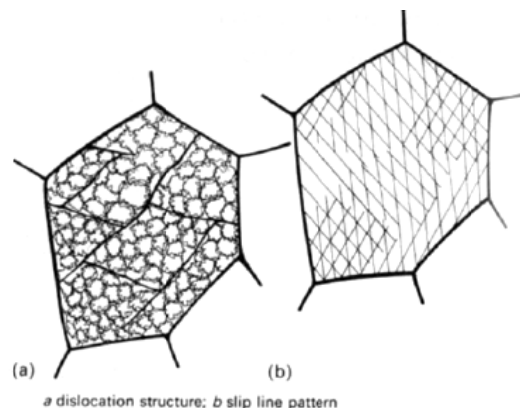
Figure 2-9 Dislocation structure and slip line pattern in grains where individual regions deform by fewer than five independent slip systems; in (a), dense dislocation walls delineate volumes containing ordinary equiaxed cells [97].

2.5.2 Deformation Microstructures

2.5.2.1 Subdivision of Grains (macroscopic)

Through hardness measurements, local strain measurements, and etching techniques the macroscopic heterogeneous nature of plastic deformation within and between grains can be observed [97]. Heterogeneous deformation is partly caused by grain subdivision; in which each subdivided region contains a homogeneous deformation pattern different from neighboring regions. These regions are distinguished by dense dislocation walls (DDWs) which are dislocation boundaries with about three times higher misorientation than ordinary dislocation cells (2° misorientation). They extend several times farther than ordinary cells, so as to form one continuous boundary. DDWs are boundaries in which the combination of active glide systems changes, unlike steady glide systems of ordinary dislocation cell walls [97].

2.5.2.2 Subdivision of Grains (microscopic)

Macroscopic subdivision of grains is followed by microscopic subdivision by the formation of cell blocks [96, 97]. Cell blocks are volumes of continuous dislocation cells that display the same combination of operating glide systems but, which are too few to satisfy the Taylor criteria. The cell blocks are distinguished by DDWs and microbands (MBs) (see Figure 2-10).Microbands are plate-like zones of material bounded by dislocation boundaries situated on DDWs, which have a combination of slip systems different than that of the adjoining material. Microbands generally contain a high dislocation density, have a width of a few tenths of a micrometer, and extend over tens to hundreds of microns [96, 97].

First generation microbands develop from DDWs and are usually parallel to the (111) planes or the pattern of flow [97]. Since DDWs accommodate misorientations between cell blocks of different operating glide systems, they contain excess energy and hence, are optimal sites in which MBs can nucleate. MBs can exist in various forms such as strings of small pancake shaped cells, paired dislocation walls, or sections of double walls. As strain increases the number of DDWs and MBs increases thus, decreasing the

size of ordinary cells and increasing the degree of misorientation across the cell walls [97].

Second generation microbands are oriented close to the (111) planes and associated localized shear [97]. The misorientation across the MBs is small and they generally exist in grains with ordinary cell structures. At larger strains, ranging from 0.5 to 1, deformed microstructures can still contain MBs. These microbands survive because they rotate according to the flow pattern or were in a favorable orientation with respect to the specimen geometry. Eventually, the MBs may lose their distinct appearance and be replaced by a flat/laminar subgrain structure oriented in the direction of flow. Further increasing the strain will result in deformation by local shearing exemplified through shear bands, which are not limited or oriented with respect to grain boundaries [97].
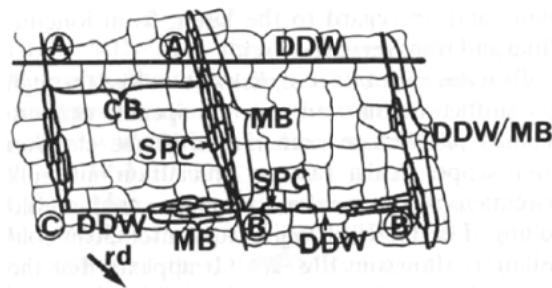
Figure 2-10 Idealized microstructure in a thin foil from a longitudinal section of an f.c.c. metal such as aluminum, after rolling in direction (rd), including DDWs and MBs which are dubbed DDW-MBs when occurring in combination. DDWs are boundaries delineating cell blocks (CB) composed of ordinary dislocation cells. MBs are composed of small pancake-shaped cells (SPC) in layers in 1 to 4 lying side by side. [96]

2.5.2.3 Surface Relief Structures

Surface deformation structures compliment those observed in the bulk, but are not always identical [97]. They provide permanent records of the structural changes, while the bulk matrix develops continuously with deformation. Surface relief structures provide insight into the deformation mechanisms. For example, the number of slip systems operating, typically 1 to 3, within an individual grain has been observed to increase with strain. In addition, the change in slip line length with increasing strain and its relation with microstructure is of importance. In general, it has been observed that the

slip line length decreases with increasing strain, dependent upon the development of sub-boundaries or spacing between dislocation walls which inhibit dislocation motion. At intermediate strains the slip line length is larger than the cell size and hence, dislocation glide cannot be retained by the cell walls. Conversely, at large strains the slip line length is about the size of subgrain cells and thus, limiting dislocation motion [97].

2.5.2.4   Grain Size

In general, the effect of grain size does not scale with microstructural evolution [97]. This can be observed by comparing cold rolled aluminum and tensile strained copper. For cold rolled aluminum well developed MBs tend to form in specimens containing large grain sizes (80-400 μm). On the other hand, in the case of tensile strained copper DDWs and MBs are more readily found in specimens having small to medium grain sizes (20-50 μm). Clearly, the deformation pattern is different for specimens with varying grain sizes; and it appears that grain subdivision becomes less prominent in finer grained microstructures. This could be a result of an increase in intergranular interactions that raise the number of operational slip systems and possibly promote homogeneous deformation as in the Taylor condition [97].

2.5.2.5   Effect of Plastic Strain

Microstructural evolution of f.c.c. materials appear to be independent of medium and high stacking fault energies; and does not scale with grain size [97]. The first step to microstructural evolution is the subdivision of grains at low strains into regions. At larger strains subdivision of grains may produce subgrains. Both the regions and subgrain deform homogeneously within their specific slip systems. However, when comparing neighboring regions with one another heterogeneous deformation can be seen. Heilmann et al. [81] were one of the first to study heterogeneous deformation in detail by measuring the rotation of deformed cells in copper; while Zhang and Alpas [7] studied subsurface plastic deformation in Al-Si alloys after sliding. Between the first and final step (regions and subgrains), the formation of DDWs and MBs delineate cell blocks which contain ordinary dislocation cells. As strain is increased, the ordinary cells will continue to rotate and hence, deformation of the cell block will be difficult along the

same combination of slip systems. Therefore, the size of cell blocks will decrease with increasing strain [97]. Figure 2-11 illustrates the reduction of cell size nearing the worn surface as strain increases.
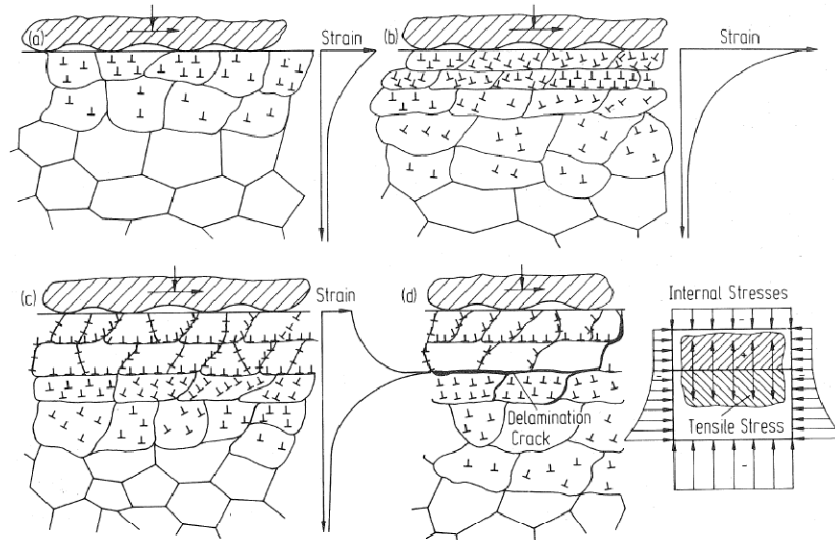
Figure 2-11 Dislocation structures, strains and stresses below a metallic surface during dry sliding contact: (a), (b) increasing dislocation density and strains, due to increasing traversals by asperities of the counterface, (c) recovered dislocation cells, resulting in a decrease of surface strains, (d) delamination cracks and internal stresses [36].

2.6 Lubrication

A lubricant operates by introducing a material of low shear strength between two sliding surfaces of higher shear strength. Lubricants reduce the strengths of junctions formed and minimize asperity contact. In most cases the use of a lubricant will reduce the rate of sliding wear [98]. Lubricants typically consist of base oils and additives. Lubrication can be classified into five types: hydrodynamic, hydrostatic, elastohydrodynamic, boundary, and solid lubrication [31].

2.6.1 Viscosity

Viscosity is the most important property of lubricating oils. Viscosity is the measure of the shear stress on a plane within a fluid, per unit velocity gradient normal to the plane. In laymen's terms, it is the resistance to shearing flow of a fluid. Fluids can support no static shear stress, as they have no shear strength. However, they do support a dynamic shear stress due to their viscous properties. The proportionality between the

dynamic shear stress τ and the shear strain rate ($d\gamma/dt$) defines the viscosity (η) of a fluid [98].

$$\tau = \eta(\frac{d\gamma}{dt})......(2-11)$$

The value of η in the above formula is termed the dynamic viscosity with dimensions of mass $\times$ length^{-1} $\times$ time^{-1}. Kinematic viscosity is simply the ratio of the dynamic viscosity to the fluid density (η/ρ).

2.6.2 Oils

Mineral oils are common in lubrication applications. They are comprised of multiple different hydrocarbon species with average molecular weights from 300 to 600. Mineral oils can be classified into three groups paraffinic, in which the naphthenes have long sidechains; naphthenic, which have naphthenes with short sidechains; and mixed. When mineral oils become unstable, for example at high or low temperatures, synthetic oils can be used as lubricants [98].

The viscosity of a mineral oil relies highly on its composition, molecular weight, and temperature. The hydrostatic pressure (P) of oil will affect the viscosity exponentially,

$$\eta = \eta_0 e^{\alpha p}......(2-12)$$

where η_o and α are constants for a particular oil [98]. A viscosity index (VI) compares the behavior of an oil to that of two reference oils with known VI. Typical vehicle oils have a VI of 150. Polymers known as viscosity index improvers can be added to an oil to enhance its viscous properties. However, these additives can lose their effectiveness at high shear rates, resulting in a sharp drop in viscosity. Other additions to gasoline engine oils will typically consist of dispersants, detergents, antiwear agents (see §2.11.1), oxidation inhibitors, corrosion inhibitors, foam inhibitors, and pour point depressants [98, 99]. Modern engine oils are a complex combination of additives and base oil. A typical engine oil composition is shown in Table 2-I.

Table 2-I Concentration range of main additives used in the formulation of engine oils [99].

Material	Weight (%)			Material	Weight (%)		
SAE 30 or 40 base oil	71	to	96.2	Antioxidant/Wear	0.1	to	2.0
Metallic detergent	2	to	10	Friction Modifier	0.1	to	3.0
Ashless dispersant	1	to	9	Anti-foam agent	2	to	15 ppm
Zinc dithiophosphate	0.5	to	3	Pour point depressant	0.1	to	1.5

2.6.3 Hydrodynamic Lubrication

Hydrodynamic lubrication takes place when sliding surfaces are separated by a thick film of fluid lubricant [98]. Pressures within this film are generated hydrodynamically and support the normal load. The pressure that supports the normal load originates from the viscous forces within the lubricant, which in turn is the product of the relative motion of the surfaces. For hydrodynamic lubrication to occur the opposing surfaces must be conformal. The gap between the sliding surfaces must converge for a hydrodynamic film to be formed [98]. Figure 2-12 shows the effects of viscosity, velocity and load on the coefficient of friction. As seen in this figure if the load is increased and speed decreased, the local pressure on the film will rise. This induces a rise in the film viscosity, possible elastic deformation under the high load, and asperity contact. Therefore the coefficient of friction will rise at high loads and low sliding velocities.
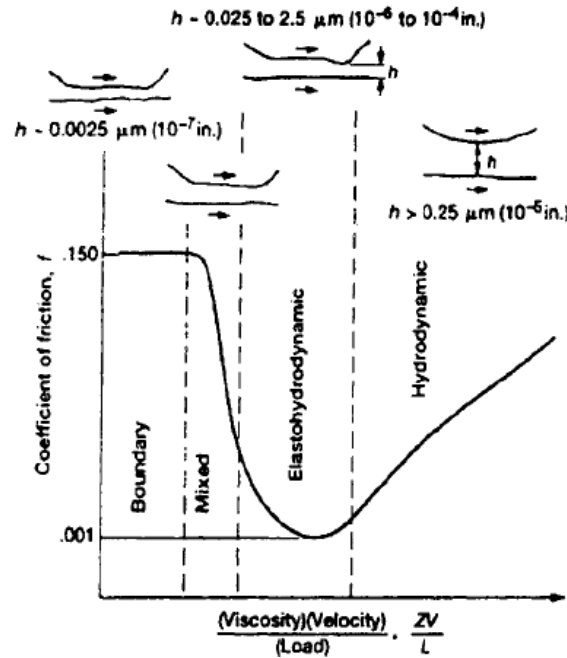
Figure 2-12 Stribeck-Hersey curve coefficient of friction (f or μ) as function of viscosity (Z), velocity (V) / load parameter (L); h = thickness of lubricant film[99]

2.6.4 Hydrostatic Lubrication

Squeeze film or hydrostatic lubrication takes place when surfaces have relative motion in the perpendicular direction, usually occurring under varied normal loads[31, 98]. The normal load W per unit width of an infinitely wide plate separated by a squeeze film is expressed in Equation 2-13, where η is the viscosity, velocity of approach V, length of plate L, and outlet film thickness h_o.

$$W = \eta V (\frac{L^3}{h_0^3})......(2-13)$$

2.6.5 Elastohydrodynamic Lubrication

Elastohydrodynamic lubrication (EHL) occurs for systems that are counterformal, where high local pressures are present compared to hydrodynamic lubrication. The elastic deformation of bearing surfaces and the dependence of lubrication viscosity on pressure influences EHL greatly. Hard EHL occurs when the contact bodies each have high elastic moduli. On the contrary, when one of the contact bodies has a low elastic modulus soft EHL takes place [98].

33

High pressures P associated with EHL will result in enormous viscosity η values [98]. Under high pressure the oil will behave more like a solid due to the rise in viscosity. Already stressed, elastic distortion of the surfaces will have a large impact on EHL, and can be modeled by an elastic sphere pressed on a rigid plane through modified Hertzian equations (see Figure 2-13). For hard EHL contact of a sphere on a plane the minimum film thickness (h_{min}) can be represented by the following,

$$h_{min} = 1.79 R^{0.47} \alpha^{0.49} \eta_0^{0.68} U^{0.68} E^{-0.12} W^{-0.07} ......(2-14)$$

where E is the reduced surface modulus, R the radius of the sphere, η_0 and α are constants for a particular oil, U the velocity, and W the normal load per unit width. Similar equations have been derived for soft EHL [98].

The breakdown of fluid film transpires when the ratio (λ) between the lubricant film thickness and the r.m.s surface roughness (σ^*) reaches a specific value, expressed in Equation 2-15 [98]. The value of λ is a measure of how severe and likely asperity contacts will occur in lubricated sliding. When $\lambda > 3$ full fluid film separates the two surfaces. However, when $1 < \lambda < 3$ partial EHL occurs and contact between asperities can arise. As the lubricant film begins to break down its thickness decreases, resulting in a rise in μ (Figure 2-12). At this point viscous energy dissipation will be enormous and thermal effects take place [98].
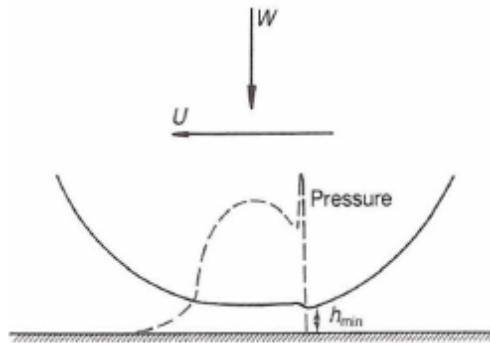
Figure 2-13 Elastic distortion of a sphere (shown exaggerated for clarity) under combined normal load and sliding motion [98].

$$\lambda = h_{min} / \sigma^* ......(2-15)$$

2.6.6 Boundary Lubrication

Under extreme loads or low sliding speeds lubrication film thickness drops drastically ($\lambda<1$), high wear rates will prevail unless boundary lubrication sets in [98]. Boundary lubrication functions by forming absorbed molecular films on the sliding surfaces. Lubricant molecules adhere strongly to the oxide layer present in the metal, align perpendicular to the surface, and are stabilized by mutual repulsion (Figure 2-14). The repulsive forces between the two boundary films help support the load. The end result is a lowered frictional force and substantially less wear. Some oils provide natural boundary lubrication, where a lubricant of only one molecule thick is sufficient to protect a surface. Extreme pressure (EP) and anti-wear additives are also used in boundary lubricants. Under severe conditions in the contact zone these additives react with the sliding surfaces and produce compounds with low shear strength, in turn creating a lubricating film at precise locations. Therefore, a comparison of the chemical attack to the mechanical damage is of great importance for optimum effectiveness of anti-wear additives (see § 2.11.1).
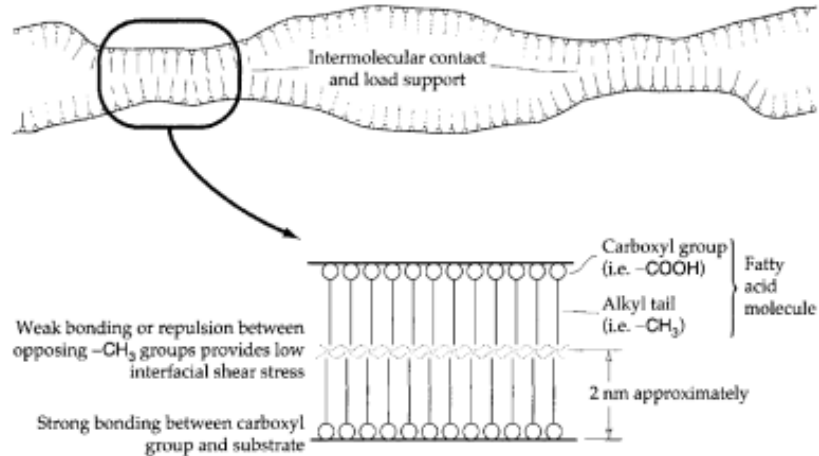
Figure 2-14 Low friction mono-molecular layer of adsorbed organic polar molecules on metallic surfaces [31].

2.6.7 Solid Lubrication

Solid lubrication is made possible with solids that exhibit low coefficients of friction. Solid lubrication is preferred over traditional liquid or gas lubricants when high temperatures evaporate the liquid or gas. Another application arises when a bearing

component is replaced by a solid lubricant, thus creating a 'self-lubricating' system. Solid lubricants can be classified as lamellar solids (e.g. graphite), other inorganic compounds, organic polymers, and soft metal films (e.g. gold electroplating) [98].

2.7   Reciprocating Internal Combustion Engines

The reciprocating internal combustion (IC) engine is the most important component in automobiles, as well as many land and sea transportation devices such as trains, motorcycles, agricultural vehicles, and ships [1]. All IC engines operate on the basis of converting chemical energy into thermal energy by explosively burning a mixture of fuel and air in a narrow cylinder when ignited [100, 101]. There are many different types of IC engines which rely on a piston-cylinder construction, namely the four stroke engine, two stroke engine, and diesel engine. These engines are differentiated by the methods in which the fuel is mixed, as well as how it is ignited (spark or compression ignition). Spark ignition (petrol) engines are the most common engines found in automobiles. Typically, compression ignition (diesel) engines are associated with increased pollutant outputs and heavy engine blocks that exert high power and torque. Hence, they are incorporated into large vehicles such as trucks. However, due to rapid improvements in technology European automakers such as Mercedes-Benz have integrated lightweight aluminum diesel engine blocks into midsized automobiles, such as the E 320, while still conforming to strict nitrogen-oxide (NO_x) emission regulations [101]. The growth of diesel engines within the lightweight automobile sector looks promising in the near future; nevertheless, spark ignition engines still dominate the market.

2.7.1   Working Principle

Nearly all passenger vehicles make use of the four stroke spark ignition (SI) engine, because its fuel consumption and exhaust emissions are relatively low when compared to the two stroke SI engine [100, 101]. The working principle of the four stroke SI engine revolves around the Otto cycle which is comprised of the following sequential strokes: 1) intake stroke, 2) compression stroke, 3) expansion or power stroke, and 4) exhaust stroke. The intake stroke draws in air and fuel mixture, which was mixed

in either a carburetor or intake port, into the combustion chamber as the piston descends in the bore; see Figure 2-15a. Here the cylinder volume increases and the pressure is equal to the atmospheric pressure. The compression stroke takes place when both the inlet and exhaust valves are closed and the piston is raised to compress the fuel/air mixture; see Figure 2-15b. As the piston ascends and reaches the top dead center (TDC) of the cylinder the spark plug is initiated and explosively ignites the compressed fuel/air mixture. The explosion causes the pressure in the chamber to increase which forces the piston down with several tons of force. This is termed the power or expansion stroke; see Figure 2-15c. Lastly, the exhaust stroke occurs when the moving piston pushes the burned fumes through the opened exhaust valve, see Figure 2-15d, and thus allowing the Otto cycle to repeat [100, 101].
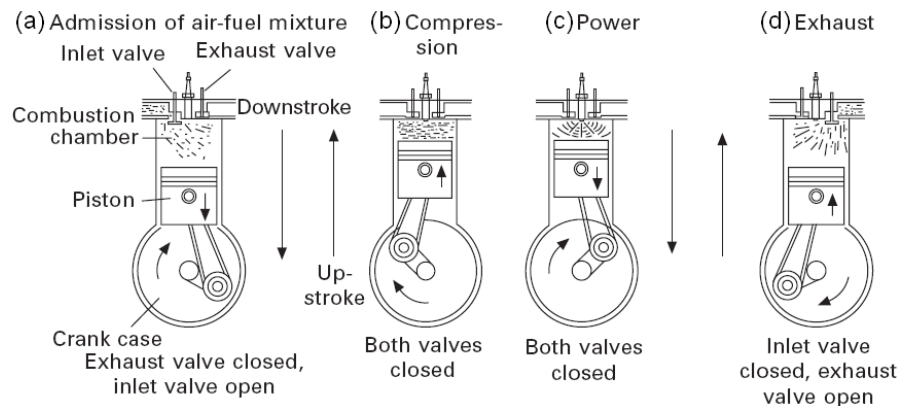
Figure 2-15 **The four stroke engine cycle [101].**

2.7.2 Piston Assembly

Internal combustion engines used for passenger vehicles incorporate a variety of different cylinder orientations and number of cylinders depending on the size of the vehicle. The most common cylinder orientations are the in-line four cylinder, V6, and V8 engines. The V engine has an angle of 90° between the two banks of cylinders designed to minimize vibration through destructive interference of harmonic overtones. These engines are typically used in larger cars and light duty trucks [100].

Regardless of the cylinder orientation, the heart of the reciprocating internal combustion engine is the piston assembly. It is the critical link which transforms the energy generated by combustion of the fuel and air mixture into useful kinetic energy [1].

37

The piston assembly is composed of a ring pack, which is a series of metallic rings, whose primary goal is to maintain an effective gas seal between the combustion chamber and crank case. The top two compression rings mainly facilitate this function; see Figure 2-16. A secondary role of the piston ring is to act as a heat conduction path removing heat away from the piston and into the cylinder wall, and thus into the coolant. Lastly, the piston rings, specifically the oil-control ring (Figure 2-16), regulate the amount of oil transported from the crank case to the combustion chamber. Along with the piston ring pack, the piston assembly also consists of the piston head, piston pin bore, skirt, pin, ring grooves, and ring lands. From a tribological perspective the most important features of the piston, aside from the rings, are the grooves, which secure the piston rings and the piston skirt, which transmits transverse loads of the piston into the cylinder wall [1, 102, 103].
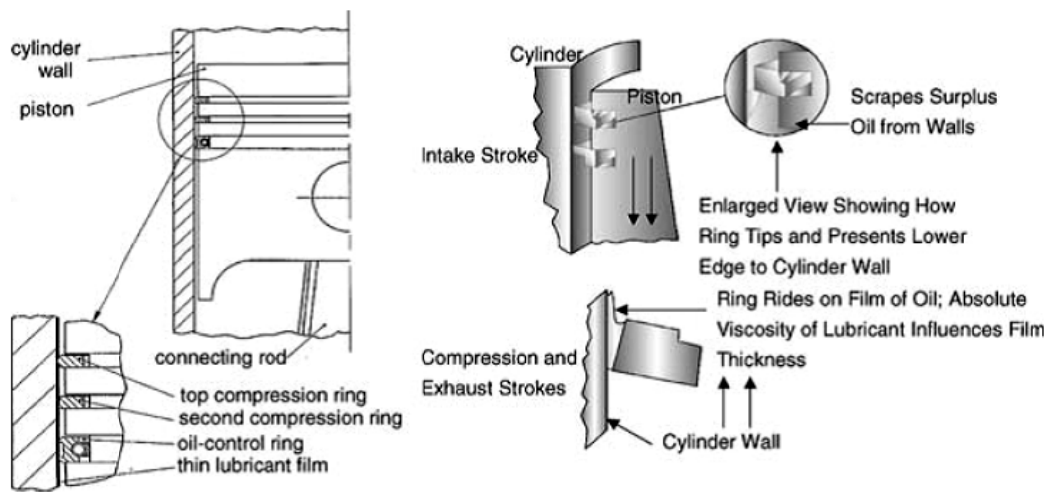
Figure 2-16 **Piston assembly and piston ring function from an internal combustion engine [1].**

2.7.3 Tribosystem of the Piston Assembly

The wear between a piston and an engine bore are of great importance in the automotive industry because approximately 40% of engine power is lost to friction between these two components [100]. To completely describe this tribosystem we must consider the basic body, the contacting body, the lubricant, and the surroundings. With regards to the piston assembly tribosystem, these single elements can be represented as the cylinder, piston and piston rings, lubricating oil, and crankcase air [102].

38

The piston ring interface with the cylinder wall is one of the most complicated tribological components in the internal combustion engine due to large variations in load, speed, temperature, and lubrication [1]. In a single stroke of the piston, the piston ring interface with the cylinder wall can experience hydrodynamic (full), elasto-hydrodynamic (mixed), and boundary lubrication depicted in the Stribeck curve Figure 2-12. The Stribeck curve is influenced by the operating parameters, materials, lubricant, and the surface. Particularly, the surface structure of the cylinder has an effect on wear, fuel consumption, and emissions caused by the lubricating oil which will be discussed later.

At top dead center (TDC) and bottom dead center (BDC) the piston velocity falls to zero and the pressure generation in the lubrication gap can be caused by the preloaded piston ring "squeezing" the lubricated oil out of the gap. Here the oil film thickness is less than the surface roughness, thus a mixed regime is observed (Figure 2-17). Therefore, at TDC and BDC local wear of the cylinder wall is typically observed. With regard to power losses caused by friction, which is directly correlated to fuel consumption, the friction in the areas of the dead centers can be neglected due to the low sliding velocity [102]. Also, during the engine cycle the entire piston can exhibit a secondary transverse movement toward the cylinder wall and tilting about the main piston pin axis. This motion results in mixed or boundary lubrication between the piston skirt and cylinder wall and accounts for 30% of the total piston assembly friction [1]. On the other hand, between TDC and BDC the piston approaches its maximum velocity. At this point, hydrodynamic lubrication is typically observed, caused by the increased piston velocity and convergent gap created by the crowned surface of the piston ring (Figure 2-17) [102].
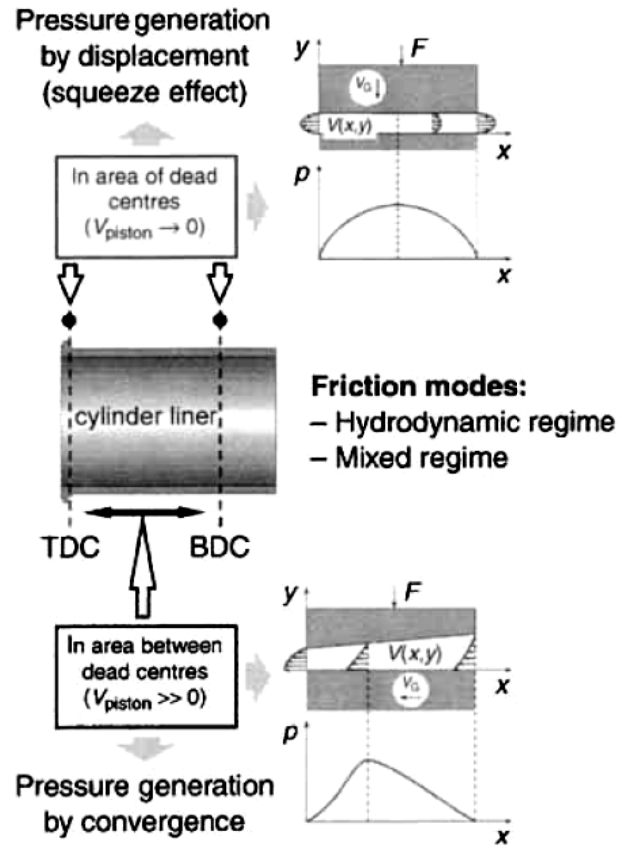
Figure 2-17 **Pressure generation in the lubrication gap [102].**

2.7.4 The Engine Block & Cylinder Wall

The design of the piston assembly is very important with respect to engine tribology; however, the design and structure of the engine block is of equal importance. The engine block acts as the frame of a car engine. It supports and holds all other engine components. It contains the cylinder, which guides the moving piston, receives the combustion pressure, and transmits heat away from the combustion chamber [101].

2.7.4.1 The Monolithic Engine Block

As previously mentioned, many different engine blocks, namely in-line four cylinder, V6, and V8, are available depending on the size and application of the vehicle. Engine blocks can also be categorized by their cylinder structure. There are four different types of cylinder block structures with a variety of material systems as seen in Figure 2-18. The monolithic block is essentially an engine block without a cylinder liner. The cylinder wall consists of the same material as the block or has a surface coating to

improve its wear resistance. The linerless design can greatly improve the compactness of multi-cylinder engines by reducing the spacing between the bores [101].

Monolithic blocks are typically made from grey cast iron due to its low cost, formability, and wear resistance. Materials which act as solid lubricants namely, graphite, MoS_2, WS_2, Sn, and Pb, can be added to the iron block to improve its machining and wear properties [3]. In addition, the mechanical strength of graphite iron monolithic blocks can be enhanced by modifying the graphite microstructure during the casting process. The conventional casting procedure produces a flaky graphite structure associated with high stress concentrations and hence, low strength and ductility. On the contrary, spheroidal graphite or nodular cast iron removes this stress concentration but thermal conductivity and scuffing resistance are somewhat lowered compared to the flaky structure. Therefore, to retain the beneficial properties of both flaky and spherical graphite a vermicular (worm-like) structure is used in compact graphite iron (CGI). CGI exhibits improved mechanical strength and good thermal conductivity. Therefore, CGI allows for the production of thinner and stronger cylinder blocks [101]. When high fuel economy and/or power to weight ratio is of importance a lightweight monolithic aluminum alloy block can be used to replace the heavy cast iron block; and will be discussed in a later section.
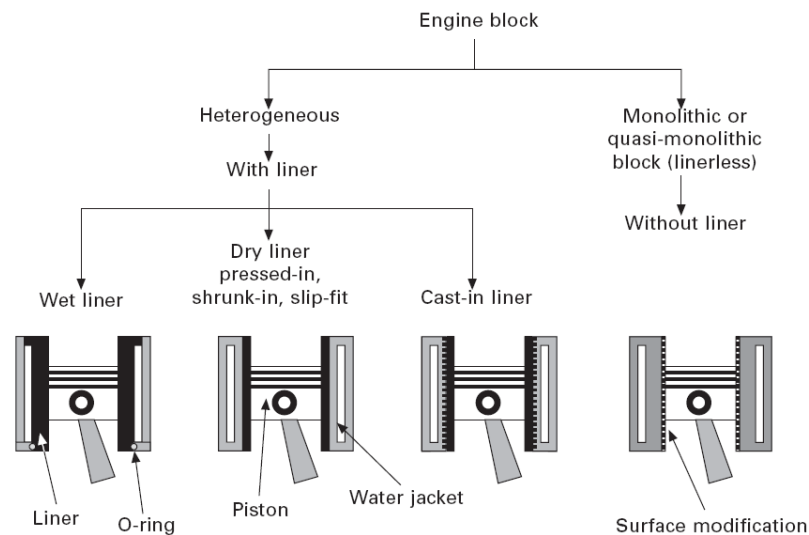
Figure 2-18 **Bore designs in engine blocks [101].**

2.7.4.2 Surface Preparation of Monolithic Al-Si Engine Bores

Lightweight monolithic engine blocks comprised of hypereutectic aluminum silicon casting alloys have been produced by various manufacturers as early as the 1960s [27-29, 104, 105]. The development of the Reynolds 390 alloy (Al-17%Si-5%Cu-Mg) was one of the first, and was used in the Chevrolet Vega engine [24, 25]. Hypereutectic aluminum silicon alloys (14-10 wt% Si) are known for their high specific strength, wear resistance, and hot strength compared to hypoeutectic alloys (Figure 2-19) [29]. This technology was later used in European cars such as the Porsche 928, Daimler Benz 450 SLC and Rolls Royce Camargue. However, their performance was limited by the low casting reliability which produced large sized, irregularly shaped, and unevenly distributed silicon particles.

Currently, a commercial material named "Alusil" (Al-17%Si-4%Cu-Mg) is the forerunner of lightweight hypereutectic aluminum silicon monolithic blocks. Alusil has been used in many high end vehicles, namely Porsche, Bentley, Audi, and BMW, some dating back to the early seventies. Alusil relies on the state of the art low pressure casting process, which brings, besides many qualitative advantages, higher costs compared to high pressure die casting or squeeze casting. Originally, Alusil used honing and etchants to expose the silicon particles from the aluminum matrix; but now it has adopted the multi-stage honing process (Figure 2-20) [106-108].

Honing is a machining process that establishes accurate roundness and straightness to a cylinder by producing grooves or pockets, usually in a crosshatch pattern in its surface to help spread and retain oil [101-103]. This system facilitates the entry of oil into the combustion chamber through the motion of the piston, and causes the emission of unburned hydrocarbons and increased oil consumption. In addition, the surface finish must be controlled and consistent to provide optimal contact characteristics to limit point pressure loading and maintain good heat transfer [103]. Surface finish is typically quantified by the average roughness (R_a). In general, a surface with a high R_a, such as plateau honing, exhibits increased oil consumption but excellent scuffing

resistance at high temperatures when compared to a lower R_a. This is due to the fact that a high R_a can maintain more lubricating oil without disrupting the oil film [101].

Depending on the type of engine and surface finish required, honing can be accomplished and combined with a variety of different techniques and tools such as ceramic stones, diamond hones, rubber tools, cork tools, composite stones of cork or diamond, laser structuring, electron beam, and chemical etching [1, 102]. For example, the surface finish of aluminum silicon bores can be accomplished by a multistage process consisting of: 1) machining, 2) rough honing, 3) semi-finish honing, and 4) mechanical reduction; see Figure 2-21 [100, 106]. The first step, machining establishes the appropriate dimensions and surface finish of the bore by making a rough cut into the bore surface, removing approximately 3 mm of material. The second stage, rough honing establishes a precise geometrical cylindrisity by removing approximately 25 μm with a honing stone. The third stage, semi-finish honing ensures that the final bore diameter criteria is met and is accomplished by the removal of approximately 10 μm of material. Lastly, mechanical reduction or "stripping" of the surface is conducted. Unlike the first three steps, mechanical reduction only removes the soft aluminum matrix not the silicon particles. This is accomplished by a diamond embedded polymer matrix that conforms to the hard Si particles, thus removing approximately 2 μm of soft aluminum matrix. This stage closely resembles the costly chemical etching method, but without negative environmental affects [100]. In addition, the silicon edges are slightly rounded due to the mechanical stripping. This avoids damage to the piston ring during the running-in period, and hence preventing high oil consumption and emissions [106]. To conclude, the honing process can involve many different stages and tools depending on the cylinder material and the surface finish required for optimal engine operation.
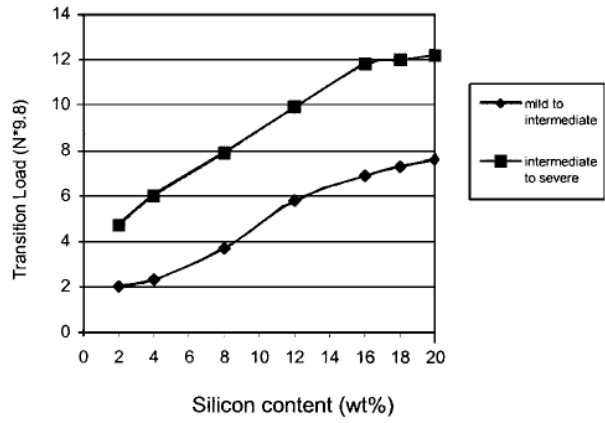
Figure 2-19 **Influence of silicon content on wear resistance of Al-Si alloy [29].**
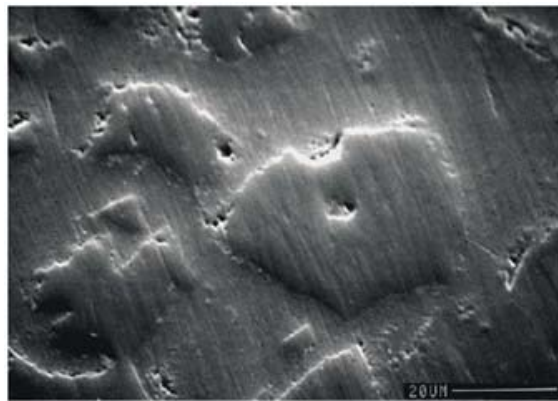
Figure 2-20 **Mechanically exposed Alusil cylinder bore surface after the honing process [108].**
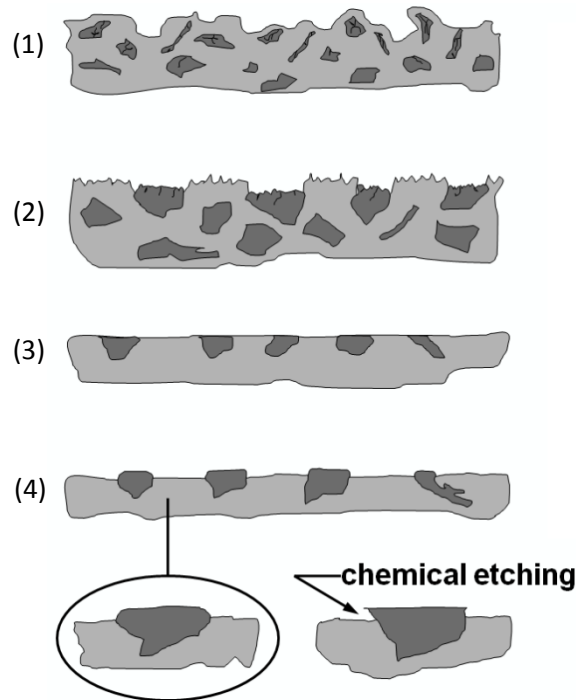
Figure 2-21 Machining sequence during honing of metal matrix composites. The figure shows from top to bottom the initial state and honing steps 2 to 4; after [106].

2.7.4.3   The Heterogeneous Engine Block

Heterogeneous engine blocks **(**Figure 2-18) incorporate a liner or "sleeve" which is usually comprised of a material that has a higher wear resistance than the bulk engine block. These liners come in three different forms: dry, cast, and wet [101]. A dry liner is pressed or shrunk into a cylinder which has already been bored out of the engine block. If the liner is incorrectly fitted into the cylinder it can loosen as a result of the thermal expansion difference of the sleeve and block material. A cast-in liner is the most popular type and is created when the molten engine block metal encompasses a mould containing the liner stuffed with a sand core. After solidification the liner is firmly enclosed by the surrounding engine block material. This firm fit is a result of residual stress caused by the difference in thermal expansion of the liner and block material. Lastly, a wet liner has an outer surface that is directly exposed to the coolant in order to quickly dissipate heat. Since a wet liner does not have the added support of a cylinder block it must be made much thicker than a dry or cast-in liner [101].

45

As previously mentioned, lightweight engines are usually made from aluminum alloys due to their excellent power to weight ratios. These engines can be made with or without liners. Cylinder liners are usually made from grey cast iron via sand casting [1, 11, 103]. To improve wear resistance small amounts of chromium, copper, molybdenum, titanium, nickel, and vanadium are added in combination or individually. Cylinder liner materials correspond to a compromise between tribological properties necessary and the mechanical properties to withstand the thermal stresses that are cyclically applied. A variety of surface coatings and techniques can also be applied to liners such as chrome plating, molybdenum spraying, nitriding, and the Laystall process to improve scuffing, wear, and corrosion resistance [103].

2.7.4.4 Quasi-monolithic Blocks

Aside from honing, a variety of surface coatings and techniques can be used to obtain a wear resistant cylinder or liner. As previously mentioned methods such as: chrome plating, molybdenum spraying, nitriding, thermal spraying, and the Laystall process are ways in which liners can be coated [103, 109]. Similarly, surface coatings can be applied to linerless aluminum engines; this establishes the quasi-monolithic engine block concept. The goal of a quasi-monolithic block is to achieve the advantages of a monolithic block with reduced costs for mass production. This can be accomplished by a number of methods summarized in Figure 2-22.

Silicon enrichment of cylinder bores can take place only locally (i.e. near the contact surface) and still exhibit good wear resistance. For example, this can be accomplished by the commercial coating "Nikasil" which is galvanically (electrolytically) applied to aluminum bores. Here, small SiC particles in the nickel based coating strengthen the matrix and its hardness. Compared to oxide coatings, Nikasil coatings offer high scuffing resistances and less damage to piston rings. However, if chrome rings are used, apparent material transfer takes place by adhesion due to the mutual solubility between Cr and Ni. In addition, the nickel based coating has been reported to react with sulfur present in fuels, causing excessive bore wear. Nevertheless,

it has been reported to demonstrate good wear resistance and has been used in BMW's M52 and M60 engines, the Corvette ZR1, and the Porsche 911 [11].

Aside from surface coatings, a quasi-monolithic block can also be created by the commercial concept termed "Lokasil". Lokasil applies highly porous, hollow cylindrical parts of silicon, so-called performs, that are infiltrated during casting under pressure with economical secondary alloy (A226) [106, 110]. Therefore, Lokasil is a unique concept which links the advantages of a lightweight monolithic block and the highly productive die casting process.
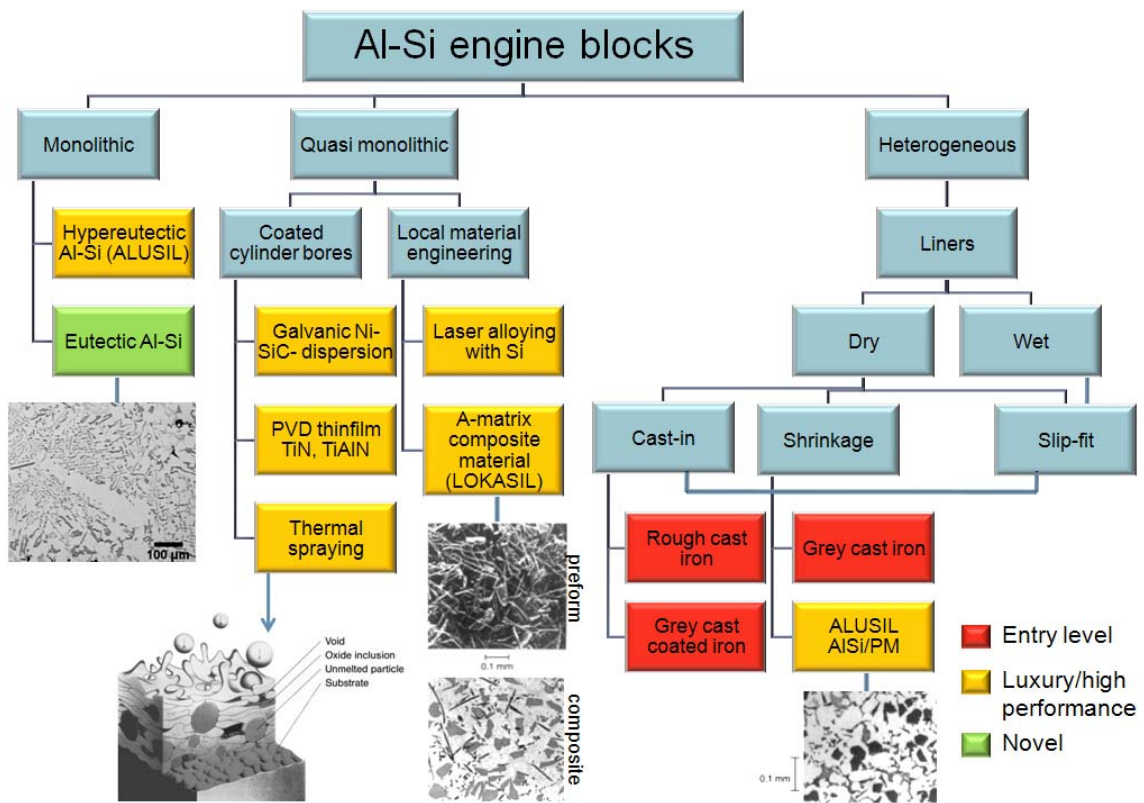
Figure 2-22 **Cylinder surface technologies for aluminum engine blocks; after [106].**

2.7.5 Engine Wear

Engines are repetitively subjected to an array of extreme operating conditions such as: high/low temperatures, high loads/stresses, varying sliding speeds, engine contaminants (e.g. soot), and insufficient lubrication. All these factors will influence the wear of an engine, some more than others. For example, cold engine temperatures are a

frequent occurrence during the initial start up of an engine; in this case little or no oil is present on the cylinder walls and the flow of oil is restricted due to its increased viscosity caused by the cold temperature. Although, high temperatures can cause excess wear in an engine due to the oil layer burning off, these conditions are not as frequent and detrimental when compared to the problems associated with a cold engine start. There are three main types of engine wear, namely corrosion, abrasion, and scuffing; each can occur separately or in unison [105].

Engine corrosion is most often associated with cold engine temperatures where natural condensation can easily form [111]. At cold temperatures the oil loses its fluidity; this results in a thin oil layer which allows moisture to make contact with the engine bore. As a result, corrosion of the engine bore takes place. In addition, the accumulated moisture can react with the normal engine deposits present in the oil, thus making the oil acidic resulting in further material loss via corrosion [105, 111]

In general, scuffing is considered the most destructive form of engine wear. It is generally accepted that once a lubricant and its protective films fail scuffing will occur; which is defined as a form of localized damage, in sliding contact, resulting from plastic deformation and adhesion [32, 36, 112]. Scuffing is not a new phenomenon; however no universal model has been accepted to explain its complexities. Fortunately, bench and laboratory experiments [11, 20, 31, 32, 36, 42, 104, 109, 111-118] are in general agreement upon the fact that scuffing is dependent upon the surface preparation, materials, lubrication, temperature, and duration of the wear system. It can take place even when there is only a limited amount of damage and/or wear. Scuffing is a progressive process which starts at the scale of a single asperity further leading to macroscopic deformation and eventually seizure of the mechanism. Plastic flow of the asperities progresses to a point where the high temperatures and stresses which are associated with the release of energy cause the lubrication film to break down, thus leading to surface damage (Figure 2-23). In this case, deformed asperities eventually break away due to plastic fatigue and agglomerate forming large work hardened particles. These particles increase contact stresses beyond sustainable fluid film

lubrication resulting in high contact temperatures and often welding or adhesion of the surfaces [31, 36, 119]. In depth reviews attempting to clarify the scuffing phenomenon have shown that no single scuffing criteria incorporates more than one or two of the many relevant variables at the sliding interface, and thus none can be applied universally [119, 120].
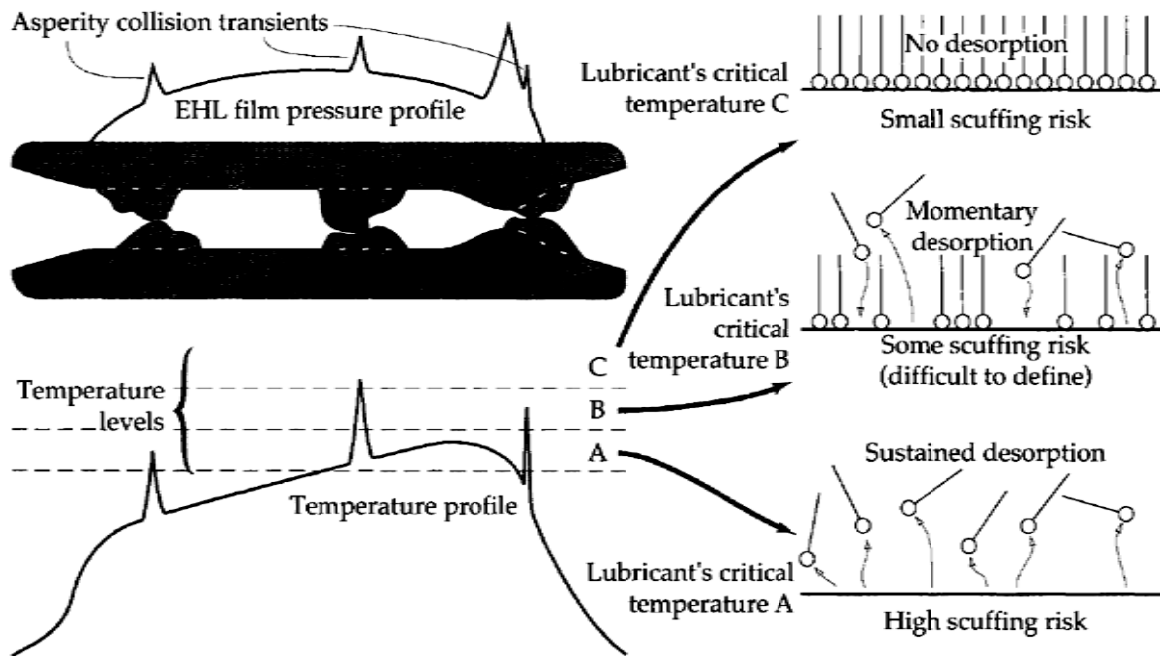
Figure 2-23 Model of transient and steady state temperatures in a mixed lubrication sliding contact [31].

2.8   Aluminum Silicon Alloys

A large number of foundry alloys are based on the aluminum-silicon system, as they typically provide excellent strength to weight ratios. These alloys are divided into three categories depending on the silicon content, which are: hypoeutectic alloys containing 5 to 10% Si, eutectic alloys with 11 to 13% Si, and hypereutectic alloys associated with 14 to 20% Si (Figure 2-24). The binary Al-Si system has a eutectic temperature at 577°C [29]. As the alloy solidifies, primary aluminum forms and grows as dendrites or the silicon phase forms and grows in angular primary particles. Once the eutectic point is reached, eutectic Al-Si phases grow and nucleate until the end of solidification. At room temperature, hypoeutectic alloys consist of a soft and ductile primary aluminum phase along with a hard and brittle eutectic silicon phase. Conversely,

hypereutectic alloys contain coarse, angular primary silicon particles complimented by the eutectic silicon phase [29, 107]. Silicon which has a low density of 2.34 g/cm^3,reduces the overall weight, increases corrosion and wear resistance, improves casting and machining characteristics, and lowers the thermal expansion of the alloy [29].

Impurities such as iron, manganese, copper, and zinc exist in varying amounts within a given alloy depending on the purity of the base material. In fact some of these elements, namely copper and magnesium, are added intentionally as alloying elements to improve the strength and hardenability of the cast material. The alloying elements and impurities partly go into solid solution with the matrix, as well as forming intermetallic particles upon solidification [121].

Specifically, for hypoeutectic alloys the following sequence of phase precipitation will take place [121]:

1. Primary α-aluminum forms a dendritic network.

2. Formation of aluminum-silicon eutectic regions.

3. Precipitation of secondary eutectic phases such as Mg_2Si and $CuAl_2$.

In eutectic alloys, pre-eutectic reactions may be avoided and in hypereutectic alloys, a primary reaction involving the precipitation of silicon will occur until the eutectic composition is attained. In addition to the main reactions, precipitation of other phases such as iron and manganese containing phases can take place [121].
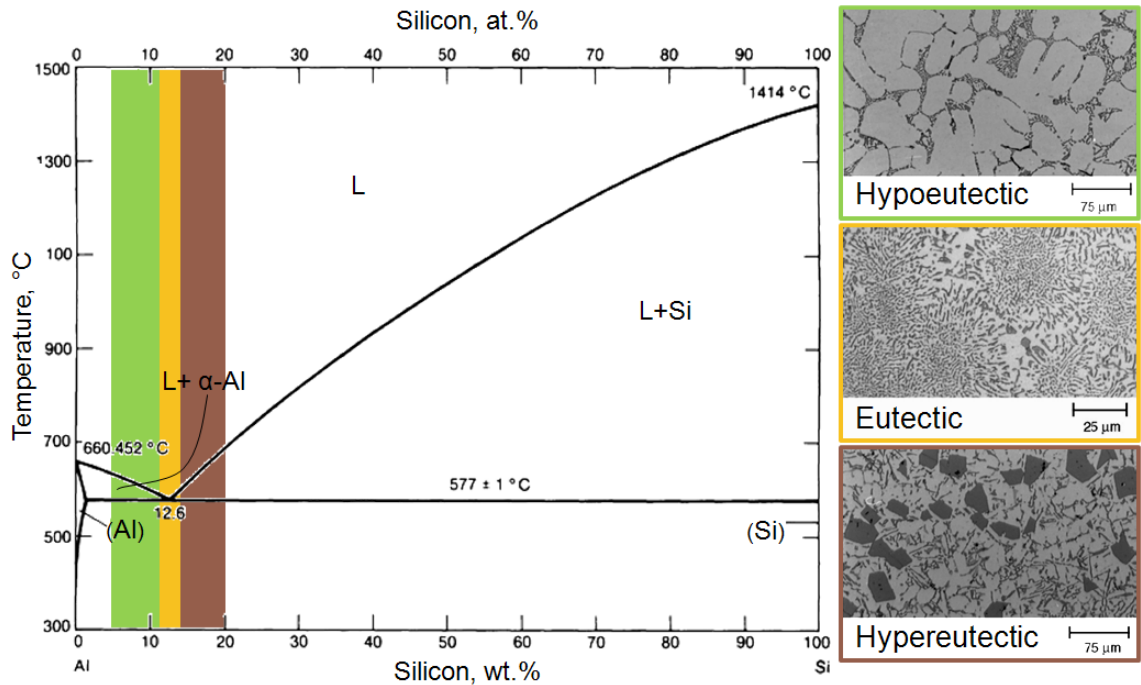
Figure 2-24 Typical microstructures of hypoeutectic (Al-5.7Si, A319), eutectic (Al-11.9Si, A339), and hypereutectic (Al-15Si, A390) aluminum-silicon commercial alloys and corresponding binary Al-Si phase diagram; after [122].

2.8.1 Al-Si Alloys Designed for Wear Resistance

Aluminum silicon alloys are known for their exceptional combination of preferable characteristics, which includes excellent castability, low density, and good mechanical properties [123]. Hypereutectic Al-Si alloys are most commonly used to provide wear resistance, as they contain coarse, angular, primary silicon particles as well as eutectic silicon. Commercial Al-Si alloys generally contain other alloying elements, as in A319 and A356 which further enhance or modify the wear resistance or impart additional properties to the alloy. The role of the microstructure, and specifically the hard phases and particles, play in providing wear resistance in aluminum casting alloys is still not fully understood. Both laboratory scale wear tests [11, 12, 20, 21] and engine tests performed on hypereutectic Al-Si alloys [16, 17] indicate that the hard particles that simply carry the entire load is not correct. Therefore, a wear resistant aluminum alloy should contain a solid solution strengthened-matrix, coherent precipitates of intermetallic compounds, and very fine, hard ceramic particles [2]. The subsequent sections will

discuss the alloying elements and their control, processing routes, strengthening methods and theories, and lastly the surface preparation of Al-Si cylinder bores.

2.8.2 Role of Alloying Elements

Silicon is an important alloying element since it reduces thermal expansion and increases fluidity of the melt. Moreover, mechanical properties such as tensile strength, hardness, wear resistance, and ductility are influenced by the silicon content. The latter being due to the reduced tendency of high silicon content alloys to form large pre-eutectic α-Fe and β-Fe intermetallics during solidification [2, 3].

Copper, magnesium, and zinc are commonly added to improve mechanical properties via solid solution strengthening and precipitation of their intermetallics (i.e. Al_2Cu and Mg_2Si). The presence of iron and nickel allow the alloy to operate at elevated temperatures [2, 4]. In a study of an Al-11.7%Si alloy [4], nickel has been reported to improve the Si modification process linked to strontium. Additionally, Yuying et al. [124] has shown that nickel can promote primary Si precipitation in eutectic Al-Si alloys.

Aside from improved elevated temperature properties, iron also prevents sticking between the mould and casting, but also creates large brittle α-Fe and β-Fe plates that lower ductility. Manganese additions are used to reduce the detrimental effects of the β-Fe phase by replacing it with the less-detrimental Chinese script α-Fe phase and improve the elevated temperature properties of the alloy [5, 123]. In addition, the ultimate tensile strength (UTS) and % elongation have been observed to increase with increasing Mn up to an amount corresponding to a Mn/Fe ratio of ~1.2, after of which excess amounts of α-Fe are observed [5]. Improved mechanical properties by the addition of Mn are due to the lower amounts of the β-Fe phase whose morphology restricts feeding during solidification, thereby increasing shrinkage porosity. In general, the best combined effects of strength and ductility will occur at low Fe contents and high cooling rates [6].

Phosphorous is an impurity that enters the aluminum casting melt through contact with tools, refractories, and crucible glazes. In hypereutectic alloys it is added deliberately to form AlP particles which nucleate primary Si [6, 125]. However, in hypoeutectic alloys the effect is negative, wherein the Si is coarsened by the

phosphorous; reasons for this are unknown. Phosphorous can sometimes be advantageous, as in a Al-9 wt.% Si-3 wt.% Cu alloy where the addition of 19 ppm phosphorous noticeably reduces the percentage porosity [29]. In general, the negative effects of phosphorous on the eutectic structure outweigh the good, and hence the phosphorous content is usually kept to very low levels.

2.8.3   Silicon Modification

In Al-Si alloys the effect of silicon content and morphology on the wear resistance is very important and has been the main focus in many studies [12, 126-131]. In general, the resistance to permanent sinking-in of silicon particles into the aluminum matrix increases with the unexposed surface area to the buried volumes of the particles [127]. Smaller silicon particles provide the stiffest resistance to sinking-in, and hence the silicon morphology will play an important role in wear resistance. Silicon morphologies will depend on the complex interaction of five variables: type of modifier (i.e. sodium and strontium), impurities present in the melt (i.e. phosphorous), amount of modifier, cooling rate, and the silicon content of the alloy [132]. In general, high solidification rates assist modification and lower modifier levels; while high silicon concentrations require large amounts of modifier for complete modification.

Modifiers such as sodium and/or strontium are believed to modify the plate-like silicon structure into a branched fibrous seaweed structure by the theory of Impurity Induced Twinning (IIT) [132]. The effect of mischmetal as a silicon modifier has also been of interest [133]. Mischmetal (MM) is a mixture of rare earth metals Ce, La, Nd, and Pr, which possesses a high chemical affinity for forming various intermetallic phases with other elements. Studies [133], show that MM does modify eutectic silicon particles and is most effective at high cooling rates. However, when MM is added to a Sr containing alloys the interaction between MM and Sr forms intermetallic phases, thereby decreasing the available Sr desired for modification. In general, traditional silicon modification by strontium or sodium is more effective than by mischmetal additions.

2.8.4   Solute Redistribution

Solidification of an alloy rarely results in a solid in which the alloying elements are distributed uniformly. In general, redistribution of solute occurs during freezing, producing a solid that is inhomogeneous on the macroscale, microscale, or both [134].

Inhomogeneous solute distributions associated with solidified alloys arise from discrepancies between the heat transfer (relatively rapid process) and solid state diffusion rates (relatively slow process) [134]. Thus, while the temperature of a system can be made to decrease rapidly, the slowness of the solid state diffusion restricts the ability for compositional change in the allotted time.

Particularly for Al-Si alloys microsegregation refers to inhomogeneities associated with the dendritic structure at the same scale size of dendrites (i.e. a few micrometers to a few hundred micrometers). Prevention of interdendritic segregation is a virtual impossibility, as it requires freezing with a planar solid-liquid interface. Ensuring that solidification takes place as quickly as possible is the best method to minimize segregation. In this way, the deleterious aspects of microsegration, such as brittle intermetallics, will be minimized by ensuring these microstructural features remain small and uniformly distributed [134].

2.8.5   Processing

Two main processing methods are available i) foundry: melting and casting, and ii) powder metallurgy: rapid solidification and consolidation. Each method has its own advantages and disadvantages [2, 135]. For this particular study, sand casting is the processing technique coupled with honing, mechanical reduction, and/or chemical etching (see §2.7.4.2), to provide the desired bore finish. A sand cast part is produced by forming a mold out of a sand mixture and pouring the molten metal into the sand mold. Once the metal solidifies by air cooling the sand mold is broken away and the cast part removed. Sand casting is associated with lower mechanical properties when compared to new casting techniques such as semi-solid processing, squeeze casting, and the Cosworth process. This is mainly due to the primary dendrites which grow and interact with each other. As a result, when only 20% of the melt freezes, viscosity decreases rapidly and

fluidity drops drastically; thus imparting poor characteristics such as porosity issues and microsegregation [29]. Sand casting may have its flaws but overall it is preferable for the mass production of engine blocks since it is cheap, can cast intricately shaped components, and is tribologically superior under boundary lubricated conditions compared to melt-spraying [2, 126].

2.8.5.1 Cell size

The cell size or interdendritic arm spacing (DAS) is controlled by the cooling rate, which in turn is a function of the casting process. These tree-like structures form during solidification as a result of crystallographically preferred directions, demonstrated in Figure 2-25. For Al-Si alloys, high and low cooling rates typically correspond to DAS values of ~40 μm and 120 μm, respectively [123, 133]. A lower DAS is preferable as it is associated with better mechanical properties.
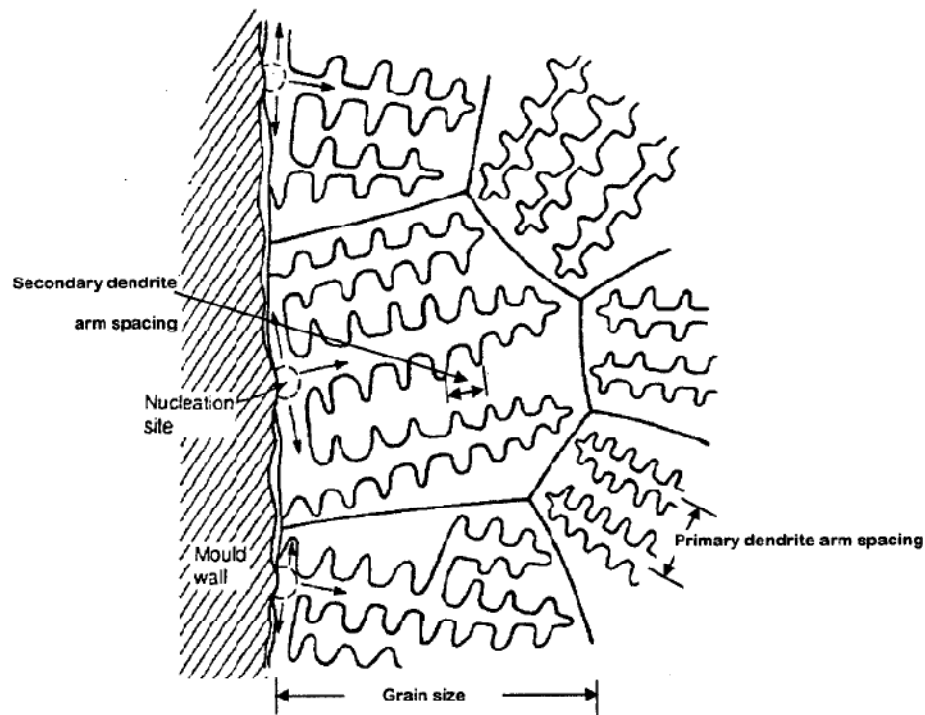
Figure 2-25 Illustration of dendrite arms forming grains in solidifying alloy [136].

2.8.6 Strengthening Methods

Increasing the hardness and toughness of a material will increase its wear resistance. The literature on the correlation between toughness and wear is scarce,

however there is much related to hardness [2]. Hardness can be increased by methods such as strain hardening, solid solution hardening, and precipitation hardening. The inside surface of an Al-Si engine bore can makes use of all these hardening mechanisms. Strain hardening can arise during running-in (see §2.5) of the engine, while solid solution hardening and precipitation hardening is introduced during heat treatment.

2.8.6.1   Heat Treatment (Solid Solution and Precipitation Hardening)

To obtain the desired combination of mechanical properties such as strength and ductility heat treatment is typically employed. For Al-Si alloys the T6 treatment has been deemed to provide the best combination of mechanical properties. The standard T6 treatment encompasses three main stages: solution heat treating, water quenching, and artificial aging; see Figure 2-26 [133, 137]. Solution heat treatment is carried out at temperatures between the solidus and solvus curves of aluminum (~500 °C) in order to i) dissolve the solutes which are responsible for hardening; ii) homogenize the casting; iii) and spheroidize the eutectic silicon. Solution heat treatment situates the alloy in a saturated condition and upon water quenching, which prevents diffusion of the solute atoms, establishes a supersaturated solid solution. Artificial aging is then carried out by further heating the alloy at low temperatures (~155 °C). It is during this stage that precipitation of dissolved elements occurs, which is primarily responsible for the hardening of the matrix; see Table 2-II. It is important to note that the standard T6 treatment described above may not be optimal for all Al-Si alloys, because different systems (i.e. Al-Si-Cu-Mg) have different aging behaviors due to more complex interactions. For example, aging at 170 °C for 8 hours of an Al-Si-Cu-Mg alloy produces optimal properties pertaining to: 432 MPa for UTS, 398 MPa for yield strength, 134 VHN, 0.98% elongation, and 3.88 J for total absorbed impact energy [137].

Table 2-II Typical hardness values of intermetallic constituents of Al-Si alloys [123].

Phase	Hardness	
	MPa	**kfg/mm^2**
CuAl$_2$	3900	400
	3800-7600	390-780
FeAl$_3$	7200	730
	6400-9400	650-960
	5160-7110	526-725
	3500	360
NiAl$_3$	6000-7600	610-770
	7100	720
	4500	460
Ni$_2$Al$_3$	9800-11,000	1000-1120
	7000-14,200	715-1450
	11,880	1211
Mg$_2$Si	4480	457
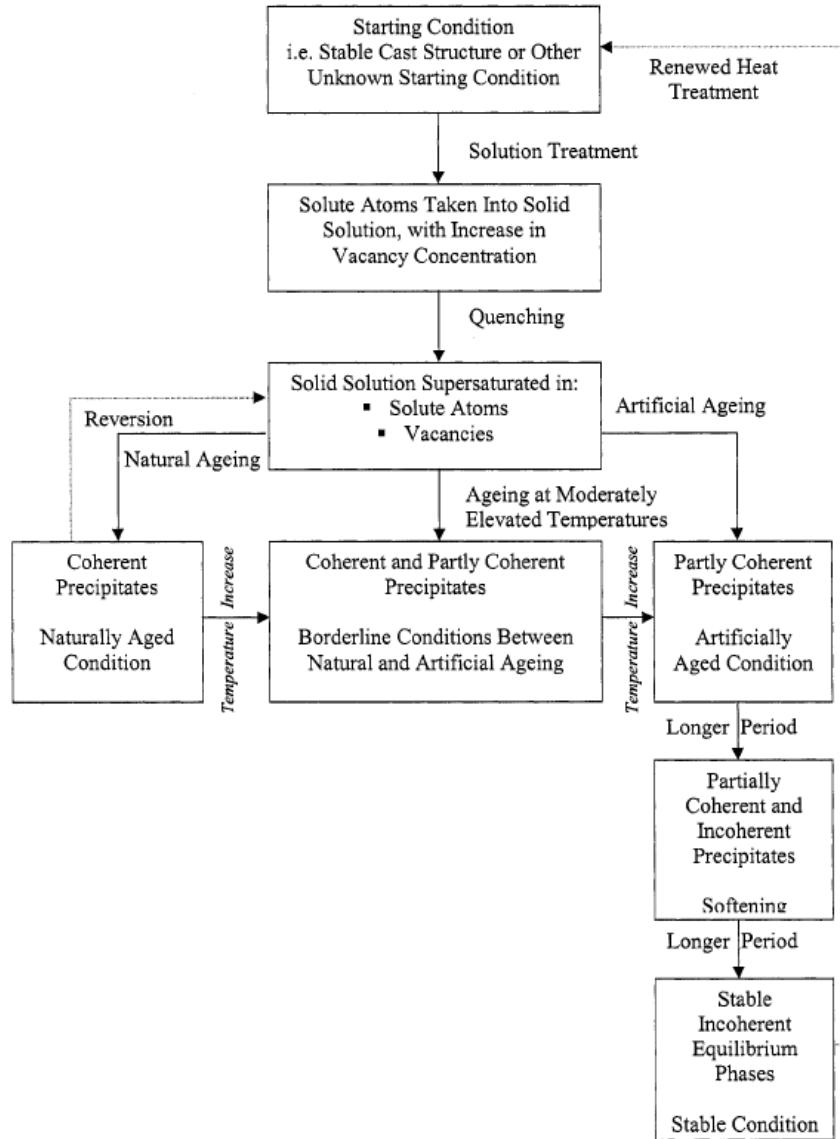
Figure 2-26 Schematic of the hardening process [138].

2.8.6.2   Grain Boundary Strengthening

Grain boundaries help limit dislocation motion because: i) dislocations alter their direction of motion due to the different orientation of grains, and ii) discontinuity of slip planes between grains [139]. Finer grains are favorable as they provide better strength, fatigue life, and fine distribution of secondary phases and microporosity [140]. The grain size of primary aluminum is controlled by the solidification rate and by the addition of heterogeneous nuclei within the melt in the form of inoculants such as Ti and TiB. Aluminum grain sizes typically vary from ~100 to 500 µm [135]. The relationship

between grain size diameter d, and yield stress σ_y is expressed by the Hall-Petch equation:

$$\sigma_y = \sigma_o + kd^{-1/2} ......(2-16)$$

where σ_o is a material constant representing the starting stress required for dislocation movement and k the strengthening coefficient. Since k is relatively small for aluminum alloys sufficient strengthening is only possible with very fine grain sizes [141]. It is important to note, that a grain size below 10 nm will result in a decrease in strength due to grain boundary sliding [142].

2.8.6.3   Strain (Work) Hardening

The interaction of dislocations with one another is the main mechanism of work hardening. Dislocations interact through their individual stress fields; for detailed descriptions of deformation structures and their formation refer to §2.5. These stress fields impede dislocation motion and hence, with increasing dislocation density entanglement and jogs are readily created which thwart dislocation motion. The correlation between dislocation density $\rho^{\perp}$ and yield strength σ_y is as follows:

$$\sigma_y = Gb\sqrt{\rho^{\perp}} ......(2-17)$$

where G is the shear modulus and b burgers vector [139].

2.9   Wear Regimes of Al-Si Alloys

In section 2.3.3.7 the conception of wear regimes in metals was introduced. Specifically, for Al-Si alloys three distinct regimes, ultra-mild wear (UMW) [7, 21, 23, 143, 144], mild wear (MW) [8, 9, 15, 145-147], and severe wear (SW) [8, 9, 15, 145-147], have been delineated. The rate of material removal and the mechanisms responsible are different in each regime.

2.9.1   Ultra-mild Wear

In general, UMW corresponds to light loads (i.e. < 10N depending on the tribosystem) and a wear rate on the order of $\leq 10^{-5}$ mm^3/m. The wear rates associated

with UMW are often immeasurable with the conventional mass loss techniques; therefore, non-traditional methods such as the radionuclide technique (RNT) are often employed [91, 148, 149]. Elmadagli and Alpas [144] have achieved UMW rates when studying the sliding wear behavior of an Al-18.5 wt.% Si (A390) alloy tested in different atmospheres and with different counterfaces. Ultra-mild wear rates were achieved via a block-on-ring (SAE 52100 type steel) configuration when tested in an argon atmosphere and under loads below 10N. Low wear rates pertaining to the UMW under the same loading conditions could not be reproduced in dry air with 5% RH and most likely due to the formation of oxidized iron-rich tribolayers easily subjected to spallation. A390 samples were also tested against diamond-like carbon (DLC) coated steel counterfaces in air and resulted in UMW rates; which resulted from the worn surfaces being free from iron-rich oxidized layers.

Chen et al. [21, 23, 143] have reported UMW rates on etched eutectic Al-Si surfaces under boundary lubricated (5W- 30 synthetic engine oil) sliding conditions using a ball (AISI 52100 steel) on-disc tribometer under light loads of 0.5 N, a sliding speed of 50 mm/s, and over sliding distances up to 2.2×10^3 m (10^5 cycles). The worn surfaces did not show evidence of material transfer, back transfer, or loose debris generation (i.e. small, equiaxed, or plate-like) typical of the MW regime. At the microscopic level surface damage in the UMW regime was observable and occurred by two ways: i) the reduction of Si particle height, by fracture and sinking-in of the harder phases into the softer aluminum; and ii) plastic deformation and flowing-out of the aluminum surrounding sunken-in particles. Chen et al. [21, 23, 143] have suggested that increasing the matrix hardness and silicon particle size, while maintaining a low aspect ratio would improve the load capacity of Al-Si alloys and prolong UMW.

2.9.2 Mild and Severe Wear

Compared to UMW, MW and SW of Al-Si alloys have been studied by numerous authors [8, 9, 15, 145-147]. In general, the MW regime pertains to a volumetric wear rate of 10^{-4} to 10^{-3} mm^3/m, while the SW regime corresponds to a loss $\geq 10^{-2}$ mm^3/m. Sarkar [9] has investigated the dry sliding wear of two Al-Si alloys containing 10.9 and 22.1 %

Si via a pin-brush tribometer with steel and grey cast iron counterfaces. Two regimes were observed: i) mixed mode of elastic plastic contact that followed Archard's law [56] (see §2.3.3.7), and ii) gross plastic flow where the wear rate was not directly proportional to the load. Sarkar also indicated that the hypoeutectic sample experienced lower wear rates than that of the hypereutectic sample; which is in agreement with the work of Clarke and Sarkar [10].

Kanth et al. [147] has identified the existence of a transition in wear rate of an Al-17% Si as-cast alloy dry slid against a hardened EN 24 steel surface at a speed of 0.5 m/s, related to the applied pressure. Two regimes were delineated: i) worn surface contained deep abrasion grooves, craters, and no evidence of a transferred iron-rich layer, and ii) an increased wear rate pertaining to a surface that is plastically deformed with a smooth topography. The transition between the two regimes is controlled by unstable material behavior in hump-shaped pockets of the near surface.

Shivanath et al. [15] divided the wear of Al-Si alloys into two categories based on the dominant wear mechanism and also investigated the effects of chemical etching using a dry pin (Al-Si)-on-disc (steel) apparatus. At low applied loads an aluminum oxide layer (10-80 μm) was generated. Wear initially took place by oxidation of asperities, and secondly by the fracture and compaction of oxidized wear debri into a film. Oxidative wear is considered to be independent of the Si content and morphology; its rate is controlled by the thickness oxide film. With increasing loads metallic wear became the predominant process whereby, the surface was characterized by plastic deformation, fracture, wear debris formation, and significant material transfer. The high wear rates prevented the formation of a protective oxide layer. Higher silicon contents were reported to extend this regime to higher loads. Interestingly, an intermediate wear regime with high wear rates was identified in hypoeutectic samples; however, this intermediate metallic wear was completely suppressed by means of chemical surface etching which left Si particles standing above the Al-matrix.

Conversely, Reddy et al. [146] have reported that binary Al-Si alloys containing 7-17 % Si, when considered as a function of load and dry slid against steel in a pin-on-

disc tribometer, exhibit three distinct regimes: mild, severe, and seizure (see Figure 2-27). MW took place at low loads and was characterized by the in situ formation of a protective iron-rich compacted layer; here, wear debris resulted from abrasion and cracking of this layer. As load increased SW set in and operated by a delamination mechanism [7, 50]; whereby subsurface deformation and cracking resulted in fragmentation of Si particles and elimination of the iron-rich layer. Eventually, when near surface temperatures reached levels high enough to lower the shear strength of the subsurface layer, seizure became inevitable.

Zhang and Alpas [8] have studied the transition from mild to severe wear in aluminum alloys as a function of the applied load and sliding velocity. In addition, they have studied the effects of the contact temperature on the transition zone. At low loads and velocities it was found that MW was caused by the production and delamination of mechanically mixed surface layers. At higher loads and velocities, MW resulted from the delamination of aluminum material adjacent to the contact surface. Severe wear resulted in the production of large wear debris by the process of thermal softening. In addition, it was observed that when the average bulk contact surface temperature (T_b) of an aluminum alloy reaches a critical temperature, typically 0.4 of the melting temperature (T_m) of aluminum, the transition from mild to severe wear is completed for both load induced and velocity induced transitions. It was then determined that this critical transition temperature could be increased or delayed by means of forced cooling, increasing the thermal conductivity of the counterface, development of tribological layers through incremental loading and velocities, and reinforcing the microstructure with ceramic particulates.

Elmadagli and Alpas [150] further divided the MW regime into two sub-regimes using a block-on-ring tribometer under dry sliding and a dry air (5% RH) environments; which encompassed A383 (8 wt.% Si), A390 (18.5 wt.% Si), and Al-25 wt.% Si alloys. The transition from MW to SW and the sub-regimes of MW appeared in all of the tested alloys. The first sub-regime of mild wear (MW-1) took place under low loads and the second sub-regime (MW-2) under higher loads. Tribolayers formed at a faster rate with a

greater amount of material transfer in MW-1; whereas, thick tribolayers easily subjected to spallation were observed in MW-2, and thus accounting for the increased wear rate of MW-2. The wear rate of the MW regime along with its sub-regimes increased linearly with increasing sliding distance; however, the severe wear regime showed an unstable wear rate that increased exponentially with sliding distance.
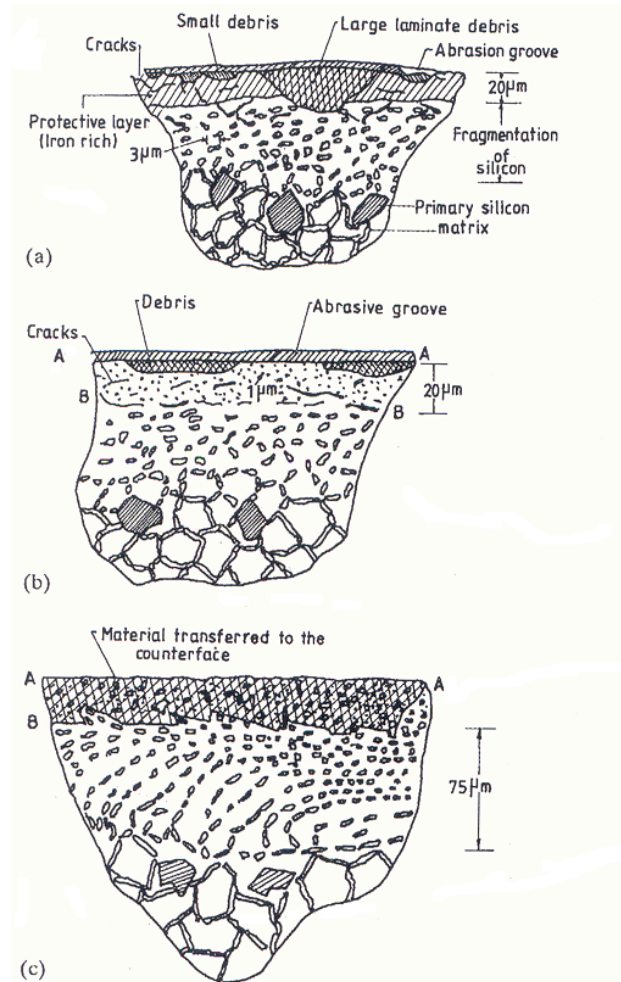
Figure 2-27 Schematic diagram of the following wear processes in Al-Si alloys: (a) mild wear, (b) severe wear, (c) seizure [146].

2.10 Dry Sliding Wear of Al-Si Alloys

2.10.1 Wear Mechanisms

As previously mentioned (see §2.3.3.7), sliding wear often involves many different modes and mechanisms operating in competition or in unison. In fact, the main reason why different wear regimes (see §2.9) exist in Al-Si alloys is essentially due to a variation or change in the dominant wear mechanism [69]. Similar to Lim and Ashby [59], Liu et al. [151] has developed an empirical wear mechanism map, shown in Figure 2-28, for Al-Si alloys using normalized test variables and a physical modeling approach. Here, normalized pressure was calculated using the nominal (apparent) contact area of the worn surface and its room temperature hardness. Similarly, normalized velocity was obtained by incorporating the thermal diffusivity of the wearing surface, along with the radius of circular nominal contact area. Wear map field boundaries delineating different wear mechanisms were constructed by using the critical wear values located at discontinuities in the slope of the wear curve. The main mechanisms distinguished in Figure 2-28 are oxidative wear, delamination wear, severe plastic deformation wear, melt wear, and seizure. As mentioned in section 2.9.2, oxidative wear typically corresponds to the MW regime and delamination or metallic wear is associated with SW. The fundamentals of oxidative wear have been discussed in section 2.3.3.3 and thus will not be elaborated any further. Delamination wear or plastically dominated wear has been proposed by Suh [50, 152]. According to this widely accepted theory, wear takes place through the deformation of the subsurface layer, nucleation of cracks at the subsurface, and the propagation of these cracks almost parallel to the surface. The combination of frictional shear stresses and normal surface adhesion stresses give rise to crack propagation which eventually forms metallic plate-like wear debris.

Zhang and Alpas [7] have investigated delamination wear in Al-7% Si alloy under dry sliding wear conditions with the use of scanning electron microscopy (SEM) and metallographic techniques similar to Moore and Douthwaite [85]. Much of the wear debris consisted of plate-like geometries thus, indicating subsurface delamination as the dominant wear mechanism. It was found that the depth of the deformed zones and

magnitude of the strains both increased with applied load and sliding distance. Plastic strain and flow stress in the deformed regions have a stress-strain curve characterized by the exponential work hardening Voce equation. Initially accelerated strain hardening was present; however, as the hardening capacity of the material is approached the rate of strain hardening decreased to zero. Void nucleation was found to initiate at the Al-Si interfaces. Voids then grew and linked together forming subsurface cracks 10-20 μm below the surface. These subsurface cracks eventually penetrated through the surface, resulting in subsurface delamination. The critical depth, where subsurface cracks most readily form, was found to be dependent upon the competition between the hydrostatic pressure (σ_h) which restricts void growth and plastic strain (ε) which supports it. As hydrostatic pressure is increased the critical depth (Z_c) increases but the rate of void growth ($\dot{R}$) based on Rice and Tracey [153] declines.

As previously mentioned in section 2.9.2, Zhang and Alpas [8] have also studied the effects of contact temperature, load, and speed on an Al-Si (6061) alloy. In this study SEM observations revealed that MW consisted of equiaxed wear debris at low loads and sliding velocities; where the debris was removed from the surface by spalling of the mechanically mixed layers. During the light load and velocity conditions a constant wear rate was obtained due to surface oxidation and iron transfer occurring concomitantly. The presence of hard iron mixed with the equiaxed particles was suggested to be caused by the abrasive action of the aluminum oxide. In the MW regime, as loads and velocities increased, debris gradually took the form of aluminum plate-like particles resulting from delamination. Severe wear set in when the load and speed increased sufficiently to raise the contact surface temperature to the critical transition temperature. Here, immense plastic deformation and large Al plate-like debris formed, resulting from direct Al detachment caused by thermal softening. It was also determined that tribolayers developed by incremental testing could extend the realm of the MW regime. Previously stated in section 2.9.2, Elmadagli and Alpas [150] examined the MW regime in greater detail with respect to the formation of tribolayers.

Shivanath et al. [15] has investigated the dry sliding response of a chemically etched Al-11 wt.% Si alloy. By comparison to an identical test using a non-etched surface they have concluded that metallic wear can be suppressed by maintaining a surface finish which leaves Si particles protruding from the Al-matrix. Silicon exposure prevents direct contact between the counterface and soft Al-matrix. Using the same basic concept, Riahi et al. [20] examined the scuffing resistances of etched Al-12% Si alloys with different particle morphologies (high aspect ratio—needle-like, low aspect ratio) using a pin (AISI M2 steel)-on-flat tribometer with a normal load of 5 N and sliding speed of 0.5 m/s. They determined that the onset of scuffing was dependent upon the etching time, and that a microstructure with a lower aspect ratio increased scuffing resistance. An etching time between 5 to 7 min using a 10% NaOH solution was deemed optimum for scuffing prevention. Samples that were over-etched resulted in a weak Si/Al interface due to excessive dissolution of the matrix surrounding the Si particles; this lead to the removal of Si particles from the contact surface eventually leading to scuffing. Low wear rates within the UMW regime were observed in all samples prior to scuffing. Once Si particles fractured damaging the soft Al-matrix (i.e. three-body abrasion), direct metal-to-metal contact occurred and scuffing became dominant; which was complimented by material transfer from the Al-Si surface to the counterface. SEM observations indicated that Si fracture developed at the root of the particles due to tensile stresses, and at the edges where contact with the counterface occurred. Fracture at the root produced large loose Si particles that were far more effective at ploughing the Al-matrix, as compared to smaller particles produced by edge fracture, have shown An optimum average surface roughness (R_a= 0.4 μm) prior to etching increased the scuffing resistance. However, increasing the R_a values past 0.4 μm had no effect on scuffing thought to be due to the micro-valleys on the rough surface entrapping loose Si particles, which prevented ploughing. Others [106] (see §2.7.4.2) have suggested that polishing prior to etching can round Si edges, reducing the probability of edge fracture. In a related study, Riahi and Alpas [154] have correlated the fracture of silicon-rich particles (SRP) to a critical thicknesses (t_c), where below this value SRPs detached from their roots that were connected to the Al-matrix below. They also suggested that the SRP critical aspect

ratio (t/l_c), where t is the particle elevation height and l_c is the width of the particle, should be considered when choosing optimal etching parameters.
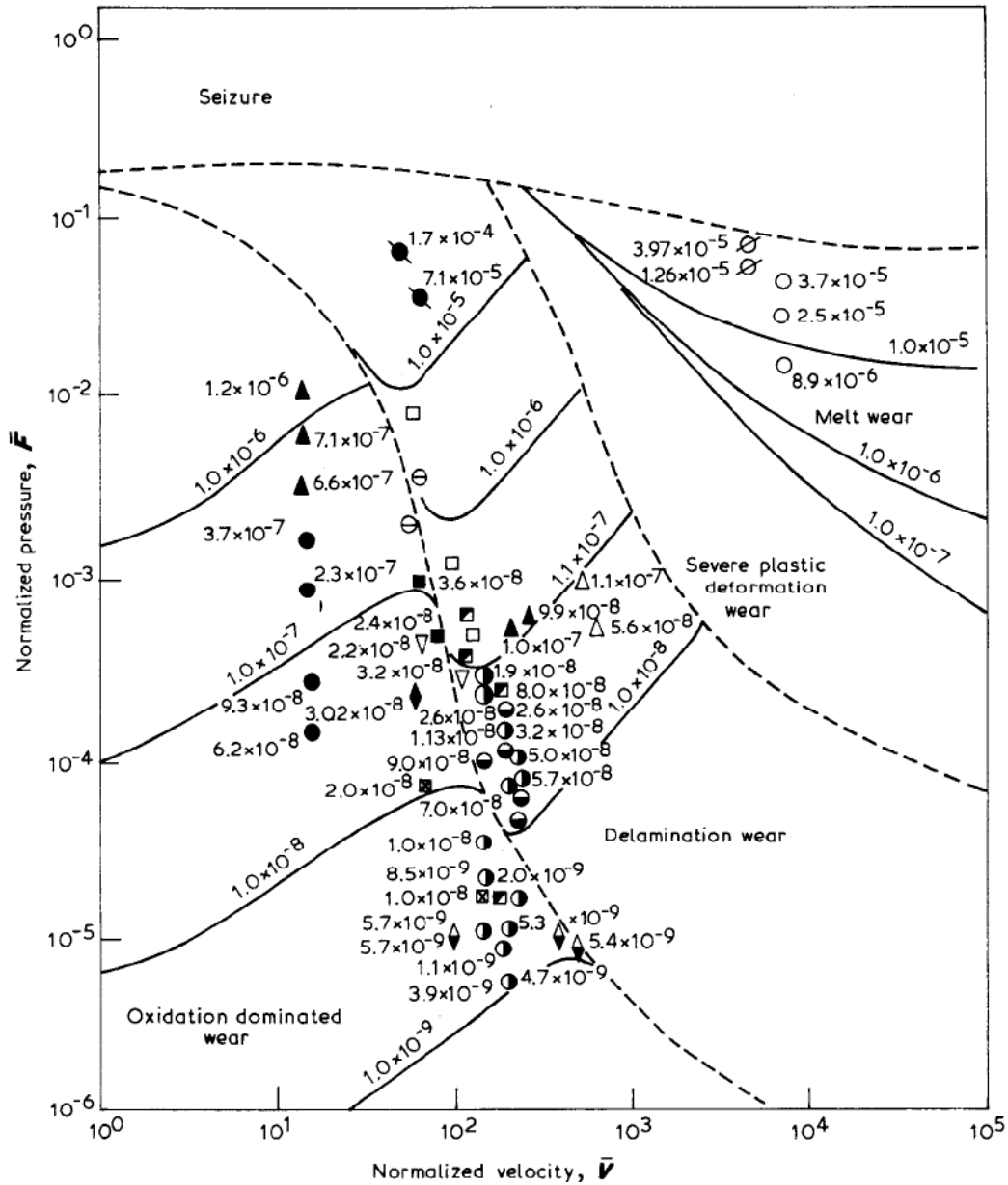
Figure 2-28 Al-Si wear map. The symbols in the figure represent various authors denoted by Lui et al. [151]. The numbers in the figure represent the normalized wear rate, $\overline{W} = W / A_n$, where W is the wear rate in mm^3/m and A_n (m^2) is the nominal area of contact.

2.10.2 Subsurface Zones and Mechanically Mixed Layers

The formation of tribolayers also termed the mechanically mixed layer (MML) in worn Al-Si alloys has been investigated by a number of authors [75, 155-161]. This layer is not to be confused with nanoscale tribofilms (see §2.11.1.2) produced by antiwear additives. Tribolayers are located on the worn surfaces and are often associated with debris formation; therefore, it is important to understand how these layers form and their influence on wear resistance.

Material properties in MMLs vary significantly from the bulk exemplified by differences in hardness, elastic modulus, stress-strain behavior, and ductility [93]. The chemical and structural changes associated with MMLs are often generated by a combination of the following processes: plastic deformation, interactions with the environment, material transfer, and mechanical mixing [95]. Kapoor and Franklin [93] have modeled the formation of tribolayers in ductile metals. They have found that MMLs can be modeled by several sub-layers that have been generated in response to stresses exceeding the shear strength of the material; as the ductility of these sub-layers is exhausted failure will occur, thus generating wear debris via rachetting. Similarly, Rainforth [75] has experimentally shown that the wear of Al-12% Si alloys follows a rachetting wear mechanism at low loads and oxidation dominated wear at higher loads. Despite the different wear mechanisms taking place at various loading conditions, he has stated that the wear rate for Al-4% Cu and Al-12% Si is a linear function of the depth of deformation. Other authors [83, 155, 159, 162] have also suggested a linear relationship between depth of deformation and the wear rate. A related (transmission electron microscopy) TEM study by Perrin and Rainforth [159], has shown that under dry sliding conditions at 0.24 m/s, under loads ranging from 6-54 N, using a pin (Al-12% Si) -on-disc (cast iron) tribometer that the minimum subgrain size (400 ± 50 nm) developed in eutectic Al-Si alloys occurs beneath the surface, with coarser subgrains nearing the surface resulting from flash temperature fluctuations.

Rice et al. [94] has done a general survey based on the development of subsurface zones in sliding wear. It was established that subsurface zones depended

(morphologically and compositionally) upon test materials and geometry, mechanical conditions of contact, and the environment. They have shown that three distinct subsurface zones exist, illustrated in Figure 2-29. Zone 1 represents the original undisturbed bulk material. This zone has experienced elastic deformation and thermal cycling but not to an extent that would change its original structure and properties. Similarly, Zone 2 contains the same material as the original specimen; however, the structure and properties have changed. Zone 2 contains significant plastic deformation resulting from the enormous strains induced by the tribocontact. These strains typically lead to the development of subgrain structures and crystalline refinement (see §2.5.1). Lastly, Zone 3 is a near-surface tribolayer that is both physically and chemically distinct from the other zones. This zone consists of original material as well as species from the counterface and environment. Often Zone 3 is homogeneous and very finely structured. Its hardness, thickness, and chemical composition are dependent upon the contact conditions (contact stress, sliding velocity, initial material properties, surface roughness, geometry, and duration of contact [94].

Mohammed Jasim [161] has investigated the subsurface damage in near-eutectic Al-13 wt.% Si and hypereutectic Al-22 wt.% Si alloys. Wear tests were conducted under dry sliding conditions using a modified pin-on-disc (steel) tribometer under several of loads (1-15 N) and sliding speeds (0.85-5 m/s). Subsurfaces were characterized using oblique mounting and polishing techniques in conjunction with SEM. It was shown that a decrease in the depth of subsurface damage occurred with increasing sliding speed. As speeds increased a distribution of interface conditions (nature and extent of track marks, crack propagation, flow of metal, and melting of asperities) brought the wear rate closer into surface layer control [161]. In general, it was found that an increase in load increased the depth of subsurface damage. Furthermore, by heat treating the hypereutectic alloy, which improved the cohesion between the matrix and Si phase, it was found that no transition in wear rate occurred due to the increased plastic flow and seizure resistance of the alloy. In both hypereutectic alloys the coarse Si particles fragmented into spheroidized particles 3-5 μm in diameter near the surface. In the hypereutectic samples, three zones were identified: i) a region near the worn surface

uniformly distributed by spheroidal particles, where no direction of plastic flow was observable; ii) a transition zone where needle-like and primary Si particles are just beginning to crack; and lastly iii) the unaltered microstructure which depends on the depth of subsurface damage. In the Sr and Na modified eutectic samples, where Si is already present as fine particles, no transition zone or further fragmentation took place. According to Mohammed Jasim [161] fragmentation was a result of material deformation, whereby Si particles were subjected to compressive and shear stresses during sliding, which caused cracking. In summary, the size of Si fragments (3-5 μm) remained constant regardless of sliding speed, bearing load, counterface hardness, heat treatment, and concentration or morphology of silicon phases.

Elmadagli and Alpas [14, 144] have investigated the dry sliding wear of Al-18.5 wt.% Si alloy (A390) in air [14] and argon [144] atmospheres. Under various loads within the mild wear regime they have concluded that wear was a result of the formation and breakdown of tribolayers. Initial tribolayer formation was a result of iron transfer from the steel counterface to the silicon particles in contact. Under the MW-1 subregime at light loads (10 N), tribolayers were thin (0-10 μm) and discontinuous. Conversely, under the MW-2 subregime at higher loads (60 N) tribolayers were thicker (40-60 μm) but showed evidence of crack propagation and spallation at the tribolayer/matrix interface. Both MW subregimes contained small surface grooves (4 μm in depth at 10 N), along with subsurface damage beneath the tribolayers in the form of fractured Si particles. Overall, the tribolayers generated in air were iron-rich, contained aluminum and oxygen, and were hard (subject to spallation); as compared to the argon generated tribolayer which at steady state was rich in aluminum and contained a lesser degree of oxide and iron. Li et al. [160] performed detailed electron probe micro-analyzer (EPMA), FIB and TEM analysis on the same Al-Si (A390) alloy worn under a constant load of 10 N and sliding velocity of 1 m/s using a dry block-on-ring (steel) tribometer identical to Elmadagli and Alpas [14, 144]. They found that a discontinuous tribolayer, 10 μm in thickness, formed in air and in argon atmospheres. The tribolayer formed in air was severely fractured due to the brittleness caused by oxides present. They have also indicated that ultra-fine grains (~100 nm) of aluminum have formed beneath the

tribolayers up to a depth of 10 μm in both atmospheres. The formation of ultra-fine grains (UFG) was explained in terms of severe subsurface plastic deformation during the wear process.
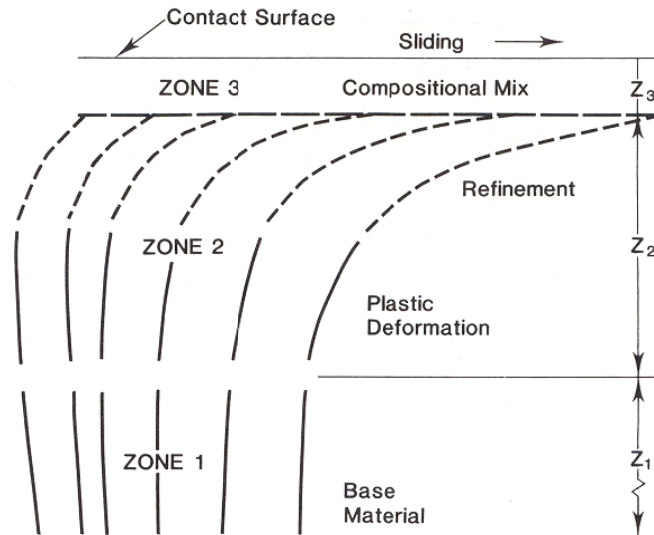
Figure 2-29 Schematic illustrating the major features of subsurface zones [94].

2.11 Lubricated Wear of Al-Si Alloys

2.11.1 Antiwear Additives

Engine lubricants are designed to operate over an extreme range of conditions and with an array of different fuels. The main function of these oils are to avert wear between the engine components, serve as a heat transfer medium, a sealant at the compression rings, and to help suspend unwanted matter keeping the engine clean [163]. Lubricants are undoubtedly the best solution to minimizing engine wear without permanently altering the engine design; however, they do have their shortcomings. The main problem of engine lubricants in combustion engines is that they react with the combustion products. This results in contamination and oxidation of the lubricant, as well as the formation of deposits on the working surfaces. In turn, these problems result in serious corrosion and wear of the engine. To prevent this from occurring antiwear additives are added to the base oil.

Zinc dialkyl-dithiophosphates (ZDDP) are by far the most effective class of "antiwear" (AW) and extreme pressure (EP) additives used in engine oils to date; see

Figure 2-30. ZDDPs are typically employed for their excellent antioxidant properties. They prevent the base oil from oxidizing during the combustion process; in turn, preventing the production of corrosive products. Also under high temperature and pressure, ZDDPs break down the volatile conditions in a combustion engine by creating reaction products which result in the formation of sacrificial films; typically comprised of varying amounts of zinc, phosphorus, sulfur, and oxygen [164, 165]. These films help reduce asperity contact and are sometimes referred to as antiwear films. Antiwear films have complex and heterogeneous structures. Atomic force microscopy (AFM) has shown that this heterogeneous surface has two distinct regions, one where the film is abundant termed antiwear pads which can exceed 100 nm from the surface and two, the regions between the pads termed valleys [165]. Large antiwear pads have been identified to form at the regions of contact between the two sliding surfaces. The centers of the large pads are much stiffer and more elastic than the lower valley regions. The valley regions are composed of softer more plastically deformable material, suggested as being antiwear film intermediates [165].

It is important to emphasize that the speed at which a film is formed will drastically affect the wear of the system. Film formation has been reported to develop 1000 times more readily on nascent metallic surfaces as compared to an oxide surface [31]. A nascent surface is far more reactive because (i) no oxide barriers are present between the metal and reactants; (ii) surface atoms release "Kramer electrons" that help initiate reactions; and (iii) nascent surfaces formed under sliding contain a number of defects that serve as catalytic sites for reactions. Based on this ideology the speed of reaction would only take a few milliseconds at nascent asperity peaks to produce a thin film possibly 5 nm thick. Between asperity peaks a slower form of chemical attack would occur closest to thermodynamic equilibrium (i.e. oxides or oxidation products of sacrificial films). Figure 2-31 illustrates this model wherein a thin film could be sustained at high contact rates several thousand revolutions per minute [31].

OIL
SOLUBILIZING   SURFACE
ATTRACTING   OIL
SOLUBILIZING

ZINC DIISOPROPYL DITHIOPHOSPHATE
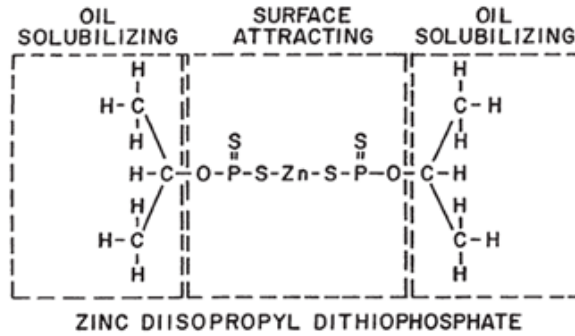
Figure 2-30 Example of chemical compounds used as boundary lubricant additives [166].

Worn asperity peaks:
· nascent surface
· fast reaction

Asperity

Asperity

Quiescent areas
only slow corrosion
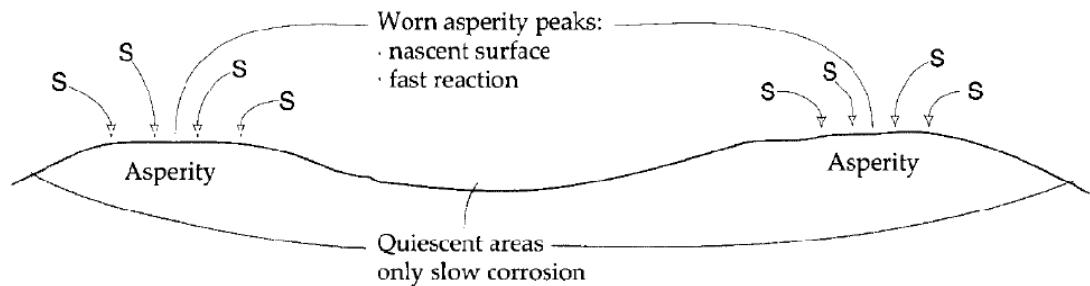
Figure 2-31 Preferential formation of sacrificial films at localized areas of nascent metallic surface [31].

2.11.1.1 Additive Interaction

The combination of ZDDP with other oil additives, for example molybdenum dithiophosphate and calcium detergents can have three possible mechanisms of interaction. First, ZDDP and the other additives can react together in the lubricant; this product can then react with the sliding surfaces. A second outcome can take place where no interaction between the additives arises. Therefore, each additive will react with the sliding surfaces independently and in competition. Lastly, a "paste" can be formed by the reaction products of ZDDP and the reaction products of the other additives. The paste will then be responsible for the wear reduction and lubrication performance of the sliding surfaces [165]. An example of one of these mechanisms can be observed between the negative interaction of ZDDP and detergents. In this case the detergent forms a thinner layer of film which obstructs the formation of the ZDDP layer by interacting with the ZDDP in solution. This decreases the wear performance when compared to the additive alone [165, 167]. Therefore an optimum lubricant not only must be compatible with the elements of the wear couple but also with the additives contained within.

2.11.1.2 Antiwear Film Formation on Al-Si Alloys

In the past, a number of authors have investigated the effects, formation mechanisms, structure and composition of boundary lubricating films [165, 168-173], with much attention being focused towards ZDDP tribofilms formed on ferrous materials [165, 174-176]. There is a general agreement that polyphosphate films do form on aluminum surfaces similar to that of steel but speculation still arises with regards to its effectiveness as an antiwear agent for aluminum surfaces [16, 165, 167-169, 177-179]. It has been observed that the presence of silicon in aluminum alloys provides a rigid surface for which phosphate films can thrive. Tribofilms formed on aluminum silicon alloys have been found to be approximately 40 nm to 100 nm in thickness identified by cross-sectional focused ion beam (FIB) and transmission electron microscopy (TEM) analysis [22, 177]. Under lubricated ultra-mild wear testing it has also been observed through TEM analysis that ultra-fine aluminum grains approximately 500 nm are developed below the worn surface which are thought to provide a hardened subsurface capable of sustaining an oil residue layer nanometers thick [22]. On a similar note with respect to hardness, others have identified that aluminum alloys containing low concentrations of silicon (i.e. 0.4-0.8 wt. %) with an overall lower hardness develop fewer phosphate films as compared to alloys containing higher concentrations of silicon (i.e. 5.5-7.0 wt. %) with an overall higher hardness [169]. These bench tests do help elucidate the role of antiwear films on aluminum silicon alloys; however, with regards to actual engine testing the available literature [16] is scarce suggesting a dire need for a link between tribometer bench tests and dynamometer tests.

2.11.2 Lubricated Al-Si Bench Tests

In comparison to dry sliding wear the literature revolving around lubricated bench testing of Al-Si alloys is far from comprehensive; more so with regards to studies focused on the wear of the alloy [21, 23, 104, 126, 143, 158, 180-182] than the formation of antiwear films (see §2.11.1.2). Das et al. [180] has extended the work of Riahi et al. [20] (see §2.10.1) to lubricated (5W-30 oil) sliding conditions using a pin (52100 steel ball)-on disk (Al-10 wt.% Si) tribometer at room temperature, under a range of loads (1-

20 N), and constant sliding velocity of 1 m/s. Using optical surface profilometry (WYKO) they have compared the wear tracks of etched and unetched samples. They found that during the early stages of sliding plastic deformation, and not wear, has formed permanent depressions in the traversed wear track for both etched and unetched samples. However, the sample etched by 10% NaOH with Si particles initially protruding 2.5 μm from the Al-matrix was found to resist plastic deformation at much greater loads as compared to the unetched sample. The improved resistance to plastic deformation was explained by contact mechanics which showed that the rough etched surface morphology reduced the peak contact pressure, in turn lowering the deformation. More interestingly, through Vickers micro-hardness measurements they have determined that etching has a surface hardening effect that reduces micro-plastic abrasion. Lastly, they have shown through subsurface nano-hardness measurements that the irregular shape of the wear groove in the etched sample was caused by the difference in hardness between the bulk (lower hardness) and near surface (higher hardness). However, they have suggested that as wear progresses the harder sides of the groove will begin to support more of the load, and eventually the wear at the bottom part of the groove in the bulk material will slow down [180].

Walker et al. [158, 182] has studied the lubricated sliding wear of unreinforced aluminum alloys (2124 and 5056) and their reinforced composites with 15 vol.% $MoSi_2$ using novel techniques such as tilted tomographic surface reconstruction, FIB, and scanning transmission electron microscopy (STEM). Sliding tests were carried out on a pin-on- (M2 steel) ring configuration, using SAE 15W-50 synthetic oil under boundary lubricated conditions; at initial Hertzian contact pressures of 0.75-1.2 GPa and a sliding velocity of 0.94 m/s. Sliding tests commenced over distances exceeding 400 km, with corresponding specific wear rates ranging from $4.5-12.7\times10^{-10}$ mm^3/Nm. Variation of the worn surface heights of 3-4 μm indicated that mild wear took place. Their tests have shown that the unreinforced alloys exhibited the highest wear rates due to 2 and 3 body abrasives originating from the counterface, which plastically deformed the surface by micro-ploughing. The reinforced alloys were shown to improve wear resistance. These lower wear rates were achieved by the optimization of the near surface layer.

Reinforcement particles which exceeded their fracture toughness produced small fractured debris, which was then re-implanted into the ductile matrix via the lubricant. The re-implantation of wear debris increased the overall surface hardness, resulting in improved wear resistance. Through TEM they have shown that the most striking difference between the reinforced and unreinforced alloys was the extent of deformation to the aluminum matrix. The unreinforced alloys at the near worn surface contained a combination of fine equiaxed sub-grains ~100 nm in size, and large debris particles embedded into the surface. This highly deformed layer extended to a depth of ~1 μm, and below it contained grains elongated in the direction of sliding. Here, it was suggested that wear debris was generated as a result of the material exceeding its ductility limit (i.e. rachetting). Conversely, the reinforced alloys did not show evidence of a highly deformed layer; instead, the reinforcement particles transferred the load to the underlying bulk material. Equiaxed aluminum sub-grains ~330 nm were observed only at the extreme worn surface and beneath the load supporting particles. Interestingly, reinforcement particles lying far from the surface but, in contact with load supporting particles were fractured. Lastly, only the unreinforced 5056 alloy was shown to support a thin (~10 nm) boundary lubricant film, which was dominant at the base of craters [158, 182].

The boundary lubricated (5W-30 oil), pin (52100 steel)-on-disk, ultra-mild wear of, chemically etched, eutectic and hypereutectic Al-Si alloys has been studied by Chen et al. [21-23]; using optical profilometry, XPS, FIB, and high resolution transmission electron microscopy (HRTEM). It was found that under lubricated ultra-mild wear conditions (0.5 N load) for an 18.5 wt% Si aluminum alloy, the wear damage was constrained to the top surfaces of chemically exposed silicon particles in the form of longitudinal surface scratches. Here, the original silicon and aluminum morphology remained unchanged. The maximum contact pressure exerted on the silicon particles was calculated to be lower than the aluminum matrix hardness, thus sustaining an unaltered morphology. Conversely, the eutectic Al-12 wt% Si alloy containing a softer matrix, demonstrated extensive damage which consisted of: silicon particles sinking into the aluminum matrix, aluminum pile-up formation, and particle fragmentation corresponding

to UMW I; once the aluminum was no longer sheltered by the Si particles a period of rapid wear or UMW II set in; lastly, wear rates decreased in UMW III due to the development of an amorphous oil residue layer (~150 nm thick) on the contact surface, which was supported by an ultra-fine grained subsurface structure. Lastly, the authors have suggested that increasing the silicon particle size, lowering the aspect ratio, and improving matrix hardness would increase the load carrying capacity of the alloys, and hence extend the duration of the ultra-mild regime [21-23].

Timmermans and Froyen [181] have studied the lubricated (15W-50 oil) fretting wear behavior of hypereutectic Al-Si alloys produced by powder metallurgy. Fretting tests were conducted with a pin (Al-Si)-on-flat (carbonized steel) test rig at 150°C. Using SEM the wear process was observed to be divided into an initial run-in period with the highest wear rate and a steady state condition with a far lower wear rate. The steady state condition and stable coefficient of friction was attributed to the effective action of the oil. Here, the authors state that oil constituents combined with rolling debris forms a protective layer which maintains low wear rates. In contrast, the unlubricated condition exhibited unstable coefficients of friction, which was attributed to the extended plastic deformation, adhesion, oxidation, and material transfer [181].

Similarily, Rainforth et al. [76] has also observed that the extent of material transfer and surface roughening in Al-11.7% Si alloys is much greater in dry sliding tests as compared to lubricated conditions. They have shown that the lubricated wear of Al-Si alloys does not take place by the classical adhesive mechanism dominant in many dry sliding tests. However, their subsurface analysis has shown that the development of sub-grain structures below the wear track in dry (min. sub-grain ~350 nm) and lubricated (min. sub-grain ~650 nm) conditions are similar, but are on different scales. Lastly, the authors have shown that at the highest loads lubrication became inefficient, resulting in wear similar to that of dry sliding but with reduced surface strains and less material transfer.

Wang et al. [104] has conducted hot scuff bench tests of various piston/cylinder combinations, which include cylinder bores made from cast iron, Al390, PEAK, and

GM396. This piston scuffing bench tester was specifically designed by Ye et al. [112] to simulate the contact and lubrication conditions between a piston and cylinder bore of an actual engine, with the exception of the combustion process. The hot scuff tests were conducted with 5W-30 engine oil at a working oil temperature of 60°C. Their results have shown that the coefficient of friction between each skirt/bore combination and within each test cycle. Three stages of wear were identified: (i) coefficient of friction increases with load as a result of break-in; (ii) steady state; and (iii) a sharp increase in the coefficient of friction causing failure/scuffing. Authors have shown with the help of optical profilometry that the initial peaks of machining marks become flattened, and the actual area of contact increases. At this point, the oil film pressure has increased enough to partially support the load, maintaining a mixed lubrication regime which lasts ~6-12 minutes until break-in is complete. As the normal load and contact temperature increases, boundary lubrication sets in and a steady coefficient of friction is maintained; even with periodic increases in load. Eventually, with extreme scuffing temperatures (~200-300 °C) and/or loads (~1000-1500 N), oil starvation will occur resulting in direct metal-to-metal contact; and thus, scuffing/failure transpires. The authors have shown that eutectic GM396 exhibits a higher scuffing load and scuffing temperature as compared to PEAK and Al390 which both contain higher concentrations of Si. It is suggested that the high scuffing resistance observed in GM396 may be attributed to the significant amount of intermetallic phases and eutectic Si which provides beneficial tribo-chemical reactions. The authors have also shown that the scuffing resistance of GM396 is reduced with increased amounts of porosity. In general, they have concluded that piston coatings, surface roughness, mechanical and chemical properties of bores, along with their tribo-chemical reactions initiated during wear are the substantial factors that govern scuffing resistance [104].

2.11.3 Lubricated Al-Si Engine Tests

In section 2.11.2 it was established that the lubricated wear of Al-Si alloys was dependent upon a number of factors ranging from interfacial temperature to basic material properties. Undoubtedly, these bench tests are helpful in elucidating the

fundamental wear mechanisms and processes associated with lubricated Al-Si wear. However, in many cases the observed mechanisms can only be reproduced with the same type of test rig geometry, thus making them somewhat ineffective in terms of real life applications. As previously mentioned in §2.11.2, Wang et al. [104] simulated high temperature engine scuffing quite reasonably using a real piston sliding against a section of a cylinder bore. However, this apparatus cannot perfectly simulate a real engine test; mainly because the combustion process, which creates significant temperature and pressure fluctuations along with the production of combustion byproducts, is omitted. Therefore, only by actual engine testing can the durability and wear resistance of linerless Al-Si engines be analyzed with 100% confidence.

Yu [100] has examined near-eutectic linerless Al-Si engines during the honing stage and after engine testing. Microscopic examination of these engines led her to identify five different types of cylinder damage corresponding to normal wear, severe scratch, comet wear, burnishing wear, and top land wear. Yu [100] has concluded that the fracture of hard phases increases the abrasive wear within the engine.

Legge et al. [183] has performed cold scuff and durability dynamometer tests on machined eutectic Al-Si engine bores. They have shown through mechanical testing and visual inspection that a microstructure which minimizes the area fraction of primary aluminum and primary silicon and also exhibits a Brinell hardness above 120 is required for sufficient cold scuff resistance. In the hypereutectic microstructure they have found that large primary intermetallics fracture and initiate cracks in the matrix; while primary aluminum dendrites provide paths of easy deformation.

Kurita et al. [17] has examined two hypereutectic Al-20% Si single cylinder engine blocks in terms of cylinder temperature, oil consumption, and endurance testing. The monolithic (DiASil cylinder) blocks were developed by a vacuum die casting process that reduces gas absorption. Authors have shown that the monolithic Al-Si engine provided superior cooling performance, 30 K less than cast iron sleeves, as well as oil consumption rates that are one half that of cast iron sleeves. These efficient engines contained exposed primary Si particles averaging 20 μm in size. The primary Si particles

were exposed to a height of 0.5 μm established by honing. After a total of 105 endurance testing hours, under EHL conditions, and a controlled oil temperature of 423 K, authors have shown through atomic force microscopy (AFM) that the Si exposure decreased to 0.15 μm within a short time, followed by becoming constant. They have also shown through simulations that EHL is generated between 0.15 and 0.3 μm Si exposures. At other exposure heights the Si particles will be directly be in contact with the counterface. Furthermore, because the initial exposed Si top surface was not flat EHL did not occur immediately during the engine tests. From these results the authors have suggested that cylinder wear proceeds initially by abrasive wear which decreases the exposure height until EHL is establishes a 0.15 μm equilibrium Si exposure; here, the EHL conditions terminate excessive wear and thus providing long term engine endurance.

Dienwiebel et al. [16] has examined the wear behavior of an Al-17%Si-4%Cu-1%Mg monolithic engine block subjected to ~250 h of dynamometer testing over the full load and torque range of the engine, which was lubricated by 5W-30 oil. Using the novel radionuclide-technique (RNT), which was first applied to engines by Scherge et al. [149], the ultra-low wear rates (< 20 nm/h) of the engine were continuously measured. The authors have shown through AFM and white light profilometry that Si grains initially protruded ~750 nm from the Al-matrix after chemical etching. In contrast, the worn surface showed no Si exposure. Furthermore, no evidence of antiwear pads was observed on top of the Si particles. In the worn condition, the Al-matrix had a grainy appearance which appeared to contain many small particles and small pits possibly generated by particle removal. Chemical comparisons of the worn and unworn surfaces by Auger electron spectroscopy (AES) confirmed that no ZDDP antiwear films formed on the Si particles. Conversely, the worn aluminum matrix showed significant amounts of foreign elements (C, O, P, Ca) detected at depths of almost 6 μm. Authors suggest that the chemically modified near-surface matrix originated from plastic deformation combined with lubricant and debris mixing. Analysis of the near surface by FIB has shown that the surface contains small wear debris, fractured Si particles, and plastically deformed aluminum. Lastly, the authors have concluded that Si exposure is important in order to initially direct the energy input into the Si grains, protecting the nascent aluminum, until

running-in is complete. Additionally, they have stated that since the detected wear rates were on the order of several tenths of nanometers per hour, antiwear films could not form; thus, suggesting that antiwear films can only form in overstressed tribosystems [16].

2.12 Summary

From the previous sections, it is clear that many parameters will determine the wear resistance of Al-Si alloys. These parameters namely, composition, processing, and microstructure are all interrelated and their combined effects will determine the wear performance of Al-Si alloys. The novel Al-Si alloys under study have been tailored to make use of all these parameters in order to optimize its wear resistance. In the present study we will see that these alloys do contain some minor flaws but, overall its wear resistance does appear to be suitable for engine durability applications. The lack of literature revolving around linerless Al-Si engine testing is significant, with none related to eutectic alloys for automotive engines. Therefore, this study reveals the wear mechanisms of novel linerless Al-Si engines by thorough materials characterization using an array of surface and subsurface techniques to obtain mechanical, microstructural, and chemical results. In addition, cylinder bores with different parameters were specifically chosen for comparative purposes elucidating the effects of alloying, surface preparation, and temperature on the overall wear progression of linerless Al-Si engines. Identifying and understanding wear in linerless Al-Si engines is crucial towards the future development of lightweight wear resistant engines which will provide a cheap yet robust solution to cast iron liners.

3   MATERIALS AND EXPERIMENTAL METHODS

Four different monolithic eutectic Al-Si sand-cast engine bores have been thoroughly examined using a variety of materials characterization techniques graphically presented in Figure 3-1. These engines vary in alloying elements, surface preparation, and dynamometer testing parameters. Henceforth, for ease of comparison these engines will be designated by the following sequence and defined below:

Major alloying element : final surface preparation : dynamometer test

Ni:MR:HT   = Nickel alloyed : Mechanical reduced : Hot tested

Cu:MR:HT   = Copper alloyed : Mechanical reduced : Hot tested

Ni:CE:HT   = Nickel alloyed : chemically etched : Hot tested

Ni:CE:CS   = Nickel alloyed : chemically etched : Cold scuff

Details regarding alloying, surface preparation, and dynamometer testing specifically for these engines is presented in §3.1, §3.3, and §3.2 respectively.
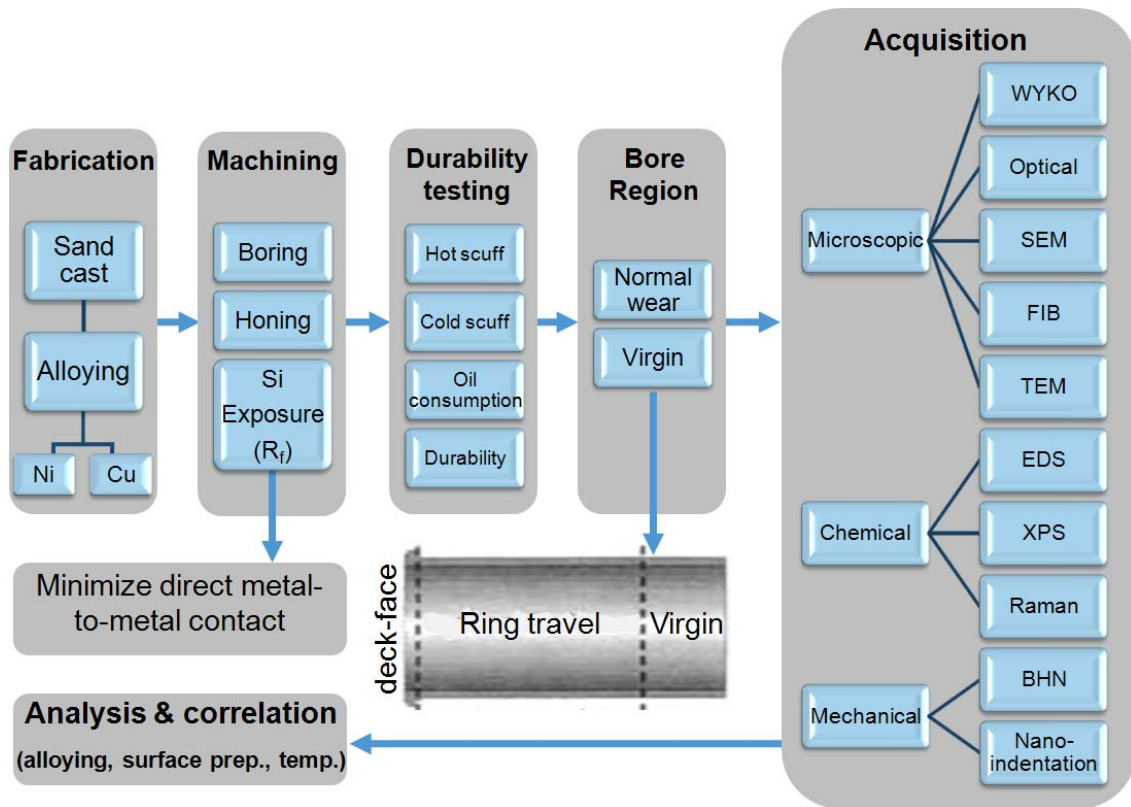
Figure 3-1 Flow chart illustrating the methodology used for engine bore characterization.

3.1 Microstructure and Phase Identification

3.1.1 Nickel Alloying

The Al-Si engines primarily alloyed with nickel, designated as Ni:XX:XX, contain 12.5 wt.% Si, 1.18 wt.% Ni, 0.9 wt.% Cu, as well as other minor alloying elements. The morphology and distribution of eutectic silicon was observed from polished cross sections of the cylinder wall within 1.5 cm from the inside bore surface beneath ring travel. Cross-sectional samples were prepared using conventional metallographic polishing techniques described in §3.5. These cross sections indicate that silicon particles exist throughout the microstructure primarily as needle-like particles or as dense silicon colonies consisting of fine particles. Some (few) primary silicon particles exist throughout the microstructure; they are attributed to segregation and temperature fluctuations during casting. The silicon particle aspect ratio (length/width) and average length were calculated by quantitative metallographic analysis (thresholding). The

average silicon needle aspect ratio (Figure 3-2a) was 19.04 ± 1.07 μm, which corresponded to an average needle length of 62.72 ± 3.81 μm obtained from 190 particles. The average silicon colony aspect ratio (Figure 3-2b) was 3.29 ± 0.22 μm, with an average length of 5.87 ± 0.35 μm taken from 98 particles. Furthermore, the average secondary dendrite arm spacing (SDAS) of α-aluminum was found to be 80.93 ± 6.58 μm averaged from 106 dendrite arm spacings. Brinell hardness testing (see. §3.5 for details) provided a bulk hardness value of 96.88 ± 3.92 HB averaged from five measurements for the Ni:MR:HT and Ni:CE:HT engine. A Brinell hardness value of 89.93± 5.16 HB averaged from five measurements was also obtained from the Ni:CE:CS engine. Both the Ni:HT and Ni:CS engines contain the same elemental composition; therefore, the low hardness value of the Ni:CE:CS engine is likely a result of the varied environment and its influence on the casting process (i.e. cooling rates and precipitation hardening).

The bulk microstructure of the alloy is presented in Figure 3-3 and was compared to the available literature [184] in order to clearly identify the morphology and composition of second phases. The micrograph clearly shows long silicon needles, fine dense silicon particles, and various intermetallic phases. Semi-quantitative chemical analysis through EDS has shown that many of the intermetallics contain nickel shown in Figure 3-4. In addition, large Chinese script α-iron ($Al_{15}(Mn,Fe)_3Si_2$) phases are observed throughout the microstructure along with small Mg_2Si phases.
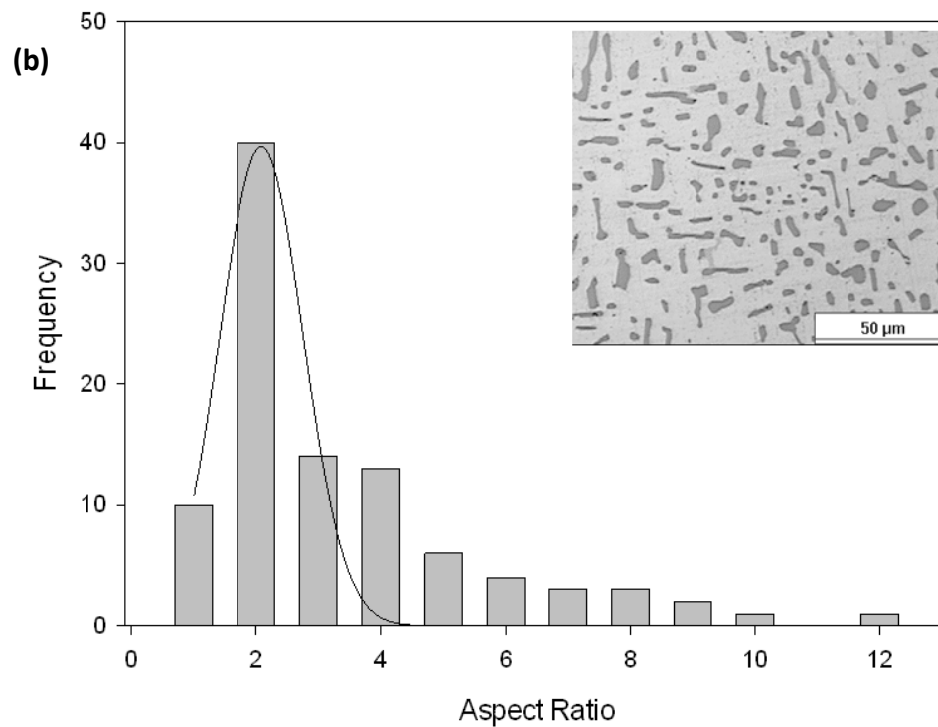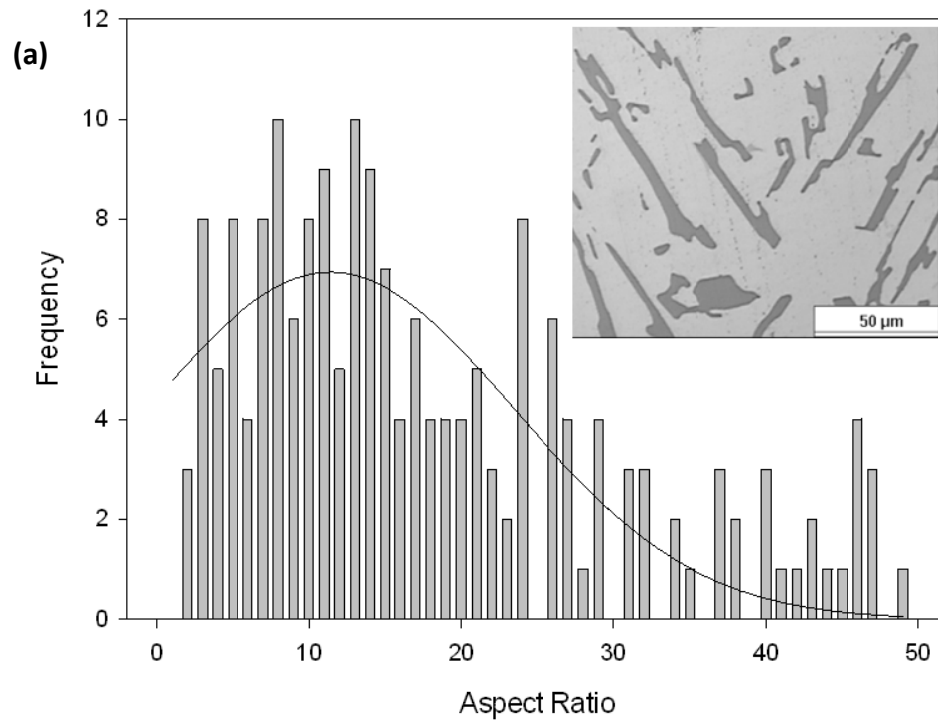
Figure 3-2 Histograms illustrating the Si needle-like and Si colony aspect ratios in (a) and (b) respectively. In (a) the mean aspect ratio and mean length are 19.04±1.07 μm and 62.72±3.81 μm respectively. In (b) the mean aspect ratio and mean length are 3.29±0.22 μm and 5.87±0.35 μm respectively.
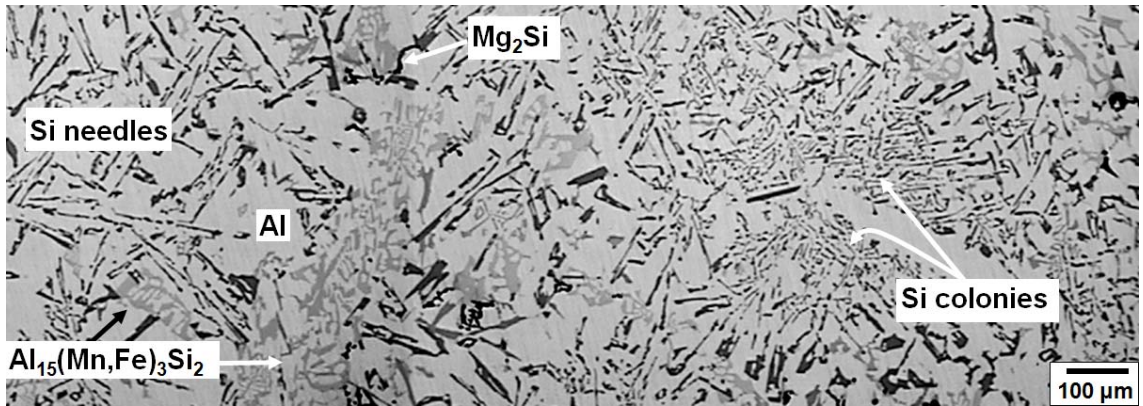
Figure 3-3 Optical micrograph revealing the various phases coexisting within the Al-matrix and overall Si microstructure; (polished, unetched).
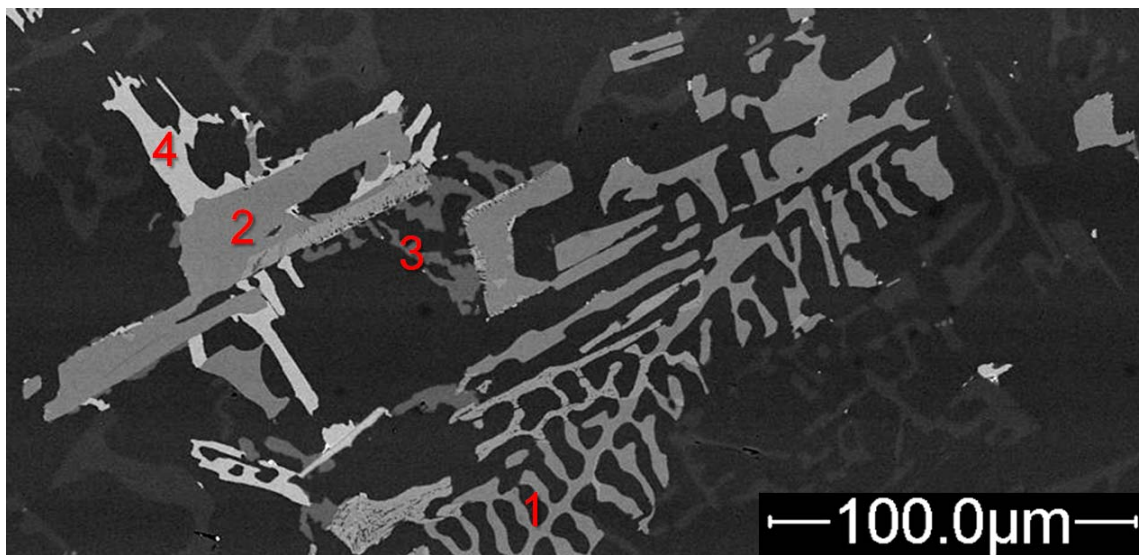
Figure 3-4 BSE micrograph showing the various phases coexisting within the α-Al matrix confirmed by EDS labeled as: 1) $Al_{15}(Mn,Fe)_3Si_2$; 2) Al+Ni+ traces of Si; 3) Al_3Ni; 4) Al+Ni+Cu.

3.1.2 Copper Alloying

The Al-Si engine primarily alloyed with copper, designated as Cu:MR:HT, contains 11 wt.% Si, 2.5 wt.% Cu, 0.0 wt.% Ni, other minor alloying elements, and the remainder being aluminum. Brinell hardness testing (see. §3.5 for details) provided a bulk hardness value of 90.89± 2.83 HB averaged from five measurements, which was lower than that of Ni:MR:HT and Ni:CE:HT (96.88 ± 3.92 HB).

The overall morphology and distribution of eutectic silicon is shown in the polished cross sections of the cylinder wall (Figure 3-5, Figure 3-6, and Figure 3-7), which were all taken from the bulk microstructure within 1.5 cm from the inside bore surface beneath ring travel. These cross sections indicate that silicon particles exist throughout the bulk microstructure primarily as needle-like particles or as dense silicon colonies consisting of fine spheroidized particles. A fine silicon microstructure indicates areas of fast cooling; compared to the needle-like silicon morphology that had more time for growth before reaching solidification. Virtually no primary silicon particles have formed. The silicon particle aspect ratio (length/width) and average length were calculated by quantitative metallographic analysis. The mean silicon needle aspect ratio is 13.42 ± 0.48 μm, which corresponds to an average needle length of 37.27 ± 1.41 μm, obtained from 526 particles (see Figure 3-5). The average silicon colony aspect ratio is 3.98 ± 0.21 μm, with an average length of 4.41 ± 0.18 μm, taken from 205 particles (see Figure 3-6). Furthermore, the average secondary dendrite arm spacing (SDAS) of α-aluminum is found to be 53.64 ± 0.53 μm. In comparison, the Ni:MR:HT, Ni:CE:HT, Ni:CE:CS bores showed a similar mixed microstructure of Si needles and colonies. However, the nickel alloyed engines exhibited a greater silicon needle aspect ratio of 19.04 ± 1.07 μm, needle length of 62.72 ± 3.81 μm, and a larger SDAS of 80.93 ± 6.58 μm. In general, Cu:MR:HT contains a finer Si microstructure that exhibits fewer needle-like silicon particles and more spheroidized silicon colonies as compared to the nickel alloyed engines. The difference in silicon morphology is likely due to the differences in initial alloy composition.

The bulk microstructure of the alloy, presented in Figure 3-7a, displays intermetallic phases in addition to silicon and α-aluminum patches. Large Chinese script α-iron ($Al_{15}(Mn,Fe)_3Si_2$) phases [121], are observed throughout. Many copper containing phases, each of which has been confirmed by EDS (see Figure 3-7b) are also present. The nickel alloyed engines showed similar α-iron phases; however, no $CuAl_2$ phases were found, and many of the intermetallics contained traces of nickel. Intermetallics are significant as they impart specific alloying characteristics and mechanical properties that can enhance or lower wear resistance [2-6].
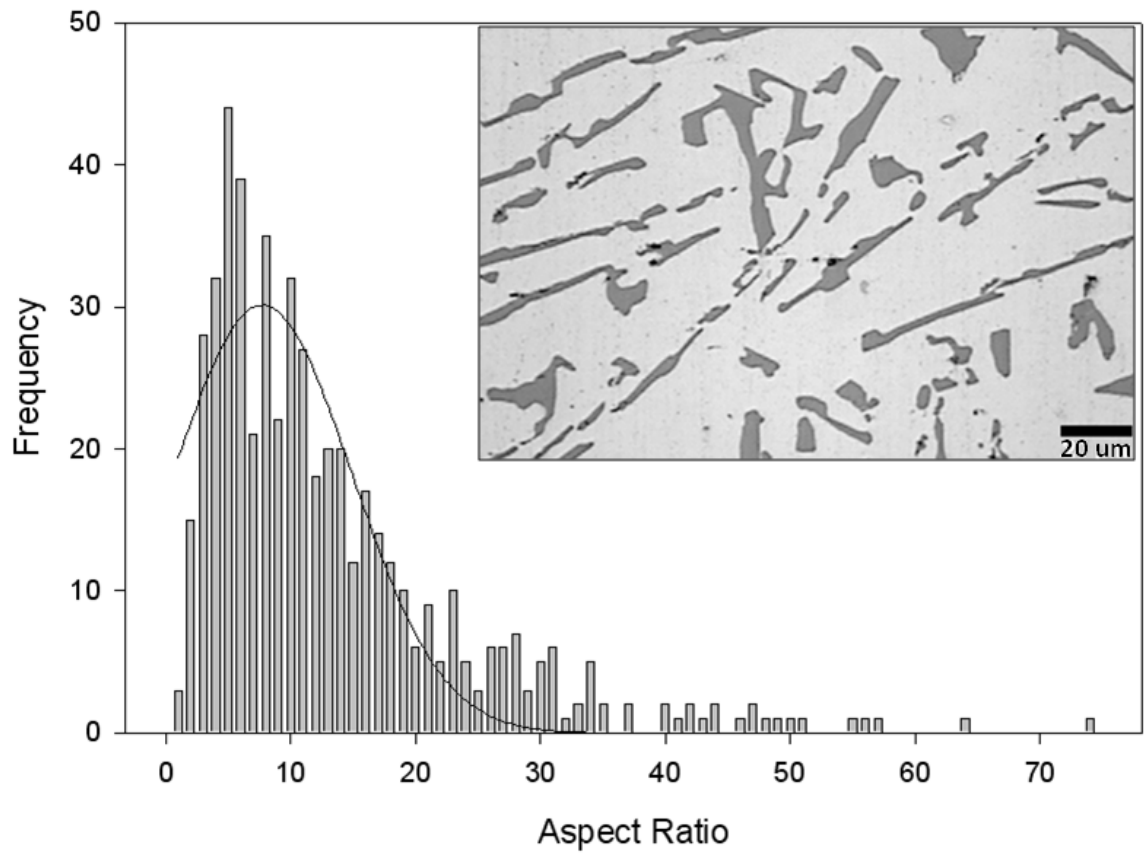
Figure 3-5 Histogram showing the silicon needle-like particle aspect ratio distribution. Mean aspect ratio and mean length are 13.42±0.48 μm and 37.27±1.41 μm respectively and obtained from 526 particles.
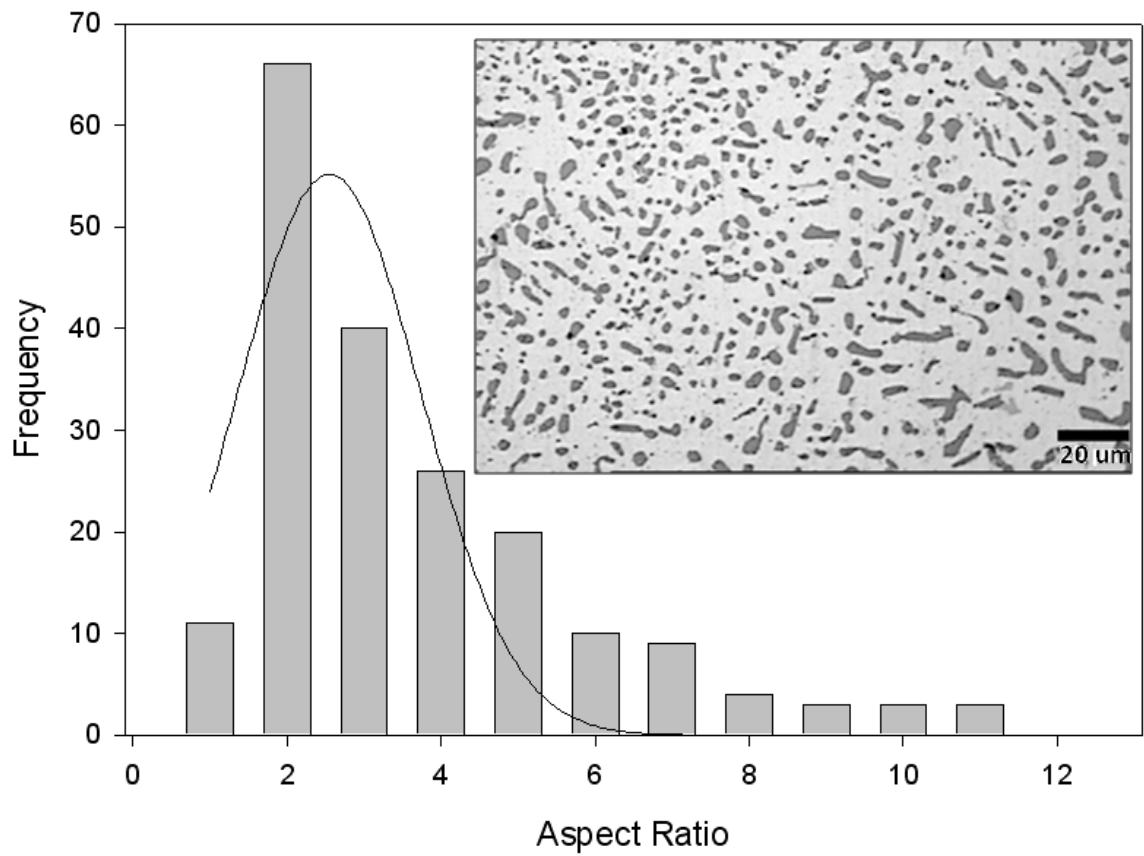
Figure 3-6 Histogram showing the spheroidized silicon colony aspect ratio distribution. Mean aspect ratio and mean length are 3.98±0.21 μm and 4.41±0.18 μm respectively and obtained from 205 particles.
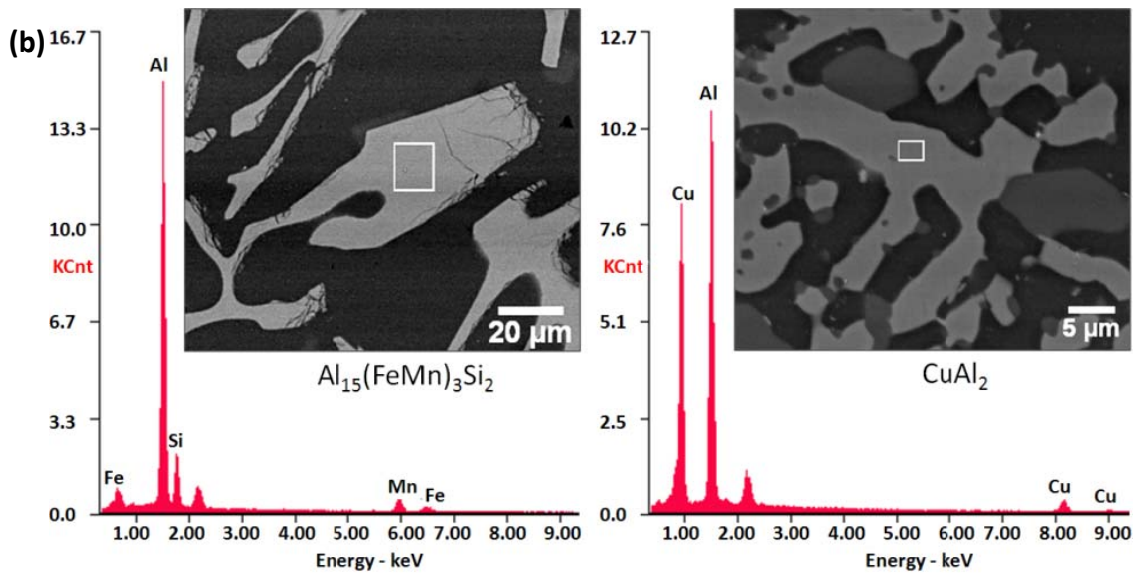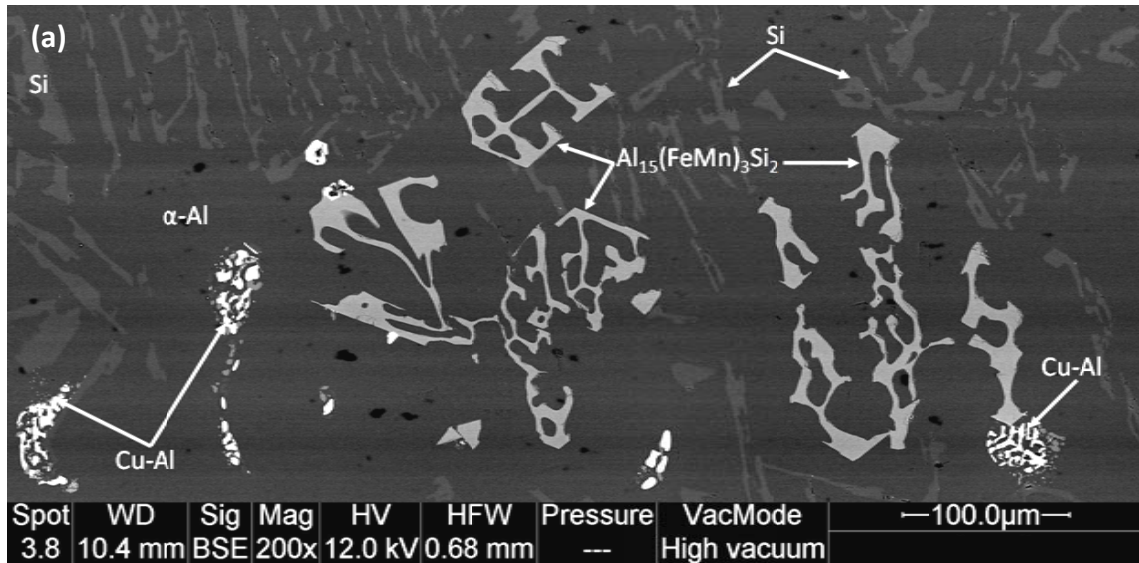
Figure 3-7 a) BSE micrograph showing the various phases coexisting within the α-Al matrix confirmed by; b) corresponding EDS spectrums; (polished, unetched).

3.2 Dynamometer Testing

3.2.1 Hot Testing

Hot engine testing was carried out with V8 internal combustion engines that were fired and operated in a dynamometer cell, which subjected engines to a total of 222 hours (Cu:MR:HT) or 260 hours (Ni:MR:HT and Ni:CE:HT) of high load, high speed, and high temperature conditions. These conditions included new engine (break-in) hot scuff

testing, oil consumption testing, and durability testing all of which stress the engine to conditions beyond typical operating conditions, insuring that a robust and highly durable engine will be developed. During testing, engine oil temperatures reached values of approximately 150 °C while operating under the full speed and torque range of the engine. All piston rings were nitrided cast iron with the exception of the top compression ring that was diamond-like carbon (DLC) coated.

3.2.2 Cold Testing

Cold engine testing of a V8 internal combustion engine was carried out in a dynamometer cell, which subjected it to 3 hours of new engine (break-in) cold scuff testing. In the cold scuff testing procedure the engine was turned on and off fifty times; engine start commenced at an oil temperature of -20 °C and engine shut off took place once the oil temperature reached 65 °C. Oil consumption and durability testing was not performed thereafter, due to the engine failing to pass the initial scuffing procedure. All piston rings were nitrided cast iron with the exception of the top compression ring that was DLC treated.

3.3 Cylinder Surface Finish

Prior to engine testing cylinder bore surfaces were prepared solely using a mechanical reduction process (MR) or by a combination of mechanical reduction followed by chemical etching (CE). Both of these processes allow the hard phases to stand above the aluminum matrix and minimize contact between the aluminum and the counterface (piston rings). Mechanical reduction exposes silicon by means of hard diamond particles embedded in a soft polymer matrix that removes only the soft phases. Furthermore, it has been suggested that the mechanical reduction process polishes and rounds silicon edges, improving their performance if piston rings were to come in contact [106]. This process is abrasive in nature and thus, care is taken to insure the least damage to the hard phases. The second step, chemical etching further exposes silicon using a 10% NaOH bath and completely removes any traces of smeared aluminum from the mechanical reduction process. A diagram depicting both surface preparations was previously presented in §2.7.4.2.

3.4 Bore diameter, Sample Sectioning, and Preparation

Before and after dynamometer testing macroscopic wear data was measured by comparing the change in bore diameters. This was accomplished with a digital bore gauge, using 3 point measurements, at 6 mm, 98 mm, and 120 mm below the deckface, corresponding to the Top Ring Reversal point (TRR), the Bottom Ring Reversal point (BRR), and a point below ring travel, respectively. Four measurements were taken 90° apart at each of these locations and averaged.

After engine testing individual engine bores were cut out from the block and a single bore whose wear and appearance was identical to the rest of the cylinders was chosen for further sectioning. Coupons approximately 1.5 cm × 2.5 cm in size were sectioned from various locations along the cylinder with the use of a low speed circular diamond saw and/or by a wire electrical discharge machine (EDM) which used de-ionized water as the dielectric fluid. Sectioning with wire-EDM kept residual stresses to a minimum and more importantly insured that any oil deposits formed on the cylinder surface during wear were not removed. Every coupon from a sectioned bore was carefully cleaned in a hexane bath immediately after cutting and stored in a desiccator. The orientation of the coupons with respect to their position in the engine was marked on the specimens.

3.5 Observation of Surfaces and Cross-sections

Cylinder bore surface topographies were examined using an optical interference (white light) surface profilometer (WYKO NT-1100), which aided in the measurement of silicon height distribution. Microstructural observations, on and below the cylinder surface, was examined by a scanning electron microscope (JEOL 5800) fitted with an energy dispersive X-ray spectrometer (EDS).

Semi-quantitative chemical analysis of the cylinder surface was accomplished by X-ray photoelectron spectroscopy (XPS) using a PHI Quantera Scanning X-ray Microprobe instrument. This technique operates by irradiating a sample with photons that are in the X-ray energy range, specifically mono-energetic X-rays. The photons

cause the atoms on the specimen surface to emit photoelectrons due to the direct transfer of energy from the photon to the core-level electron. The number of electrons emitted from a particular atom is linked to the concentration of the specific atom in the sample. Furthermore, the photoelectron energy is associated with the molecular and atomic atmosphere from which they originated. Therefore, with the use of an electron energy analyzer the binding energy of the photoelectrons, elemental identification, chemical state, and quantity can be readily determined [185, 186]. The XPS procedure took place with elemental survey scans that were obtained before and after argon ion etching ~10 nm from the surface (based on the etch rate of SiO_2 = 14.3 nm/min). A 200 μm X-ray beam was rastered over a 0.5 mm × 0.5 mm area to obtain the elemental results.

Chemical structure analysis was carried out via Raman spectroscopy using a Dilor spectrometer (slit size of 200 μm, hole size of 400 μm, and a moving grating) equipped with a Coherent DPSS 532 green laser with an excitation wavelength of 531.114 nm. To prevent laser induced phase transformations (laser annealing) of the samples, the laser intensity was kept low and Raman spectra were obtained from 32 second intervals.

Bulk microstructure and phase identification, as well as, hardness profiles of the aluminum matrix with respect to the depth beneath the worn and unworn surfaces were attained from cross-sectional samples (transverse to the sliding direction) cold mounted in Lucite epoxy. These samples were ground with 220, 320, 500, and 800 SiC grit paper, followed by polishing with 3 μm and 1 μm diamond paste, and lastly washed in ethanol. Prior to cold mounting, some samples were nickel-plated to insure that no edge damage would occur during the cross-sectional polishing stages. The electroless nickel plating process is an auto-catalytic chemical technique that deposits nickel metal ions in solution with the aid of a reducing agent (phosphorous) that reacts with the ions to deposit nickel onto a metal surface. To insure that a uniform nickel coating would form even on non-metal areas (i.e. silicon) the cylinder samples were coated in a thin layer of gold prior to the electroless process. The electroless nickel-plating process took place by submerging the samples in a acid-nickel bath containing 5 to 7 % phosphorous, at a temperature of 90.5 °C for 30 minutes. Samples were hung from copper wire (see. Figure 3-8) to the

middle of the beaker full with the acid-nickel solution to insure that temperature fluctuations at the bottom of the beaker, near the hot plate, would not interfere with the plating process which could potentially produce blisters on the nickel plating. Hardness measurements were acquired using a nano-indenter (Hysitron TI 900 Triboindenter) equipped with a blue diamond three-sided pyramidal probe (Berkovich geometry) with a tip radius of ≈ 80 nm. Indents were performed with an applied load of 300 μN, at a loading rate of 60 μN/s, and with loading and unloading times of 5 s each. The first indent was positioned 1 μm below the cylinder surface followed by subsequent indents spaced 1 μm apart until the final indent was performed at a depth of 15 μm beneath the cylinder surface. Indents were imaged in-situ using the atomic force microscope (AFM) option of the nano-indenter. Lastly, bulk hardness measurements were obtained from polished un-mounted cross-sections via Brinell hardness testing using a 10 mm diameter tungsten carbide ball, 500 kg load, and a 20 second dwell time. This method of bulk hardness testing was chosen as it is the industry standard for accurately providing the macro-hardness of a material that is heterogeneous and containing multiple grain structures since the indent is the deepest and widest compared to other hardness methods.

In depth site-specific cross-sectional analysis was accomplished by focused ion beam (FIB) techniques using a gallium ion source FIB instrument (LEO/Zeiss 1540XB CrossBeam). To prevent gallium atoms from being implanted into the sample, prior to sputtering, each chosen area of interest was protected by a deposited layer of platinum and/or carbon via a gas injection system. For cross-sectional analysis all ion trenches were milled at a tilt angle of 54° with the beam operating at 30 kV. Transmission electron microscope (TEM) samples were prepared using the in-situ "lift-out" technique; refer to Figure 3-9. Two trenches were milled on either side of the site of interest creating a thin plate. A U-shaped cut was made alongside the bottom of the plate followed by welding a tungsten needle to the top of the plate. The TEM sample was then detached from the bulk sample by completing the U-cut, lifted-out with the tungsten needle, then transported and welded to a copper grid where milling took place at a low ion current (40 pA) to minimize damage. Milling of the plate/membrane took place until electron

94

transparency was attained at a thickness of ≤ 100 nm. Microstructures were examined with a JEOL 2010F field emission TEM equipped with EDS and operated at 200 kV.
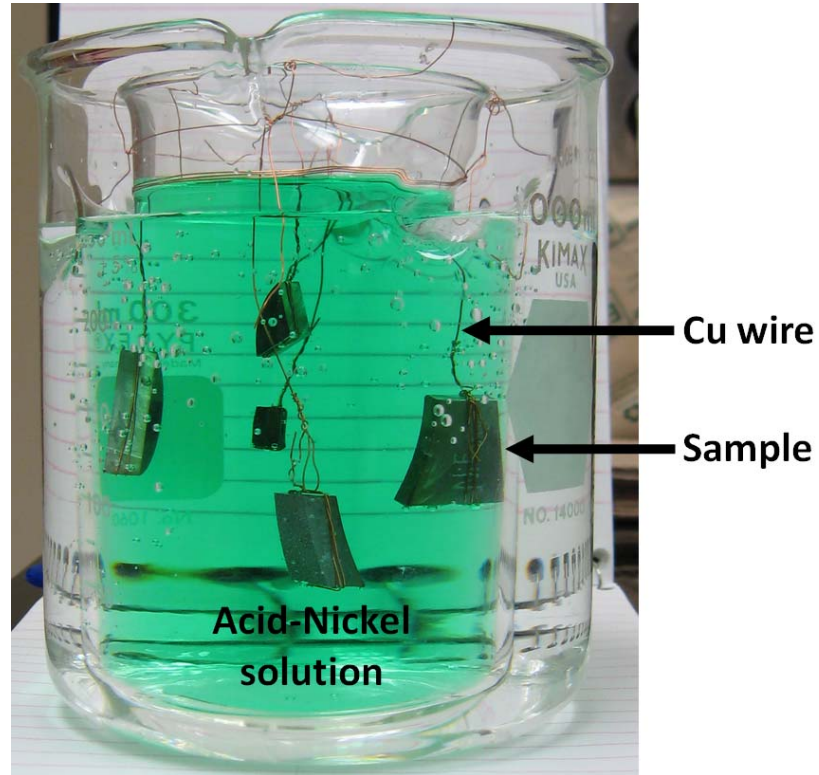
Figure 3-8 Electroless nickel-plating experimental configuration showing gold coated engine bore samples hung from Cu wires immersed in solution prior to heating.
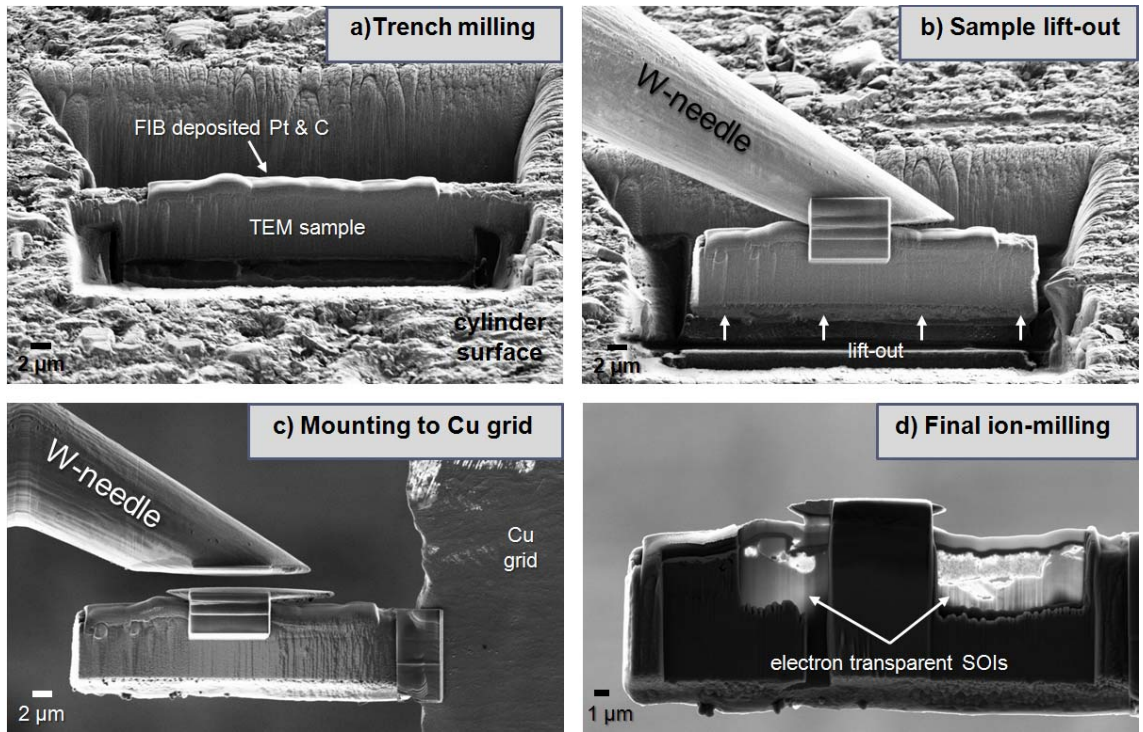
Figure 3-9 FIB in-situ lift-out TEM sample preparation.

4   RESULTS

4.1   Nickel alloyed, Mechanically Reduced, Hot Tested Engine (Ni:MR:HT)

4.1.1   Visual Inspection and Macroscopic Wear

The microstructure from two regions of the Ni:MR:HT bore was studied (Figure 4-1). These areas were i) normal wear region and ii) unworn region. The normal wear region, which represents most of the cylinder surface, extends through most of the zone where the rings run, excluding the ring reversal areas. This area is believed to operate under mixed or hydrodynamic lubrication conditions [187]. The second zone of interest, the unworn area, represents the as-prepared topography that has not been subjected to sliding contact. This area is found at the bottom of the bore, below the ring travel, on the front and back of the cylinder, where clearance for the piston pin is cut in the piston skirt. Comparison of these regions is important for understanding the evolution of the surface. The major face is shown in Figure 4-1, containing the various regions.

As previously mentioned, a single bore was used for the microstructural work presented; the wear and appearance of this bore was similar to the rest of the cylinders. Visual inspection of the unworn region showed a smooth metallic appearance, whereas the normal wear region had a soft grey matted texture with very few surface scratches. These scratches (ring marks) are visible on the major and minor sides of the cylinder. It is important to note that no distinguishable surface characteristics were observed between the major and minor faces, nor were there any forms of severe wear (scuffing, ploughing) present on the bore. Macroscopic wear results are presented in Table 4-I. The average bore growth was worst at TRR, but was only 6.4 μm. For an aluminum engine bore the amount of wear is remarkably low considering the harsh testing conditions.
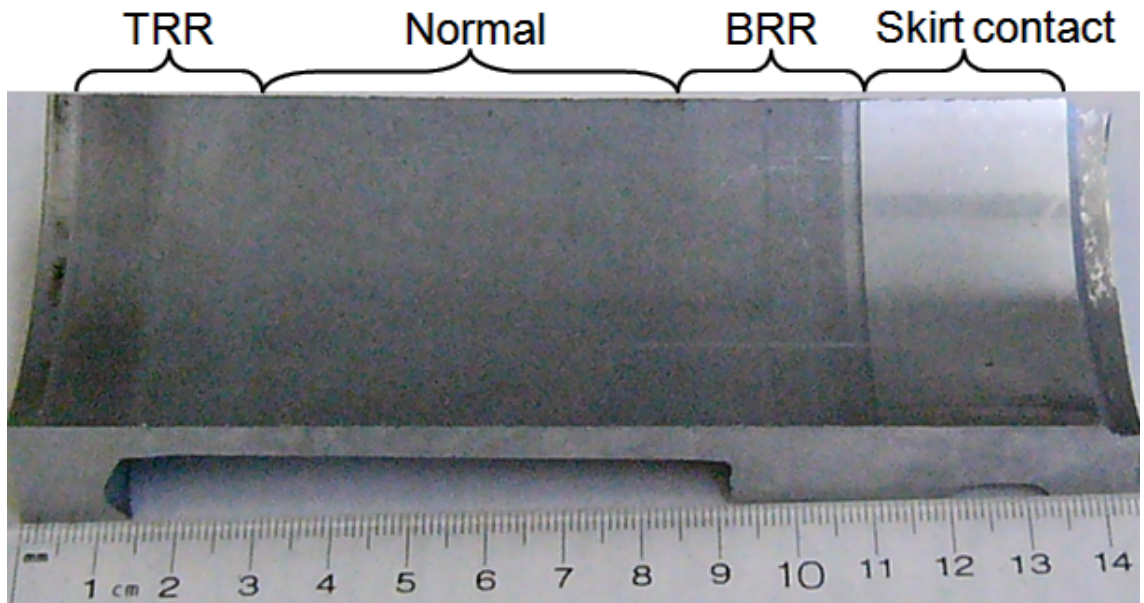
Figure 4-1 Engine bore highlighting ring reversal marks (TRR and BRR) at top dead center and bottom dead center, in addition to the normal wear region, and area of no ring travel.

Table 4-I Ni:MR:HT macroscopic bore wear

	Initial Bore Diameter	Average Bore Δ at TRR	Average Bore Δ at BRR
Characterized bore	99.009 mm	1.27 μm	3.81 μm
Average of bores	99.009 mm	6.4 μm	4.1 μm

4.1.2 Unworn Region

Analysis of the unworn surface indicates that the surface preparation used on this engine did expose hard phases. Figure 4-2(a) is a 3D WYKO image of the unworn surface, which shows silicon particles standing proud from the aluminum matrix and hone marks. An analysis of the profilometery data found the average surface roughness to be 0.118 μm. Figure 4-2(b) is the typical histogram height distribution of the unworn surface; it shows what appears to be a single asymmetric peak. Fitting the peak to Gaussian line shapes reveals that there are two dominant features in the data separated by approximately 0.2 μm. The peak associated with the silicon particles standing above the nominal surface, consistent with Figure 4-2(a), shows that there is variation in the silicon particle exposure (R_f).

A secondary electron micrograph taken from the unworn surface, Figure 4-3, shows fractured silicon particles and hone marks on the aluminum matrix. There was no shear of the matrix in any of the surface or subsurface investigations; instead, damage was localized to the hard phases. Damage to silicon particles was restricted to the near surface, since fracture of the silicon particles was not observed throughout the particle in subsurface sections. Needle-like silicon particles were observed to fracture more readily when compared to the silicon colonies; damage is prominent along the particle edges. Similarly, the iron phase shown in Figure 4-3 is severely damaged; however, almost no damage is observed for the more ductile nickel phase. Additional SEM observations of the unworn surface show scratches perpendicular to the piston sliding direction, even on some of the primary silicon particles. These primary silicon particles are also fractured along their edges. The silicon particles on the unworn surfaces must have been fractured by the bore preparation, since this area was not subjected to sliding contact.
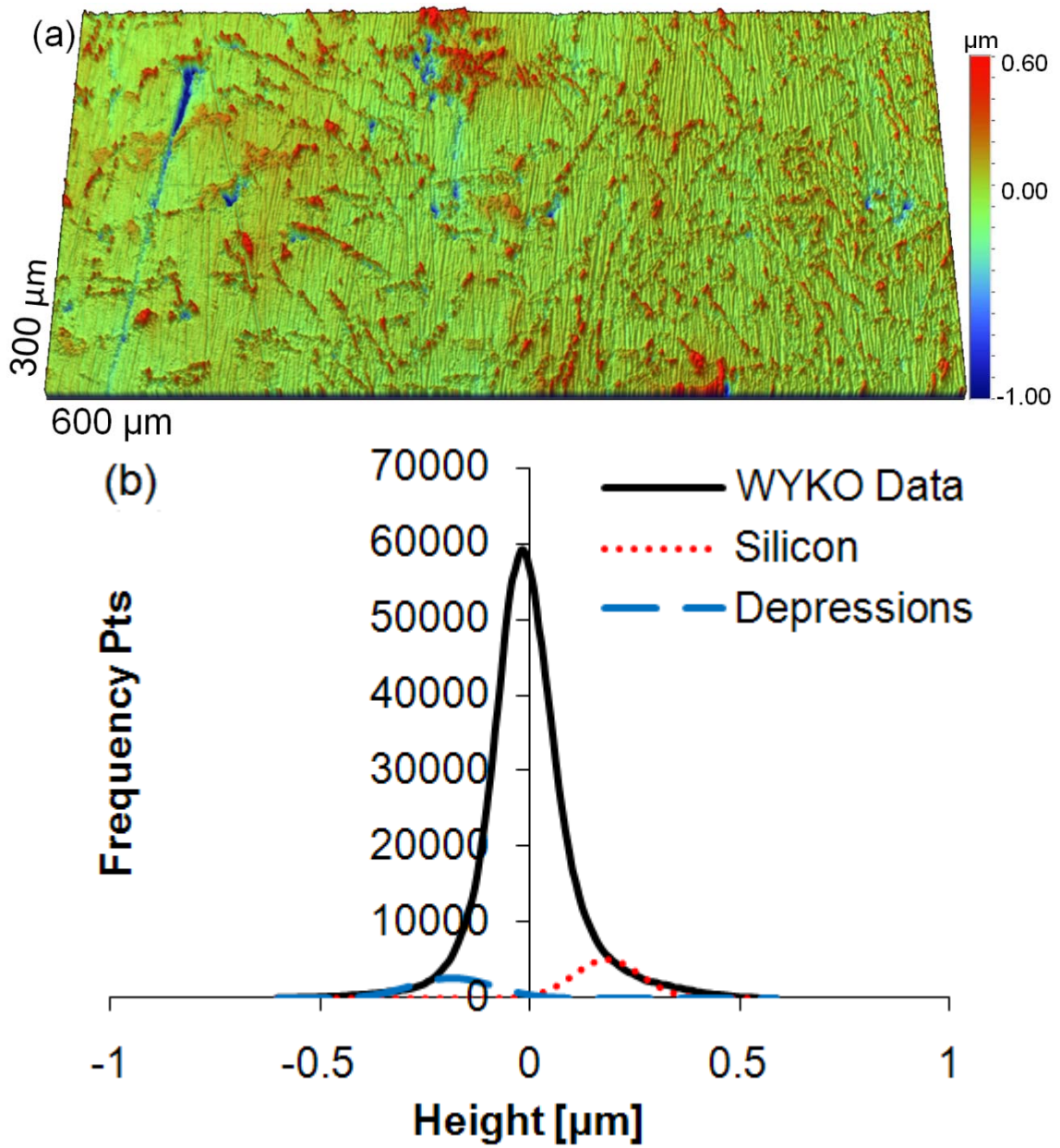
Figure 4-2 (a) WYKO image of unworn region, showing Si particles (red) and particle pull out (blue); (b) corresponding histogram showing the overall height distribution.

Figure 4-3 SEM micrograph of the unworn region showing hone marks on the Al-matrix, Si particles, fractured iron phases and smooth Al-Ni phase; (60° tilt).

4.1.3 Worn Region

A three-dimensional WYKO image from the worn surface, shown in Figure 4-4(a), is presented for comparison with the unworn region, Figure 4-2(a). The average surface roughness is ~ 0.406 μm, which is approximately 5 times the roughness of the unworn surface. Figure 4-4(b) is the corresponding histogram height distribution. The exposure height of the silicon particles is difficult to resolve, given the increased roughness of the matrix, but estimates based on high magnification optical profilometer images suggest that the exposure is actually greater (~0.6 μm) than on the as-prepared surface (0.2 μm).

Another WYKO image presented in Figure 4-5, depicts an aluminum-nickel phase that is severely scratched parallel to the ring motion direction; many of these intermetallic phases are fractured. The aluminum-nickel phase (confirmed by EDS) contains surface scratches as deep as 0.70 μm; in contrast to the smooth silicon particles with minute scratches averaging only 0.03 μm in depth. These scratches imply that the surface texture is a result of the sliding motion of the rings.

The SEM image of Figure 4-6 was taken at a tilt angle of 60 degrees. This figure shows silicon particles that protrude from the surface. Most of the exposed silicon on the worn surface actually appears better than in the as-prepared surface. Silicon surfaces appear smoother, with no evidence of any hone marks, and the edges are rounder, with

significantly less fracture. The rest of the surface exhibits a high roughness with a mixed granular texture. The change in appearance of the "matrix" between Figure 4-3 and Figure 4-6 is the most dramatic element.

EDS analysis shows that the matrix regions of Figure 4-6 are a mixture of Al, Si, C, O, and Ca, whereas a similar analysis from the unworn area shows only aluminum. EDS is at best semi-quantitative, but the reduction in the aluminum signal at the expense of the growth of the other species is consistent with evolution of worn surface. The tilt angle clearly shows that the matrix contains fine particles of varying shape. In addition, the matrix displays fine scratches parallel to the sliding direction. The micrograph also shows calcium deposits embedded into the matrix.

Semi-quantitative chemical results of the worn surface were also obtained via X-ray photoemission spectroscopy (XPS). XPS elemental scans over a 0.5 mm x 0.5 mm area were obtained before and after 0.5 min of Ar-ion etching, which removed ~10 nm from the surface. Results summarized in Table 4-II, indicate that small amounts of Zn, S, Ca, and P (oil additive elements) were present on the worn surface. However, after Ar-ion etching these elements were quickly removed, with the exception of Ca, suggesting that the antiwear film was thin. A review of the lubrication of metallic surfaces demonstrated similar results, wherein wear was primarily governed by the shear strength of the alloy which limited the effectiveness of the antiwear additives and film formation [165].

Table 4-II XPS semiquantitative elemental composition of the Ni:MR:HT worn surface, atomic %, except H

	C	O	Al	Si	Ni	Ca	N	Mg	Zn	S	P	Other
Surface	48	35	6	5	-	0.7	2.4	-	0.2	0.4	0.5	Na, Cl, K
0.5 min etching	16	41	27	4	1.1	1.2	1.2	6	-	-	-	Cu, Na, Cl, K

The backscattered SEM micrograph in Figure 4-7(a) displays the area of interest used for the FIB trench in Figure 4-7(b). This area contains deposits that resemble a spongy texture, a nickel phase, and a silicon particle. The FIB trench highlights the

cross-sectional view of each of these features. The oil deposits are porous, and are located in crevices on the aluminum surface. EDS analysis of the spongy deposit, shows it contains C, P, S, Ca and Zn from the engine oil, as well as, aluminum debris and silicon fragments resulting from wear. It is noteworthy to mention that the nickel phase adheres to the aluminum completely. Furthermore, the nickel/silicon interface contains a small void and a hairline crack ending in the nickel phase.

Another cross-section of the worn surface, shown in Figure 4-8, depicts oil deposits, soot, and silicon particles all confirmed by EDS analysis. The large sharp edged silicon particle in the center of the trench exhibits a smooth contact surface with fine scratches parallel to sliding direction. This silicon particle exhibits no bonding to the aluminum, unlike silicon particles observed in other FIB cross-sections. It is likely that this silicon particle originated elsewhere, and is a fragment of a larger fractured particle. The important points regarding this particle are that when selected for FIB milling, there was no evidence that the particle was not fully bound to the surface and that the adhesion is strong enough that it remained part of the surface, even after some amount of firing cycles, and cleaning and sectioning for these tests. The aluminum matrix under the larger silicon particle shows evidence of plastic deformation.
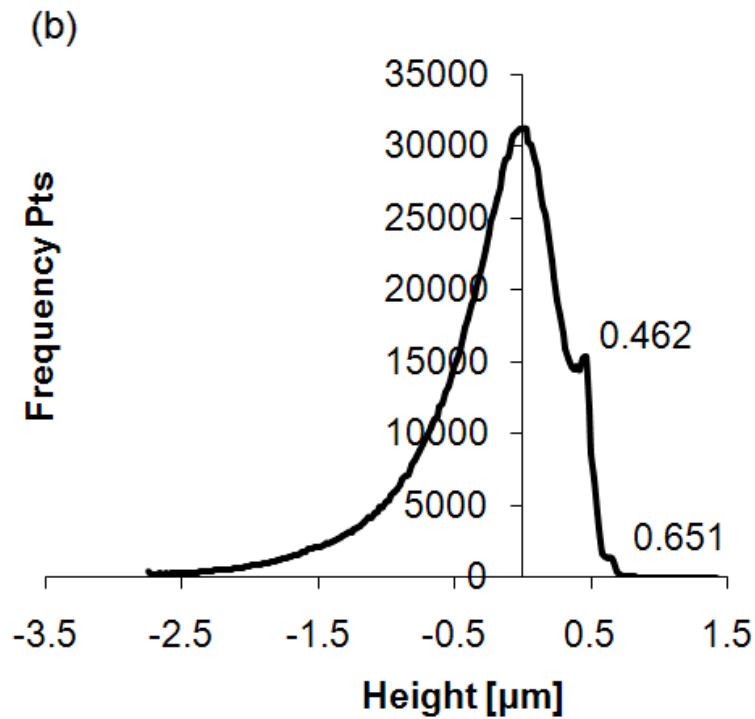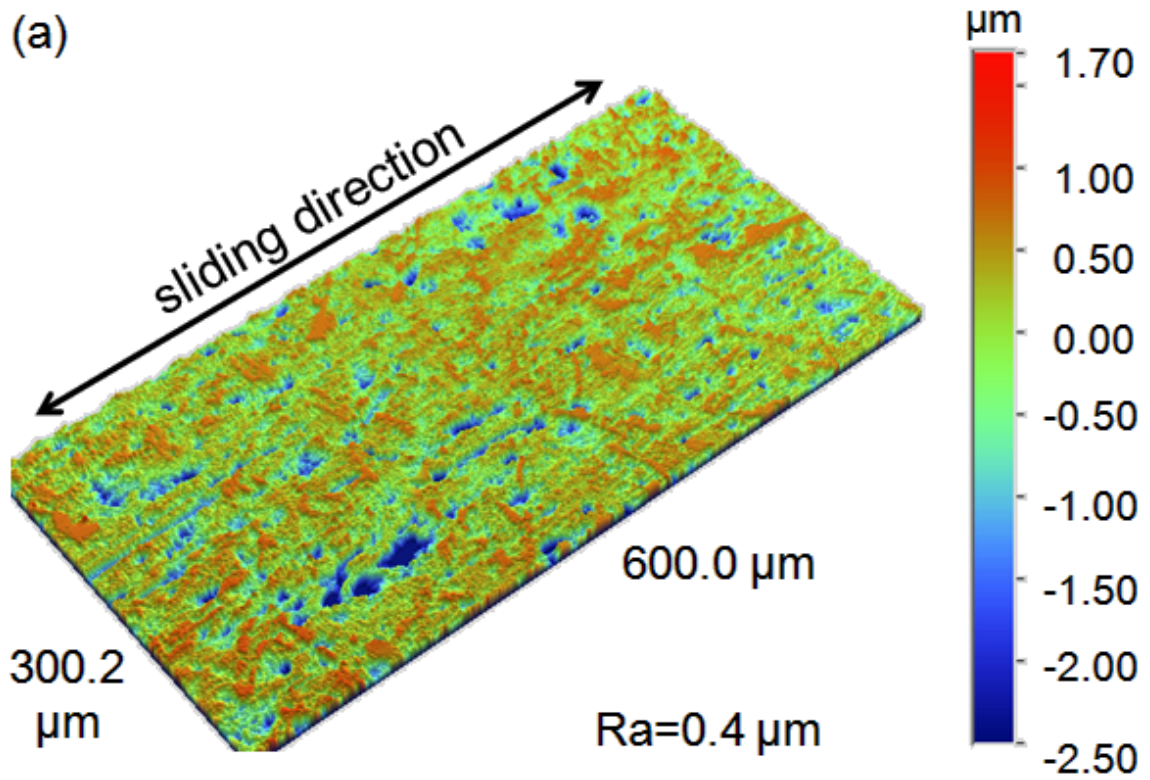
Figure 4-4 (a) WYKO image of normal wear region, showing Si particles and intermetallics (red), fine scratches parallel to sliding, and a few pores/cavities (blue) on the surface; (b) corresponding histogram showing the overall height distribution.
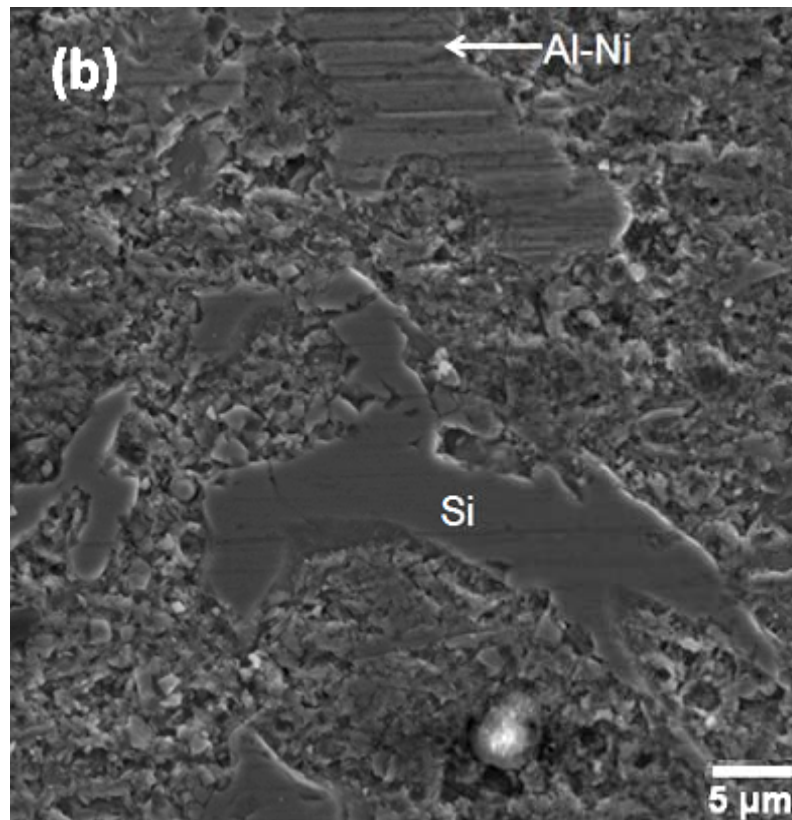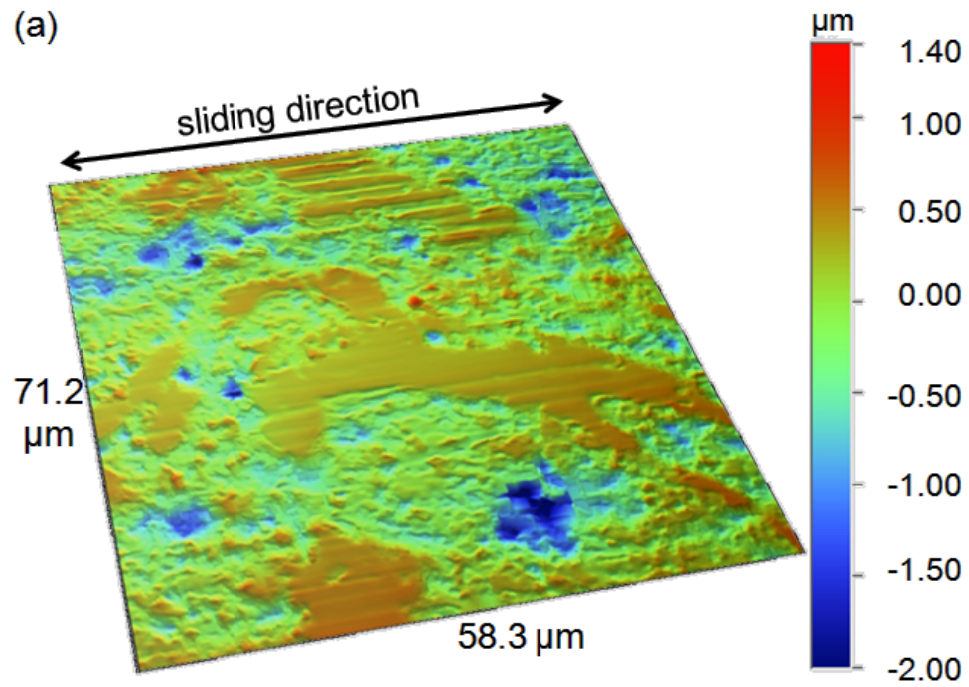
Figure 4-5 (a) WYKO image, and (b) SEM micrograph (0° tilt), showing a heavily scratched Al-Ni phase next to a lightly scratched Si phase; (Ra (Si) = 27.70 ± 2.80 nm, Ra (Al-Ni) = 108.67 ± 10.43 nm).
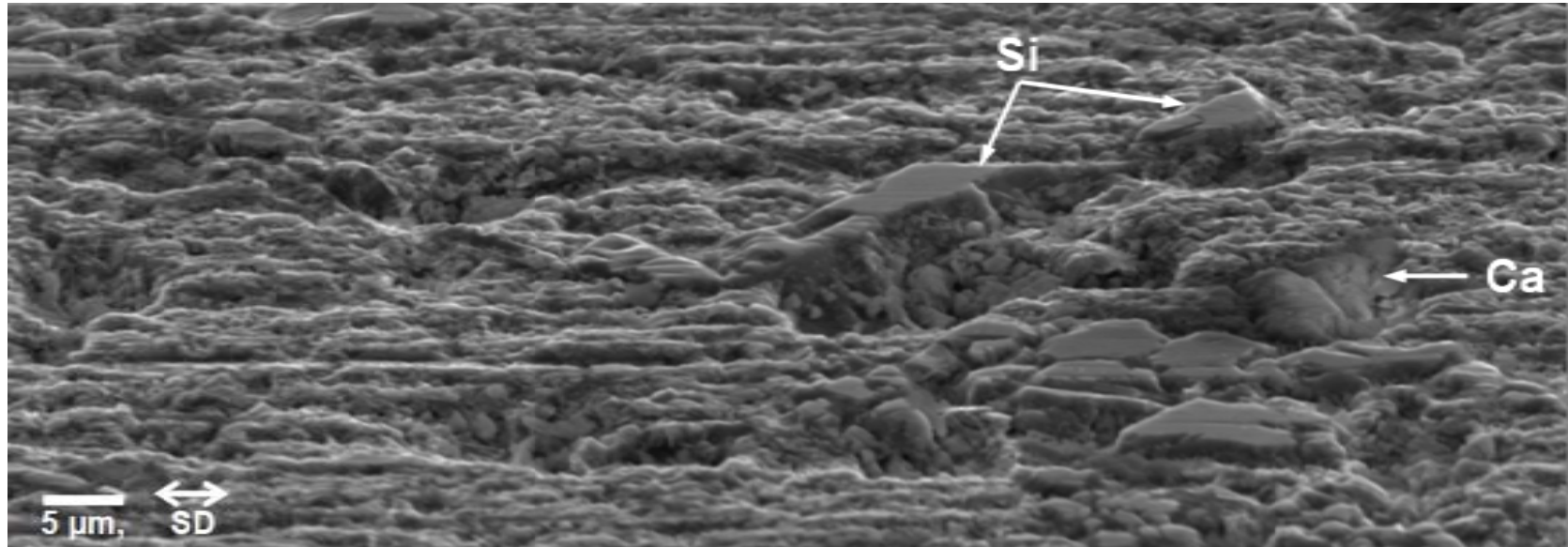
Figure 4-6 SEM micrograph of the worn surface illustrating Si particles that protrude from the surface, small fractured particles existing throughout the Al-matrix, and Ca deposits; (60° tilt).
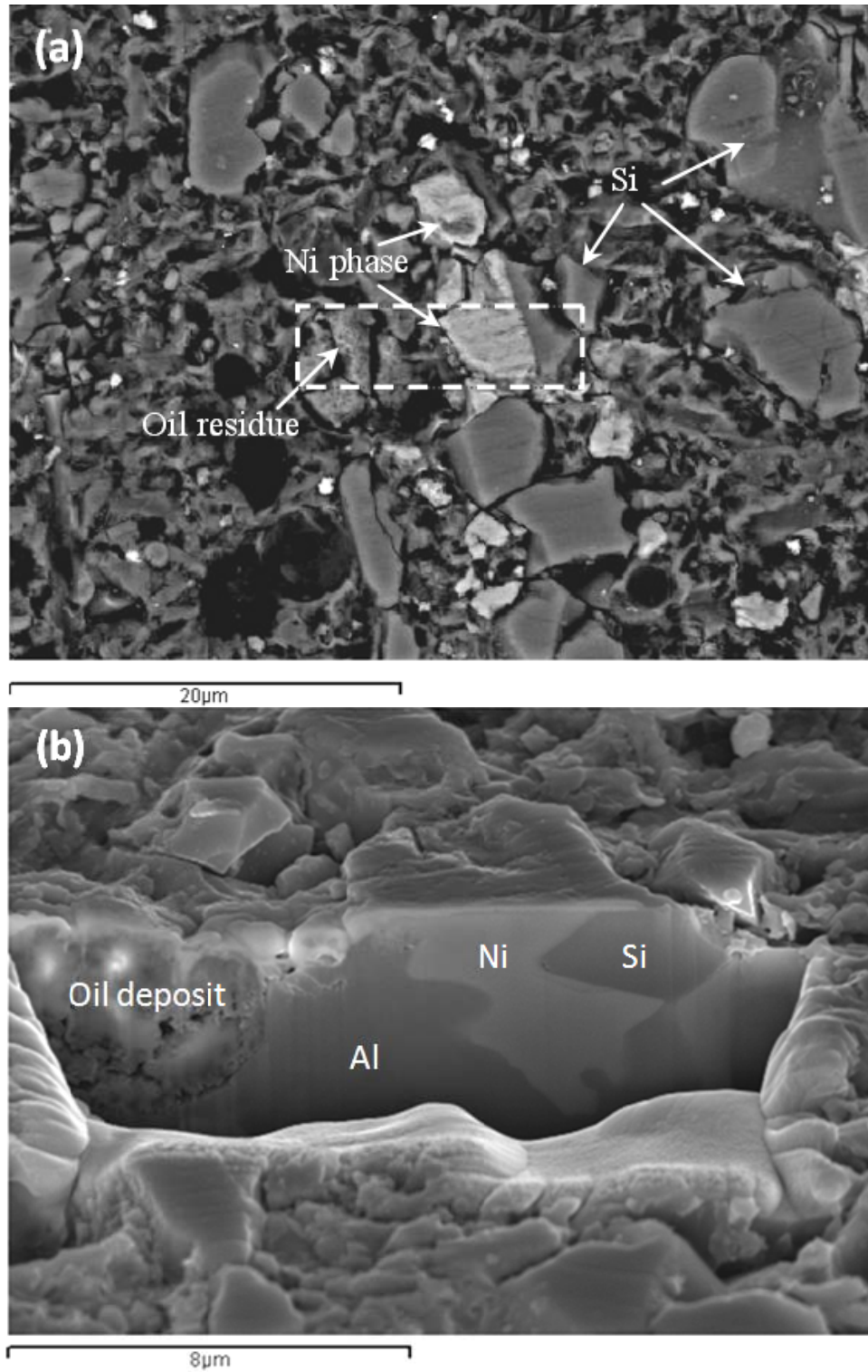
Figure 4-7 (a) Backscattered SEM micrograph displaying the area of interest used for FIB sputtering of the worn surface; (b) corresponding cross-sectional FIB trench.
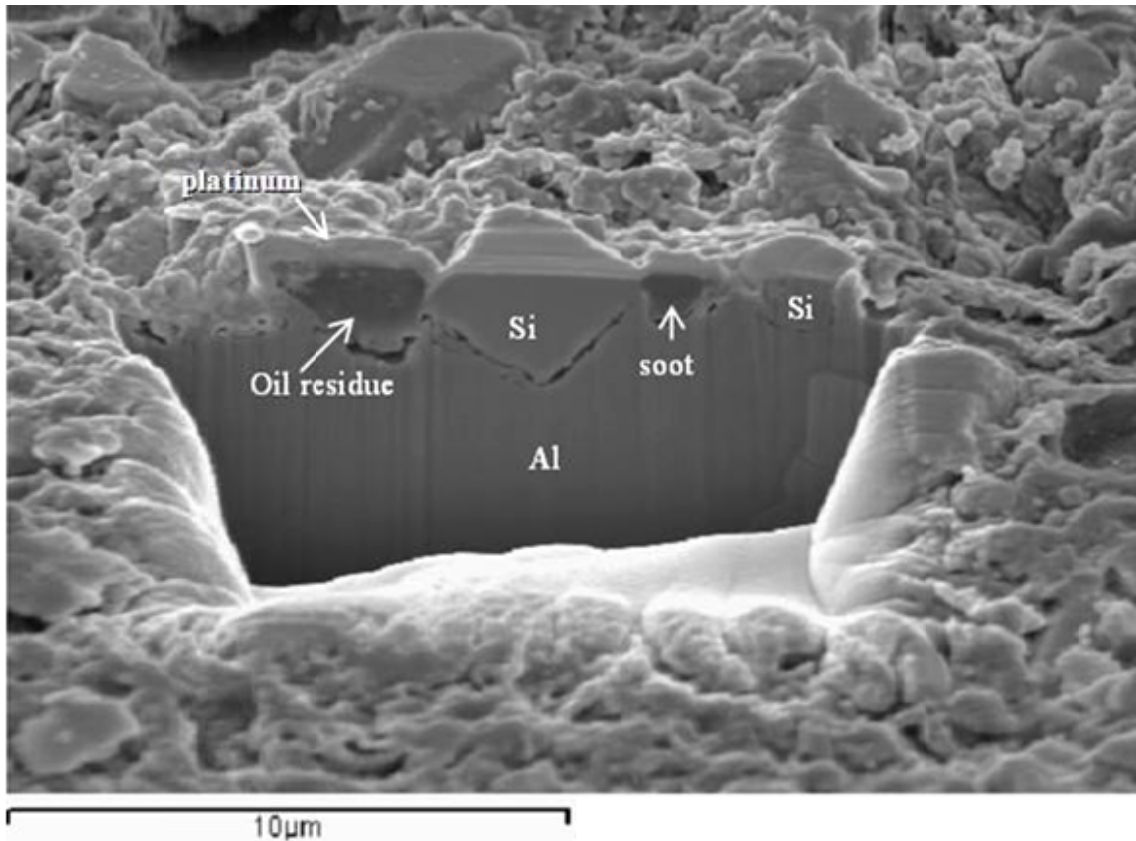
Figure 4-8 FIB cross-section of the worn surface highlighting oil deposits, soot, and Si particles.

4.2 Copper alloyed, Mechanically Reduced, Hot Tested Engine (Cu:MR:HT)

4.2.1 Visual Inspection and Macroscopic Wear

Similar to the Ni:MR:HT engine, the microstructure of two areas from the Cu:MR:HT engine has been examined. These areas are the unworn and worn regions previously described in §4.1.1. Again, comparison of these regions is vital for understanding the evolution of the surface.

After dynamometer testing visual inspection of the entire engine bore indicated no evidence of any severe wear (scuffing, ploughing, pitting). The unworn region visually has a metallic shiny appearance. Conversely, the worn area consisted of a soft grey matted texture containing several pores and some scratches parallel to piston motion. More importantly, no distinguishable surface characteristics were observed

between the major and minor faces, nor were there any severe scuff marks present on the bore (see Figure 4-9).

A single bore representative of the rest of the cylinders was used for the microstructural work presented. Macroscopic wear results of this bore and the engine average are presented in Table 4-III. The bore growth was worst at TRR, but was only 5.1 μm and comparable to Ni:MR:HT which was 6.4 μm. Again, for an aluminum engine bore the amount of wear is remarkably low considering the harsh testing conditions.
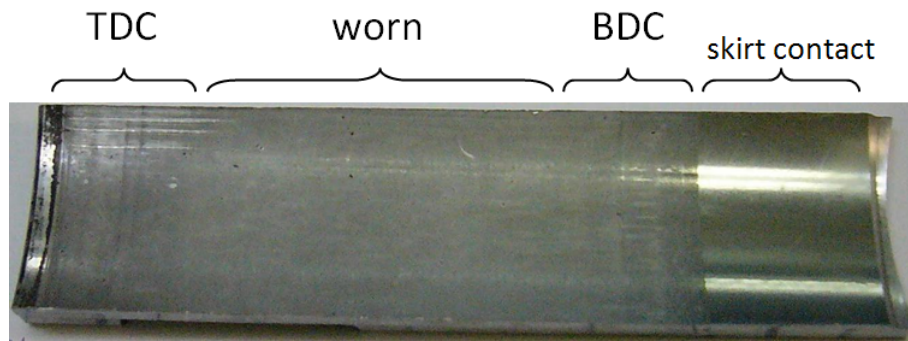
Figure 4-9 Engine bore highlighting ring reversal marks at top dead center (TDC) and bottom dead center (BDC), and area of no ring travel from the major thrust face.

Table 4-III Cu:MR:HT macroscopic bore wear

	Initial Bore Diameter	Average Bore Δ at TRR	Average Bore Δ at BRR
Characterized bore	99.0117 mm	5.1 μm	2.6 μm
Average of bores	99.0159 mm	1.2 μm	3.4 μm

4.2.2 Unworn Region

Analysis of the unworn surface indicates that the surface preparation used on Cu:MR:HT did expose hard phases but not to the extent expected. A 3D profilometry image (Figure 4-10) of the unworn surface shows silicon particles standing proud from the aluminum matrix and fine hone marks. Analysis of the profilometery data determined the average surface roughness (R_a) to be 0.093 μm; which is comparable to Ni:MR:HT ($R_a \approx 0.118$ μm). The corresponding histogram height distribution is

presented in Figure 4-11; it shows a single asymmetric peak. By fitting the peak to two Gaussian line shapes, the exposure height of the silicon (R_f) is determined to be 0.32 μm. This value is lower than the prescribed 0.6 μm exposure recommended by PEAK [28]; but it is comparable to bore Ni:MR:HT ($R_f \approx 0.2$ μm).

A secondary electron micrograph taken from the unworn surface, Figure 4-12, shows exposed silicon particles on the aluminum matrix. The relatively small, spherical silicon particles do not appear to be heavily damaged. However, many of them display evidence of fracture and voids around their edges near the surface, likely caused by mechanical stripping. Cross-sectional FIB micrographs shown in Figure 4-13, further illustrates these small fractures and shows possible decohesion from the matrix below some silicon particles. These silicon particles show no evidence of their remaining fractured chips; instead, the fractured chips are removed during the mechanical stripping and cleaning process of the bore, leaving empty voids at silicon/aluminum interfaces. The greatest degree of void formation was confined to the larger hard phases. Figure 4-12 shows the extent of void formation at the interfaces of larger silicon particles. Softer phases, shown in Figure 4-14, are not fractured; instead, they are removed during the mechanical stripping process along with the aluminum and thus have no height exposure or damage accumulation. Comparatively similar results from the Ni:MR:HT bore (see Figure 4-3) show that larger silicon particles, particularly with needle-like morphologies, frequently exhibit a greater degree of interfacial void formation during surface preparation, as compared to the smaller spherical silicon particles. For both bores, large iron containing phases were prone to fracture and phases containing soft constituents appeared to be at the same exposure level as the matrix with little or no interfacial void formation. Figure 4-15 from Cu:MR:HT shows the subsurface fracture of these iron phases, along with a silicon particle that shows no evidence of fracture or decohesion. No extensive damage to the aluminum matrix was observed in any surface or subsurface investigations; even in areas where large patches (40 μm in diameter) of α-aluminum have formed.

110

A chemical summary of the unworn surface is displayed in Figure 4-16. The EDS map shows silicon particles, intermetallics, and aluminum patches. The corresponding EDS spectrum and semi-quantitative data (Figure 4-16c) suggests a high silicon concentration, approximately 14 wt.%, likely due to the location of the scanned area situated over dense silicon colonies. Overall, the semi-quantitative results agree with the suggested alloy composition.
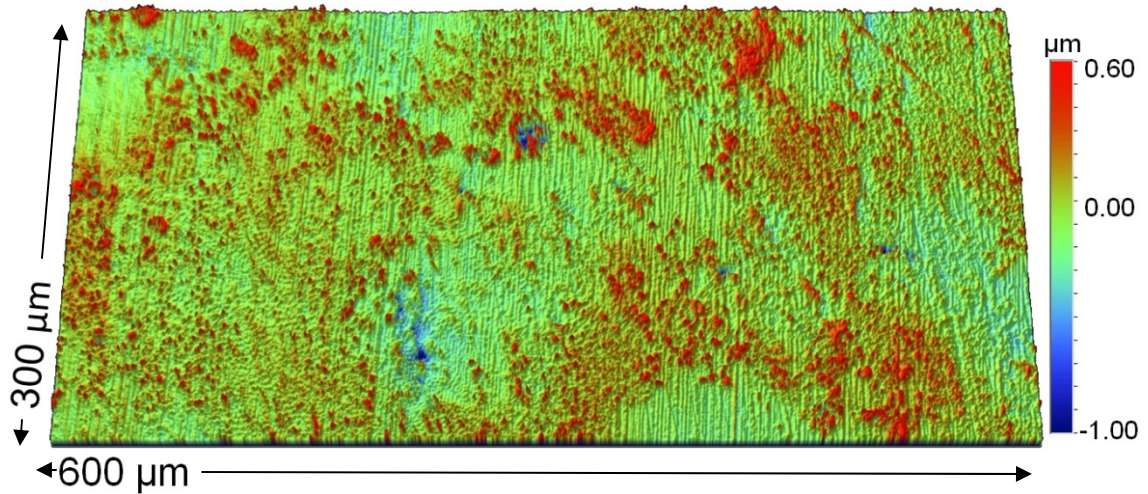
Figure 4-10 WYKO 3D profile of unworn region, showing exposed particles (red) and matrix (green).
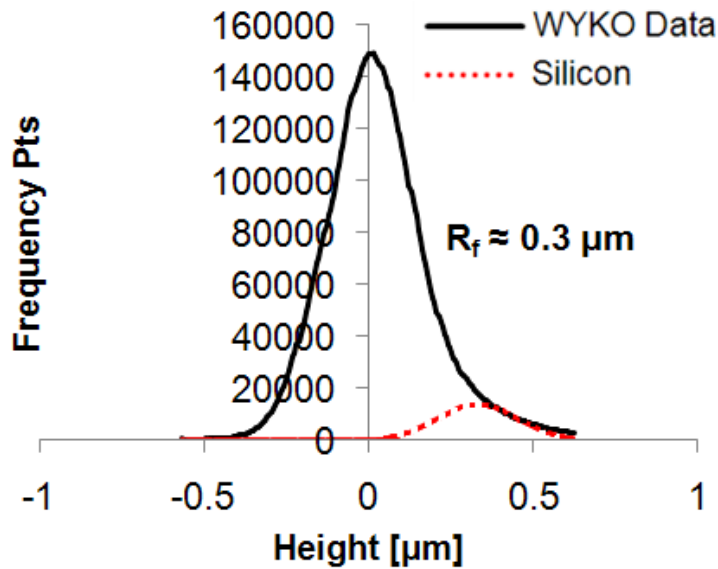
Figure 4-11 Histogram showing the overall Si height distribution of the unworn surface.

111
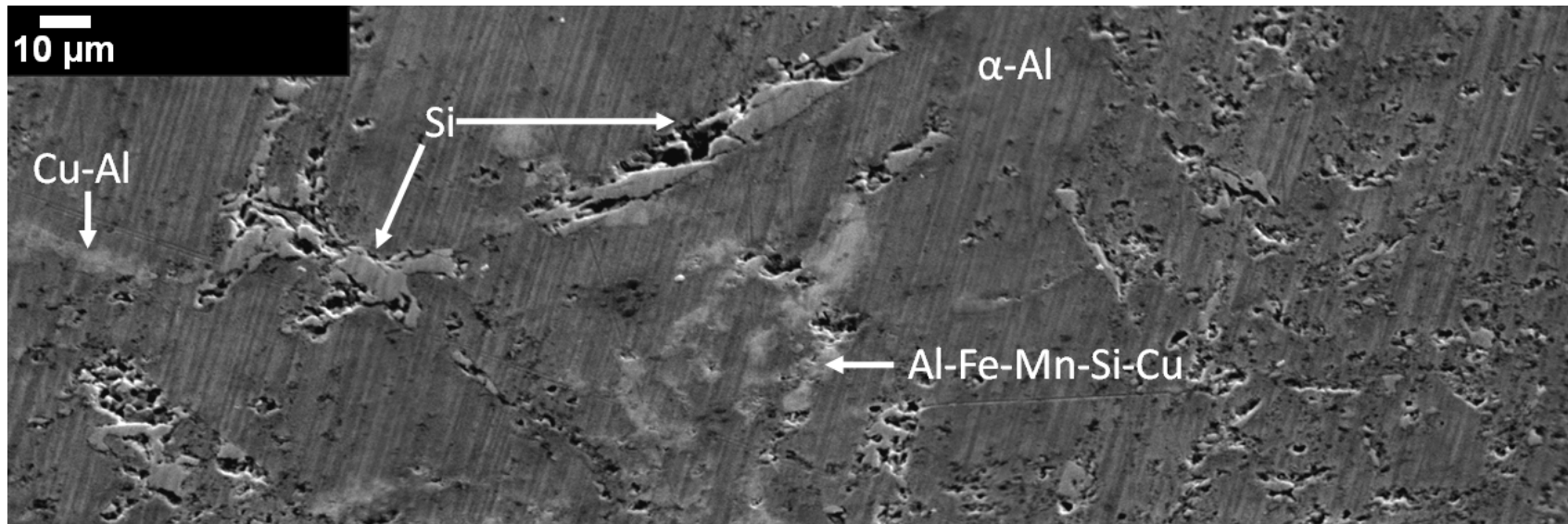
Figure 4-12 SEM micrograph of the unworn region showing hone marks on the Al-matrix, voids at the interfaces of Si particles, and intermetallics (1000x, 50° tilt).
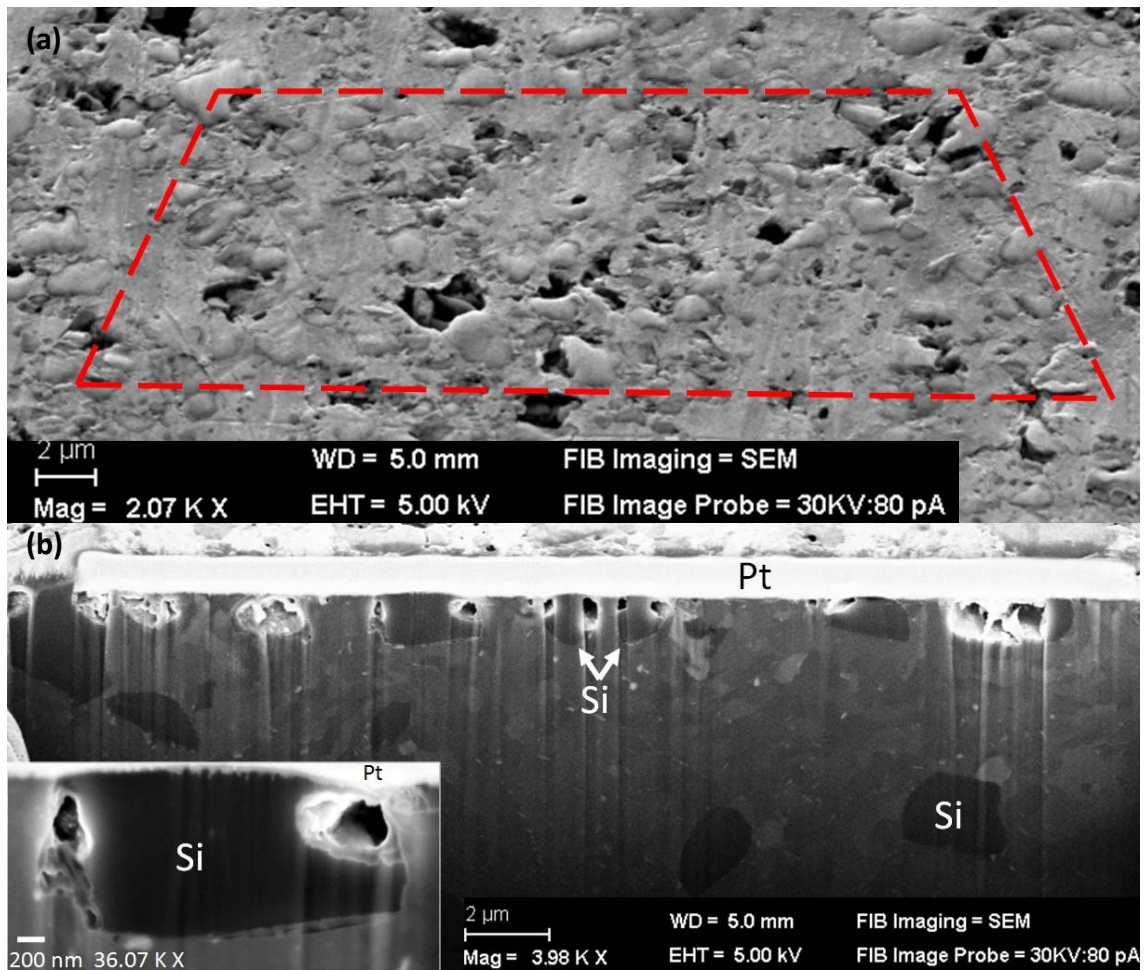
Figure 4-13 a) Unworn area chosen for FIB milling boxed in red; b) SEM observation of the corresponding FIB cross-section showing fracture voids around small Si particles at the surface and evidence of particle decohesion; (tilt 54°).
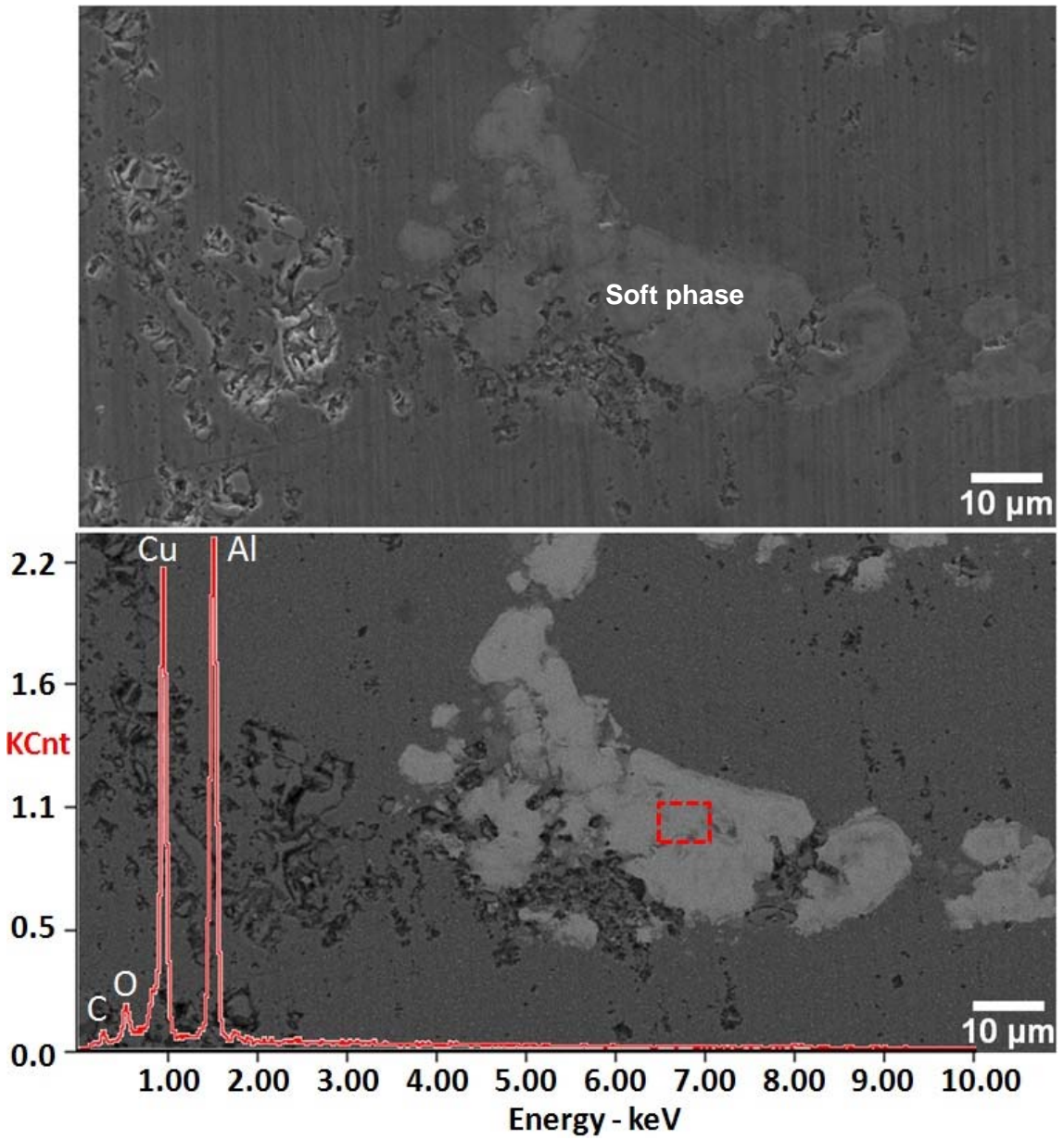
Figure 4-14 SE (top) and BS (bottom) micrographs of the unworn region including an EDS spectrum of the area boxed in red; showing soft phases (white) that appear to be level with the matrix (900x).
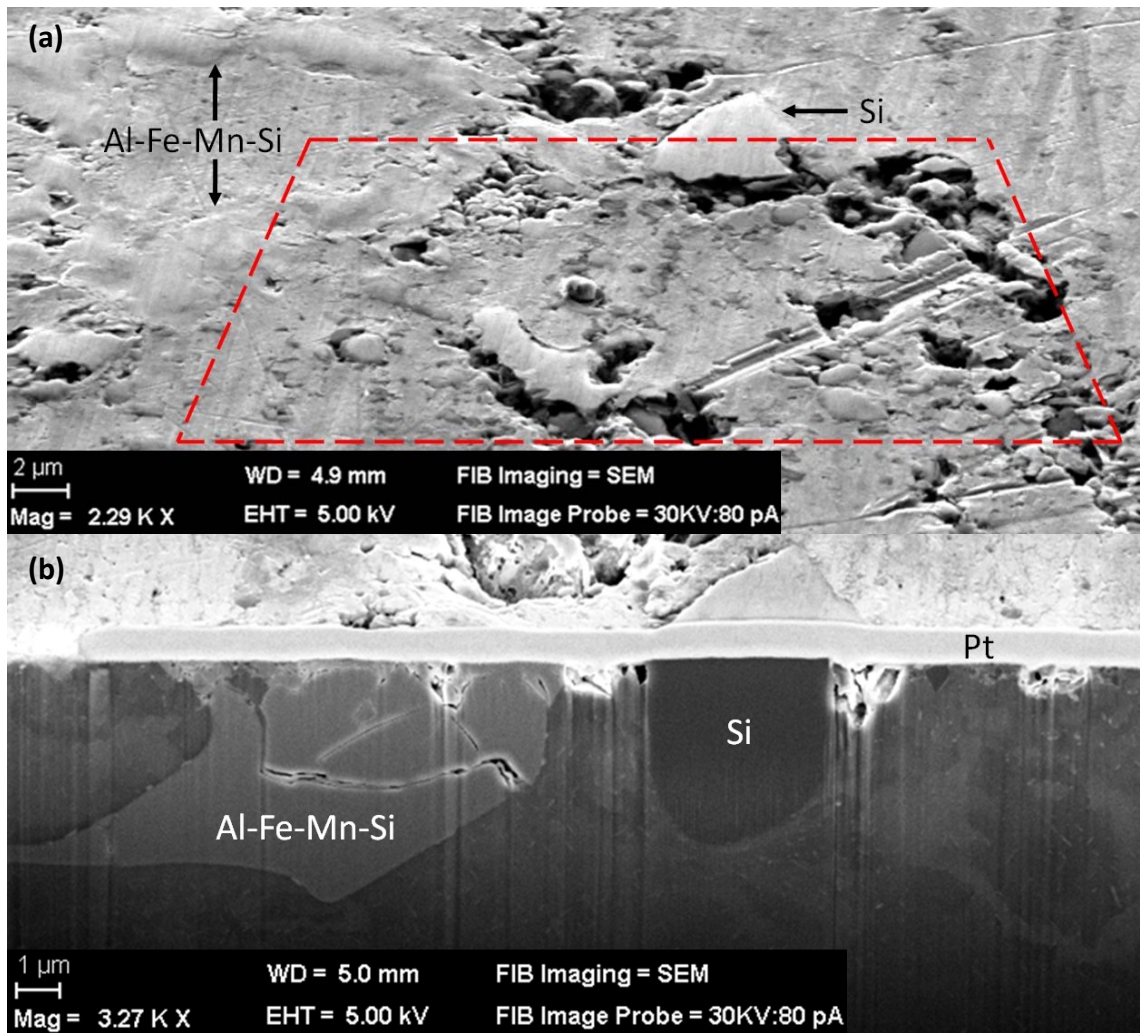
Figure 4-15 a) Unworn area chosen for FIB milling boxed in red; b) SEM observation of a FIB cross-section showing a fractured iron phase next to a fully adhered Si particle; (tilt 54°).
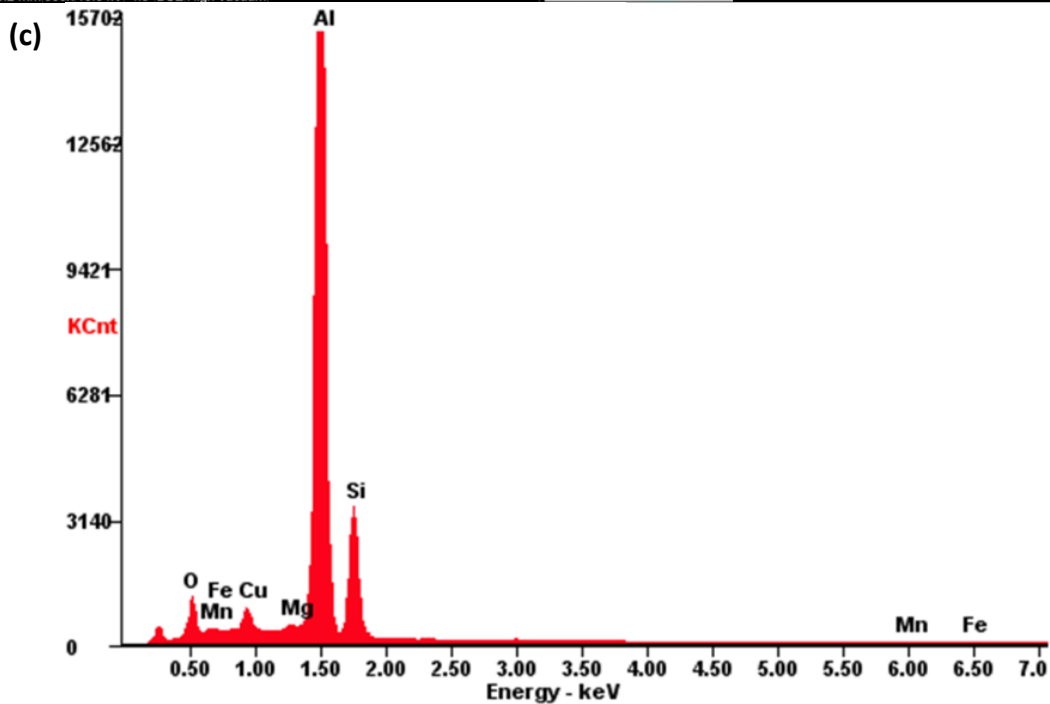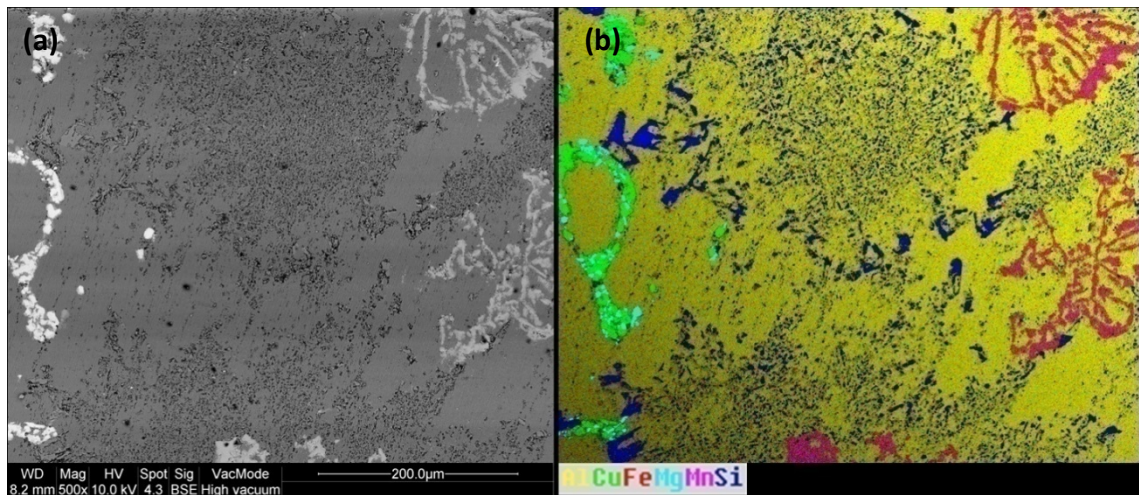
Element	Wt%	At%
OK	03.06	05.19
CuL	02.51	01.07
MgK	00.45	00.51
AlK	78.03	78.41
SiK	14.74	14.23
MnK	00.93	00.46
FeK	00.27	00.13

Figure 4-16 a) BSE micrograph of the unworn surface; b) corresponding EDS map showing intermetallic elements; c) corresponding EDS spectrum and semi-quantitative data of the entire mapped area; (0° tilt).

4.2.3 Worn Region

The topography of the worn surface from Cu:MR:HT is shown in Figure 4-17 which can be directly compared to that of the unworn surface in Figure 4-10. The average surface roughness $R_a \approx 0.373$ μm, which is comparable to Ni:MR:HT ($R_a \approx 0.406$ μm), is over 2.5 times that of the unworn surface which is an indication that significant surface changes took place during engine testing. The corresponding histogram height distribution shown in Figure 4-18 is much different from that of the unworn surface. The increased roughness of the matrix makes it difficult to resolve the silicon exposure of the worn surface. Nevertheless, high magnification optical profilometer images, Figure 4-19, suggest that the exposure is approximately 0.4 μm. This exposure is greater than the as-prepared surface. A similar result was also shown in the Ni:MR:HT bore, where the silicon exposure increased from approximately 0.2 μm to 0.6 μm after engine testing.

The most distinctive characteristic between the worn and unworn regions is the change in matrix morphology. All evidences of hone marks are removed and the matrix is replaced with a much rougher texture. Large smooth patches of α-aluminum observed on the unworn surface are now rougher in texture and are instead, scattered with oil deposits and small particles. Direct SEM comparisons of the matrix in Figure 4-20 clearly shows a resemblance to that of Ni:MR:HT in Figure 4-6. The high magnification SEM images of both bores have shown that the matrix is comprised of fine fractured particles of varying size, grooves parallel to sliding, and oil deposits. These particles reside in a tribolayer; they remain tightly bound to the surface and were not removed in any of the cleaning steps associated with sample preparation.

Compared to the unworn secondary electron micrograph of Figure 4-12, the silicon particles in Figure 4-20 appear to be exposed to a greater extent, supporting the profilometry data. Figure 4-20 shows that the larger silicon particles are fractured and they contain small surface scratches parallel to sliding, suggesting contact with the counterface. The small spheroidized silicon particles are difficult to resolve with the magnification in Figure 4-20, as they blend in with the surrounding topography. The

same silicon surface characteristics were observed in Ni:MR:HT. High magnification FIB cross-sectional images are presented next to investigate these smaller particles.

FIB techniques, described in §3.5, were used to mill micron scale trenches into the worn surface in order to attain cross-sectional subsurface micrographs of large silicon particles, small spherical silicon particles, and the underlying aluminum matrix. The area of interest used for FIB milling of a large, fractured, and damaged silicon particle is shown in Figure 4-21(a). This particle was chosen for subsurface analysis because it represents some of the higher degrees of surface damage observed on silicon particles. The evolved matrix around the particle does not show any evidence of severe wear or any nascent aluminum patches; furthermore, it appears that silicon particles are still protruding from the matrix and their contact surfaces are smooth with scratches parallel to sliding. The cross-sectional view of this particle is presented in Figure 4-21(b). In this image the large silicon particle, although fractured, exhibits full adhesion to the aluminum matrix below it. Combustion byproducts, such as carbon, are observed to reside in crevices between the fractured particles, as confirmed by EDS. The tooth-shaped silicon particle, which exhibits almost no bonding to the aluminum, is magnified in Figure 4-21(c). Small precipitates likely belonging to the θ family are indicated by the white arrows in the aluminum matrix. These uniformly dispersed precipitates strengthen and increase the hardness of the aluminum matrix and are a product of phase transformations induced by heat treatment [188-190]. In fact, studies have shown that aluminum alloys containing high amounts of copper (i.e. 3 wt. %) exhibit an increase in hardness and strength when compared to alloys with low amounts of copper [191, 192]. Some of the precipitates appear to be larger than 100 nm in length. This is consistent with the T7, overaged heat treatment. This condition is known to produce incoherent precipitates that do not effectively block dislocations, i.e., reduced hardness, but good dimensional stability.

Another FIB trench shown in Figure 4-22 displays a cross-sectional view of small spherical silicon particles. Each of these particles has a smooth flattened contact surface with fine scratches parallel to sliding. More importantly, these silicon particles are

protruding from the matrix as indicated by the dashed line. The far-left and far-right silicon particles both show different degrees of interfacial decohesion. The far-right particle shows almost no bonding to aluminum, and plastic deformation of the matrix is seen at the interface. It is possible that this particle originated elsewhere, or was a fragment of a larger particle. Conversely, the far-left particle only shows signs of decohesion closer to the contact surface; the lower portion of the particle appears to be fully adhered to the matrix. Although these particles are not fully bound to the surface, they still remain attached, even after the engine test and after subsequent sample cleaning. These results suggest that silicon particles are in contact with the counterface and most likely act as the primary, but not sole, contact points. In addition, these silicon particles do not show any signs of voids or damage near their edges previously observed on the virgin surface Figure 4-13, suggesting that these silicon particles were exposed during the engine test and that the wear process is less abrasive than the surface preparation. Overall, FIB cross-sectional analysis of Ni:MR:HT showed the same subsurface features, wherein larger silicon particles were fractured and typically showed little or no evidence of interfacial decohesion and smaller spherical particles exhibited cohesion and decohesion. All silicon particles showed evidence of contact with the counterface in the form of flattened surfaces with minute scratches parallel to sliding. The subsurface aluminum matrix was identical, showing no evidence of excessive wear and protected by a tribolayer comprised of small particles and oil deposits.

Semi-quantitative chemical results of the worn surface were obtained via XPS. XPS elemental scans over a 0.5 mm x 0.5 mm area were obtained before and after 0.5 min of Ar-ion etching, which removed ~10 nm from the surface. The results, summarized in Table 4-IV, indicate that small amounts of Zn, S, Ca, and P (oil additive elements) were present on the worn surface. After Ar-ion etching, these elements, with the exception of Ca, were quickly removed, showing that the antiwear film was thin. XPS etching results of Ni:MR:HT showed similar trends, wherein higher degrees of silicon and lower amounts of Al, Ca, and O were detected on the surface compared to after etching. A review of the lubrication of metallic surfaces demonstrated similar results,

wherein wear was primarily governed by the shear strength of the alloy which limited the effectiveness of the antiwear additives and film formation [165].

Table 4-IV XPS semiquantitative elemental composition of the Cu:MR:HT worn surface, atomic %, except H

	C	O	Al	Si	Ni	Ca	N	Mg	Zn	S	P	Other Trace
Surface	54	32	6	2.8	-	1.0	1.8	-	0.2	0.7	0.7	Na, Cl, K
0.5 min etching	24	38	25	2.7	-	2.4	1.2	5	-	-	-	Cu, Na, Cl, K

Qualitative chemical observations of second phases and oil deposits were carried out using EDS. These results can also be used to point out the wear mechanisms involved during the engine operation. EDS analysis of spherical oil deposits shown in Figure 4-23(a), indicates that they are comprised of a mixture of oil additives (Zn, Ca, P), combustion byproducts (C, O, S), and wear debris (Al, Fe, Si). Many of the oil deposits appear to have an amorphous texture (Figure 4-23(b)).

A secondary electron micrograph along with the corresponding back-scattered image from various phases confirmed by EDS is presented in Figure 4-24. Compositional and microstructural studies [4, 6, 19, 184], suggest that the phases in Figure 4-24 are most likely $Al_{15}(FeMn)_3Si_2$, Al_2Cu, and $Al_5Mg_8Si_6Cu_2$. Phases containing softer constituents generally show a greater degree of wear as compared to harder phases. This is indeed the situation, where phases containing large amounts of copper appear to be worn to a greater extent than the other phases; they are fractured and scratched. The phase containing magnesium is damaged and even appears to be at a lower elevation that the surrounding matrix. In contrast, brittle phases containing iron are fractured but exhibit far fewer scratches compared to the softer phases. The same applies to silicon, wherein its surface is smoother in comparison to all other phases. Engine Ni:MR:HT also showed similar characteristics where phases containing Ni, Cu, and Al exhibited greater degrees of surface damage compared to the harder phases, primarily in the form of deep surface scratches parallel to sliding.

The overall chemical evolution of the surface is summarized by the EDS maps shown in Figure 4-25; which when compared to Figure 4-16 shows a significant decrease in aluminum and increase in oil deposits and combustion byproducts. A slight decrease in silicon has occurred but likely caused by limitations in resolution when detecting small fractured silicon particles mixed in the tribolayer. Silicon surfaces are shown to support Zn and S with little or no traces of P, Ca, C, or O. High concentrations of Zn have been detected to form readily on copper containing phases.
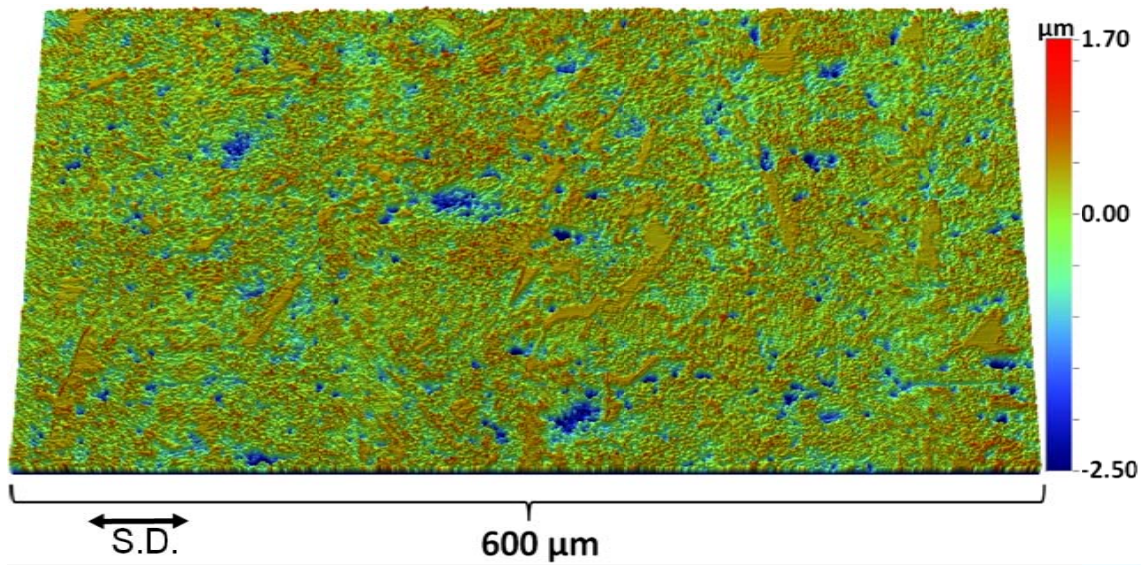
Figure 4-17 WYKO 3D profile (300 × 600 µm) of the worn region, showing elevated portions (red), fine grooves parallel to sliding, and a cavities (blue) on the surface.
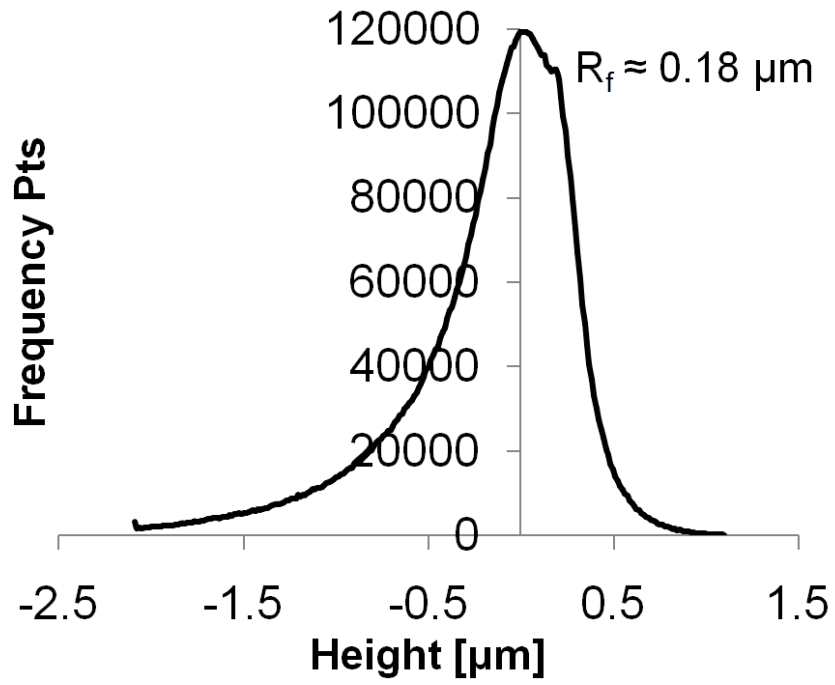
Figure 4-18 Histogram showing the typical height distribution of the worn surface.
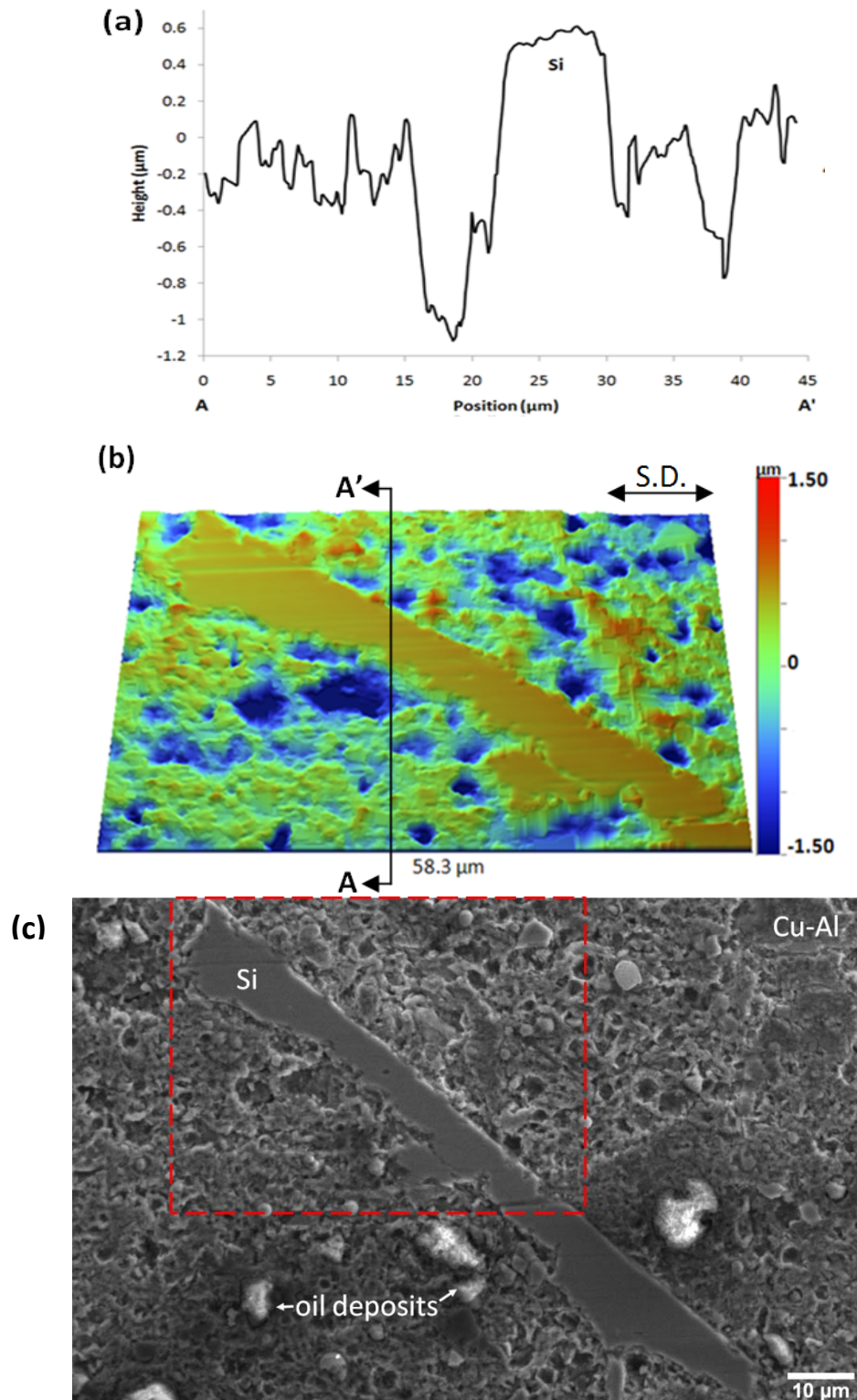
Figure 4-19 a) cross-sectional height distribution of section A-A'; b) corresponding WYKO 3D profile of Si needle of the worn region; and c) corresponding SEM micrograph with WYKO region boxed in red and phases identified by EDS (1000x).
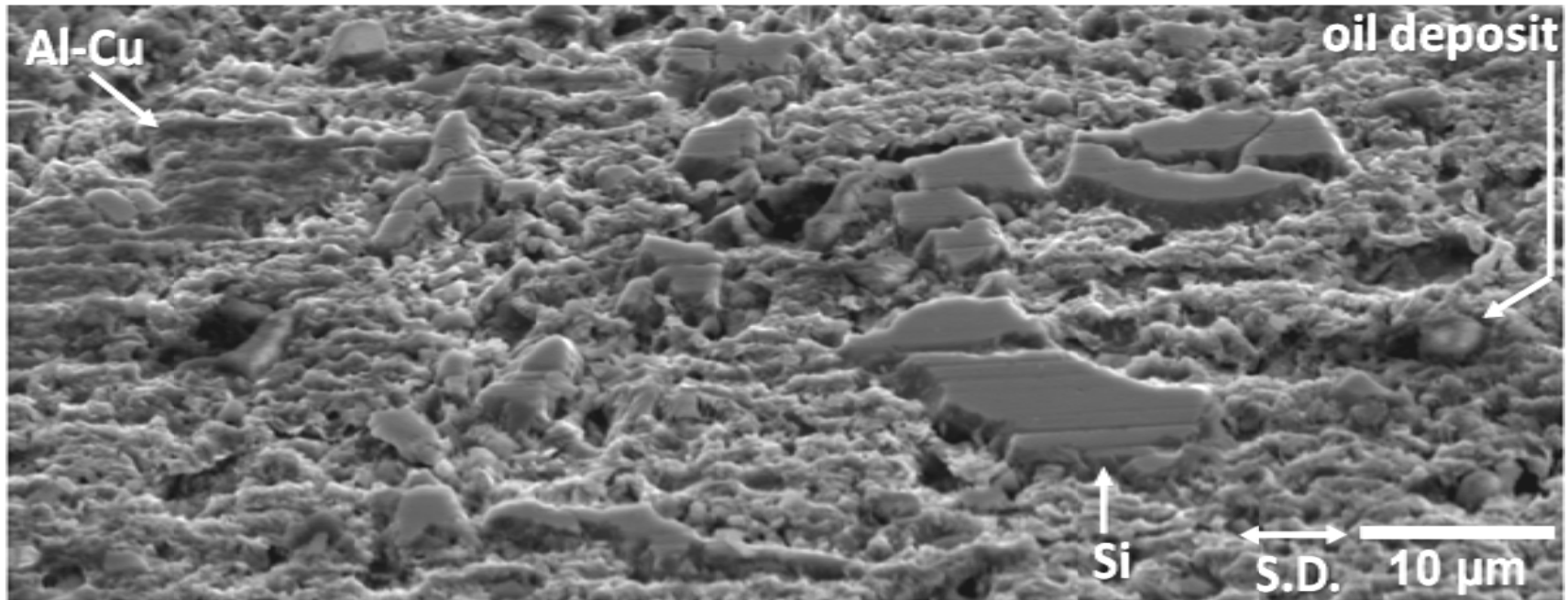
Figure 4-20 SEM micrograph of the worn surface illustrating fine scratches parallel to sliding on exposed Si particles; (1500x, 60° tilt).
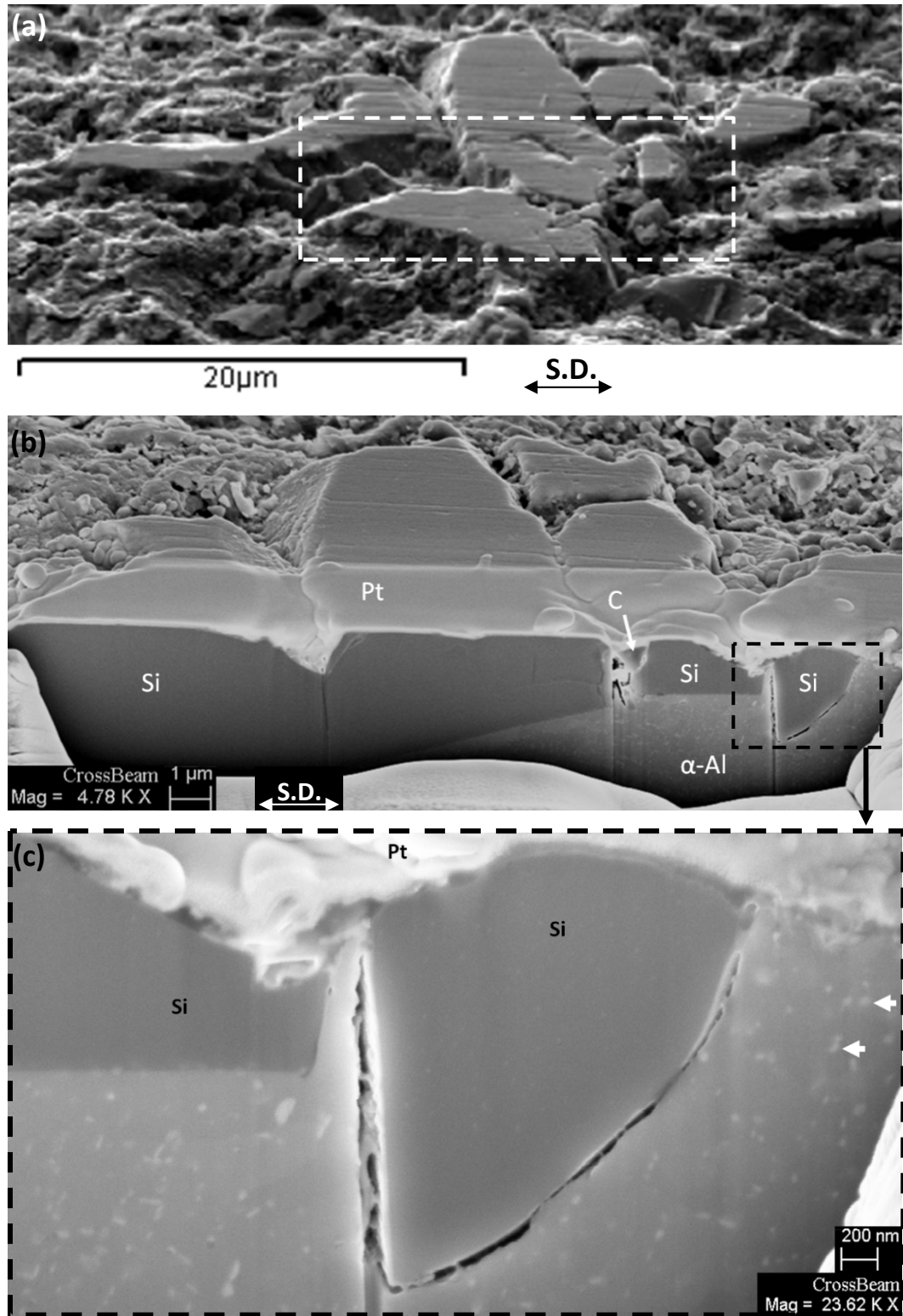
Figure 4-21 a) Worn area for FIB analysis; b) FIB trench of fractured Si particle; c) Magnified region of Si particle that exhibits decohesion; precipitates are denoted by the white arrows.

125
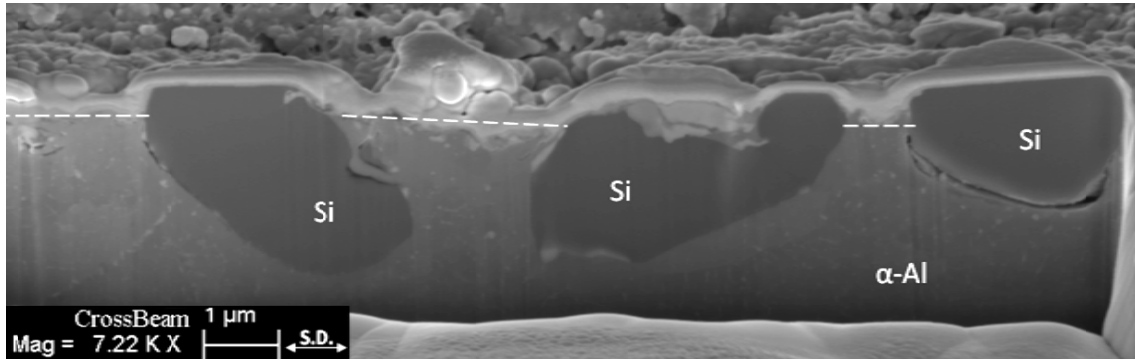
Figure 4-22 FIB cross-section of the worn region showing small spherical Si particles; contact surfaces are flattened and the matrix is indicated by the dashed line.
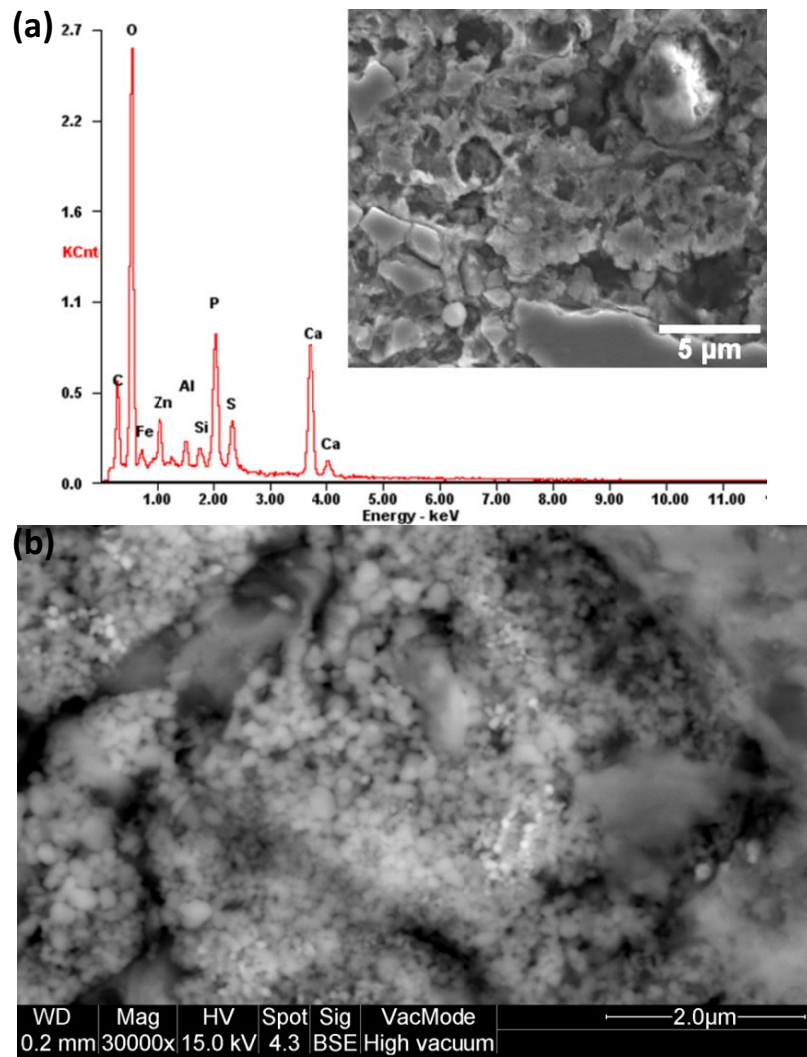
Figure 4-23 a) EDS spectrum and SEM image of a spherical oil deposit residing on the worn surface (3000x); b) BSE micrograph showing the amorphous texture of oil deposits residing in valleys on the worn surface; (0° tilt).

126
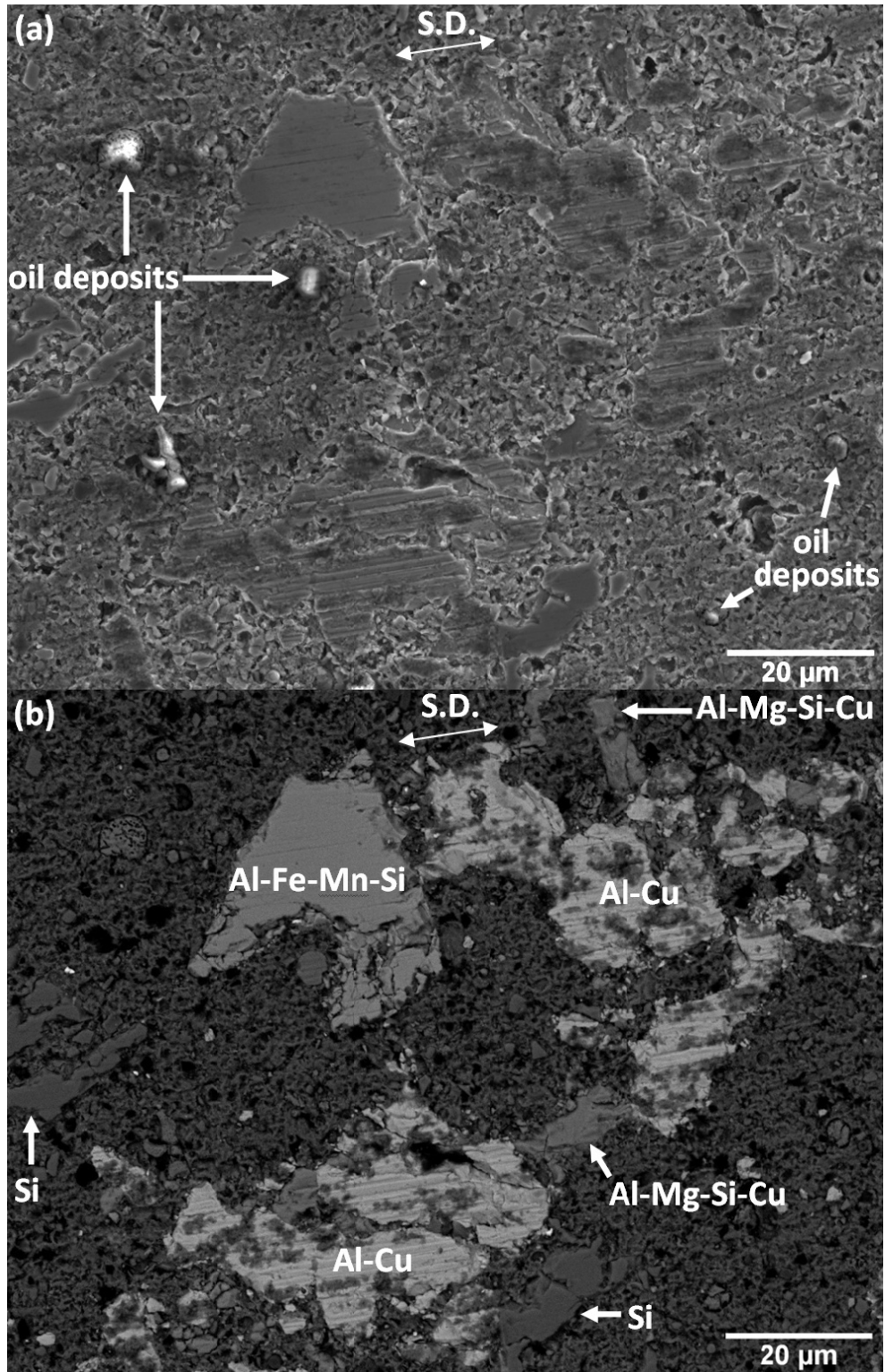
Figure 4-24 a) SE micrograph of the worn surface showing various phases; b) corresponding BSE micrograph; (1000x).

Element	Wt%	At%
CK	17.10	31.48
OK	05.75	07.95
FeL	01.05	00.41
CuL	01.86	00.65
ZnL	00.15	00.05
MgK	00.39	00.36
AlK	59.59	48.83
SiK	10.32	08.13
PK	00.83	00.59
SK	00.06	00.04
CaK	02.31	01.27
MnK	00.58	00.23
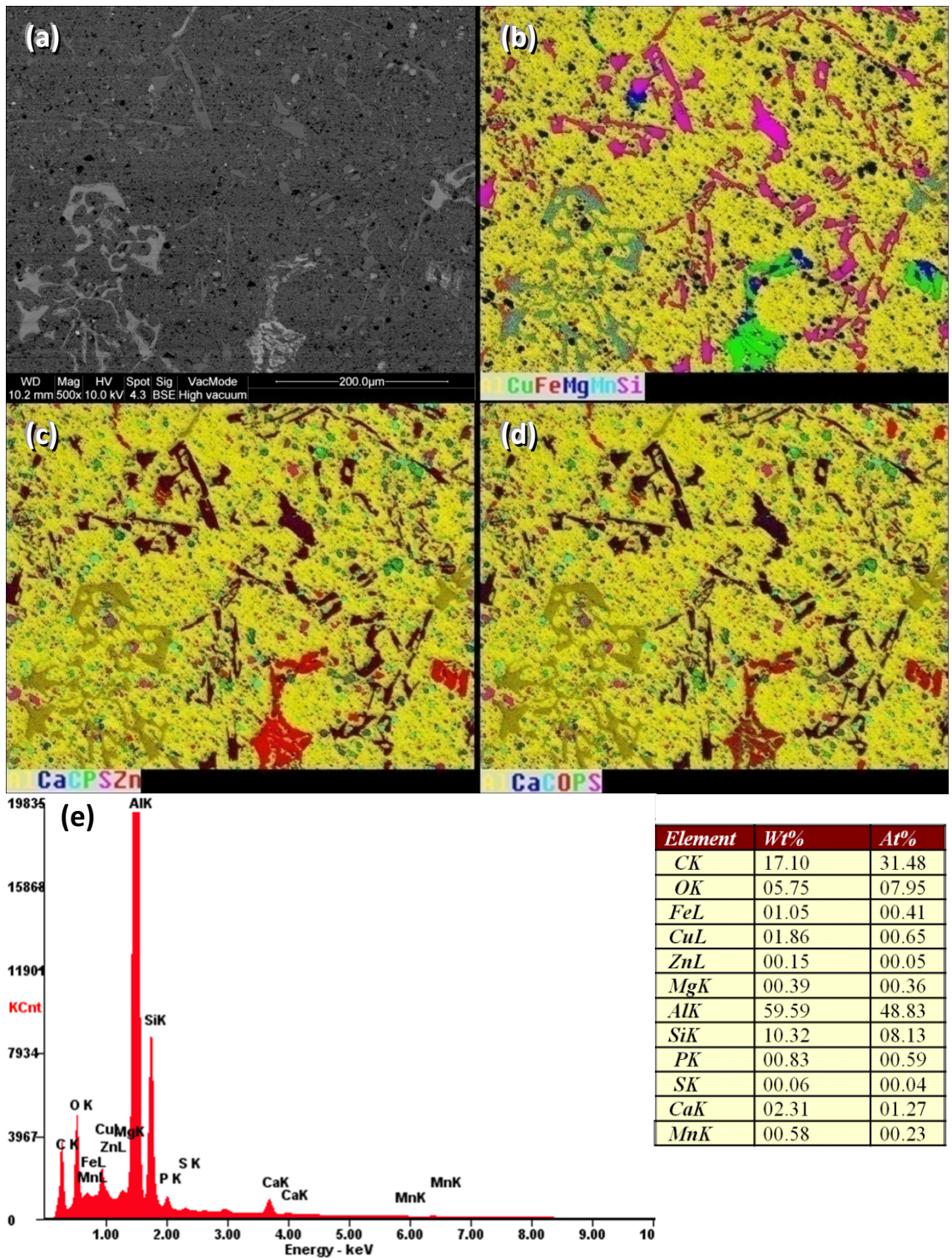
Figure 4-25 a) BSE micrograph of the worn surface; b) corresponding EDS map showing intermetallic elements; c) and d) are EDS maps showing oil and combustion byproducts embedded in the tribolayer; e) corresponding EDS spectrum and semi-quantitative data of the entire mapped area; (0° tilt).

4.3 Nickel Alloyed, Chemically Etched, Hot Tested Engine (Ni:CE:HT)

4.3.1 Visual Inspection

After dynamometer testing visual inspection of the Ni:CE:HT engine indicated no evidence of severe wear (scuffing, ploughing). The unworn region is visually described to be grey and non-lustrous, resulting from the chemical etchant. In contrast, the worn area consisted of a darker grey matted texture containing several pores and few scratches. More importantly, no distinguishable surface characteristics were observed between the major and minor faces, nor were there any severe scuff marks present on the bore. The major face and front face containing the various regions is shown in Figure 4-26. To the naked eye the Ni:MR:HT bore has shown slight indications of ring marks parallel to sliding; however, the Ni:CE:HT bore is completely free from longitudinal marks. To the touch both the worn surfaces of both the Ni:CE:HT and Ni:MR:HT bores felt smooth in the longitudinal and radial directions.

Similar to previously examined engines, a single bore was used for the microstructural work presented. The wear and appearance of this bore was similar to the rest of the cylinders with the same surface preparation. Macroscopic wear results are presented in Table 4-V. The average bore growth was worst at BRR, but was only 5.5 μm. Again, it is important to note that for an aluminum engine bore the amount of wear is remarkably low considering the harsh testing conditions.

Table 4-V Ni:CE:HT macroscopic bore wear

	Initial Bore Diameter	Average Bore Δ at TRR	Average Bore Δ at BRR
Characterized bore	99.0 mm	1.2 μm	3.8 μm
Average of bores	99.0 mm	5.2 μm	5.5 μm
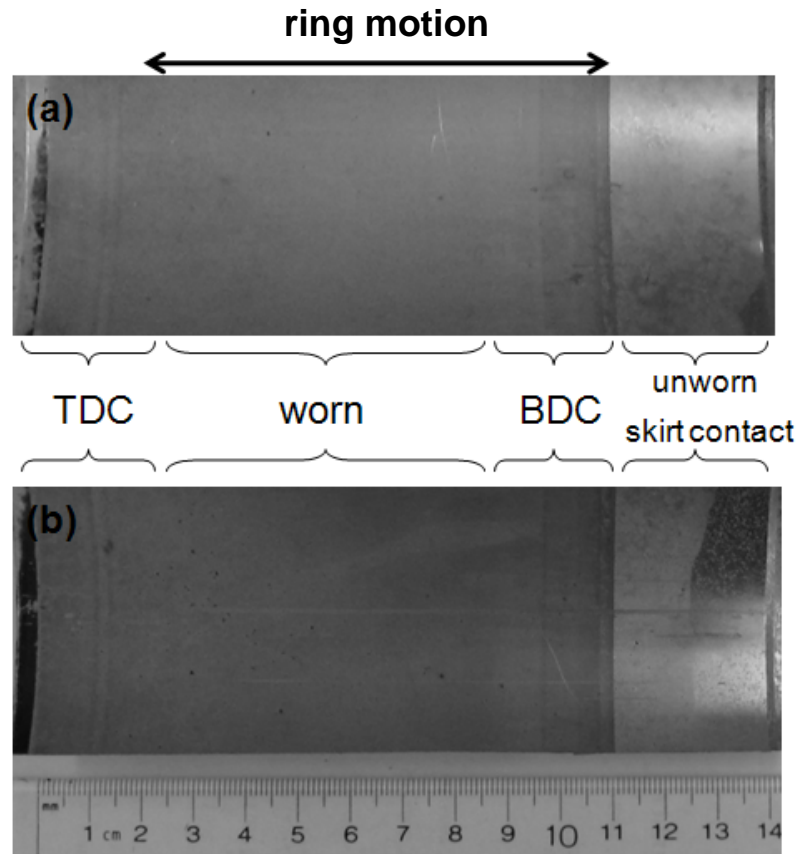
Figure 4-26 Engine bore, highlighting ring reversal marks at top dead center (TDC) and bottom dead center (BDC), and areas of no ring travel of both the front face (a) and major face (b).

4.3.2 Unworn Region

In order to minimize direct metal-to-metal contact between the piston rings and the aluminum matrix, cylinder surfaces were prepared by honing followed by chemical etching. Surface profilometry as well as site-specific cross-sectional analysis before and after etching has been performed. The profilometry data obtained from the unworn cylinder indicates that the mechanical surface preparation was successful at exposing hard phases from the aluminum matrix. However, localized damage to the harder phases was apparent and resulted from mechanical reduction. Surface profilometry scans after mechanical reduction (Figure 4-2 and Figure 4-27(a)) indicates that silicon particles are exposed from the aluminum matrix only ~0.2 μm. The SEM micrograph in Figure 4-27(b) shows hone marks on the aluminum matrix and the same cross-sectional line A-A′ outlining the site of interest for FIB milling shown in Figure 4-27(c). The FIB trench

indicates that even small silicon particles exhibit minute silicon fragments near their edges. Particles at depths > 2 μm show no evidence of fracture. For in depth subsurface investigations the same cross-section A-A′ was removed from the FIB trench and prepared for TEM analysis shown in Figure 4-28. The TEM micrograph in Figure 4-28(a) clearly shows the structure of fine grains in the aluminum matrix beneath the surface. On average these grains were ~ 0.329 μm in size measured from 69 grains and extended ~ 0.8 μm in depth from the surface. The SAD pattern of a small spot on this layer is shown in Figure 4-28b. An EDS line scan (Figure 4-28(c)) near the circular silicon particle confirms that small silicon particles or fragments (< 1 μm) exist near the surface. More pronounced evidence of silicon particle fracture is shown in a subset (Figure 4-28(e)) of the rectangular silicon particle. Here, fracture completely through the particle. The SAD patterns of the silicon particle and the aluminum that has been pushed into the crack is shown in Figure 4-28(d) and (f) respectively. In summary, the TEM results presented in Figure 4-28 demonstrate that silicon particle fracture is more apparent in high aspect ratio morphologies. These observations are in agreement with literature [18, 154], wherein particles with low aspect ratios have an increased resistance to fracture. It is important to note that when choosing the site for FIB/TEM analysis (Figure 4-27(c) and Figure 4-28) we could not identify from the surface (Figure 4-27(a) and (b)) if silicon particles were fractured or contained specific aspect ratios. Lastly, no severe damage or shearing of the aluminum matrix was observed and damage was concentrated along the edges of silicon particles identified as small fragments (Figure 4-28(c)).

A typical area of the chemically etched cylinder topography is revealed in Figure 4-29(a) with an average surface roughness (R_a) of 0.33 μm. The histogram height distribution for the chemically etched surface is shown in Figure 4-29(b). Here, the solid black curve represents the unfitted data; on this curve the large peak represents the aluminum matrix, which is set as the datum point and corresponding height of zero, while the smaller less pronounced peak represents silicon particles. The aluminum peak and silicon peak both exhibit a significant width, indicating a varied height distribution.

By fitting the data to Gaussian line shapes the silicon height/exposure (R_f) with respect to the aluminum matrix is determined to be ~1.09 μm measured by the separation between the aluminum peak and fitted silicon peak; the fitted data is distinguished in Figure 4-29(b) by the red dashed curve. Likewise, data below the aluminum matrix has been fitted and distinguished by the blue dashed curve. This corresponds to areas on the surface where a high dissolution of the matrix took place during etching, thus creating cavities/pits which reside ~0.26 μm below the datum (Figure 4-30). By comparing the surface topographies between the honing stage (Figure 4-2(a) and Figure 4-27(a)) and chemically etched condition (Figure 4-29(a)), and setting silicon surfaces as reference points, the amount of aluminum removed during chemical etching is calculated to be ~ 0.89 μm. Therefore, etching completely removes the fine grained aluminum layer but at the same time increasing the silicon exposure. With regards to surface observations it is seen that large primary silicon particles contain the greatest degree of surface damage, although they are few in number. In the chemically etched state, surface damage to primary silicon particles is readily apparent due to the nature of the etching process which dissolves any smeared aluminum covering the damage sites created during mechanical reduction (Figure 4-30). Lastly, a nano-hardness map presented in Figure 4-31 illustrates the differences in hardness of the aluminum matrix with respect to the depth below the subsurface for both the mechanically reduced and etched conditions. Both the etched and mechanically reduced surfaces show a drop in hardness at approximately 7 μm beneath the cylinder surface where the unaltered bulk material resides. Moreover, at a depth of 2 μm the etched sample shows a substantial increase in hardness, complimentary to other literature which suggests that etching causes a surface hardening effect [180].

Similar to the MR stage in Figure 4-27, surface and subsurface analysis was carried out after chemical etching using SEM and FIB techniques. Site specific areas prior to platinum deposition including their corresponding cross-sectional FIB trenches of silicon colonies and needles are shown in Figure 4-32 and Figure 4-33 respectively. Overall results suggest that small spherical silicon particles exhibit less surface damage

132

and fracture compared to larger needle-like particles; see Figure 4-32 and Figure 4-33. The cross-sectional FIB micrograph in Figure 4-32(b) indicates that some of the small silicon particles do not extend deep into the aluminum matrix, suggesting that they could be easily susceptible to removal during the initial stages of engine testing. Conversely, Figure 4-33 shows that silicon needles that extend deep into the aluminum matrix exhibit a greater degree of surface and edge damage compared to the smaller spherical particles. Nevertheless, the important point is that no subsurface fracture or decohesion from the matrix is observed for the large silicon needle. The same cannot be said for the heavily fractured iron phase, confirmed by EDS, located next to the silicon needle. It is noteworthy to mention that Figure 4-33(b) shows voids conglomerated around the iron phase. This is likely a result of fractured particles that permit the etchant to seep deeper causing a higher dissolution of the matrix.
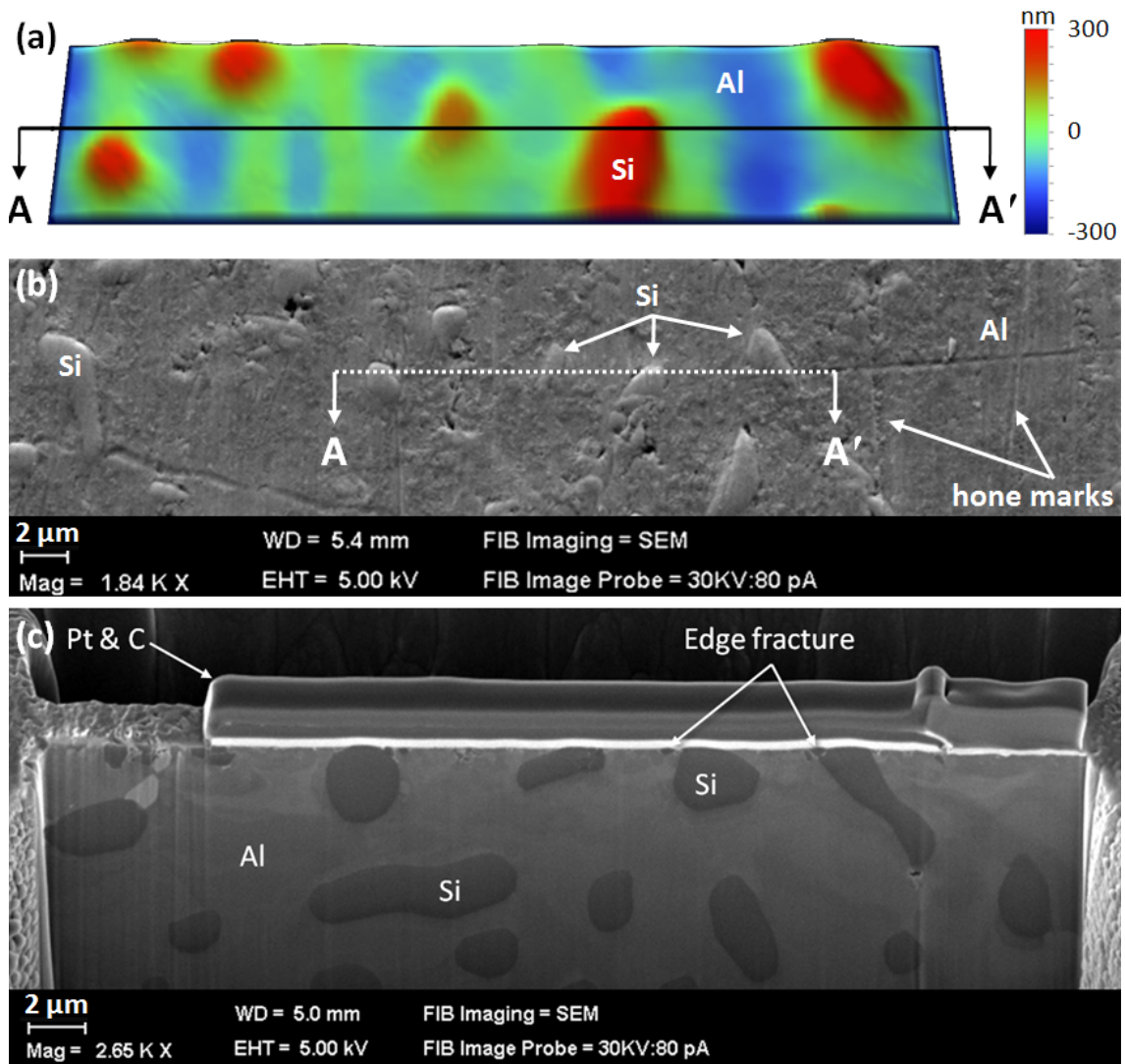
Figure 4-27 (a) 3D optical profilometry image of the mechanically reduced unworn surface, A-A′ representative line for FIB milling; (b) corresponding SEM image tilted at 54°; (c) corresponding FIB trench through Si colonies.
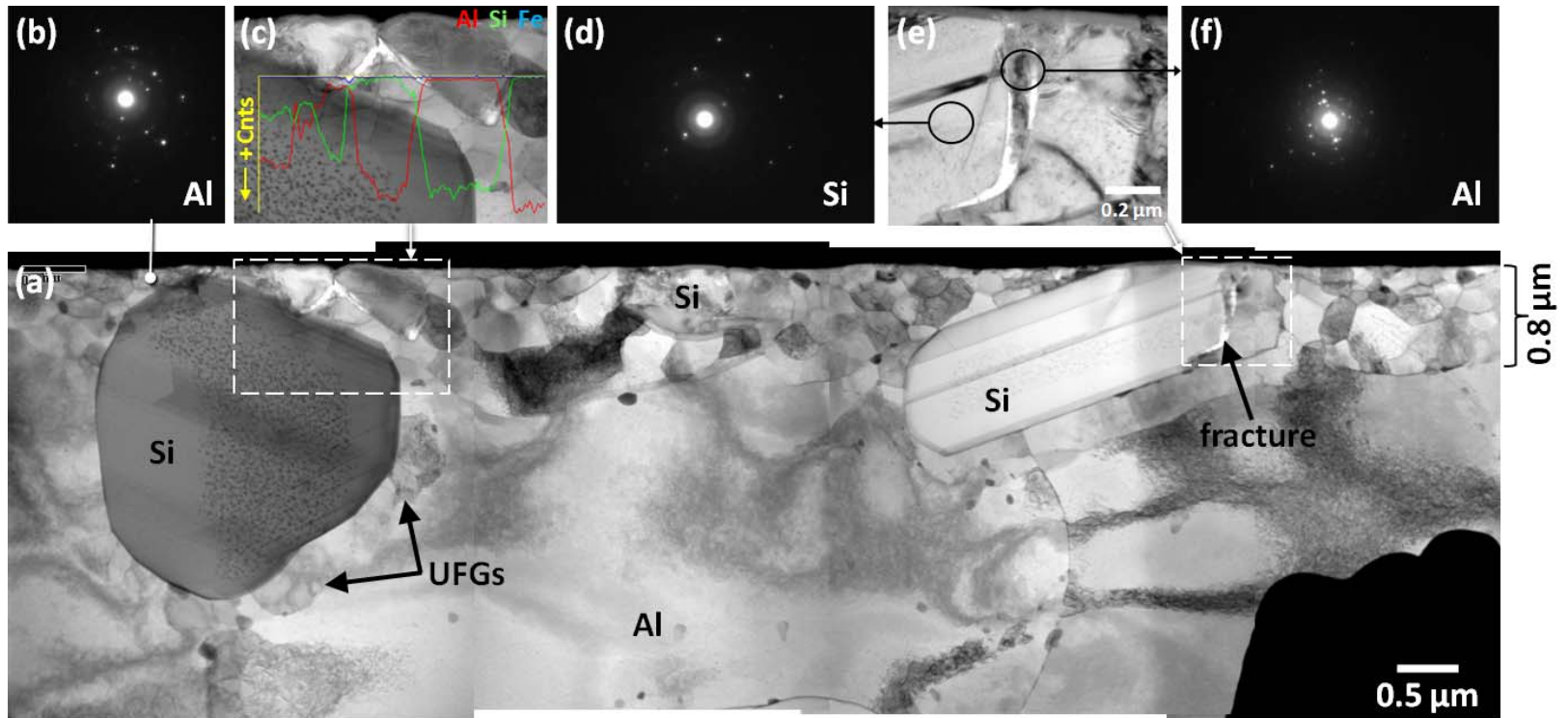
Figure 4-28 TEM micrograph (a) with corresponding SAD patterns (b, d, and f) and EDS line scan (c) after mechanical reduction. [See text for details.]
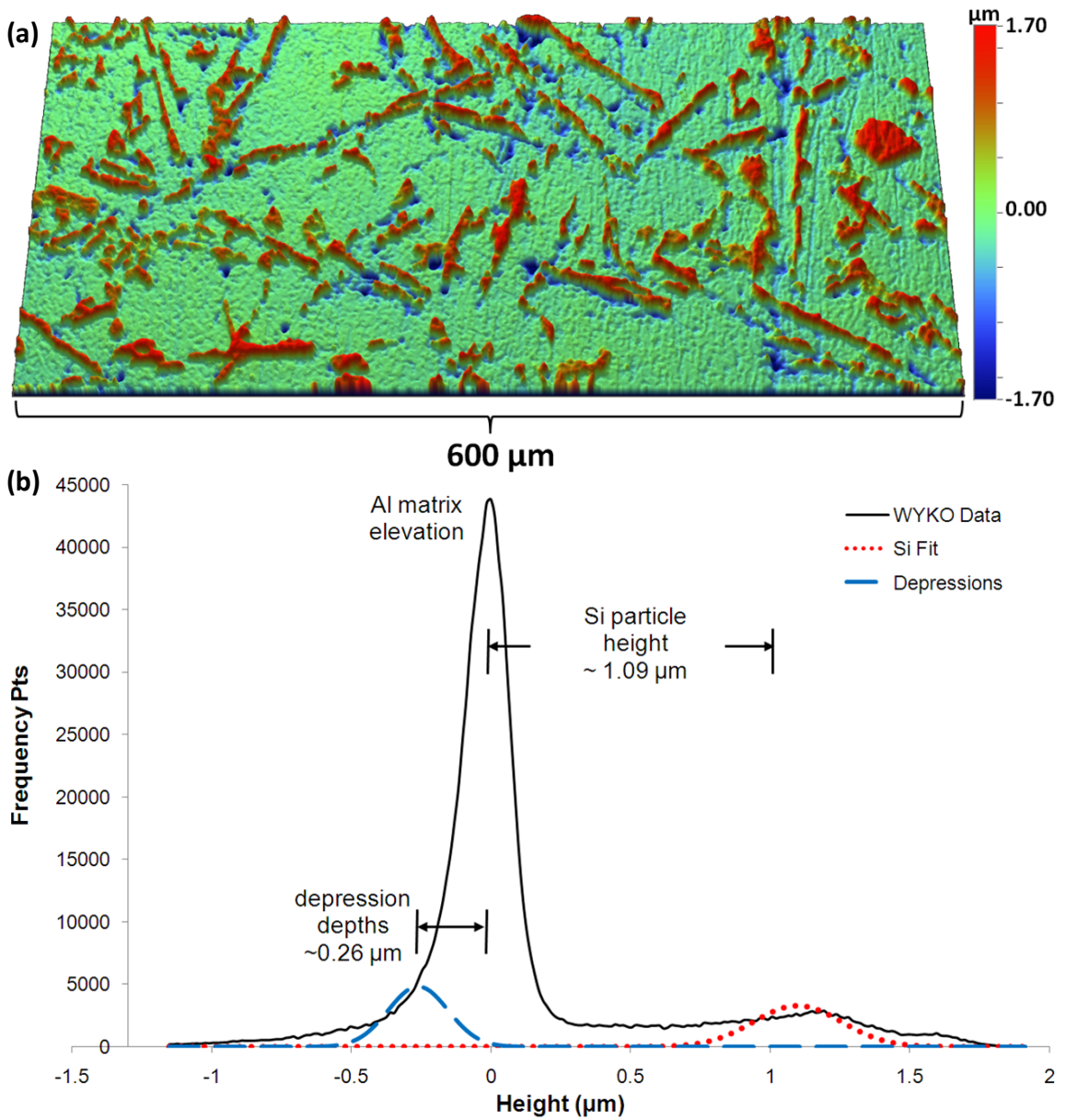
Figure 4-29 (a) 3D optical profilometry image (600 µm × 300 µm, R$_a$ = 332.27 nm) after chemical etching showing Si particles protruding from the matrix; (b) typical histogram showing the Si height distribution of the etched surface; dotted and dashed lines represent Gaussian curve fitting of the Si particles and depressions/cavities respectively.
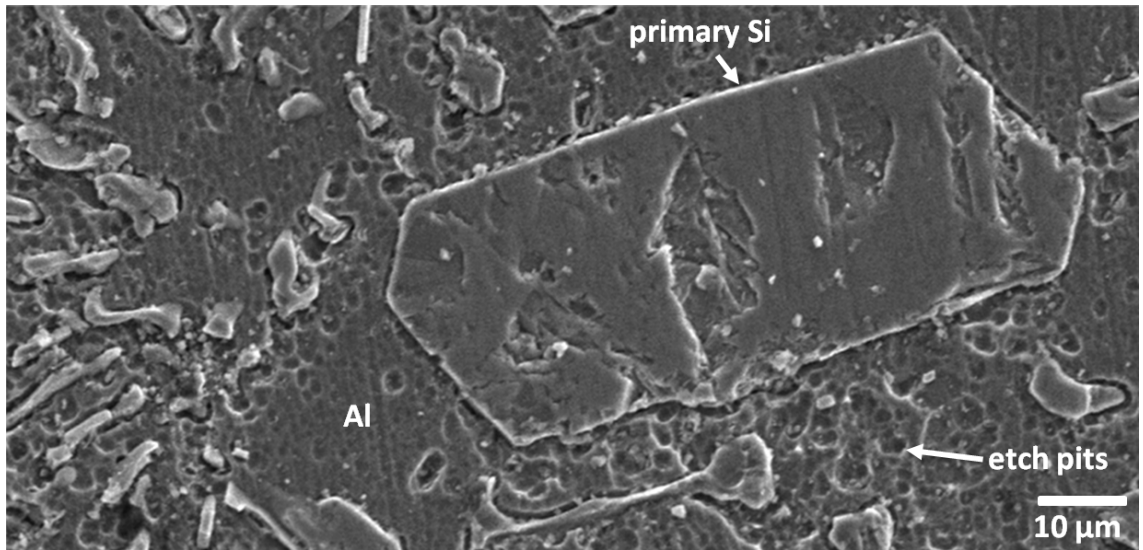
Figure 4-30 SEM micrograph of the etched surface showing the typical damage to large primary Si particles; (0° tilt).
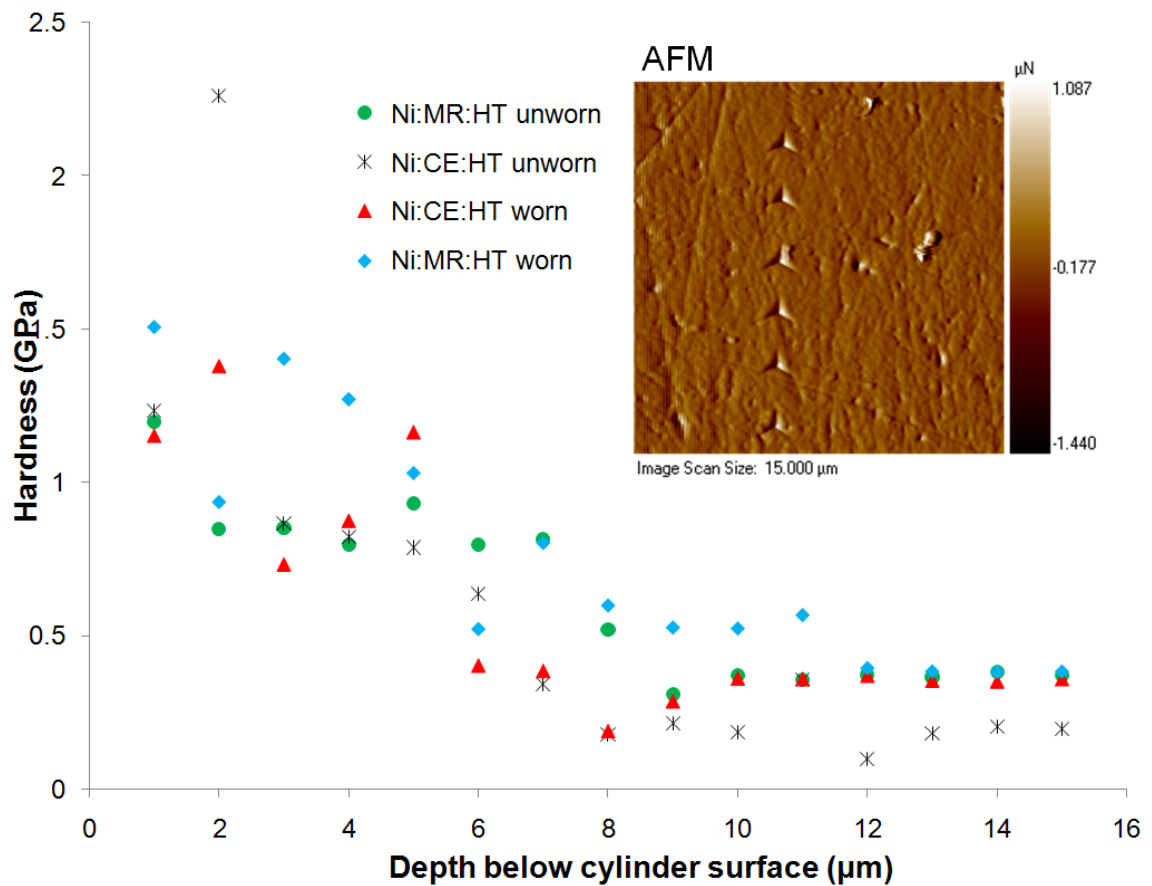
Figure 4-31 Aluminum matrix nano-hardness vs. depth beneath the subsurface; load = 300 μN, loading rate = 60 μN/s, loading time = 5 s, unloading time = 5 s. Figure shows the average of four sets of data per sample.
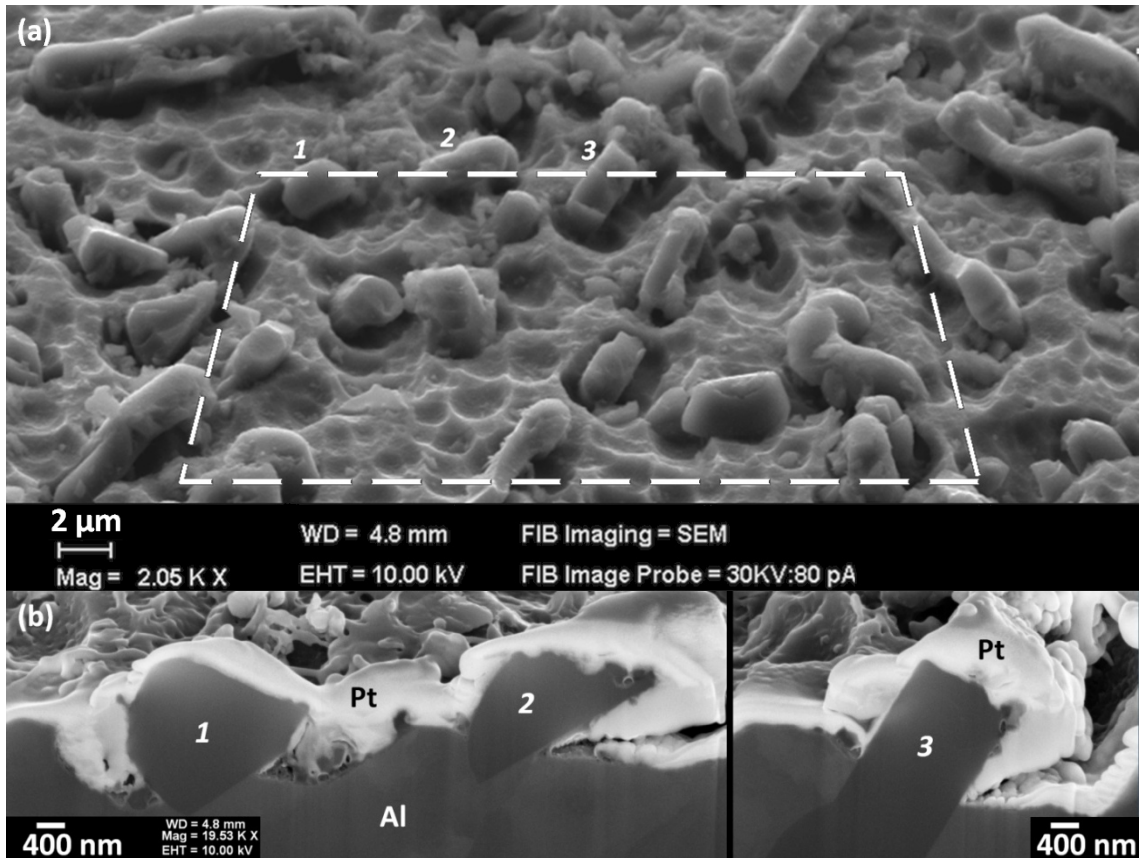
Figure 4-32 (a) SEM micrograph (tilt 54°) of Si colonies on the etched surface with dashed line representing the area for the FIB trench; (b) corresponding FIB cross-sectional view of Si colonies.
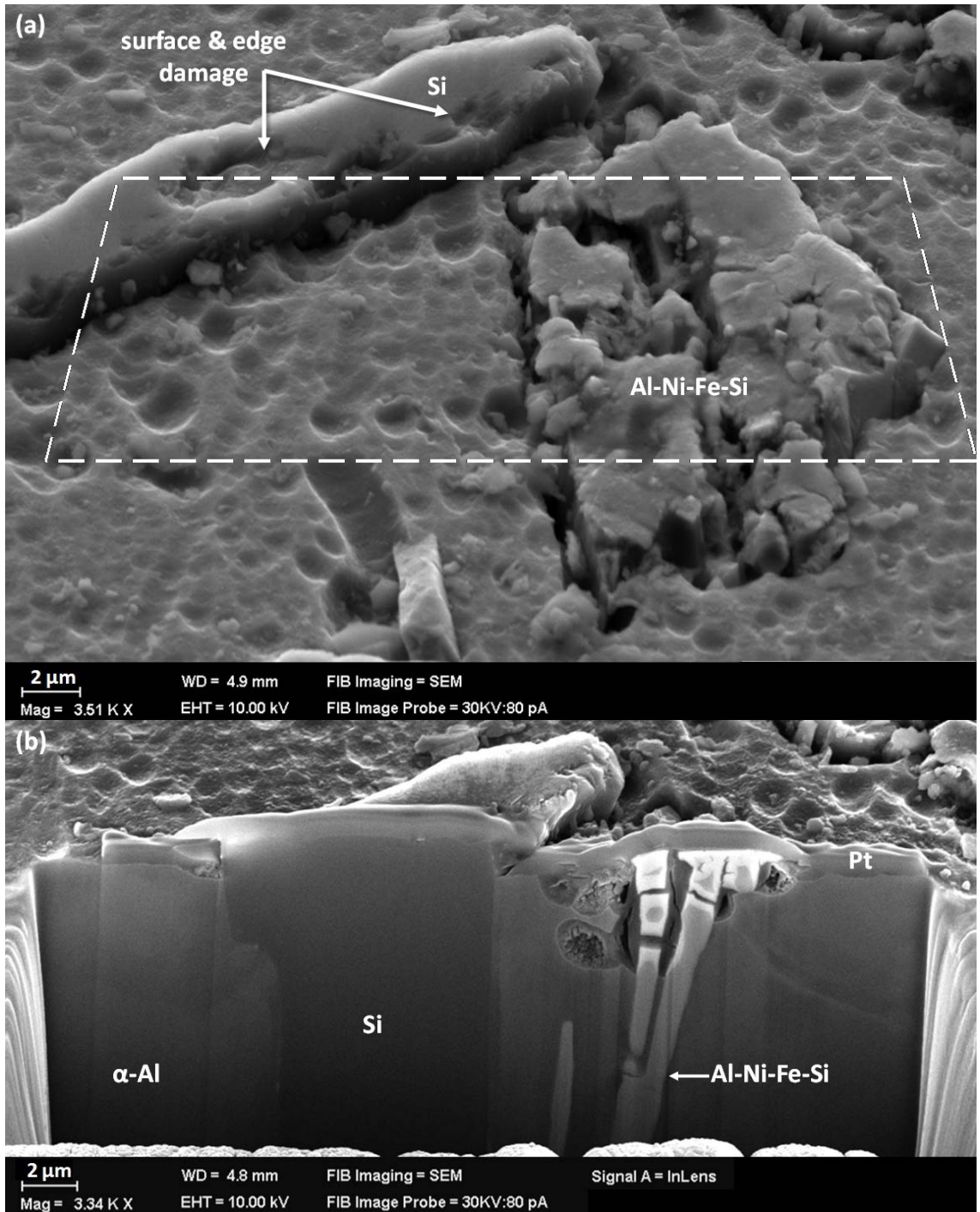
Figure 4-33 (a) SEM micrograph (tilt 54°) of damaged Si needle and intermetallic on the etched surface with dashed line representing the area for the FIB trench; (b) corresponding FIB cross-sectional view illustrating subsurface fracture and excessive etching around the intermetallic.

4.3.3 Worn Region

A typical three-dimensional surface profile of the worn surface is presented in Figure 4-34 and can be directly compared to Figure 4-29(a) of the unworn surface. The worn surface has an average roughness of approximately 0.43 μm. The corresponding histogram height distribution of the worn surface (Figure 4-34(b)) contains two distinct peaks, one pertaining to the matrix and the other protruding particles. The histogram suggests a maximum final silicon exposure height of $R_f \approx 0.6$ to 0.70 μm from the nominal matrix peak; a significant decrease in R_f of ~0.4 μm compared to the as-prepared surface. The typical morphology of the worn surface is shown in Figure 4-35(a), with the dotted line representing the cross-section (Figure 4-35(b)) used prior to platinum deposition and FIB milling. Here, it is demonstrated that the most distinctive characteristic between the worn and unworn regions is the change in matrix morphology. Any large patches of α-aluminum previously observed on the unworn surface are now indistinguishable. Direct comparisons of the matrix between Figure 4-33(a) and Figure 4-35(a) clearly indicate that a discontinuous tribolayer is formed during break-in. As seen from an overall micrograph of the worn surface (Figure 4-36), the matrix is comprised of fractured particles of varying size, micro grooves parallel to sliding, circular micropores, and a mixture of mainly Al, Si, C, O, Ca, P, and S confirmed by EDS. Semi-quantitative elemental analysis of the worn surface obtained by XPS shows similar results to EDS but has also detected other oil elements such as Zn. An XPS spectrum of the worn surface is presented in Figure 4-37 and data obtained before and after argon etching is summarized in Table 4-VI. The results suggest that oil deposits are abundant on the worn surface and thrive even after etching 10 nm below the surface. The hardness of the aluminum matrix as a function of depth beneath the worn surface was measured by nano-indentation and presented in Figure 4-31 along with the corresponding AFM subset. An increase in hardness near the worn surface is observed up to a depth of approximately 5 μm; thereafter the hardness drops to steady values associated with the bulk unaltered material. This increase in hardness of the aluminum matrix nearing the worn surface suggests that the wear process can alter the matrix up to approximately 5 μm in depth; similar trend was observed for the Ni:MR:HT bore and also shown in Figure 4-31 for comparative purposes.

Table 4-VI XPS semi-quantitative elemental composition of the Ni:CE:HT worn surface, atomic %, except H

	C	O	Al	Si	Ca	N	Zn	S	P	Na	Other
Surface	50	33	5	5	1.7	3	0.1	0.7	0.3	1.1	Cl, Mg, F
~ 10 nm etch	46	33	6	6	1.9	2.8	0.1	0.6	0.7	2.2	Cl, Mg

Aside from the matrix, qualitative observations of second phases before and after engine testing can also be used to elucidate the wear process. Figure 4-36 and Figure 4-35(a) show intermetallic phases as well as silicon particles confirmed by EDS. The brittle iron phase in Figure 4-36 is fractured and damaged extensively compared to the silicon particle adjacent to it. In fact, the surfaces of silicon particles appear to be in better condition than in the as-prepared surface (Figure 4-30). As seen in Figure 4-36, the damage caused by honing to silicon particles is completely removed. Silicon surfaces are smooth with minute scratches running parallel to the reciprocating motion of the rings. In addition, Figure 4-36 shows deep grooves parallel to sliding on the softer more ductile phases.

Information regarding the chemical structure of Si particles before and after wear was obtained by Raman spectroscopy. Raman spectra were obtained from five different unworn and worn Si particles. A typical spectra from the worn and unworn states is presented in Figure 4-38. By comparing the spectra to literature [193-196] distinct Raman bands are identified; indicating that Si-I is present in the unworn state, and after wear Si particles are composed of Si-I and Si-XII.

Another distinctive characteristic between the worn and unworn regions revolves around qualitative observations of the small silicon colonies and oil deposits. The small spherical silicon particles which were easily observed on the unworn surface are now difficult to resolve in the worn state. Therefore, FIB techniques were used in order to attain cross-sectional subsurface micrographs of these smaller particles and the underlying aluminum matrix. A cross-section of the worn surface is shown in Figure 4-35(b), which contains a small silicon particle along with various oil deposits whose EDS spectrums are shown in Figure 4-35(c). These deposits reside on, and fill in, uneven areas of the worn surface, protecting the underlying aluminum. Furthermore, these deposits (i.e. EDS spectrum #2 of Figure 4-35(c)) may act as replenishment pathways for

sacrificial films [170]. The protruding silicon particle shown in Figure 4-35(b) displays no signs of subsurface fracture or decohesion from the underlying aluminum matrix.

Surface observations indicate that silicon needles are fractured with light scratches parallel to sliding. Subsurface observations (Figure 4-39) demonstrate that these larger hard phases are more susceptible to subsurface fracture as compared to smaller more spherical particles. This micrograph indicates that the fracture of silicon needles can occur well below the surface; within a 2 to 6 μm range. Nevertheless, it is remarkable that these fractured particles still maintain a significant exposure height (R_f) from the matrix after engine testing. More importantly, oil deposits have been observed to fill in valleys likely created by particle pull-out that are strikingly similar to Figure 4-35. It is important to note that when choosing this area for FIB milling the small oil deposit blended in with the surroundings and could not be distinguished.

In conjunction with the FIB trench previously shown in Figure 4-35, TEM analysis was performed at the indicated dashed line to better characterize the subsurface features. From Figure 4-35(a), the small silicon particle and large oil deposit are distinguishable; however, smaller oil deposits near the silicon particle are not. An EDS line scan, shown in Figure 4-40, was performed through an oil deposit (oil #1) and beneath the silicon particle. Qualitatively, this line scan shows a significant reduction in the aluminum signal when passing through the oil deposit. Moreover, a large reduction in the aluminum signal complimented by an increase in the Ni and Fe signals took place when passing through the dark phase directly beneath the silicon particle. This phase containing mostly Ni, Fe, and Al contains a void directly beneath it partially filled in with oil deposits. Likewise, these oil deposits are observed beneath the silicon particle presented in Figure 4-41 with corresponding SAD and high resolution (HR-TEM) subsets shown in Figure 4-41(d) and (e). The HR-TEM micrograph clearly demonstrates that nano-scale crystalline aluminum particles and amorphous material coexists beneath the silicon particle. The deformed structure also beneath the silicon particle with HR-TEM and SAD micrographs corresponding to Figure 4-41(b) and (c) respectively has also been analyzed. These results only yielded crystalline deformed/compacted aluminum structures confirmed by the lattice spacing designated by the white arrows in

Figure 4-41(b). It is unknown whether the silicon particle originated from a different location or maintained its current position throughout engine testing. Regardless of silicon origin it is clear that the particle maintains an exposure height from the matrix, and that ultra-fine aluminum grains, including deformed aluminum structures are present beneath the silicon particle annotated in Figure 4-41.

In depth HR-TEM analysis was also performed on the oil deposit (oil #2) to the right of the silicon particle as a subset in Figure 4-41(f). Here, it is confirmed that this oil deposit is porous ,which is in agreement with previous studies [18]. EDS analysis of oil deposit #1 and #2 indicates that they are chemically similar (i.e. Ca, Zn, O, C, and S); however, oil deposit #2 appears to be comprised of smaller conglomerated particles compared to oil deposit #1. The HR-TEM micrograph (Figure 4-41(f)), has shown that oil deposits contain amorphous material combined with nano-scale fragments of silicon confirmed by the lattice spacing annotated by the white arrows.

The TEM analysis of the large oil deposit from Figure 4-35 is presented in Figure 4-42. This oil deposit previously observed with EDS in Figure 4-35(c), is porous and similar in appearance to oil deposit #2 in Figure 4-41. Analysis has shown that the large oil deposit, which extends ~ 2 μm in depth from the surface, is comprised of amorphous and crystalline material. In the vicinity of this oil deposit cracks and aluminum grain detachment are observed. A subset from the oil which has seeped between the detached aluminum grain is displayed in Figure 4-42(b), with corresponding SAD pattern shown in Figure 4-42(c). The SAD image contains a distinctive ring pattern, indicative of amorphous material. Furthermore, evidence of UFG structures is apparent beneath the oil deposit, at a depth of ~ 3 μm, and labeled in Figure 4-42(a). It is obvious that a large void is present beneath the oil deposit and along the edges; however, nearing the surface the void decreases in size and begins to taper-off eventually becoming flush with the matrix. Lastly, it is important to emphasize that although there are signs indicating deformation to the aluminum matrix, there has been no evidence of excessive wear such as scuffing, gross material transfer, delamination, or pitting on this engine bore.

In summary, the results previously discussed will be utilized in §5.3 to identify the microstructural changes and mechanisms that occurred between the unworn and worn surfaces.
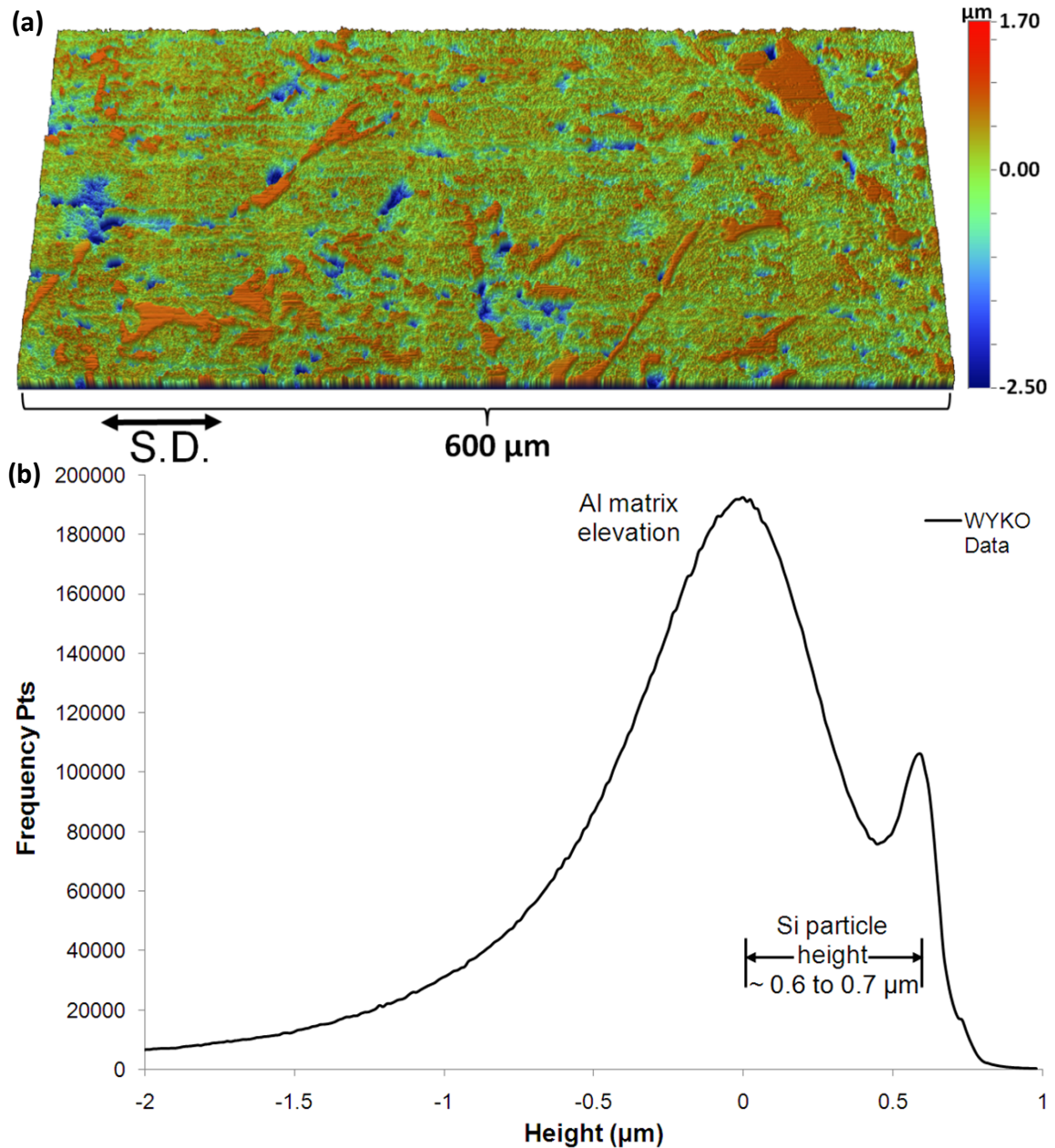
Figure 4-34 (a) 3D optical profilometry image (600 μm × 300 μm, R_a = 433.73 nm) of the worn surface showing Si which continue to stand proud from the matrix; (b) typical histogram showing the Si height distribution of the worn surface.

144

(a)

Si

TEM

FIB

oil deposits

Si

| 2 µm | WD = 4.8 mm | FIB Imaging = SEM | ←→ |
| Mag = 4.51 K X | EHT = 10.00 kV | FIB Image Probe = 30KV:80 pA | S.D. |

(b)

Pt

Si

1

2

3

C

α-Al

oil deposits

| 2 µm | WD = 4.8 mm | FIB Imaging = SEM | ←→ |
| Mag = 3.37 K X | EHT = 10.00 kV | FIB Image Probe = 30KV:80 pA | S.D. |
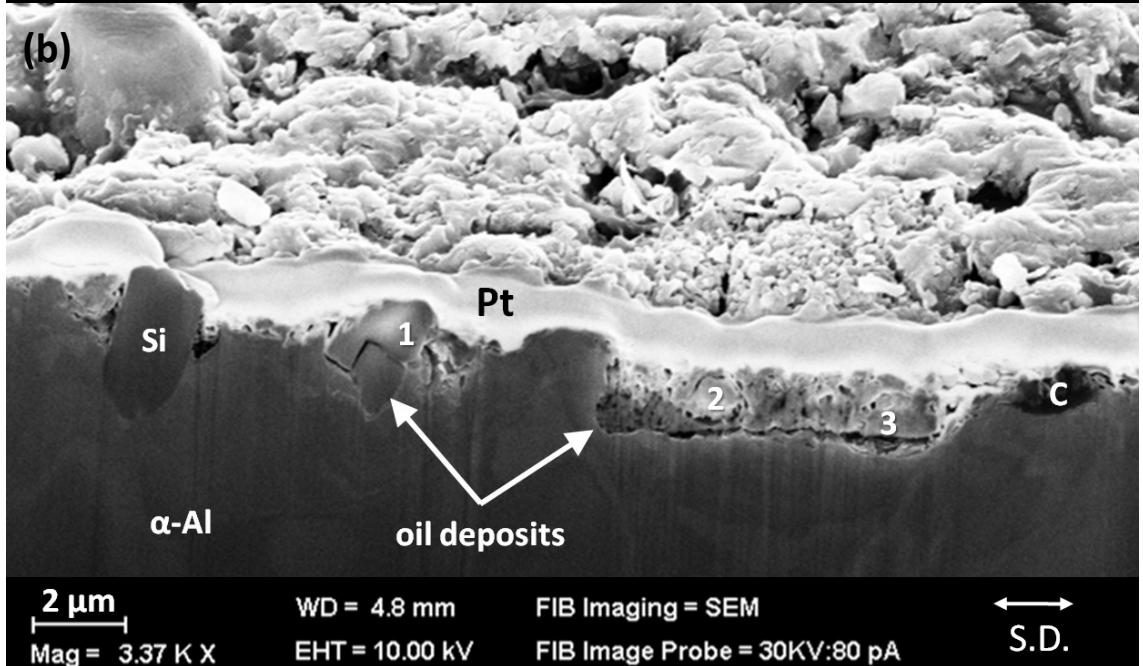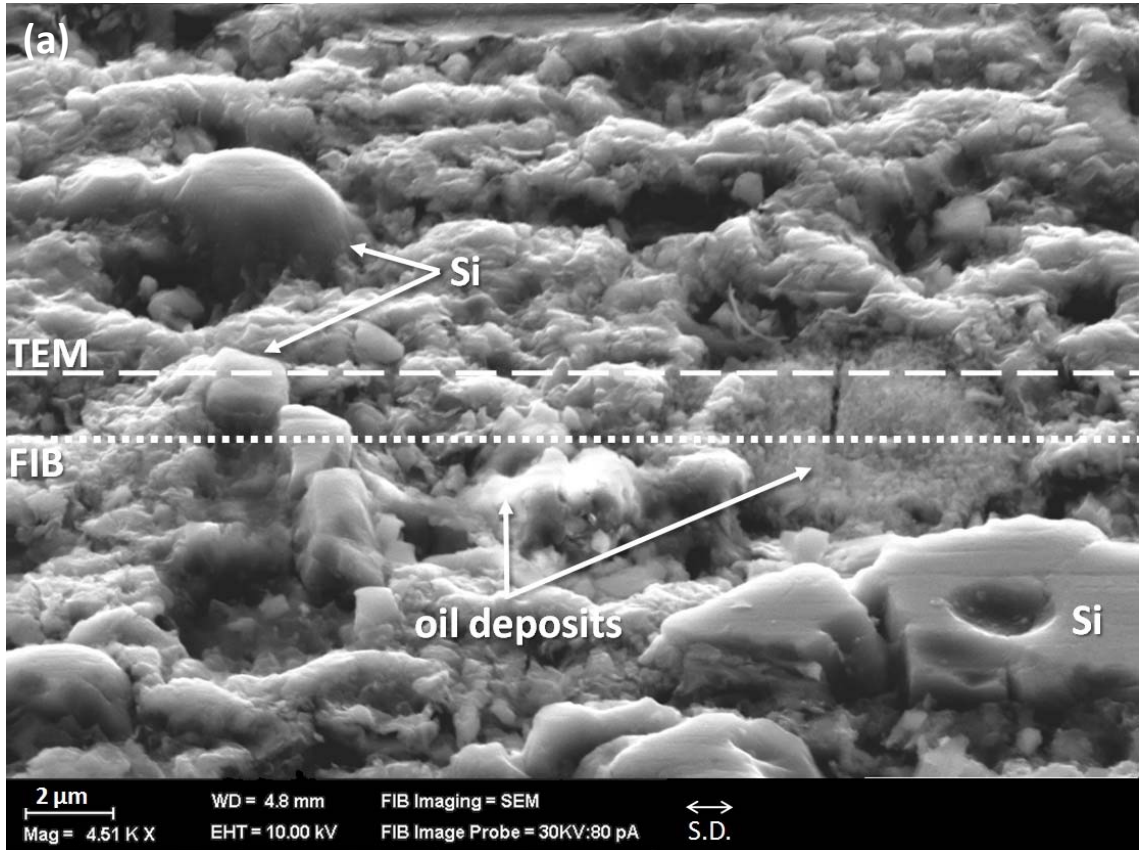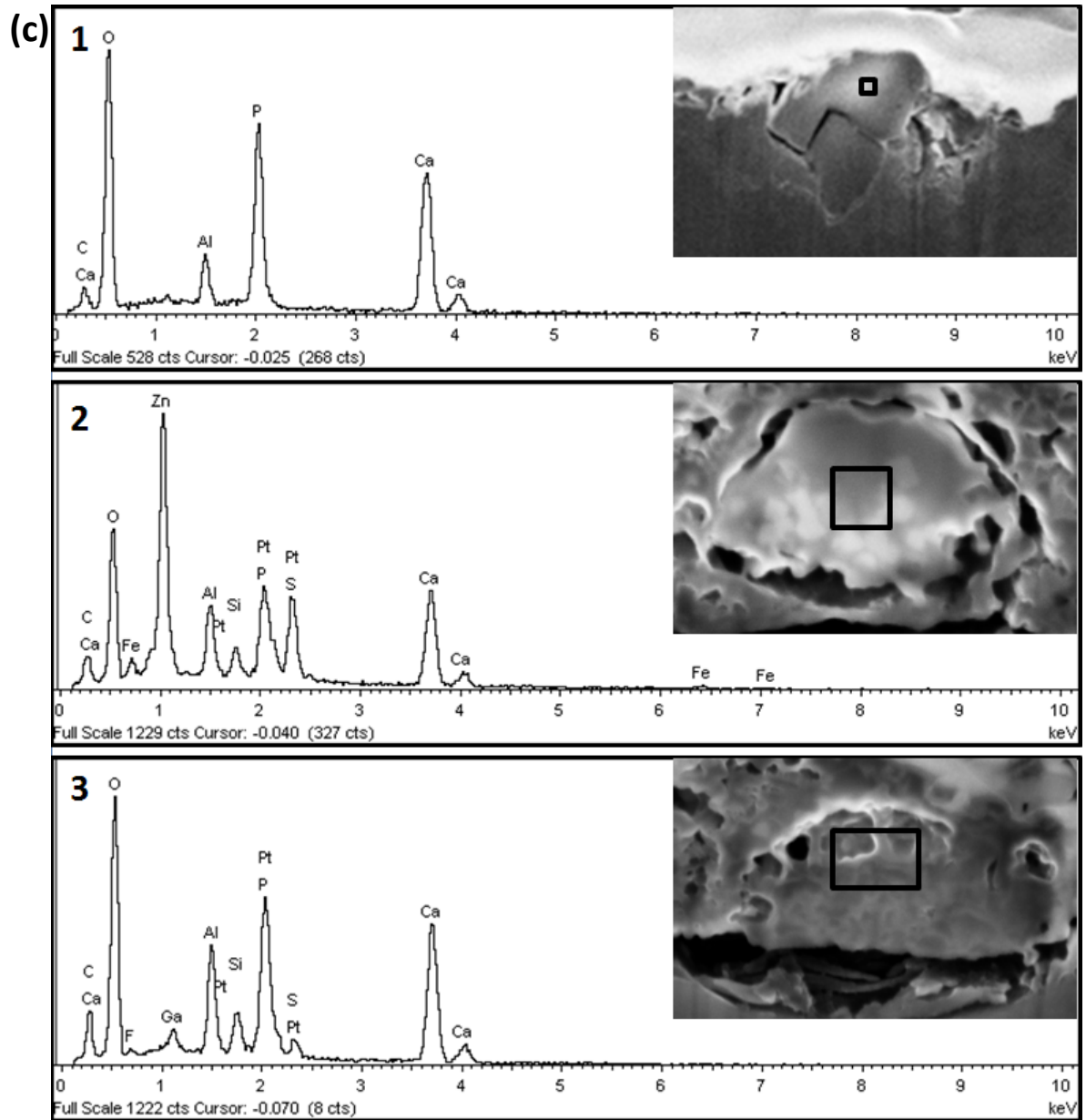
Figure 4-35 (a) SEM micrograph illustrating the texture of the worn surface with small particles scattered throughout, smooth exposed Si particles, and oil deposits; (54° tilt).. The dotted and dashed lines represent the cross-sections prior to FIB and TEM respectively; (b) corresponding FIB trench; (c) corresponding EDS spectra of areas 1, 2, and 3 annotated in (b).
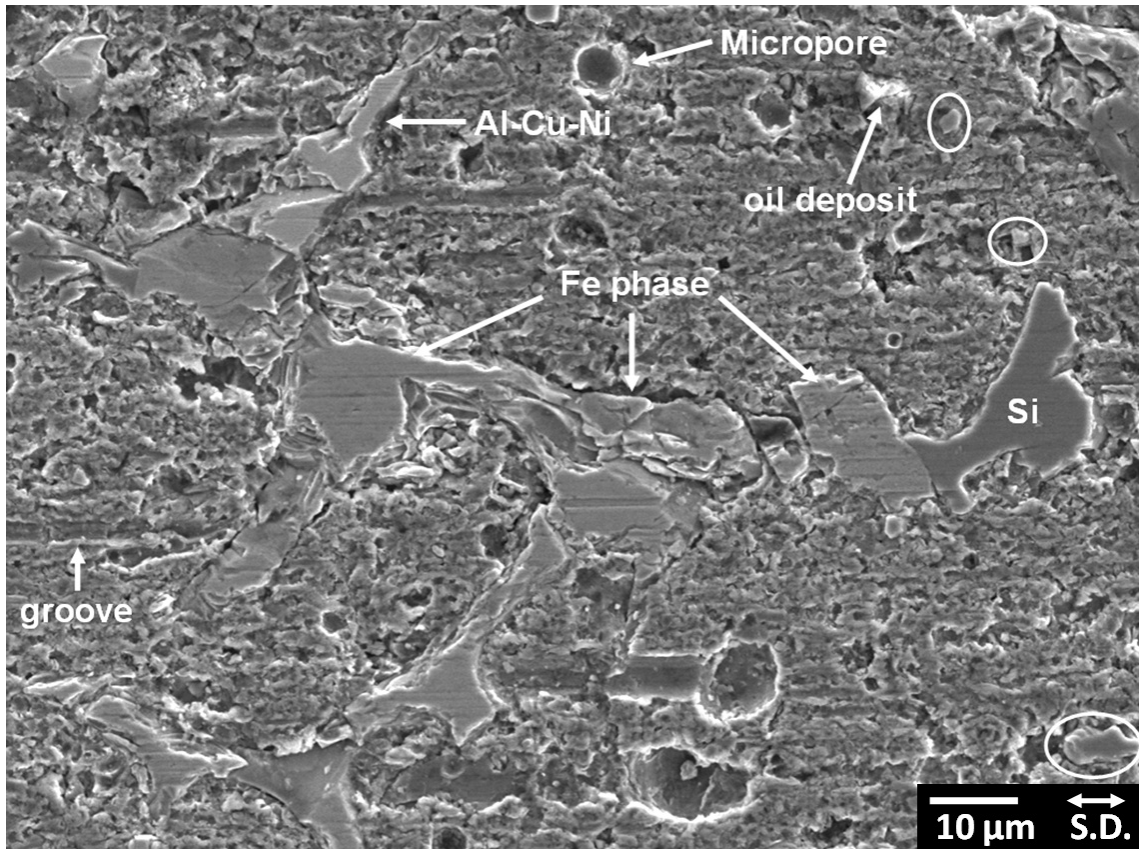
Figure 4-36 SEM micrograph of the worn surface showing various phases confirmed by EDS. Silicon particles are intact and smooth in contrast to softer second phases that are fractured and scratched; small particles are circled; (0° tilt).
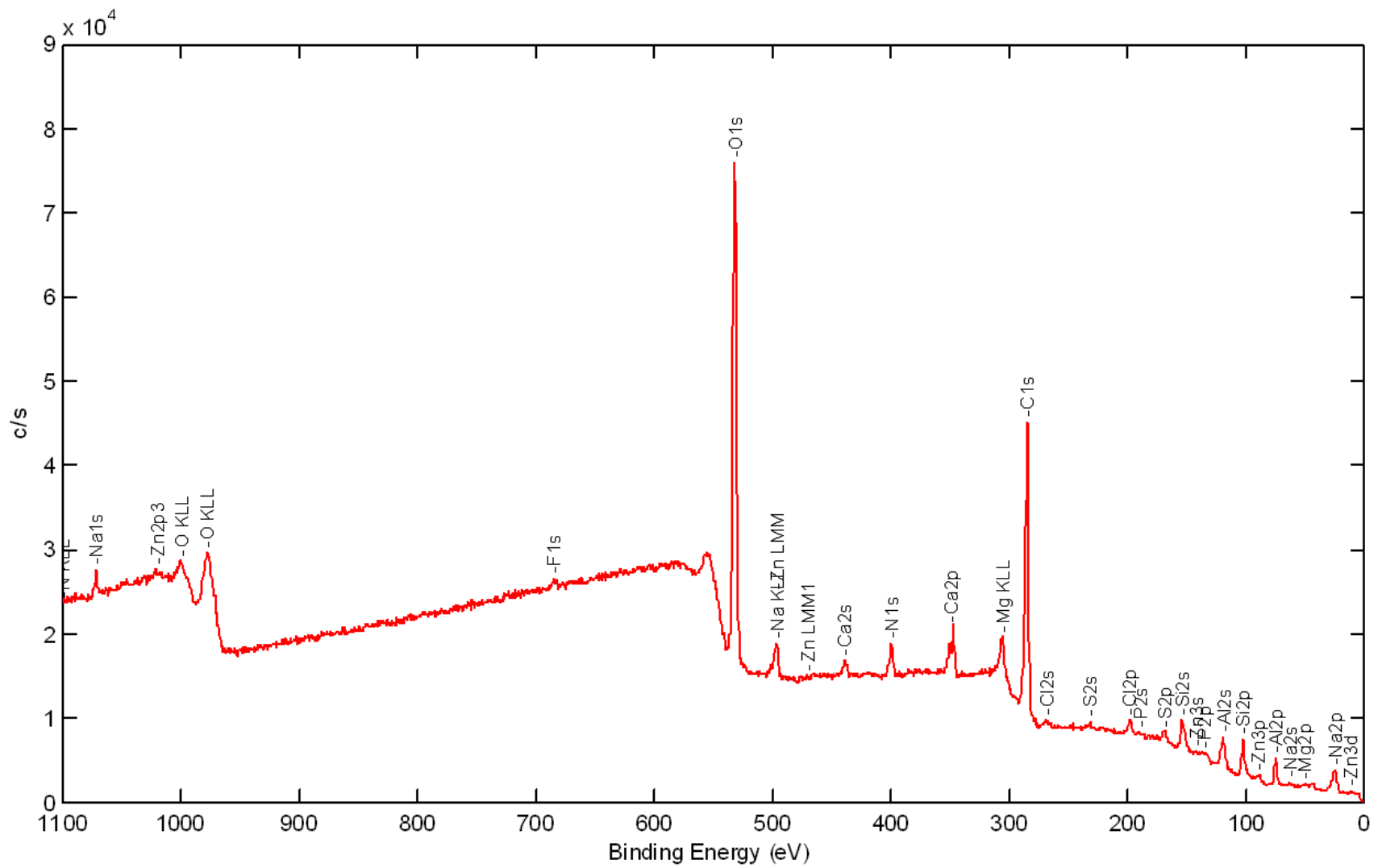
Figure 4-37 XPS wide scan survey spectrum of the Ni:CE:HT worn surface.
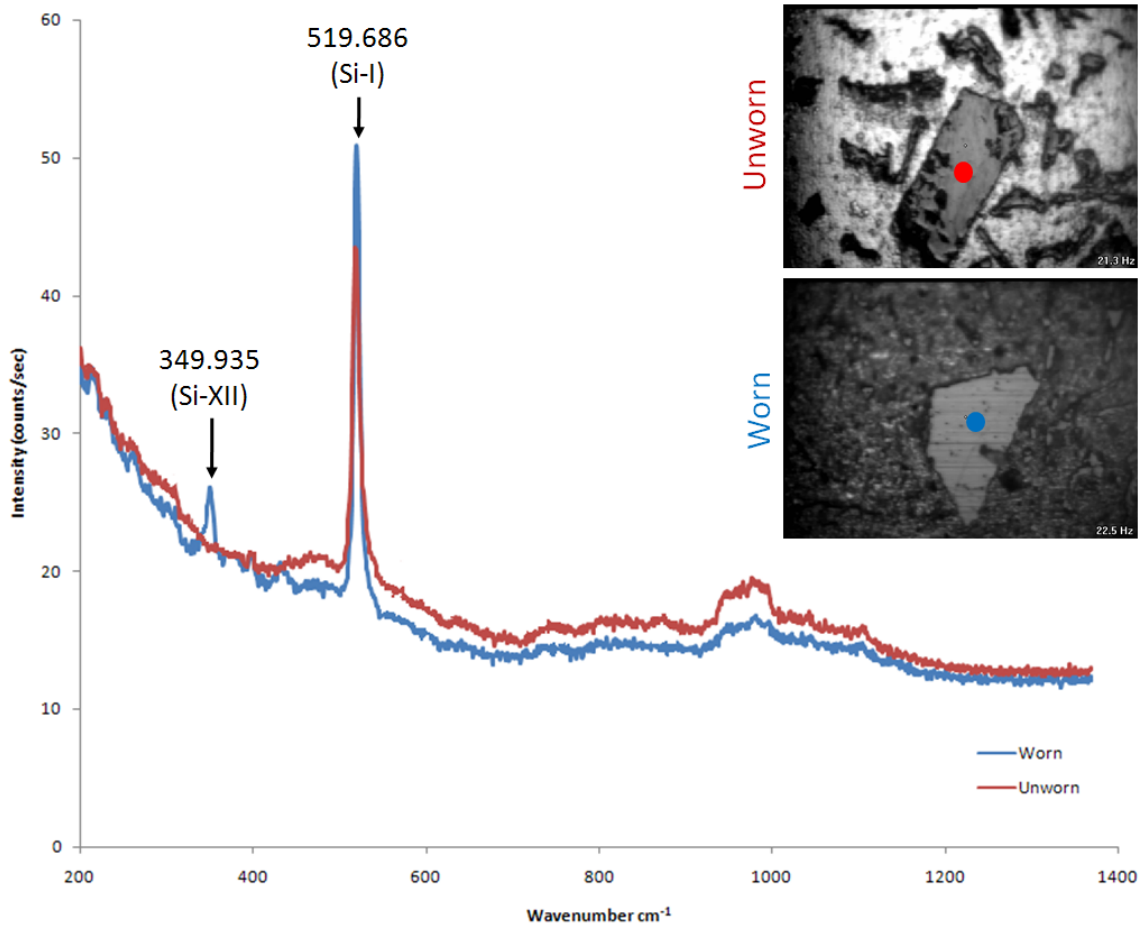
Figure 4-38 Typical Raman spectra obtained from worn (blue) and unworn (red) Si particles of the Ni:CE:HT engine bore.
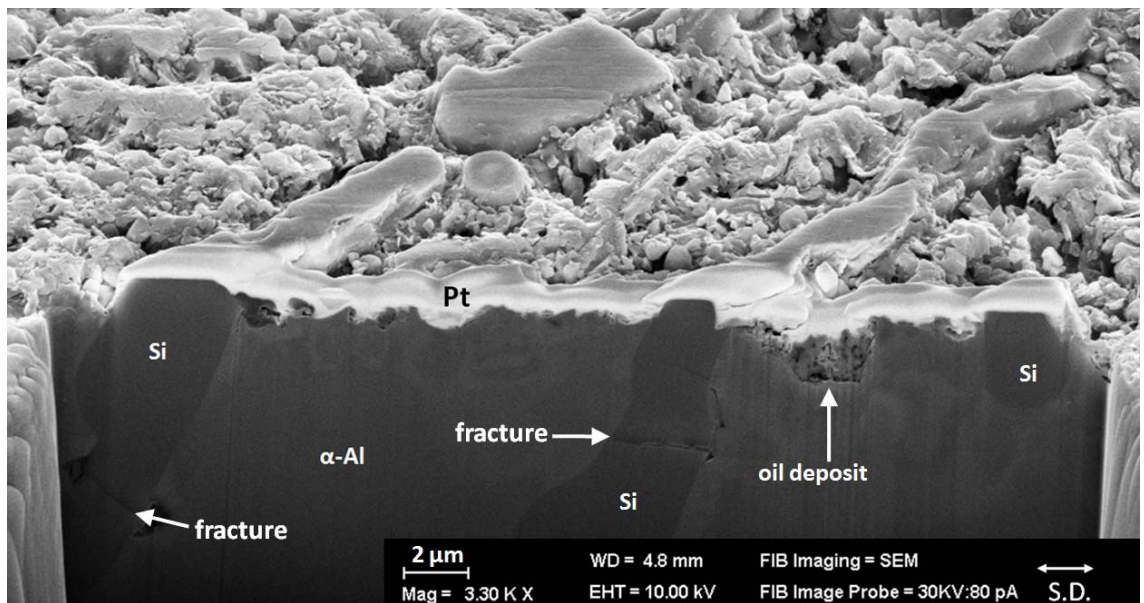
Figure 4-39 Cross-sectional FIB micrograph of the worn surface illustrating subsurface fracture in Si needles.
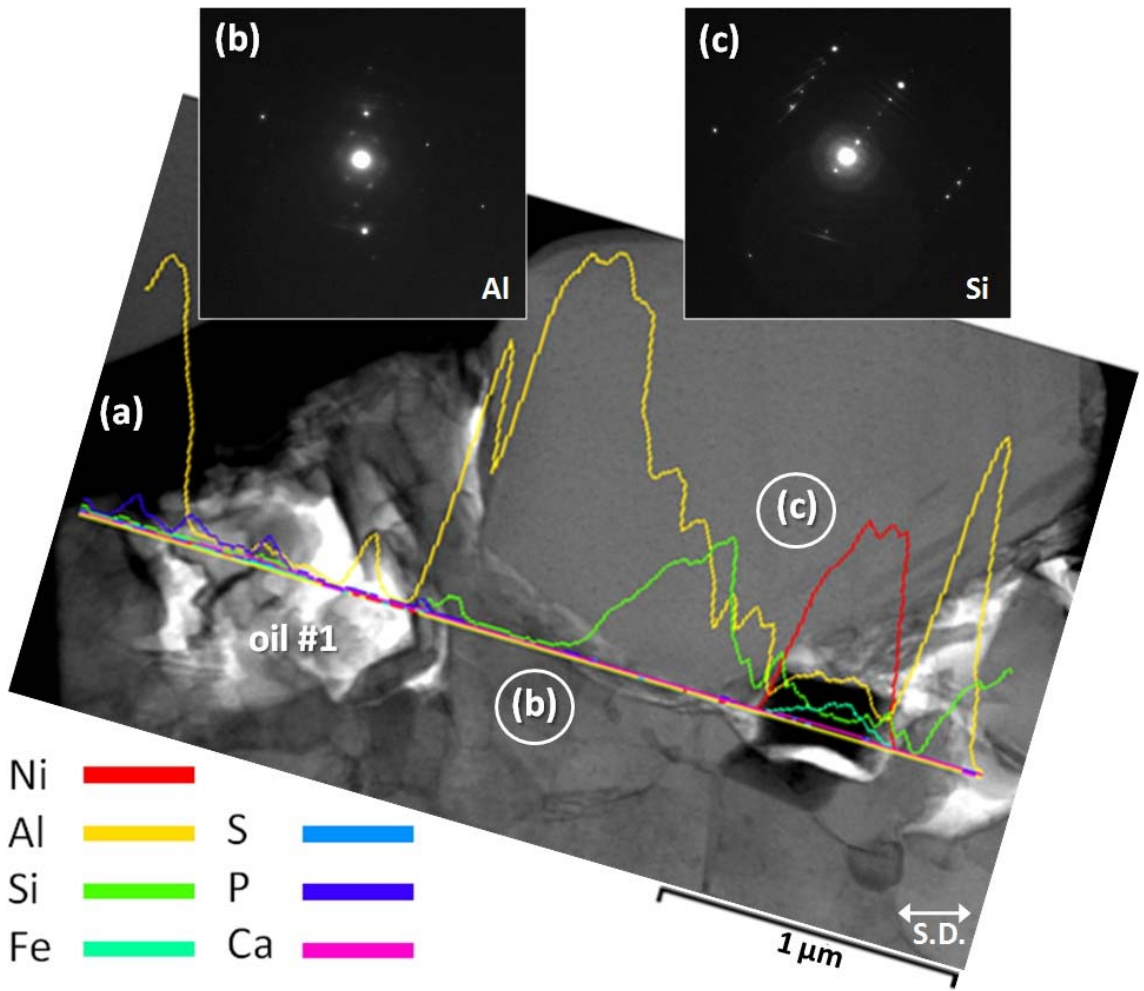
Figure 4-40 (a) TEM micrograph from the worn cylinder with corresponding EDS line scan taken beneath a Si particle and through oil deposits and intermetallics; (b) and (c) are SAD patterns taken from Al and Si respectively.
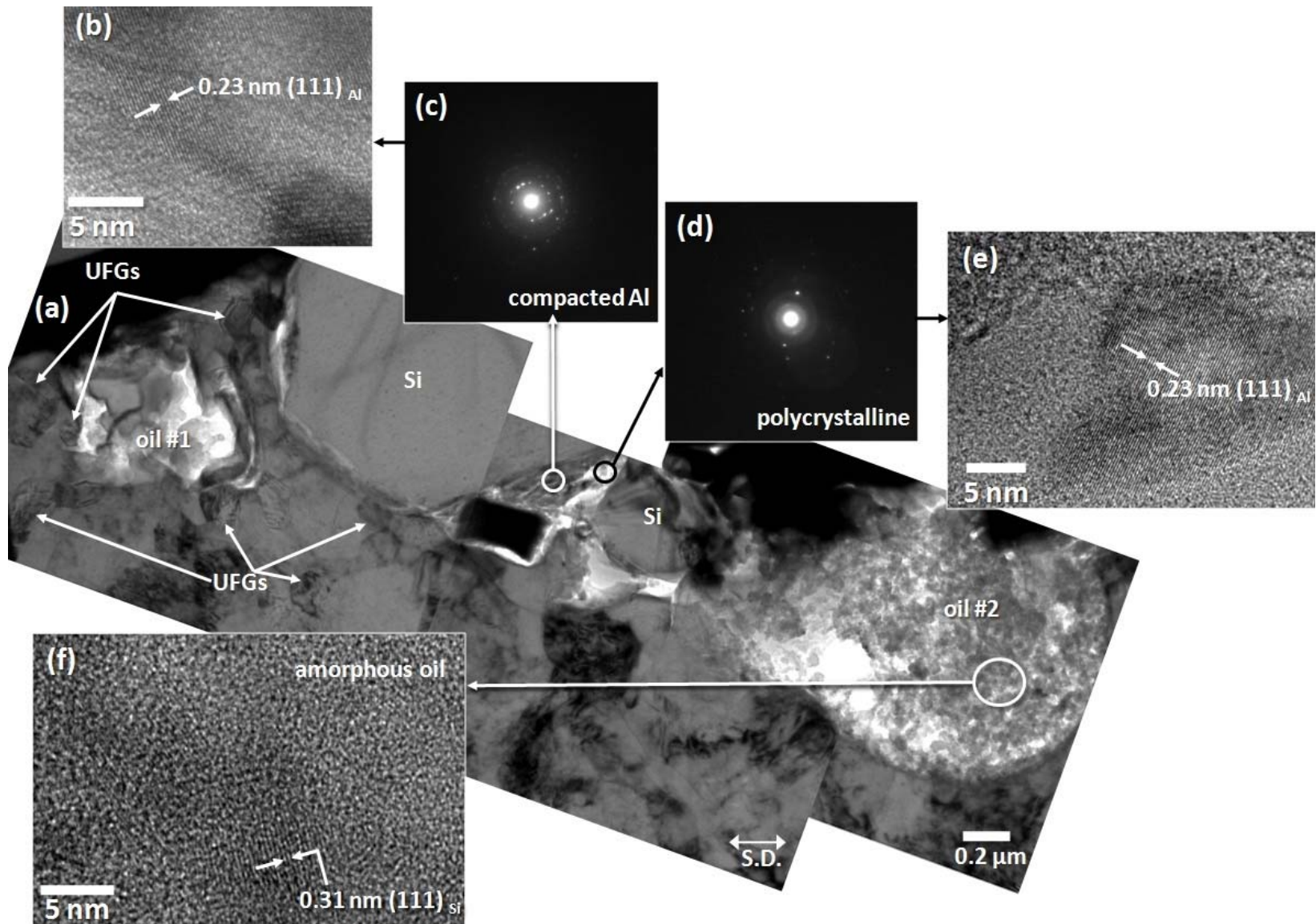
Figure 4-41 TEM micrograph (a), SAD patterns (c and d), and HR-TEM (b, e, and f) from the worn state illustrating ultra-fine grains, deformed Al, and amorphous oil deposits. [See text for details.]
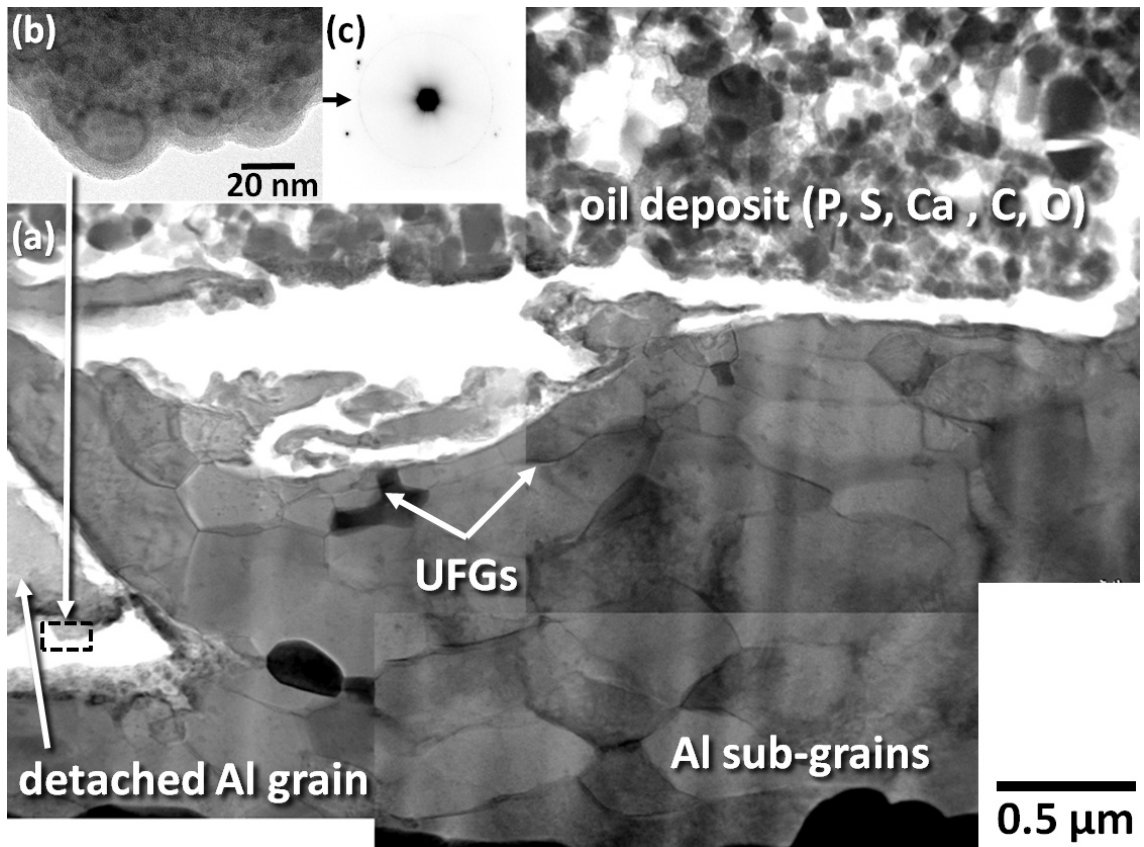
Figure 4-42 (a) Bright field TEM micrograph showing detached Al grains and UFGs below the large oil deposit previously shown in Figure 4-35; (b) subset of oil surrounding detached Al grain; (c) corresponding SAD pattern of the oil.

4.4   Nickel Alloyed, Chemically Etched, Cold Scuffed Engine (Ni:CE:CS)

4.4.1   Visual Inspection

After dynamometer testing visual inspection of the Ni:CE:CS engine indicated that scuffing arose during engine operation. A single bore, representative of the other seven cylinder bores, was chosen for in depth examination (Figure 4-43). From visual inspection the most dominant feature was the difference in appearance between the major and minor faces compared to the front and back faces. Both major and minor faces were abundant with non-lustrous ring marks parallel to sliding and smooth to the touch (Figure 4-43(a)). More severe scuff marks, which were lustrous and metallic in appearance, were also found parallel to sliding. Compared to ring marks, scuff marks were not as abundant; however, they were larger and, to the touch, deviated from the normal cylinder roundness. The front and back faces did show evidence of ring marks but at the center-line of these faces evidence of wear was virtually indistinguishable from the unworn

surface (Figure 4-43(b)). Here, the virgin surface appeared identical to engine Ni:CE:HT which is described to be grey and non-lustrous resulting from the chemical etchant, see Figure 4-43(b). Lastly, below ring travel in both the major and minor faces no evidence of piston skirt contact could be observed (Figure 4-43(a)).
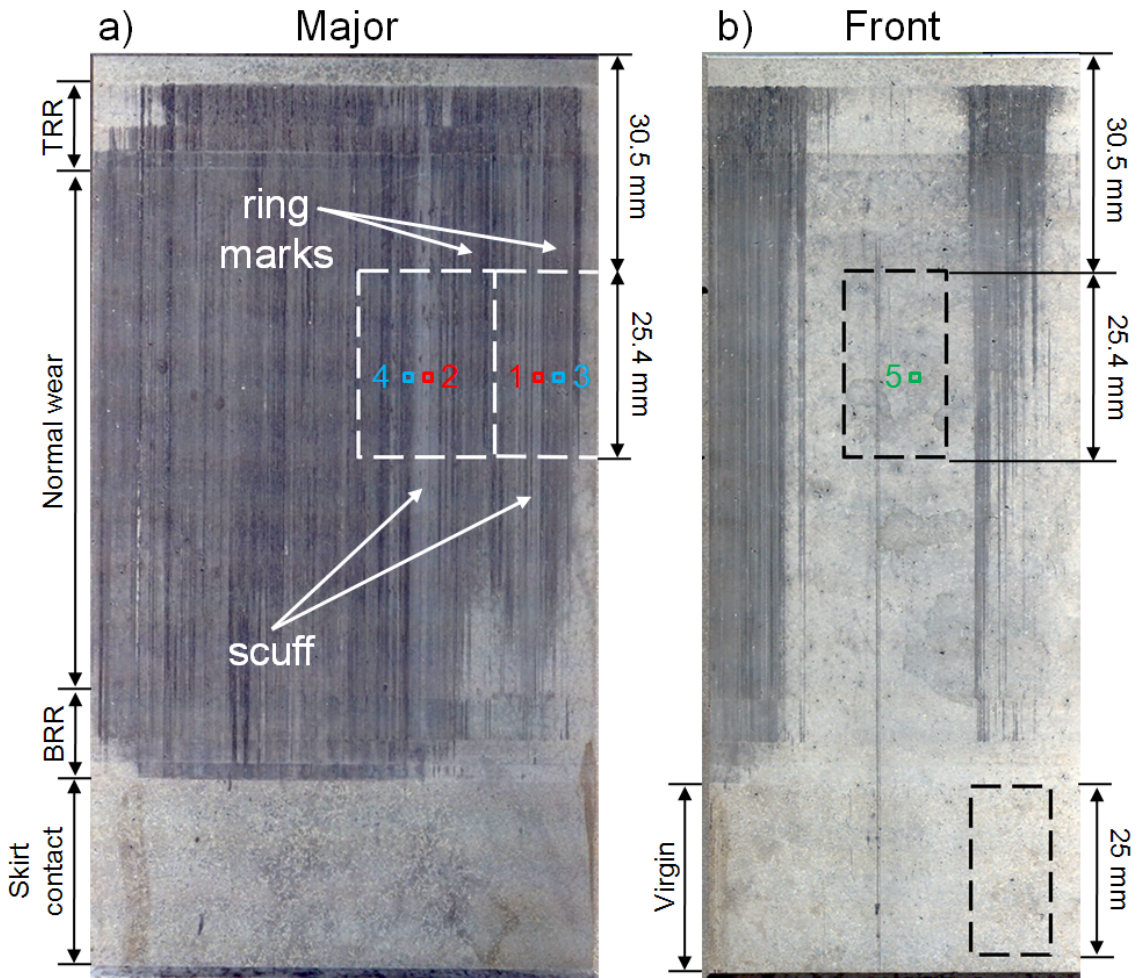
Figure 4-43 Engine bore of the major (a) and front (b) face from Ni:CE:CS highlighting ring marks, scuff marks, areas of no ring travel, sites of interest numbered 1 through 5, and sectioned coupon areas delineated by the dashed white and black boxes.

4.4.2   Unworn Region

Analysis of the unworn surface indicates that the surface preparation used on this bore did in fact expose hard phases from the aluminum matrix. However, localized damage to the harder phases was apparent and possibly resulted from honing. Surface profilometry data indicates that the average surface roughness (R_a) of the unworn surface is approximately 0.76 μm. A typical area of the chemically etched cylinder topography is

revealed in Figure 4-44. The histogram height distribution for the chemically etched surface is shown in Figure 4-45. Here, the solid black curve represents the unfitted data; on this curve the large peak represents the aluminum matrix, which is set as the datum point and corresponding height of zero, while the smaller less pronounced peak represents silicon particles. The aluminum peak and silicon peak both exhibit a significant width, indicating a varied height distribution. By fitting the data to Gaussian line shapes the silicon height/exposure (R_f) with respect to the aluminum matrix is determined to be ~1.23 μm measured by the separation between the aluminum peak and fitted silicon peak; the fitted data is distinguished in Figure 4-45 by the red dashed curve. In the unfitted results (solid black curve) the data below the aluminum matrix elevation does not produce a distinct peak; however, a significant amount of data exists below the aluminum matrix elevation. Therefore, data below the aluminum matrix has also been fitted and distinguished by the blue dashed curve. This corresponds to areas on the surface where a high dissolution of the matrix took place during etching, thus creating cavities/pits which reside ~1.29 μm below the datum (Figure 4-45). A gold-coated and nickel-plated cross-section of the radial bore direction from the unworn surface is presented in the optical micrograph of Figure 4-46, which is in agreement with the profilometry data showing that Si particles are indeed exposed from the aluminum matrix.

Due to the nature of chemical etching neither traces of smeared aluminum nor any severe remnants of honing are seen on the surface of the aluminum-matrix; this is shown in Figure 4-47 which is an overall SEM micrograph typical of the unworn surface. From Figure 4-47 it is shown that large aluminum patches display signs of small etch pits, however a much higher dissolution of the matrix is observed around second phase particles which coincides with the surface profilometry observations in Figure 4-44. Riahi and Alpas [154] have examined the fracture of silicon particles during the sliding contact of Al-Si alloys and have demonstrated that a high dissolution of the matrix around silicon particles increases their susceptibility to root fracture by increasing the tensile stress developed in a given particle during sliding contact. Therefore, the increased dissolution of the matrix around silicon particles observed on the unworn surface will most likely lead to premature particle fracture. However, premature silicon

particle fracture has already been observed prior to sliding on the unworn surface most likely caused by the mechanical honing process; this has also been observed in engines Ni:MR:HT, Cu:MR:HT, and Ni:CE:HT. Chemical etching has exposed silicon particles to a degree which reveals that root fracture (Figure 4-47) most likely took place during honing stages.
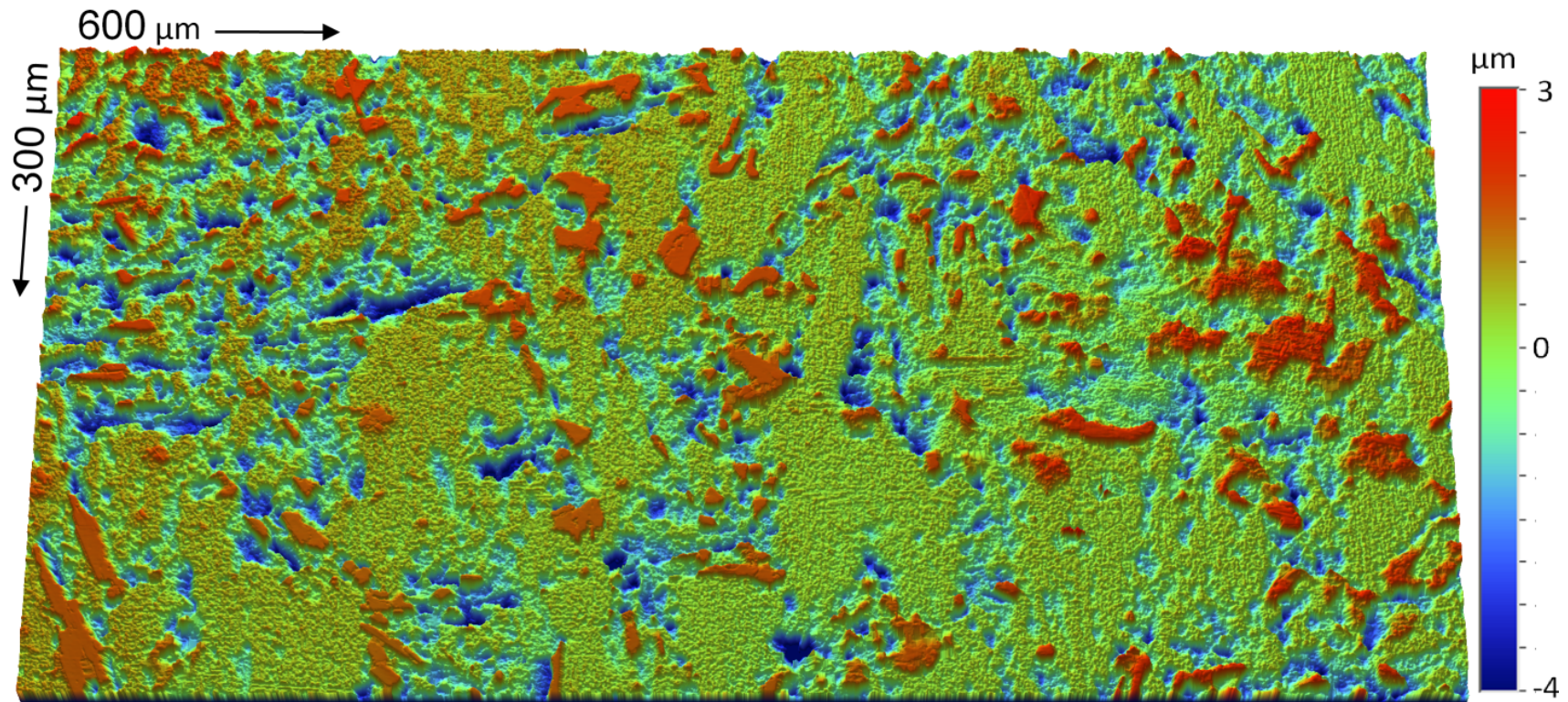
Figure 4-44 3D optical profilometry image (600 μm × 300 μm) after chemical etching showing Si particles protruding from the matrix (red) and cavities/valleys (blue) etched into the matrix.
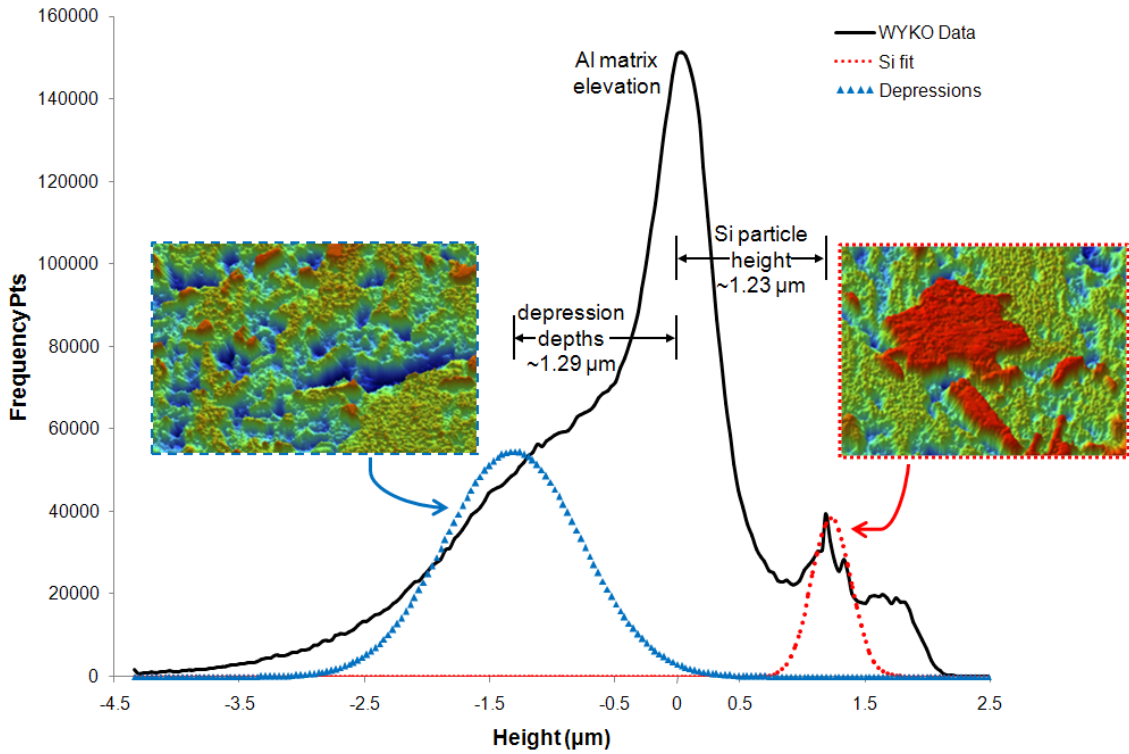
Figure 4-45 Typical histogram showing the Si height distribution of the etched surface; red dotted and blue triangle lines represent Gaussian curve fitting of the Si particles and depressions/cavities respectively.
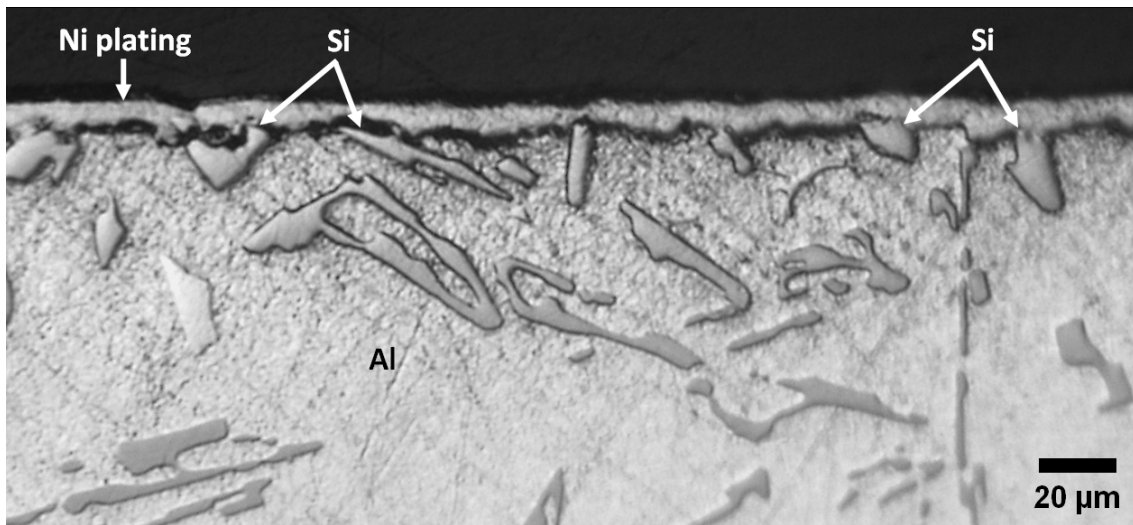
Figure 4-46 Gold-coated and nickel-plated polished cross-section of the radial bore direction from the unworn region; 1000x.
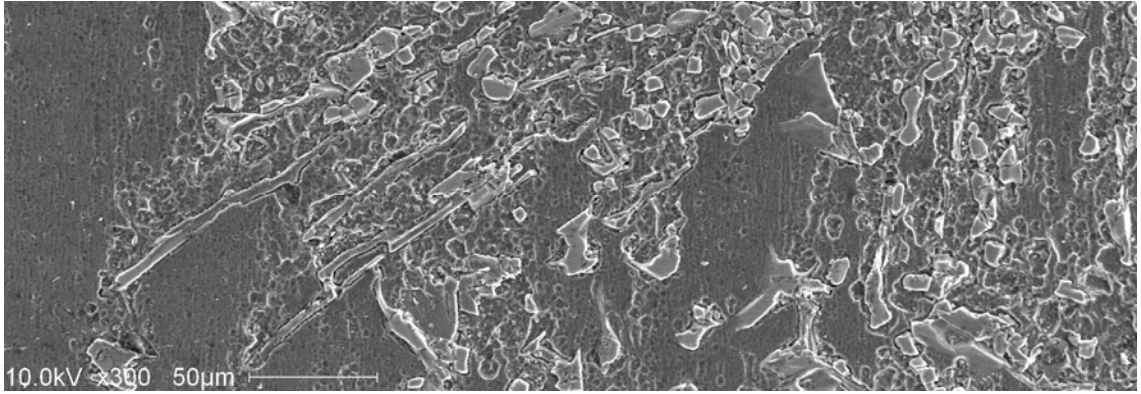
Figure 4-47 SEM micrograph of the etched virgin surface showing a high dissolution of the matrix around second phases; (0° tilt).
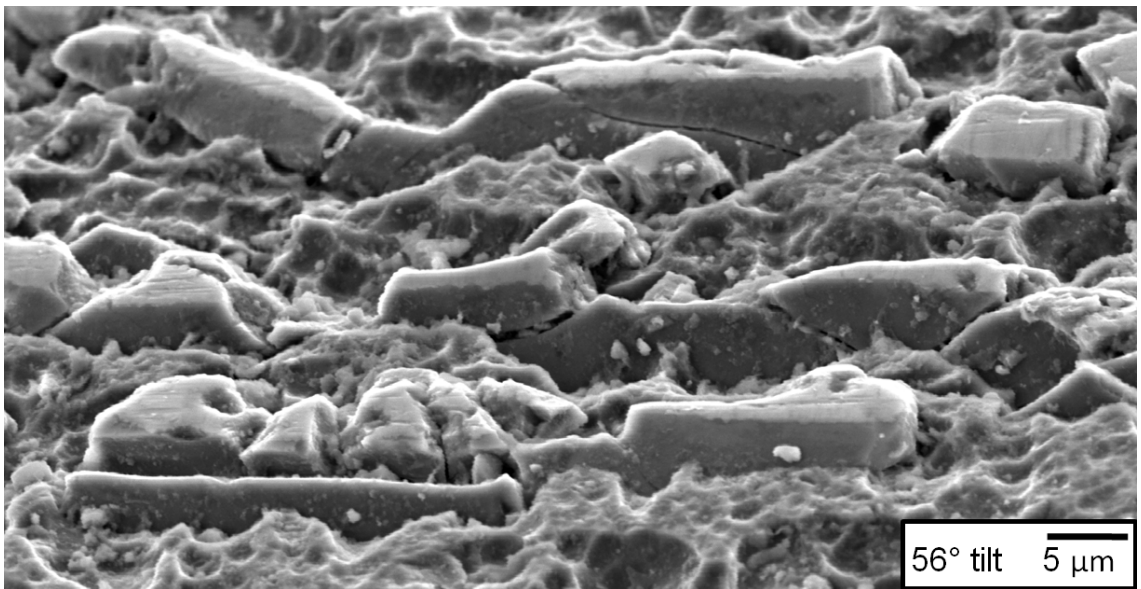
Figure 4-48 SEM micrograph of the etched virgin surface showing fracture to Si particles; (56° tilt).

4.4.3 Scuffed Region

Scuffed areas have been examined from two regions on the normal worn major face of the cylinder bore outlined in Figure 4-43 with red and numbered. The average surface roughness of the scuffed regions is approximately 0.90 μm. A typical surface profilometry image shown in Figure 4-49 indicates that scuffed regions contain deep grooves parallel to sliding, large cavities, and flattened areas. A gold-coated and nickel-plated cross-section of the radial bore direction from the scuffed region is presented in the optical micrograph of Figure 4-50, which exemplifies the grooves formed parallel to sliding. Similar to the unworn region, the histogram height distribution (Figure 4-51) combined with Gaussian peak fitting indicates that the depth of valleys/depressions on

158

the scuffed surface is approximately 0.655 μm. The unfitted data (solid black curve) shows a distinctive peak below the aluminum-matrix elevation representative of the depressions; here, the distinctive silicon exposure peak is no longer present in the scuffed region.

The first site of interest designated as SOI #1 of the scuffed region in Figure 4-43 has been thoroughly investigated with a combination of surface profilometry, SEM, and EDS. The overall surface profile and corresponding SEM micrographs of SOI #1 are presented in Figure 4-52. The original unworn microstructure containing silicon particles and second phases is completely indistinguishable in Figure 4-52(b). Here, the scuffed surface is flattened containing grooves parallel to sliding as well as spalled patches which are better observed under higher magnification shown in the subset Figure 4-52(c). Three distinct patches, boxed in red within Figure 4-52(b), appear to be a result of spalling and have been analyzed with EDS. The EDS spectrums from all three areas were identical (Figure 4-52(d)), all containing a high silicon signal and low aluminum signal. Grooves and flattened areas have also been examined with EDS (Figure 4-52(e) and (f) respectively) and indicate that grooves contain traces of small silicon fragments while flattened areas consist of mainly aluminum.

A second area of interest within the scuffed region outlined in Figure 4-43 as SOI #2 has been examined and presented in Figure 4-53. Even from visual inspection it is obvious that this scuff is much larger and more pronounced than the scuff mark examined in SOI #1. Surface profilometry (Figure 4-53(a)) indicates that the large groove parallel to sliding is approximately 2.7 μm in depth. The corresponding SEM micrograph boxed in black dashes of the groove is displayed in Figure 4-53(b). EDS scans boxed in red (Figure 4-53(c)), inside and outside the groove of flattened areas indicate that aluminum is the dominant element. Similar to SOI #1, spalled areas shown in the magnified subset Figure 4-53(d) along with the corresponding EDS spectrum, indicate a high concentration of fragmented silicon beneath the flattened/smeared aluminum. Lastly, a high magnification subset of the large groove presented in Figure 4-53(e) clearly shows the onset of aluminum spalling as well as the formation of smaller grooves parallel to sliding residing within the large groove.
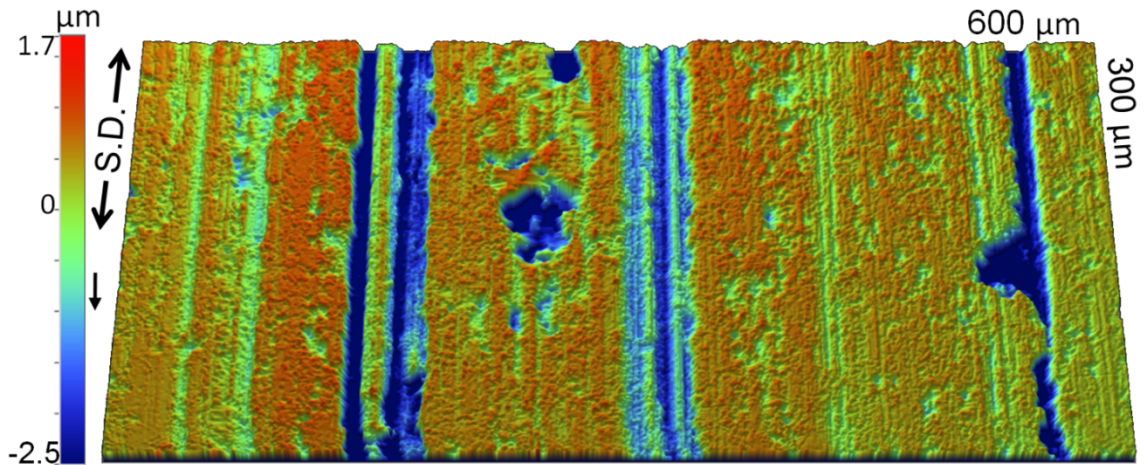
Figure 4-49 3D optical profilometry image (600 µm × 300 µm) typical of the scuffed region containing deep grooves parallel to sliding, large cavities, and flattened areas.
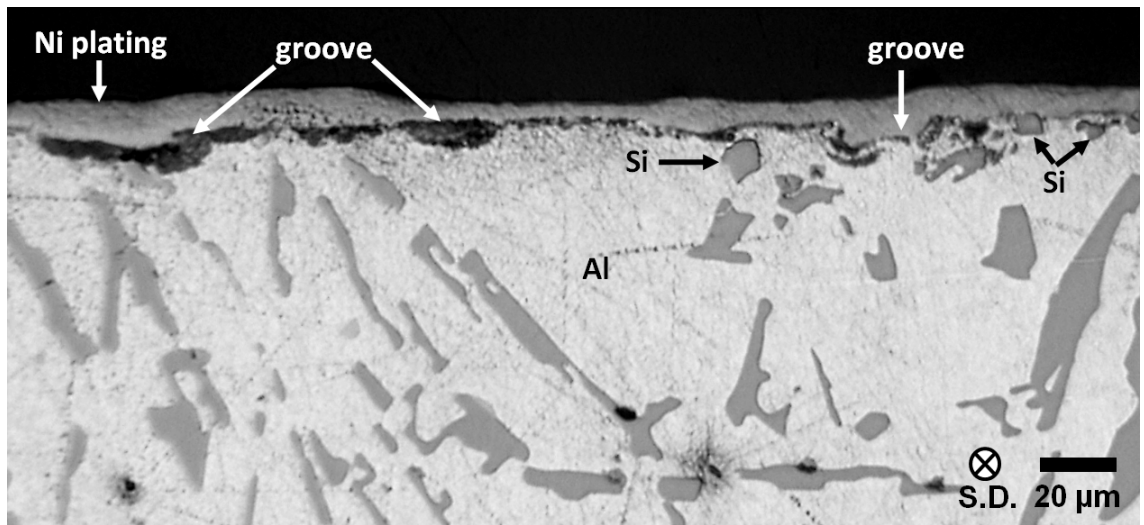
Figure 4-50 Gold-coated and nickel-plated polished cross-section of the radial bore direction from the scuffed region showing grooves formed parallel to the reciprocating motion of the rings which into the page; 1000x.
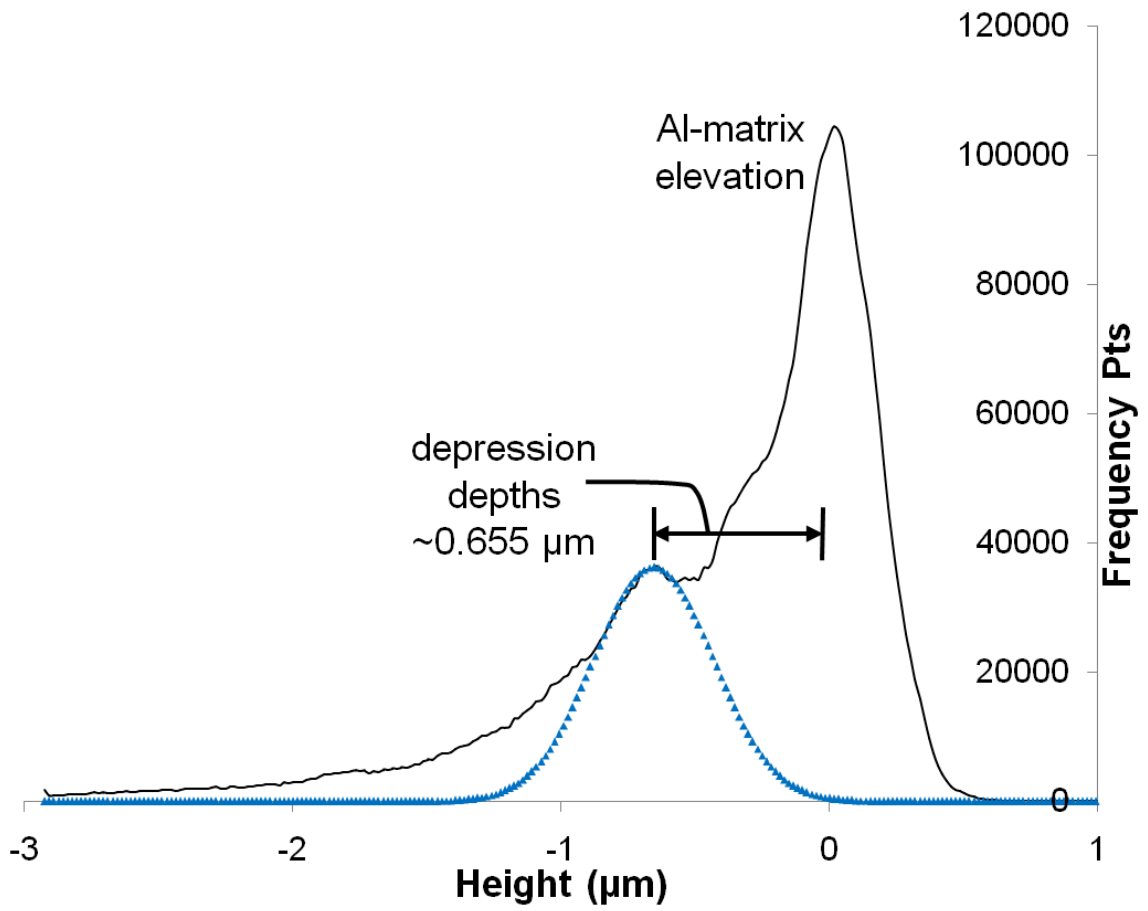
Figure 4-51 Typical histogram height distribution of the scuffed region; the blue triangle line represents Gaussian curve fitting of the grooves and depressions/cavities.

a)

296 μm

225 μm

μm

1.7

0

-2.5

b)

20 μm

c)

d)

Element	Wt%	At%
CK	22.80	39.54
OK	05.43	07.07
AlK	05.37	04.15
SiK	66.40	49.24
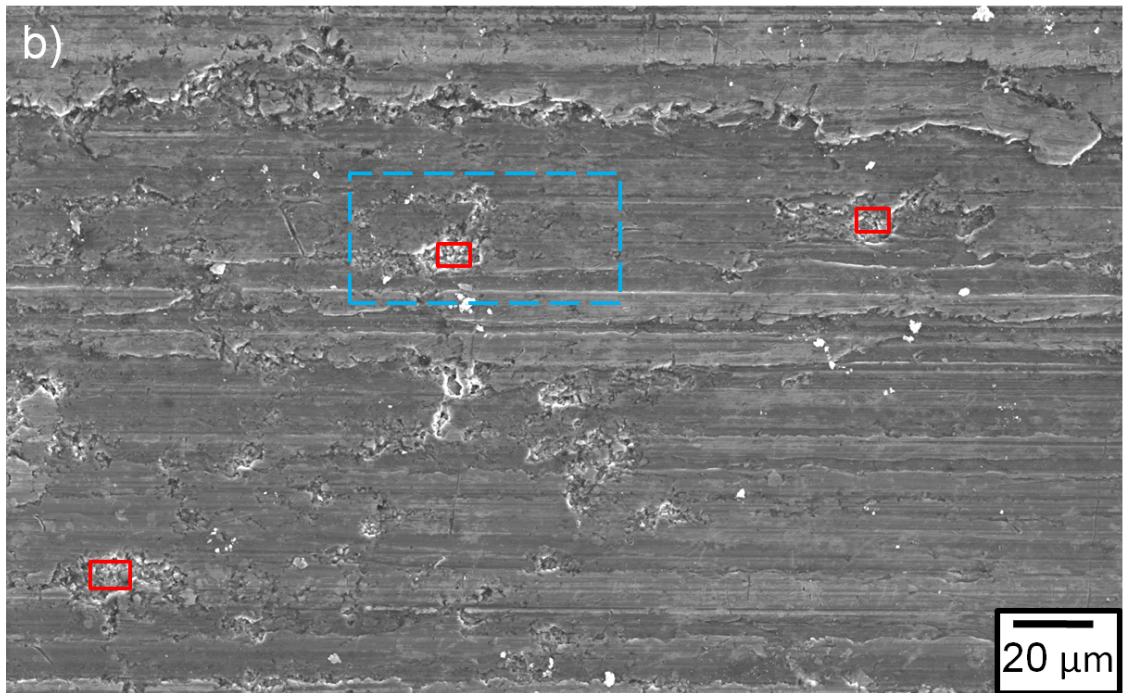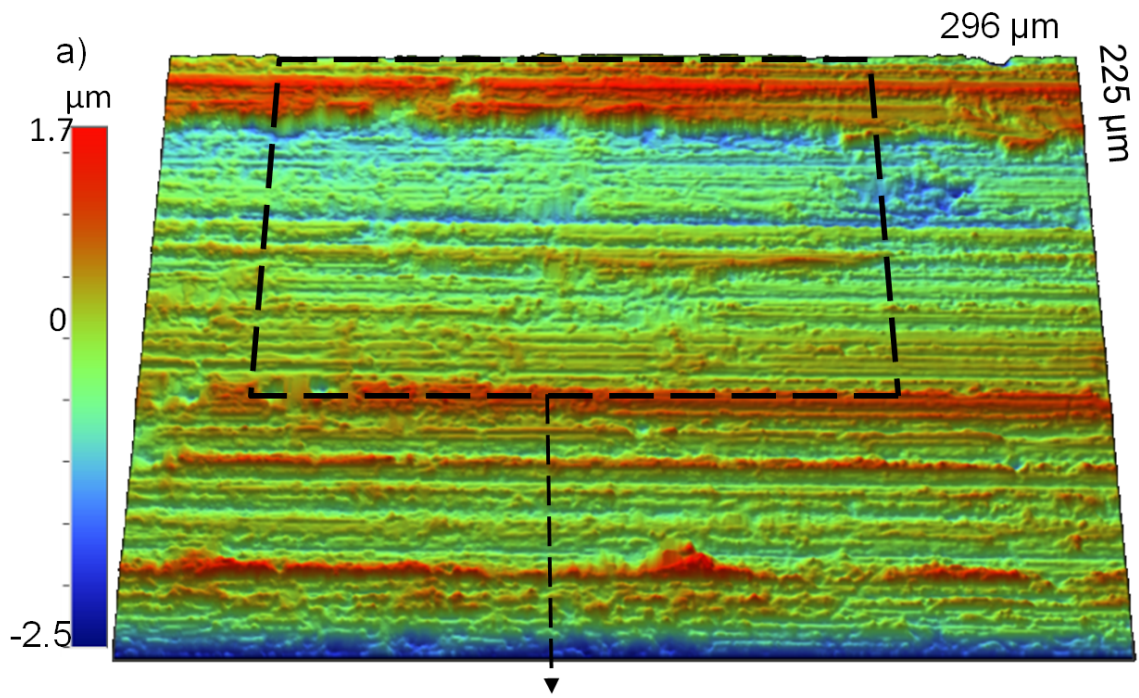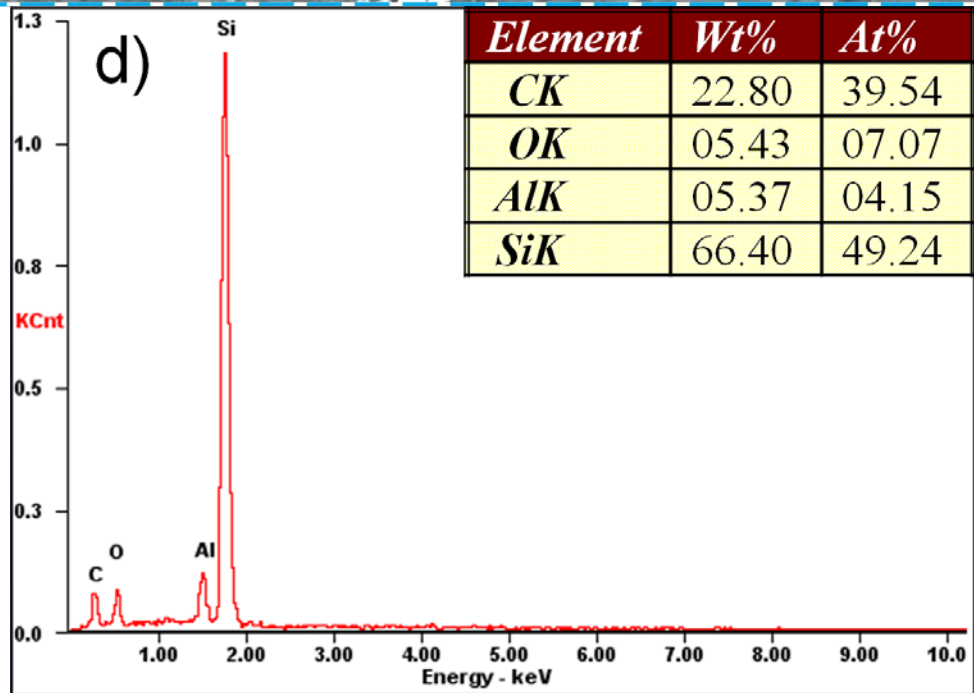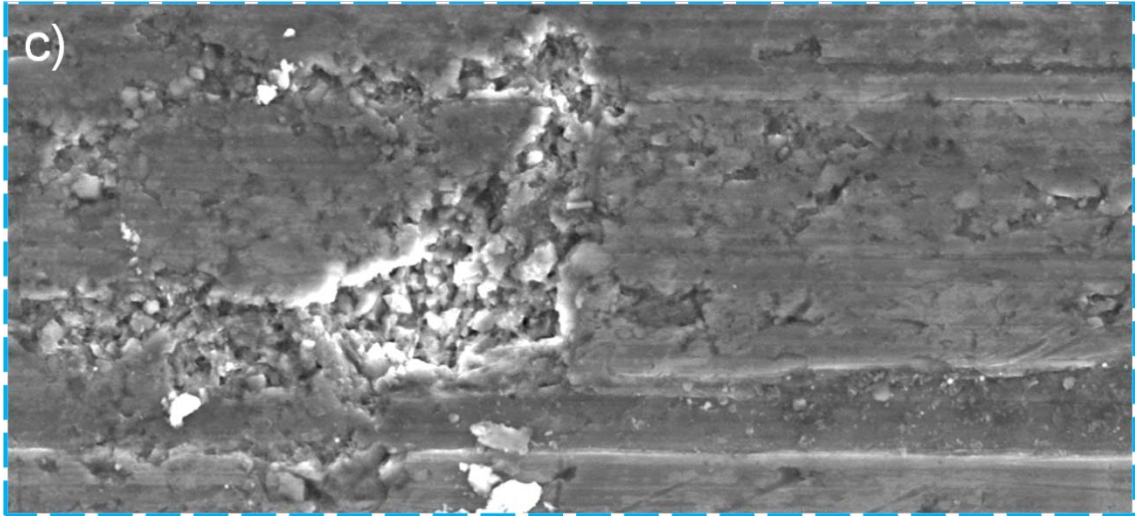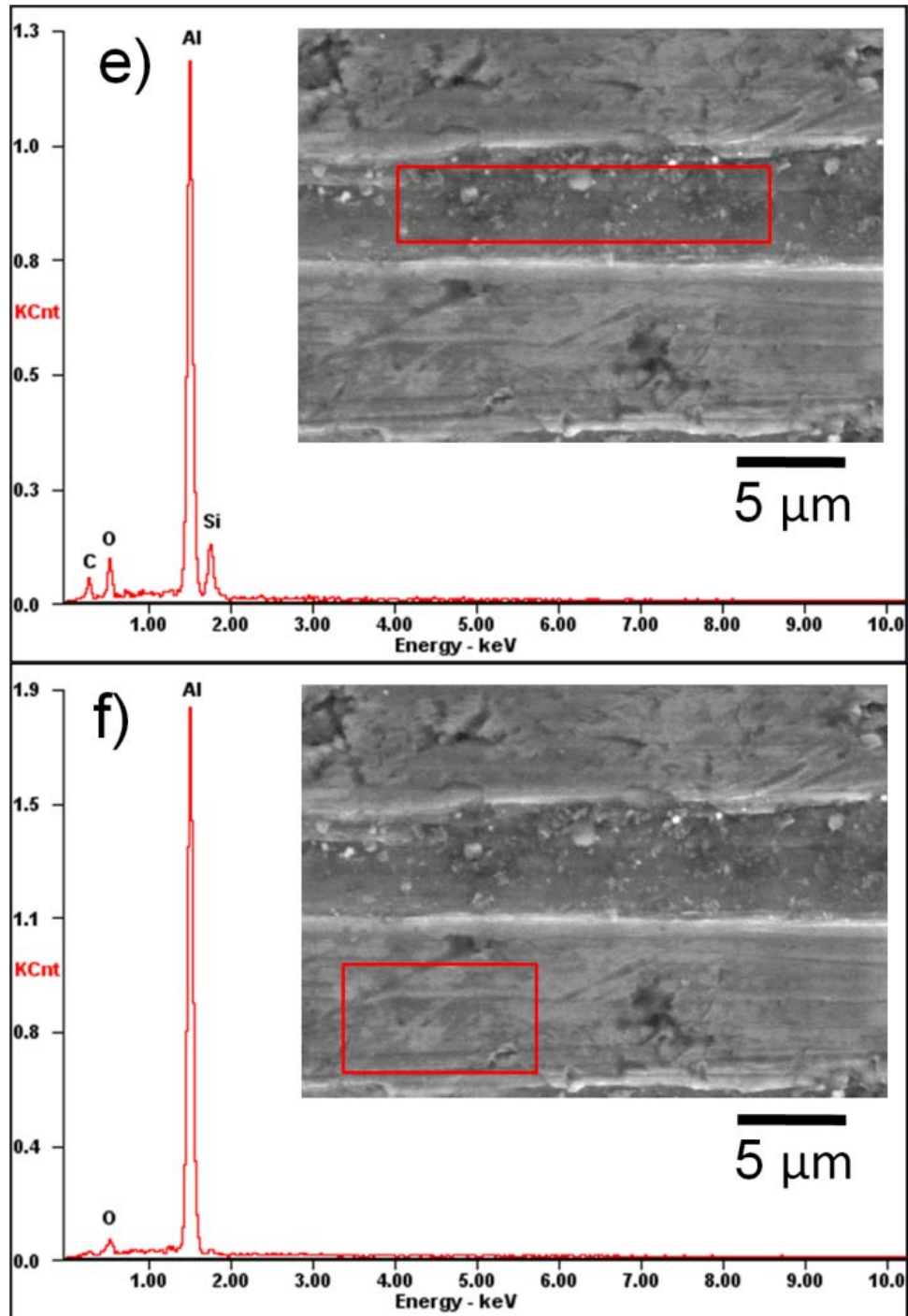
Figure 4-52 (a) 3D optical profilometry image of SOI #1 of the scuffed region; (b) corresponding SEM micrograph; (c) magnified subset of (b) (blue dashed box) from spalled patch revealing fragmented Si beneath the deformed Al; (d) corresponding EDS spectrums of spalled areas boxed in red from (b); (e) and (f) are EDS spectrums taken outside and inside a groove parallel to sliding; all micrographs are 0° tilt.

a)

296 μm

225 μm

μm

1.7

0

-2.5

b)

S.D. 56 ° tilt 10 μm

Element	Wt%	At%
OK	07.07	11.40
AlK	86.26	82.47
SiK	06.66	06.12

Element	Wt%	At%
CK	27.73	45.33
OK	07.02	08.62
AlK	15.21	11.07
SiK	50.04	34.99
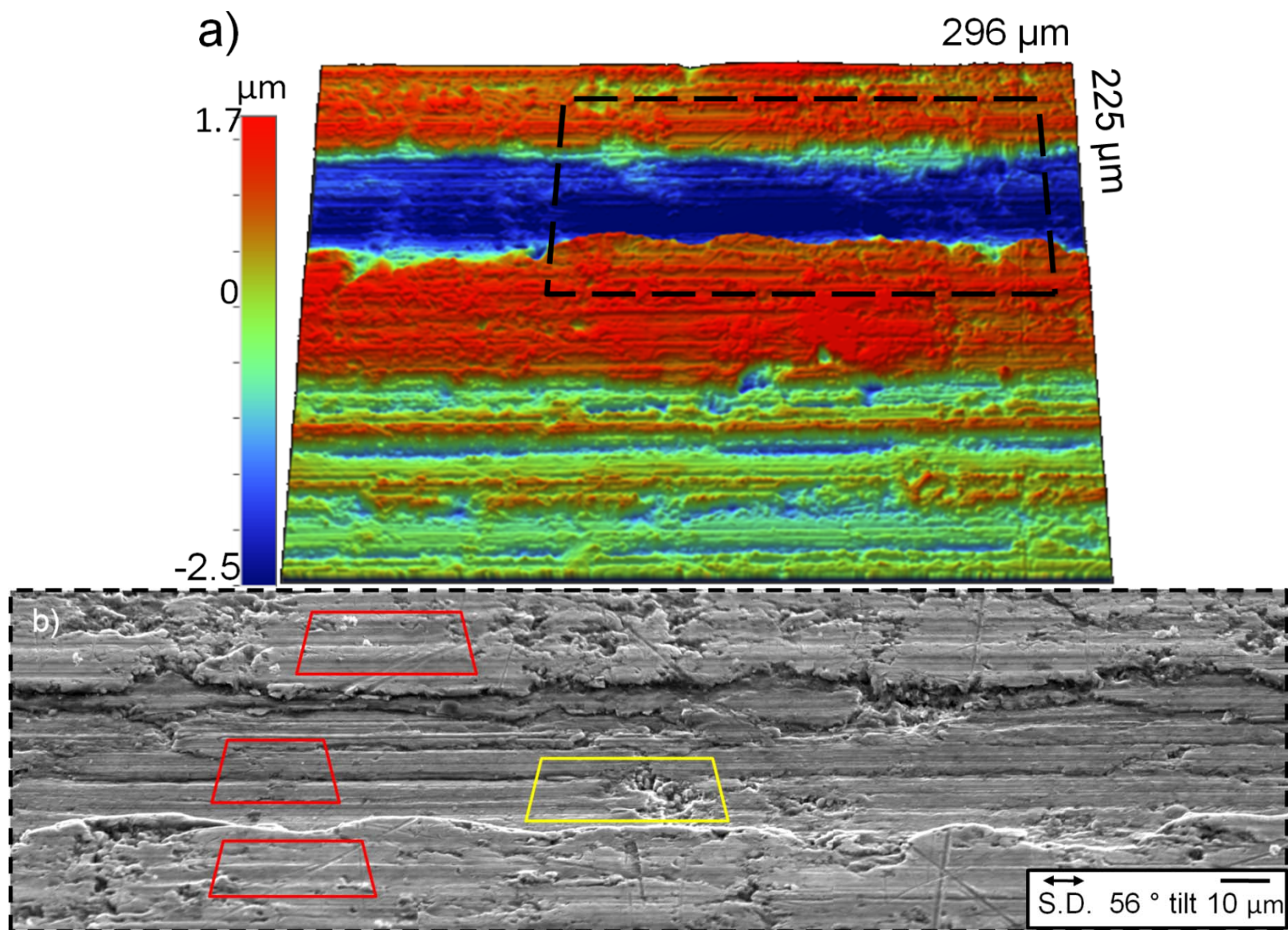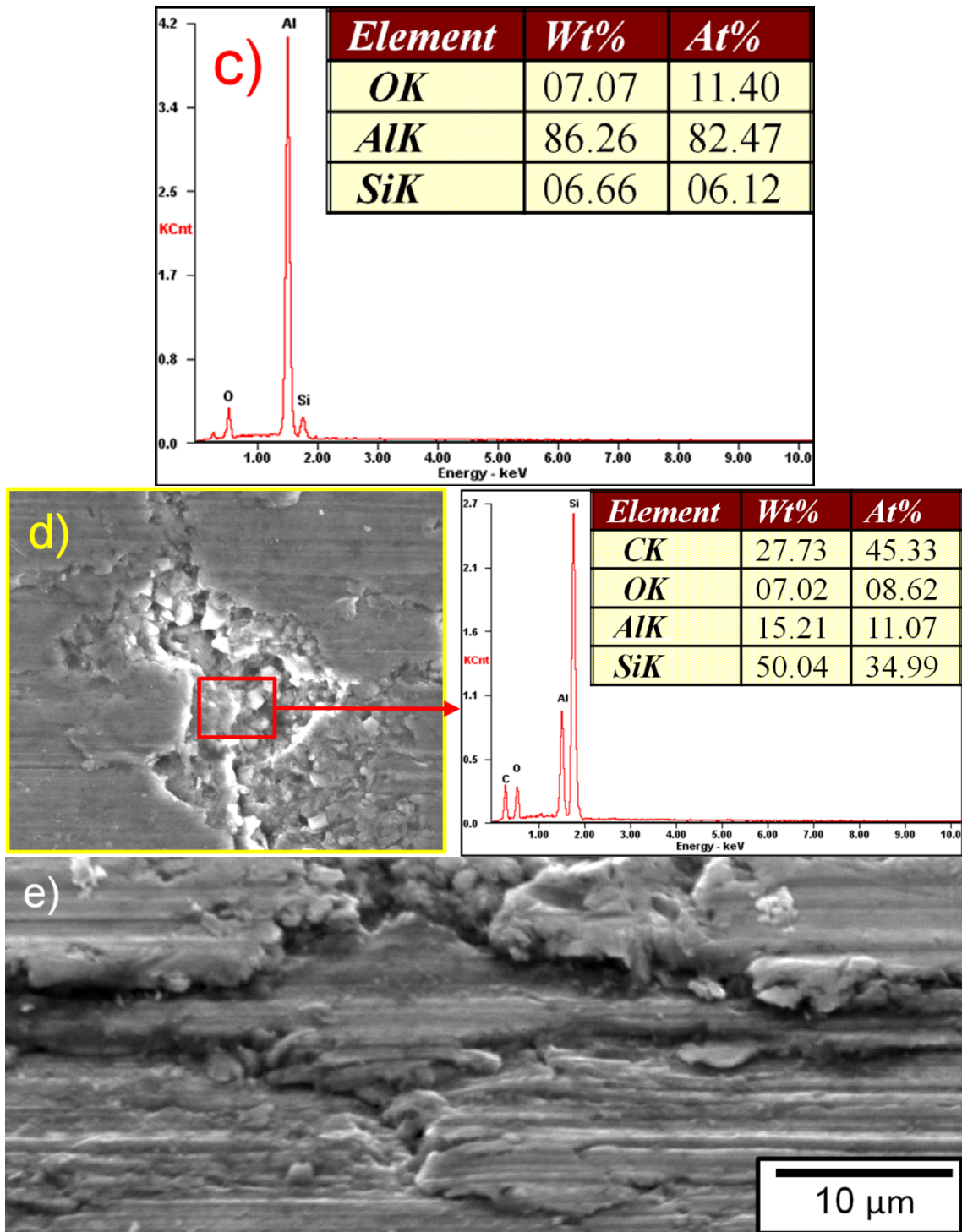
Figure 4-53 (a) 3D optical profilometry image of SOI #2 of the scuffed region; (b) corresponding SEM micrograph, 56° tilt; (c) corresponding EDS spectrums of flattened areas boxed in red from (b); (d) yellow boxed magnified subset and EDS spectrum of (b) from spalled patch revealing underlying Si fragments; (e) magnified area from (b) showing the onset of spalling.

4.4.4 Ring Mark Region

The ring mark region has been examined from two areas on the normal worn major face of the cylinder bore outlined in Figure 4-43 with blue and numbered. The average surface roughness of the ring mark region is approximately 0.39 μm. A typical surface profilometry image shown in Figure 4-54 indicates that the ring mark region contains grooves parallel to sliding, large cavities, and flattened areas. However, unlike the scuffed region the grooves observed in the ring mark region are not as large. A gold-coated and nickel-plated cross-section of the radial bore direction from the ring mark region is presented in Figure 4-55 for comparison to the scuffed region (Figure 4-50), which indicates that the grooves from the ring mark region are indeed smaller; such that they cannot be resolved in Figure 4-55 clearly with optical microscopy. On the other hand, the histogram height distribution (Figure 4-56) does not show any distinct silicon exposure peak. In fact, the histogram shows evidence that more cavities/depressions are emerging as more data is slightly shifted to the left of the main peak. Much like the scuffed region, the ring mark region also shows no signs of the original silicon microstructure.

The SEM micrograph, corresponding surface profile, and EDS spectrums are presented in Figure 4-57 from SOI #3 of the ring mark region which shows that the worn surface is flattened some areas but at the same time the containing fragmented silicon particles that are not completely covered by aluminum. The WYKO profile (Figure 4-57(a)) indicates that grooves and cavities are beginning to form on the surface but not to the same extent as the scuffed surface. It is important to note that during observation of the ring mark region no large silicon particles were observed (i.e. primary and needle-like silicon); instead the only observable silicon particles were those that were fractured or were initially too small to initiate fracture. Although the EDS spectrums at best are considered semi-quantitative their results presented in Figure 4-57(c) suggests that flattened/smeared areas (red-boxed area #1) often display a decreased silicon signal, with an increase in oxygen and aluminum compared to area #2.

The second area of interest within the ring mark region designated as SOI #4 in Figure 4-43 lies near the large scuff mark and could be considered an intermediate zone with characteristics between that of the scuffed region and ring mark regions. The surface

profile, along with corresponding SEM micrograph outlined by the white dashes, and EDS spectrum is presented in Figure 4-58. The 2d surface profile (Figure 4-58(b)) of line A-A′ shown in Figure 4-58(a) indicates that deep cavities have formed on the surface but at the same time the surrounding surface is relatively flattened containing grooves parallel to sliding. Observations of the tilted SEM micrograph (Figure 4-58(c)) shows evidence of a large light colored second phase near the large cavity. Further inspection with EDS (Figure 4-58(d)) revealed that the large intermetallic phase contained nickel similarly found in engines Ni:MR:HT and Ni:CE:HT. It is possible that the cavity formed from the fracture and removal of the large intermetallic during wear, by macro-porosity forming near the intermetallic during casting, or was a result of spalling and deformation of the matrix.
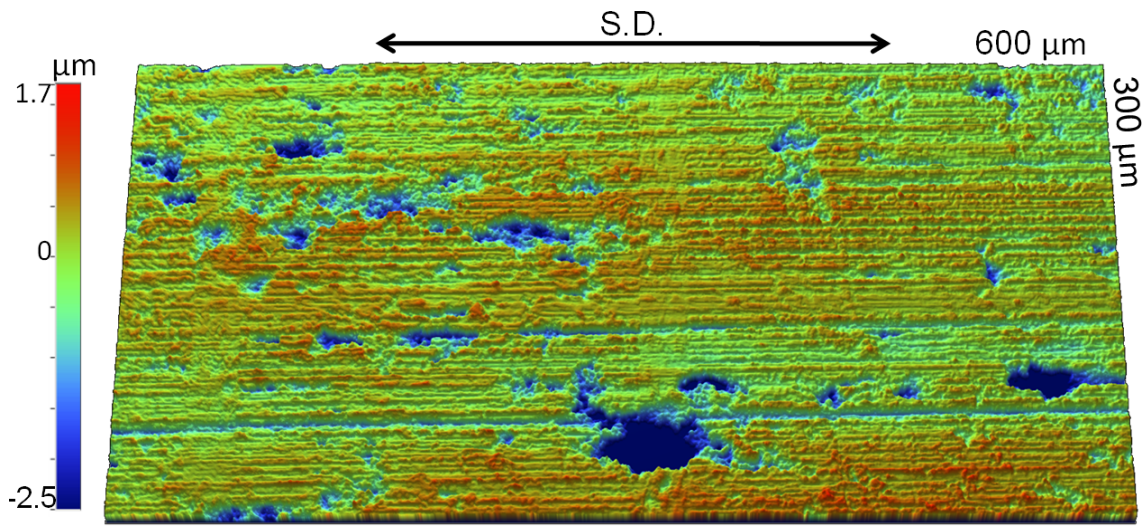
Figure 4-54 3D optical profilometry image (600 µm × 300 µm) typical of the ring mark region containing grooves parallel to sliding, large cavities, and flattened areas.
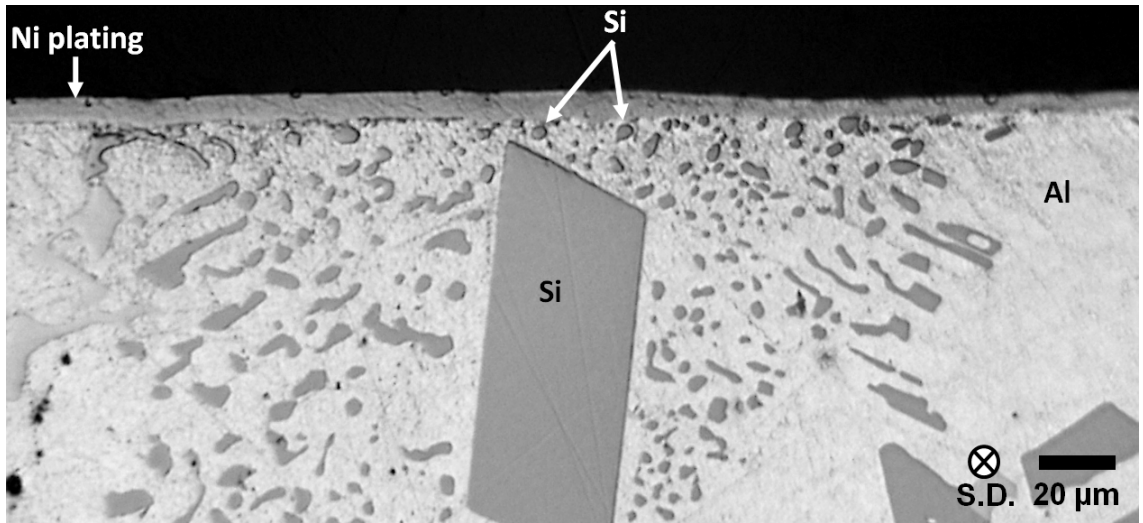
**Figure 4-55 Gold-coated and nickel-plated polished cross-section of the radial bore direction from the ring mark region ; 1000x.**
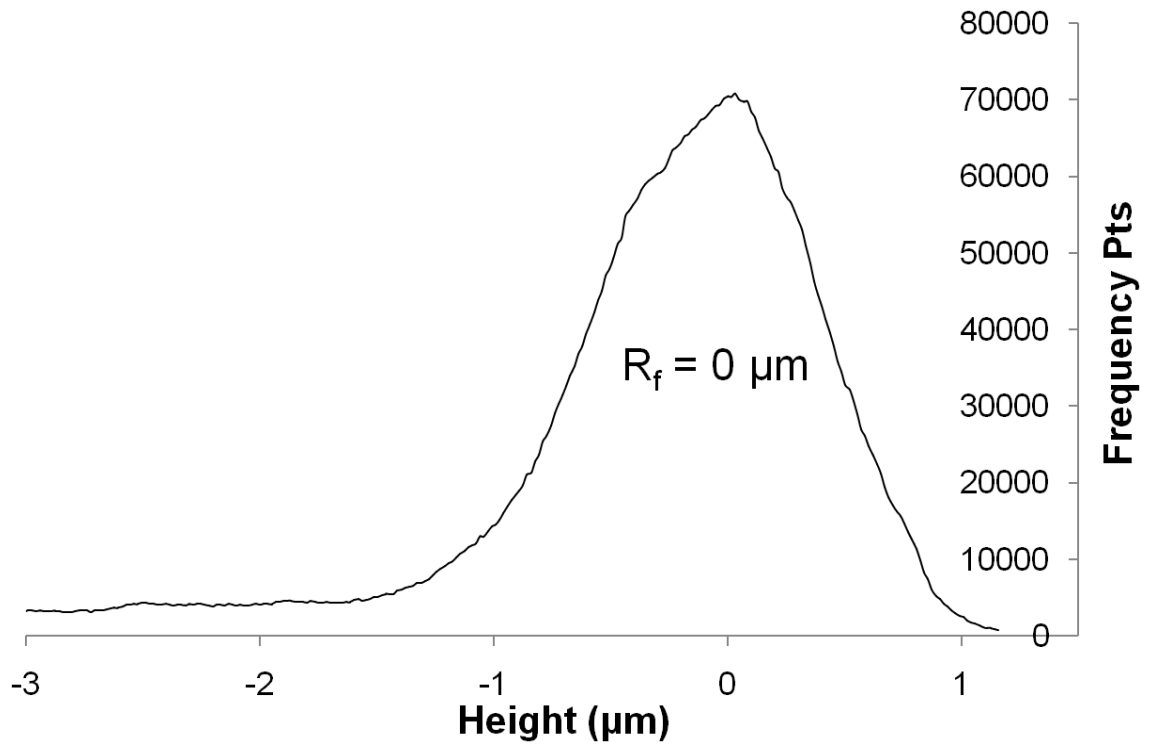
Figure 4-56 Typical histogram height distribution of the ring mark region showing only one common peak.
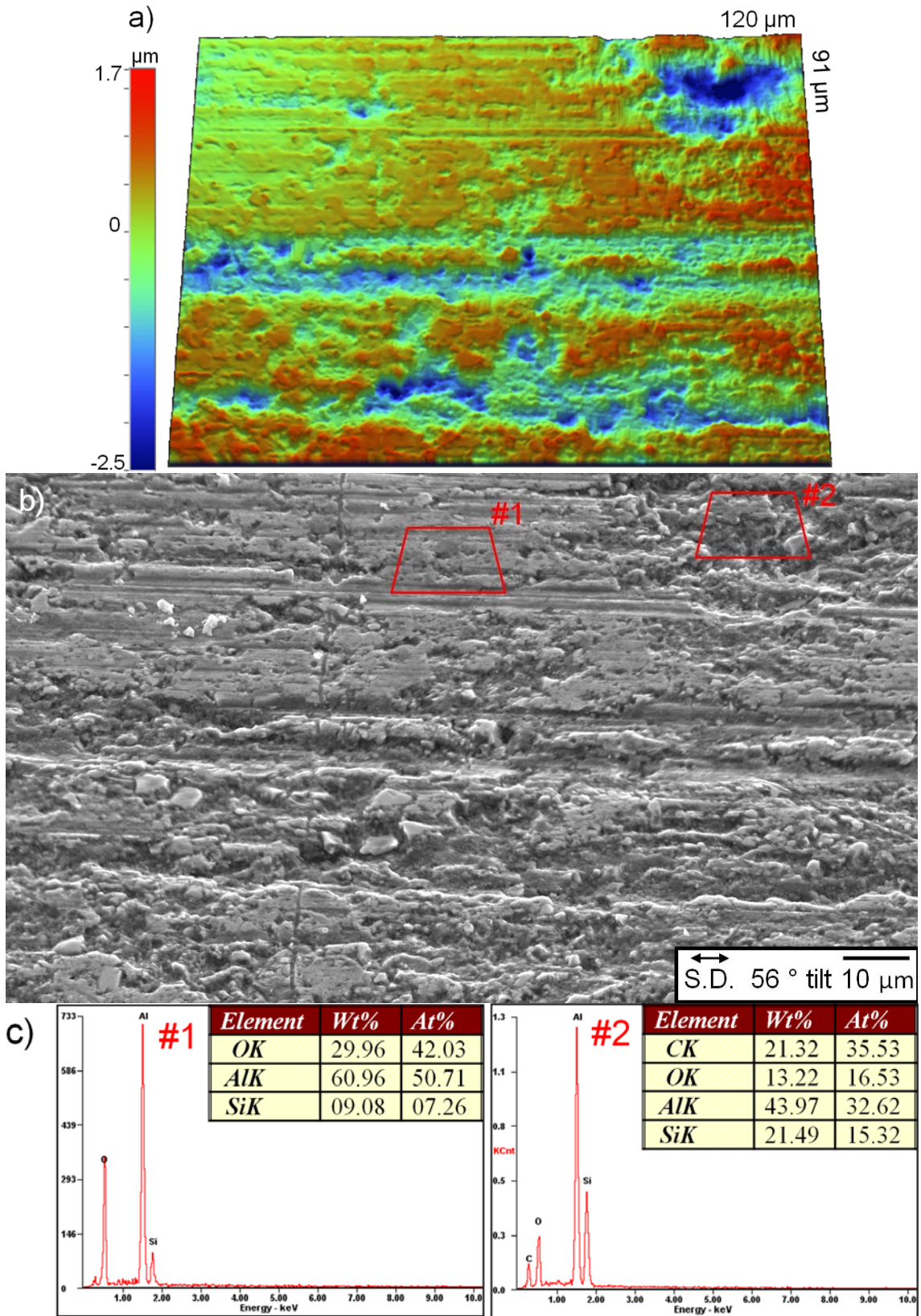
Figure 4-57 (a) 3D optical profilometry image of SOI #3 of the ring mark region; (b) corresponding SEM micrograph, 56° tilt; (c) corresponding EDS spectrums of red boxed areas #1 and #2 from (b).

a)

c)

b)

cavity
~ 9.2 μm

A   A'

S.D. 56 ° tilt 10 μm

172

Element	Wt%	At%
OK	10.95	17.21
AlK	83.78	78.07
SiK	05.26	04.71

Element	Wt%	At%
CK	19.80	35.46
OK	11.24	15.11
NiL	12.38	04.54
AlK	50.49	40.24
SiK	06.09	04.66
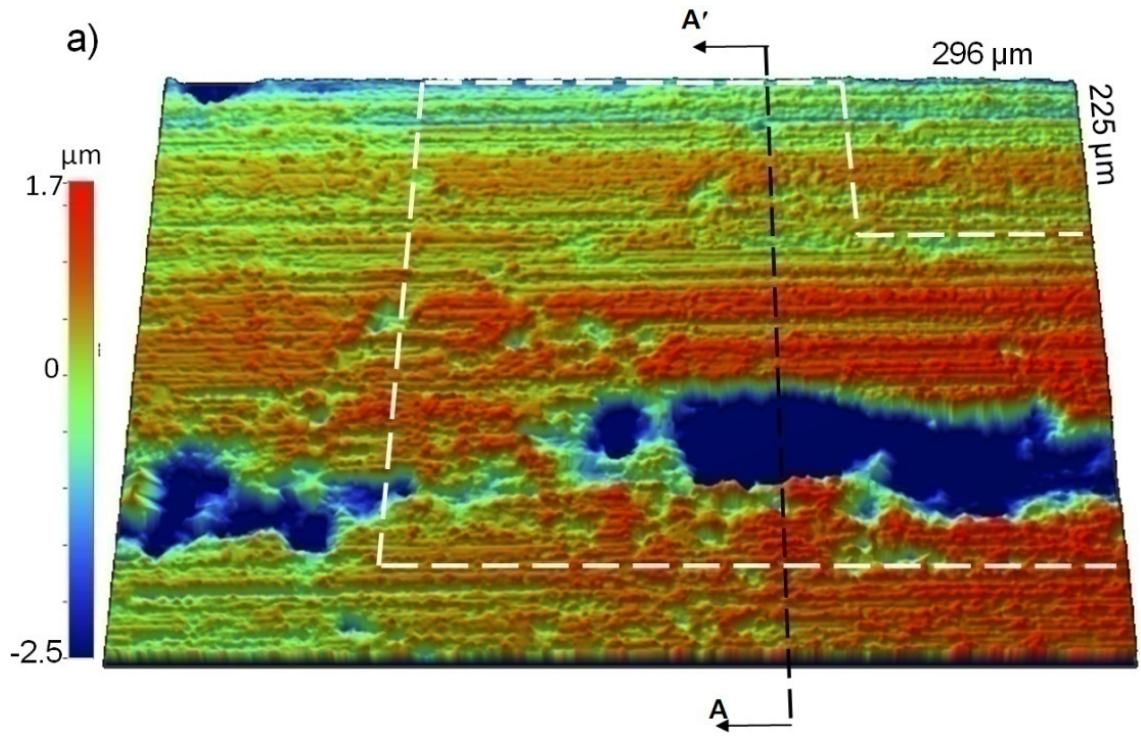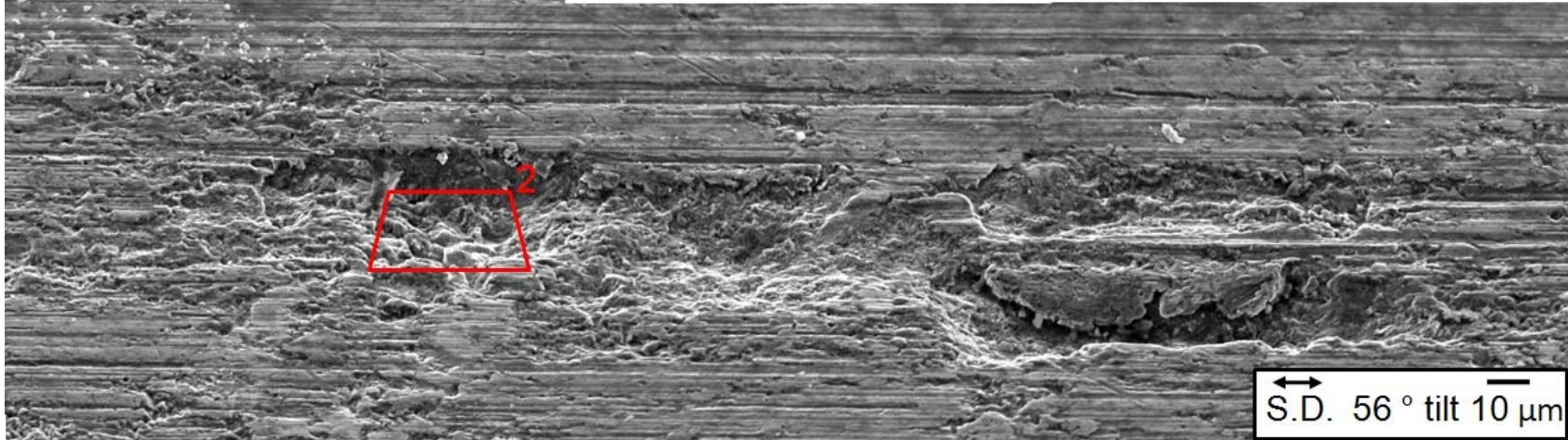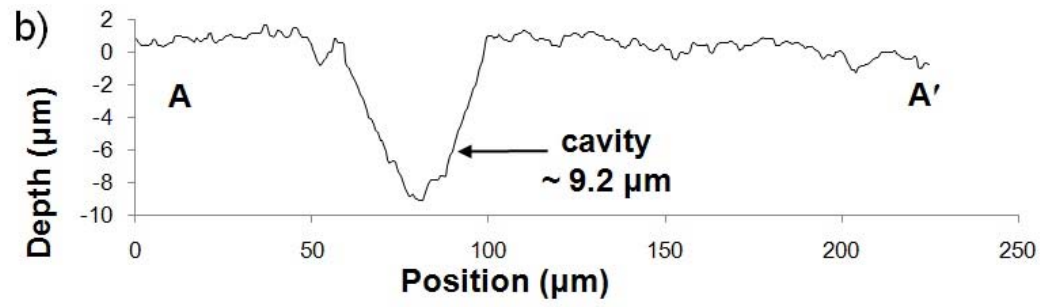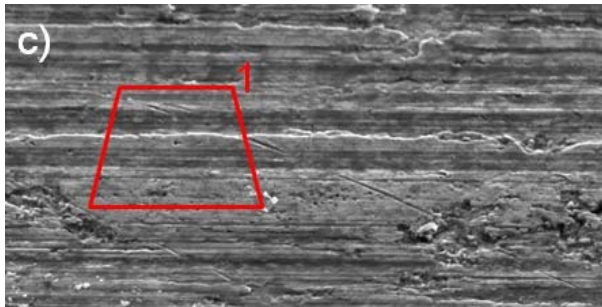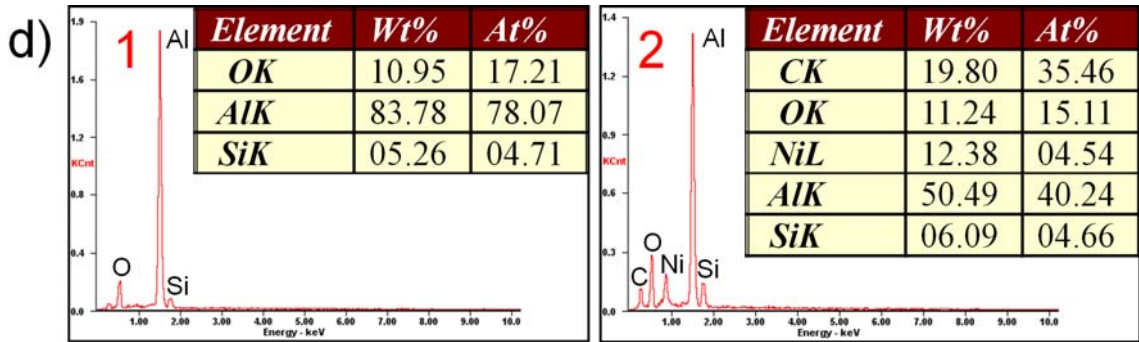
Figure 4-58 (a) 3D optical profilometry image of SOI #4 from an intermediate region; (b) corresponding 2d profile of line A-A′ in (a); (c) corresponding SEM micrograph from white dashed area in (a), 56° tilt; (d) corresponding EDS spectrums of red boxed areas 1 and 2 from (c).

4.4.5 Worn Front Face

To further obtain insight as to how the unworn surface transformed to the heavily deformed major face the worn front face was analyzed. This region boxed in green designated as SOI #5 shown in Figure 4-43 has been analyzed by the same techniques as previously examined areas to maintain consistency. The average surface roughness of the worn front face is approximately 0.55 μm. A typical 3d surface profile of the worn front face is presented in Figure 4-59, which shows silicon particles that are not completely fractured as well as a matrix that is not highly deformed in comparison to the major face. A histogram height distribution typical of the worn front face shown in Figure 4-60, indicates that a significant number of asperities protrude from the common matrix level by approximately 0.32 μm. This exposure peak represents the highest asperities which can include silicon particles as well as aluminum; this is visually shown in Figure 4-59 wherein silicon particles are level with the adjacent aluminum; however, both are colored in red representative of the highest asperities. Similar observations were obtained with optical microscopy and SEM presented in Figure 4-61 and Figure 4-62. The gold-coated and nickel-plated cross-section of the radial bore direction from the worn front face (Figure 4-61) indicates that Si particles are not protruding from the matrix to the same degree as the unworn surface (Figure 4-46). In addition, no large grooves, as previously observed in the scuffed region (Figure 4-50), are seen in Figure 4-61 of the worn front face. Figure 4-62(a) is a typical SEM micrograph showing a large fractured silicon particle which is level with the adjacent matrix containing smaller fragmented particles. Figure 4-62(b) is an un-tilted SEM image demonstrating that small silicon fragments/particles are pushed into the matrix confirmed by EDS (Figure 4-62(c)).

173

Moreover, larger silicon particles are fractured and signs of flattening of the matrix are apparent. In addition, a spherical oil deposit containing Zn, Ca, O, and C has formed and is identical to the spherical oil deposits previously reported in the hot tested engines. Overall, even after specifically searching the surface for oil deposits virtually no others were found.
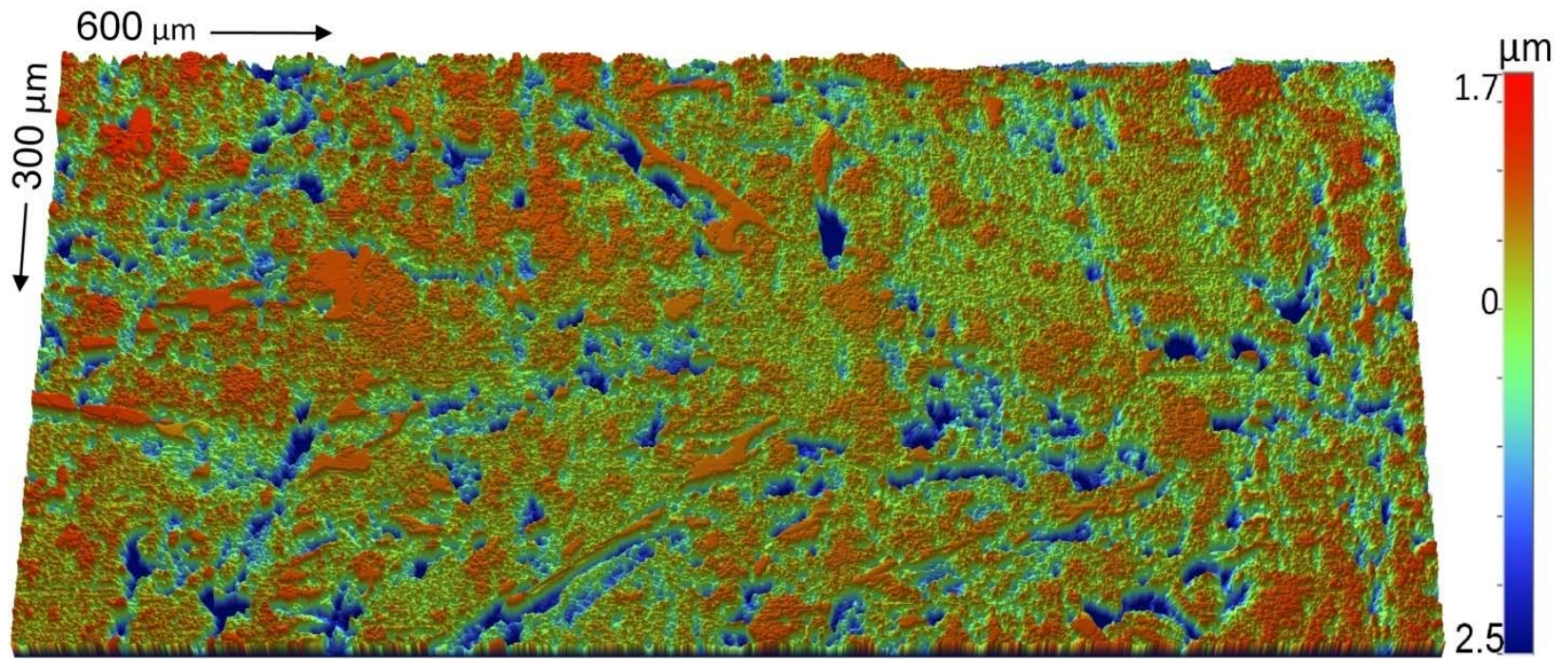
Figure 4-59 A typical 3D optical profilometry image (600 μm × 300 μm) of the worn front face highest asperities are red and cavities/valleys are blue.
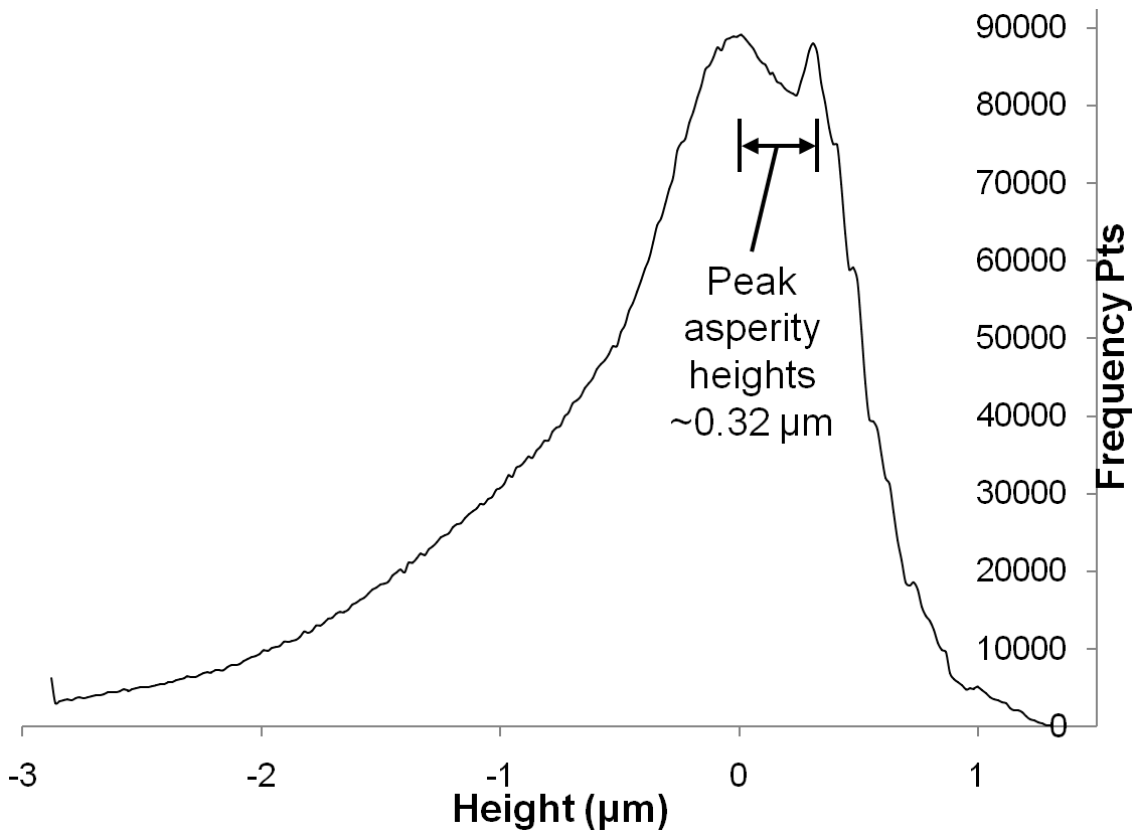
Figure 4-60 Typical histogram height distribution pertaining to the worn front face.
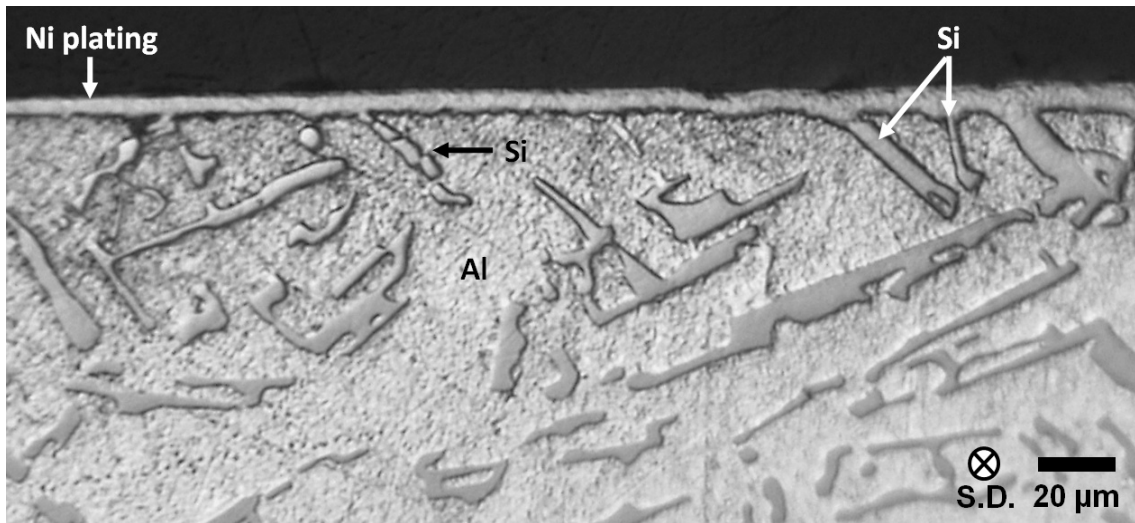
Figure 4-61 Gold-coated and nickel-plated polished cross-section of the radial bore direction from the worn front face illustrating Si particles level with the aluminum matrix; 1000x.

Element	Wt%	At%
AlK	08.43	08.75
SiK	91.57	91.25
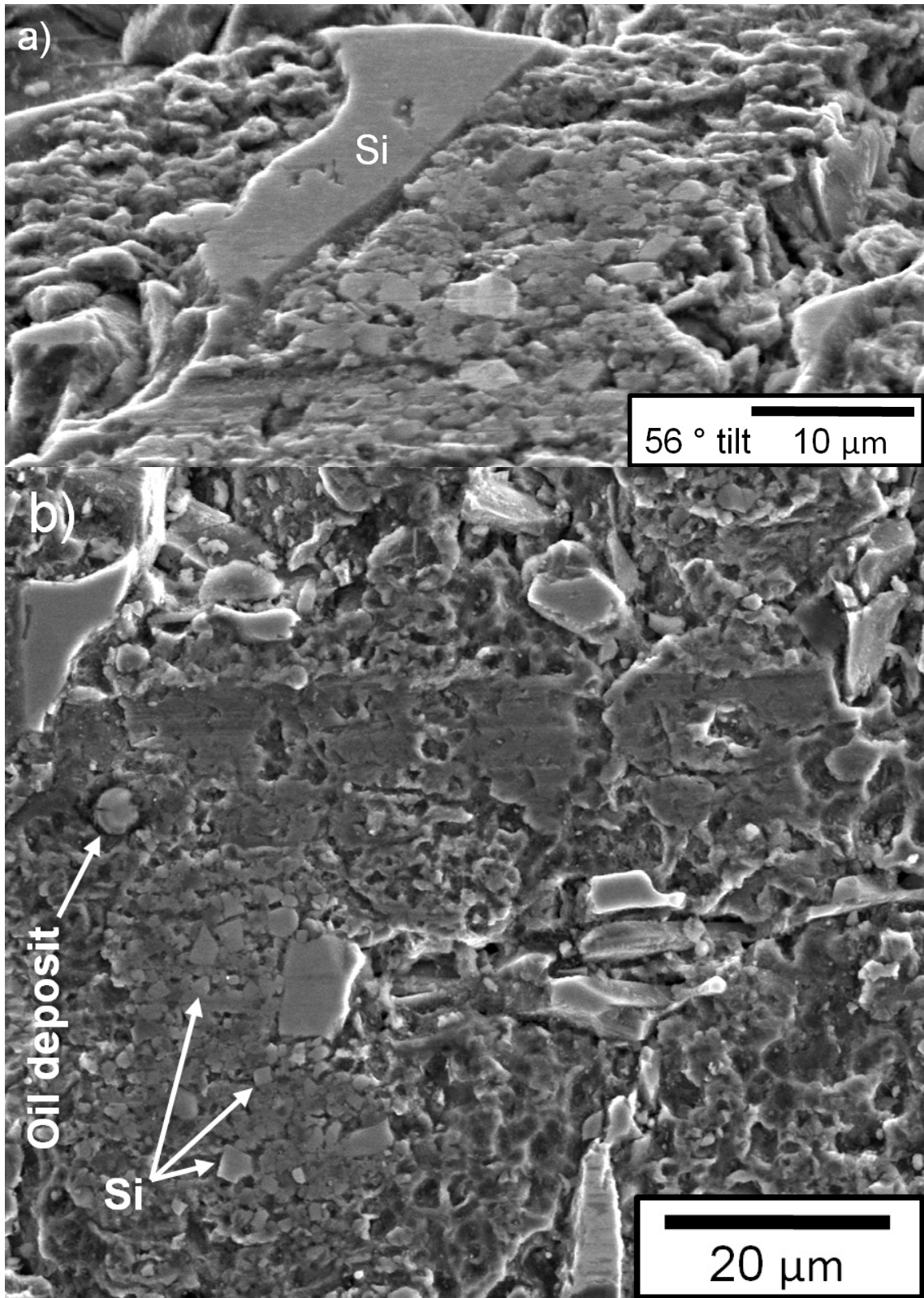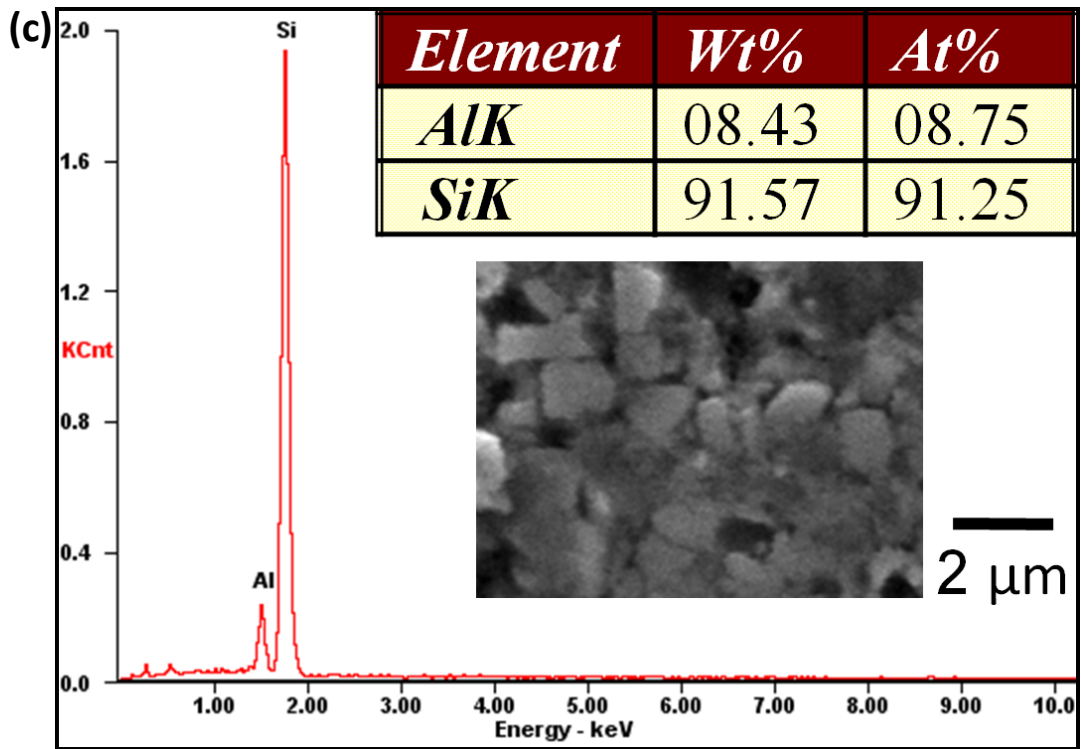
Figure 4-62 (a) SEM micrograph of the worn front face showing Si particles level with the matrix, 56° tilt; (b) un-tilted SEM micrograph showing fragmented Si particles embedded into the matrix and confirmed by corresponding EDS spectrum in (c).

5   DISCUSSION

5.1   Wear Mechanism (Ni:MR:HT)

In terms of surface morphology, the normal wear region compared to the unworn region is significantly different in the Ni:MR:HT engine. The macroscopic wear data from the normal wear region showing that the bore diameter grew by ~4 μm and the metallographic and optical profilometry data presented in this section both show that the bore exhibited considerable evolution of the microstructure. The evolution of the worn surface can be summarized by examining the changes in the aluminum matrix and the exposed hard phases separately. The aluminum matrix is very different from the unworn region. There is no evidence of hone marks, and the matrix has an apparently much rougher texture. There is some evidence of abrasive scratches parallel to the ring motion direction, but this is not severe. Another very important feature of the aluminum matrix in the normal wear region is the cavities on the surface; these are not restricted to the proximity of the hard phases. These cavities are circular in appearance and are typically 1 - 10 μm in diameter. Due to their size and geometry they are interpreted as microporosity [140, 197]. The fact that they are visible in the normal wear region, but not the unworn surface, is attributed to a polishing, or lapping, mechanism described shortly. FIB and SEM results further exemplify the evolution of the bore; wherein, the worn surface is a mixture of fine silicon particles, fine aluminum debris, and oil additive deposits. This layer is tightly bound to the surface. It was not removed by cleaning or preparation steps associated with sample preparation, and the FIB/SEM images showed that many of the refined particles are in intimate contact with the underlying matrix.

A mechanism that accounts for the evolution from the unworn to the worn wear microstructure is presented in Figure 5-1. Typical damage as a result of surface preparation is illustrated in Figure 5-1(a). Damage in the form of hone scratches on silicon particles establishes an uneven surface, thus creating small silicon peaks that are easily subjected to fracture. These silicon peaks break off into fragments during sliding; this acts to reduce their surface roughness when compared to silicon in the unworn region. The crosshatched scratches are not observed on any silicon particles in the normal wear region. Another mechanism that forms silicon fragments originates from

fractures present at the edges of silicon in the unworn surface. These fractures are susceptible to removal during running-in, and hence also facilitate the formation of small silicon fragments [20]. This is consistent with the macroscopic growth of the bore diameter, which is accounted for by 2 μm of wear. The silicon fragmentation mechanisms are shown schematically in Figure 5-1(b). The sharp silicon fragments abrade the softer phases with a polishing action. Removal of the matrix by silicon fragments is the reason that silicon particles continue to stand proud from the matrix and even increase in relative height. Furthermore, this causes softer intermetallic phases, such as nickel, to become scratched parallel to the sliding direction. The aluminum matrix would also exhibit similar scratches that end at harder phases, namely silicon and/or iron phases.

The evolution of the aluminum matrix is very prominent and includes other characteristics that are more dominant than the surface scratches just discussed, notably the presence of exposed spherical gas pores, and a tribofilm. The gas pores did not appear in the unworn surface, as they were covered by smeared aluminum. During sliding, small silicon fragments erode the smeared unworn aluminum with a polishing action and thus, exposed the pores. This has a negative impact on oil consumption, but it does help elucidate the polishing mechanism. Some of the larger sharp silicon fragments penetrate, and become embedded, into the soft aluminum-matrix, as is seen in the FIB/SEM micrographs. In addition, extremely fine silicon fragments are mixed into the oil deposits and reside in uneven surfaces on the matrix. These fragments and deposits, along with fine aluminum particles form a tribofilm that protects the underlying aluminum grains from further abrasion, as illustrated in Figure 5-1(c). The combined action of polishing and deposition of the polishing debris as an irregular tribofilm covering the aluminum matrix results in a "new" running surface where silicon particles act as the primary contact points, and a stable surface is established.
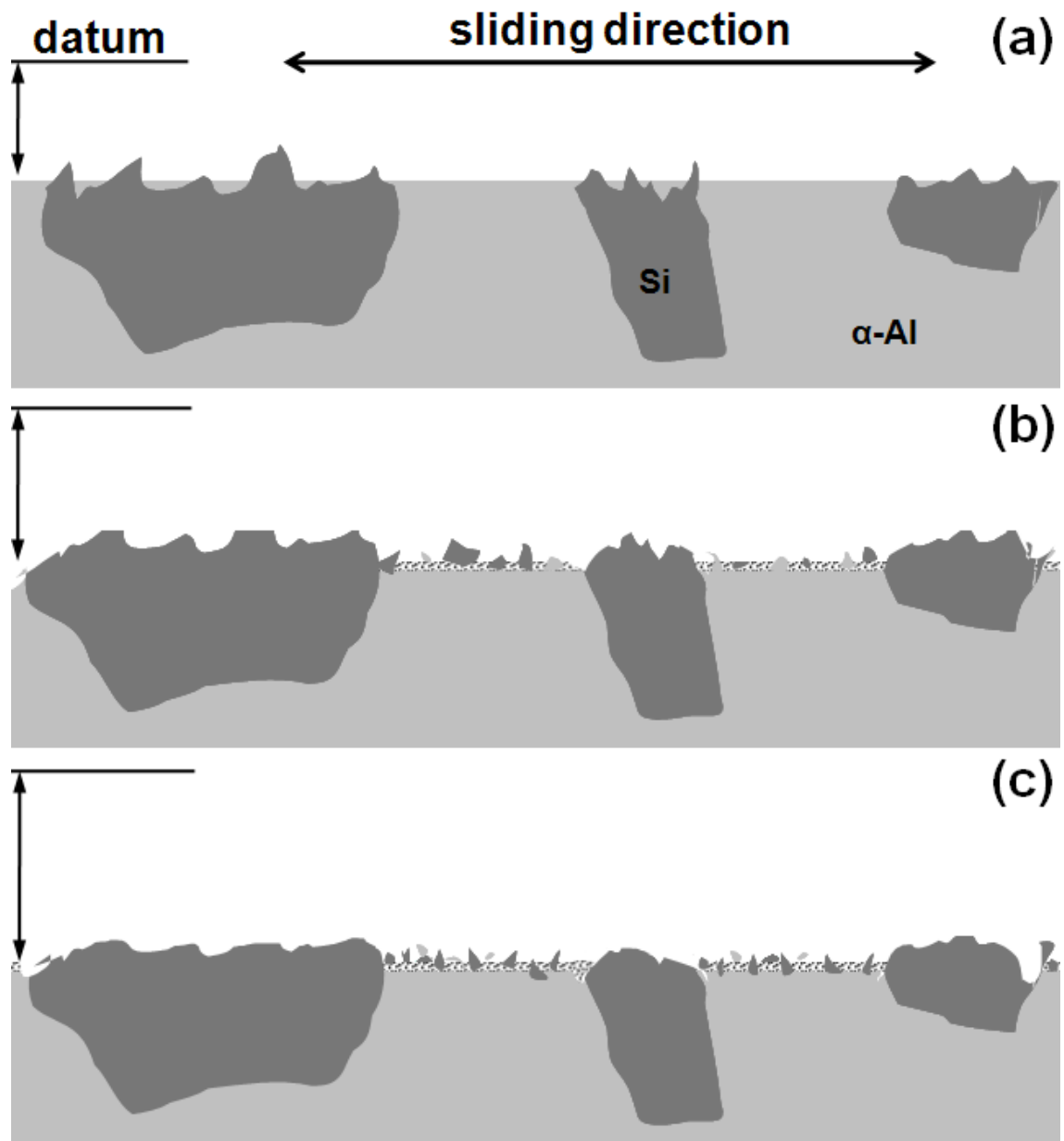
Figure 5-1 Schematic illustrating the mechanism of wear; (a) typical surface damage to Si particles as a result of surface preparation; (b) sharp fragments abrade the softer phases mainly aluminum and expose a fresh aluminum matrix and polish the Si surfaces; (c) surface equilibrium conditions show a matrix that is comprised of fractured particles, aluminum debris, oil deposits, and Si particles with rounded edges, smooth surfaces, and standing above the matrix.

5.2 Effect of Alloying (Ni:MR:HT vs. Cu:MR:HT)

The wear mechanisms responsible for obtaining a stable equilibrium surface after rigorous dynamometer testing for the Cu:MR:HT engine can be explained in terms of the changes observed in the aluminum matrix and exposed hard phases. The mechanism responsible for the evolution of the surface is illustrated in Figure 5-2 and is essentially identical to that of Ni:MR:HT (Figure 5-1) with the exception that the bulk Si microstructure is slightly more refined. Prior to engine testing the contact surface is prepared via honing and mechanical stripping. These mechanical procedures expose the hard phases from the aluminum matrix but at the same time causing damage to some silicon particles. Typical damage as a result of surface preparation is illustrated in Figure 5-2(a). Small interfacial voids between silicon particles and the aluminum matrix are formed at surface making them more susceptible to removal during wear. Although few large silicon particles exist throughout the microstructure the ones that do exist typically show larger interfacial voids and fracture.

It is obvious from the surface profilometry scans and SEM micrographs that significant microscopic changes took place during the engine test. The microstructural evolution begins with the interaction of silicon particles with the piston rings. Here, few of the large silicon particles get fractured, release small fragments and begin to micro abrade the softer phases illustrated in Figure 5-2(b). More importantly, some of the small spherical silicon particles that initially showed signs of interfacial voids after surface preparation (Figure 4-13) become detached from the matrix, begin to abrade the softer phases, and over time break off into smaller fragments that mix with the oil and aluminum debris. Not all small silicon particles are susceptible to removal; some remain exposed and attached to the matrix (Figure 4-22) caused by the micro abrasion process of the aluminum matrix by silicon fragments. Similar to Ni:MR:HT, removal of the matrix by silicon fragments is the reason that silicon particles continue to stand proud from the matrix and why only softer phases exhibited deep scratches parallel to sliding.

As the reciprocating motion of the rings proceeds, silicon particles become smoother, crosshatched scratches on the matrix initially caused by bore preparation are completely removed, and any fine silicon colonies observed on the as-prepared surface

are now indistinguishable due to the mechanical polishing action illustrated in Figure 5-2(c). More importantly, equilibrium surface conditions become more apparent as silicon particles appear to show an increase in relative height from the matrix (i.e. Figure 4-18, Figure 4-19, Figure 4-20, and Figure 4-22) compared to the unworn surface (i.e. Figure 4-11 to Figure 4-13). Large oil deposits can be randomly observed on the surface and contribute to the increased surface roughness as they are not detected by the optical interference surface profilometer. Small valleys caused by silicon particle removal also contribute to the increased roughness; many of which are partially filled with debris and oil deposits. The final surface is comprised of exposed silicon particles and extremely fine silicon fragments that are mixed with fine aluminum debris and oil residue; these features help serve to protect the underlying aluminum grains from further abrasion. The combined action of polishing and deposition of the polishing debris as an irregular tribolayer covering the aluminum matrix results in a "new" running surface where silicon particles act as the primary contact points, and a stable surface is established.

Overall, the varied nickel and copper alloying elements between the Ni:MR:HT and Cu:MR:HT engines did not lead to any significant differences in cylinder wear or engine performance. Regardless of initial composition, both engines evolved to the same final surface microstructure, which consisted of exposed silicon particles, oil deposits, and a tribolayer that protected the underlying aluminum from further abrasion.
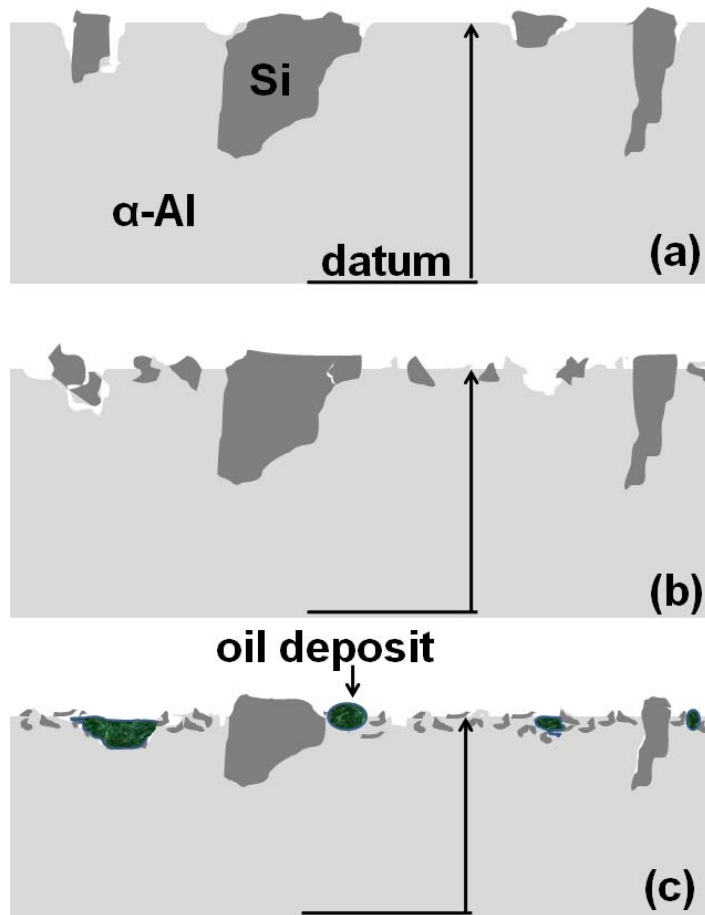
Figure 5-2 Schematic illustrating the mechanism of wear; (a) typical surface damage to Si particles as a result of surface preparation; (b) sharp fragments abrade the softer phases mainly aluminum and expose a fresh aluminum matrix and polish the Si surfaces; (c) surface equilibrium conditions show a matrix that is comprised of fractured particles, aluminum debris, oil deposits, and Si particles with rounded edges, smooth surfaces, and standing above the matrix.

5.3   Effect of Surface Preparation

5.3.1   Ni:CE:HT Wear Progression

The wear mechanisms responsible for obtaining a stable equilibrium surface for the Ni:CE:HT engine after rigorous dynamometer testing can be explained in terms of the changes observed in the aluminum matrix and exposed hard phases separately; but first, an examination from macroscopic bore measurements will set the perspective as to how much wear actually occurred. Macroscopic wear results obtained by measuring the change in bore diameter at key locations (see. §4.3.1.), has indicated that the average change in bore diameter for all the cylinders is 5.24 μm taken at the TRR and 5.56 μm at BRR (see. Table 4-V). Considering the lengthy and severe engine test conditions and the

184

fact that the engine was not previously broken-in, this minor change in diameter is quite remarkable and indicates that the surface must have reached a stable condition which confines wear to low levels.

Before wear even proceeds, the honing stage creates scratches on top of silicon particles and establishes an uneven surface (Figure 4-30). These silicon particles tend to fracture at their edges; and upon chemical etching some of these fractured particles are released from the surface. In addition, spherical silicon particles were observed to resist fracture to a greater degree than high aspect ratio particles. This was demonstrated previously in Figure 4-28 where a rectangular silicon particle was fractured completely through, while the spherical one stayed intact. In addition to exposing silicon, chemical etching also removed any traces of smeared aluminum on top of silicon particles. Here, the fine grained aluminum layer (Figure 4-28) formed during honing is completely removed, leaving only large aluminum grains and some ultra-fine grains beneath the silicon particles. By the end of chemical etching silicon particles are exposed ($R_f \sim 1.09$ μm), establishing a rough surface that easily retains oil between the protruding particles. As a result, during the early stages of break-in the piston rings will be in contact primarily with the exposed particles. As mentioned by Ludema et al. [119] and Wang et al. [104], during break-in oil film pressures will increase as asperity heights decrease. Therefore, at the beginning of engine break-in exposed silicon particles act as the asperities which will support most of the load while the lubricant residing in valleys between the particles will contribute to a lesser degree.

It is obvious from the surface profilometry scans and SEM micrographs previously presented that significant microscopic changes took place as a result of engine testing. The microstructural evolution begins with the interaction of exposed particles with the piston rings. Here, the peaks of uneven silicon particles break off into fragments during sliding and at the same time, some of the larger fragments become embedded into the matrix. In addition, some of the small spherical silicon particles that were only slightly bonded to the aluminum matrix (Figure 4-32) become detached, possibly forming micro-voids, and over time break off into smaller fragments that mix with the oil residing on the surface. This process is physical in nature, thus suggesting that the Si-XII Raman bands observed from worn Si particles (Figure 4-38) are caused by the

fragmentation process. Here, Si particles may transform from the Si-I diamond structure to the S-XII amorphous rhombohedral polymorph. However, the Si-XII Raman band is quite small and the S-I band is still very dominant, even after wear, suggesting that Si transformation is minimal. Another possibility explaining the lack of Si transformation detected could be due to the fact that Si surfaces are acting as the primary contact points with the rings and thus any transformed Si-XII, which would most likely occur at these contact points the near surface, is worn away over time exposing Si-I beneath. This is in agreement with laboratory tests [193] whereby Si transformation was found to occur mainly during the beginning of sliding and decreased as sliding duration increased. However, in an actual engine test it is difficult to precisely identify the cause of the slight transformation in Si with 100% confidence.

As the reciprocating motion of the rings proceeds silicon particles become smoother (Figure 4-36) and decrease in exposure height until equilibrium is attained at approximately $R_f \approx 0.6$ to 0.7 μm. Therefore as R_f decreases, the depth of valleys/gaps between silicon particles decreases proportionally and thus, pressures exerted on the lubricant begin to increase. Eventually, oil deposits begin to form as a result of the extreme temperatures and pressures of the engine [31]. Here, extremely fine silicon fragments (Figure 4-41(f)) and aluminum debris (Figure 4-41(e)) become mixed into the oil and reside in uneven surfaces on the matrix as well as between decoheared particles (Figure 4-40). These oil deposits vary in size and can be easily overlooked; many of which are only observable with high magnification cross-sectional analysis. The fact that oil deposits can form and fill large voids as deep as 2 μm (refer to Figure 4-35 and Figure 4-42) suggests that these deposits could be just as crucial as silicon exposure in protecting and maintaining a wear resistant surface. Filling in voids may prevent the voids from increasing in size while at the same time serving as oil replenishment pathways [170] during over-stressed operating conditions.

A stable silicon exposure height will not only depend on the formation of oil deposits which could act as replenishment pathways and/or a sacrificial material under extreme pressures but, also on how the surrounding matrix interacts with the harder phases. By comparing the subsurface grain structures of the aluminum matrix before (Figure 4-28) and after wear (Figure 4-41 and Figure 4-42), profound differences in the

microstructure are revealed. The 0.8 μm layer of fine grains shown in Figure 4-28 is dissolved during chemical etching leaving only large unaltered grains. In contrast, the worn subsurface (Figure 4-41 and Figure 4-42) is abundant with UFGs and sub-grains even at depths extending ~ 3 μm. Much like the unworn subsurface (Figure 4-28) UFGs surround silicon particles but are now more abundant and coexist with compacted and deformed aluminum (Figure 4-41). These observations suggest that silicon particles are in fact supporting loads beyond the capacity of the aluminum matrix; and thus, in order for the underlying aluminum matrix to support these load bearing particles deformation structures begin to form beneath and around them.

After in-depth surface and subsurface analysis of the worn and unworn regions the general wear mechanism of the cylinder was found to be the end product of three sub-mechanisms based on silicon exposure, oil deposits, and subsurface deformation. During the early stages of the engine test the first wear mechanism emerges at asperities (i.e. exposed silicon particles) with the probability of high contact with the counterface. Over time the exposed silicon particles become smooth and eventually reach an equilibrium exposure height. This final exposure height will be dependent upon the other two sub-mechanisms. Oil deposit formation will help create lubrication pathways during overstressed conditions, while at the same time filling-in voids which were no longer protected by exposed silicon particles. On the other hand, the formation of subsurface deformation structures beneath silicon particles will allow the aluminum-matrix to support the silicon particles during peak loading conditions and thus preventing the particles from sinking-in past the equilibrium exposure level. Therefore, the general wear mechanism which encompasses silicon exposure, oil deposit formation, and subsurface deformation is a form of ultra-mild wear in linerless Al-Si engines and will ultimately control the wear response of the cylinder under overstressed conditions.

5.3.2 Ni:MR:HT vs. Ni:CE:HT

Overall, both the Ni:MR:HT and Ni:CE:HT engines evolved to the same final surface conditions both exhibiting no evidence of excessive wear such as scuffing, gross material transfer, delamination, or pitting after engine testing. Microscopically, both worn surfaces appeared to be the same and supported by qualitative comparisons between Figure 5-3 and Figure 4-6. Here, it is observed that both engine bores contain

microgrooves parallel to sliding and a surface containing oil deposits and fractured Si particles. To the naked eye, the worn Ni:MR:HT bore showed faint signs of ring marks, while the Ni:CE:HT bore did not. The presence of ring marks is partially explained by the fact that the mechanically prepared surface has some smeared aluminum. Smeared aluminum may prevent Si fragments during the initial stages of break-in to be easily removed from in between the ring and liner if trapped. Here, a Si particle is more susceptible to temporarily adhere to the ring and travel back and forth across the liner forming grooves (ring marks) until its release. Smeared aluminum will likely increase adhesive forces between the ring and liner; therefore without it Si particles are more likely to remain on the liner. In addition, the chemically etched surface with a higher initial R_f and R_a will be more likely to trap Si fragments and retain oil during the initial stages of engine break-in. Although ring marks were found on the MR worn surface they are not detrimental to operation of the engine, there is no loss of power or torque, and there was no degradation of oil consumption or blow-by when ring marks are observed.

Ideally, no change in surface roughness between the worn and unworn surfaces of both the Ni:MR:HT and Ni:CE:HT bores would be favorable; suggesting almost no break-in. In reality this is virtually impossible, because engine break-in will always take place due to unavoidable geometrical tolerances between the ring pack and liner. The worn average roughness of Ni:MR:HT ($R_a \approx 0.406$ μm) was virtually identical to Ni:CE:HT. However, The change in R_a of the Ni:MR:HT bore was approximately 3.4 times greater than its unworn surface; suggesting a more significant break-in compared to the Ni:CE:HT bore.

Comparisons of histogram height distributions between the Ni:MR:HT (Figure 4-4) and Ni:CE:HT (Figure 4-34) bores quantitatively support similarities of the worn surface. Both bores show a height distribution with three distinctive peaks. Results from the Ni:CE:HT bore suggest a silicon exposure height of ~0.7 μm from the nominal matrix peak indicating a decrease in R_f of ~0.3 μm from the as-prepared surface. For the Ni:MR:HT bore, which had an initial silicon exposure below the optimal R_f value of $\geq$ 0.6 μm [28], the opposite scenario took place in that the worn surface exhibited an increase in silicon exposure, which produced a final R_f of approximately 0.6 μm. This suggests that silicon exposure can vary to a certain extent without compromising the

development of a wear resistant surface. Once again, note that the Si exposure of the etched bore was reduced by running the engine and that the non-etched bore increased, and that the equilibrium surfaces were virtually identical.

Lastly, the equilibrium surfaces of both Ni:CE:HT and Ni:MR:HT contain exposed silicon particles that are polished with rounded edges and a matrix covered by an irregular tribolayer comprised of a mixture of very fine silicon debris, aluminum debris, and oil deposits. It is this equilibrium surface, with the tribolayer, that is responsible for the low observed wear.
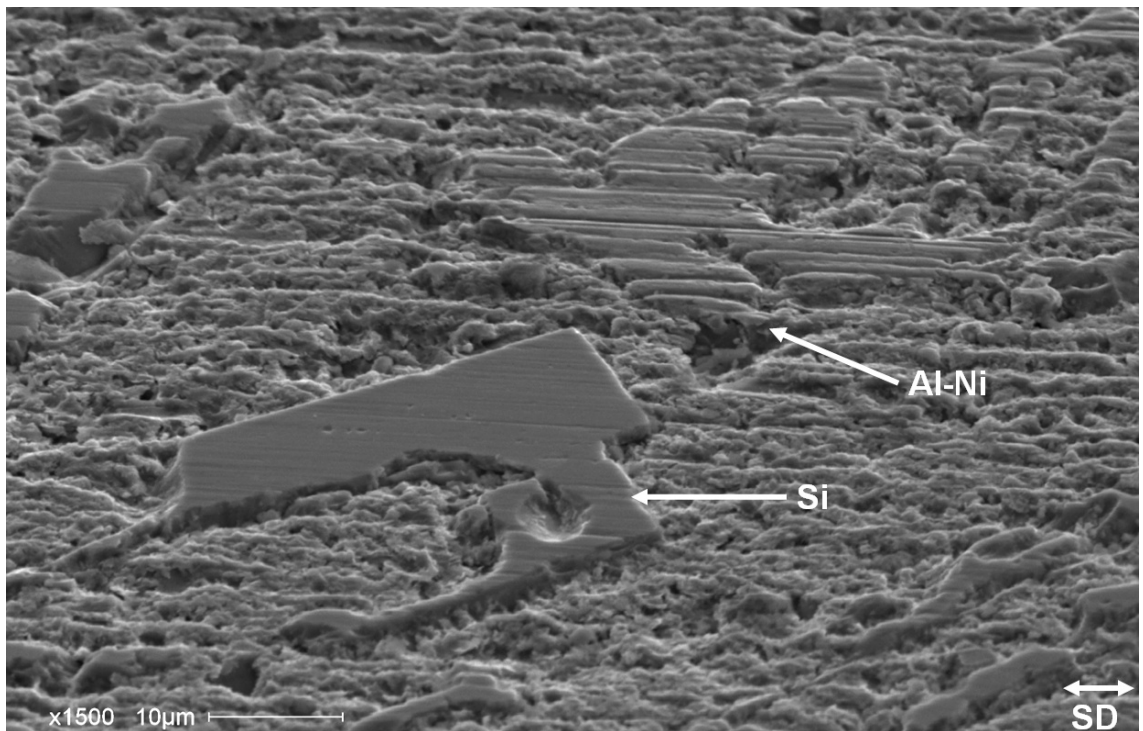
Figure 5-3 SEM micrograph from Ni:CE:HT illustrating grooves parallel to sliding on soft second phases in contrast to harder silicon particles that appear to be smooth with little damage; (60° tilt).

5.4 Effect of Temperature

5.4.1 Cold vs. Hot Engine Comparison

By comparing the cold scuffed (Ni:CE:CS) engine to an identical engine (Ni:CE:HT) subjected to hot scuff and durability testing the influence of temperature and time with respect to engine wear can be addressed. In depth microstructural and chemical investigations of Ni:CE:HT have been previously reported in §5.3.1 and results have shown that no signs of excessive wear took place and that the overall wear resistance was

derived from the combined effects of oil deposits, silicon exposure, and the formation of reduced grain structures in the aluminum-matrix. Key differences between the Ni:CE:CS and Ni:CE:HT engines is summarized in Table 5-I below. A comparison between hot engine testing and cold engine testing has been previously presented in §3.2 but tabulated here for ease of comparison.

Table 5-I Summary and comparison of engine parameters before and after wear between the Ni:CE:CS and Ni:CE:HT major faces.

	Ni:CE:CS	Ni:CE:HT
Scuff test	~ 3 hr	~ 3 hr
Oil cons. test	0 hr	~ 10 hr
Durability test	0 hr	~ 247 hr
Max oil temp.	65 °C	150 °C
Surface prep.	MR & CE	MR & CE
Initial Si exposure (R_f)	1.23 μm	1.09 μm
Surface roughness (R_a)	0.76 μm	0.33 μm
------------------------------------ ***After Wear*** ------------------------------------		
Visual appearance	Lustrous metallic	Grey matted
Final Si exposure (R_f)	0 μm	~0.6 to 0.7 μm
Observable oil deposits	No	Yes
Scuff marks	Yes	No
Observable Si microstructure	No	Yes

Although Ni:CE:HT was subjected to longer test durations the wear and appearance of the entire bore showed no signs of scuffing with slight signs of ring marks only at the TDC and BDC of the cylinder. In addition, wear and appearance of all four faces of the cylinder were identical. More importantly, silicon exposure and microstructure was maintained throughout testing while the aluminum-matrix was protected by a discontinuous tribolayer. A typical SEM micrograph taken from the major face of Ni:CE:HT is presented in Figure 5-3 for comparison to Figure 4-53. The most significant difference between Figure 5-3 and Figure 4-53 is the loss of microstructure in the Ni:CE:CS engine and the highly deformed/flattened aluminum-matrix. Evidence of spalling and large grooves parallel to sliding is readily apparent on the Ni:CE:CS matrix; however, Ni:CE:HT shows no signs of matrix flattening and spalling, only fine micro-grooves within the tribolayer are formed. Furthermore, in Ni:CE:HT large silicon particles are intact and exposed. However, small spherical silicon particles are not easily observed as they blend in with the surrounding features.

X-ray photoelectron spectroscopy results comparing the two engines are summarized in Table 5-II. XPS results from Ni:CE:HT has been previously presented in §4.3.3 but presented here again for ease of comparison. Before argon ion etching the chemical composition of the surface does not differ significantly. However, after removing any contaminants from the surface via etching significant differences between the two engines can be observed. Both the major and font faces of the Ni:CE:CS engine show a significant increase in Al and O, with a slight increase in Si compared to Ni:CE:HT. This increase in Al and O is in agreement with the smeared/deformed aluminum observed on the Ni:CE:CS bore presented in §4.4. Conversely, Ni:CE:HT shows a significant increase in C, Ca, and Na most likely a result of the combustion products and the abundance of oil deposits. Comparison between the Ni:CE:CS major and front faces also reveals that the major face contains no traces of Zn and S, which are common elements found in oil deposits. This is in agreement with the microstructural observations in §4.4, wherein no oil deposits were found on the major face and close to none were observed on the front face.

In summary, the vital difference between the Ni:CE:CS and Ni:CE:HT worn surfaces is the abundance of oil deposits which have formed on the surface of Ni:CE:HT due to the high operating temperatures which promote chemical interactions to occur between the surface and oil additives. Here, the aluminum-matrix protected by a discontinuous tribolayer could alleviate some load off from silicon particles without smearing/deforming, thus, helping to maintain silicon exposure. On the contrary, the Ni:CE:CS surface could not sustain the formation of oil deposits; and thus, aluminum-rich areas were left unprotected which resulted in deformation to the matrix. New lubricants specifically designed for aluminum surfaces capable of producing oil deposits at low and high temperatures would be a best case solution to increase wear resistance, but extremely difficult. More plausible alternatives would be to consider piston ring coatings which can prevent direct metal-to-metal contact, maintaining low adhesive forces even under starved lubrication conditions.

Table 5-II XPS semi-quantitative elemental composition of Ni:CE:HT and Ni:CE:CS worn surfaces, atomic %, except H

	C	O	Al	Si	Ca	N	Zn	S	P	Na	Other
Surface:											
Ni:CE:HT major	50	33	5	5	1.7	3	0.1	0.7	0.3	1.1	Cl,Mg,F
Ni:CE:CS major	53	31	5	4	0.3	4	0.3	0.5	0.2	0.9	Cl,F,Cu,Fe,K
Ni:CE:CS front	55	32	5	2.6	0.2	2.7	0.6	0.4	-----	0.3	Cl
~ 10 nm etch:											
Ni:CE:HT major	46	33	6	6	1.9	2.8	0.1	0.6	0.7	2.2	Cl, Mg
Ni:CE:CS major	12	51	21	10	0.6	1.8	-----	-----	0.7	0.8	Cu,Cl,Mg,K,F,Fe
Ni:CE:CS front	20	44	19	9	0.6	2.1	0.4	0.4	-----	0.7	Cu,Ni,Cl,Mg

5.4.2   Cold Scuff Wear Progression

From the results obtained in §4.4, suggestions as to how wear progressed in the cold scuffed engine can be made. Before wear even transpires, the as-prepared surface was shown to contain some surface flaws even though silicon particles were left protruding from the matrix. A significant number of silicon particles were fractured (Figure 4-48) and also displayed signs of over-etching, whereby a high dissolution of the matrix was observed around the perimeters of silicon particles (Figure 4-47). These voids produced around silicon particles leaves them more susceptible to root fracture without increasing R_f. Both the Ni:CE:CS and Ni:CE:HT cylinder bore surfaces were prepared by the same techniques. Engine Ni:CE:HT did display signs of particle fracture and etch pits, but not to the same extent as the :Ni:CE:CS surface. The large difference in R_a and R_f (see. Table 5-I) between the two engines does suggest that the Ni:CE:CS surface was possibly over-etched, which could have compromised the scuffing resistance during the early stages of break-in.

It is obvious from the surface profilometry scans and SEM micrographs previously presented that significant microscopic changes took place as a result of engine testing. The microstructural changes begin with the interaction of the highest asperities

with the piston rings. Observations from the worn front face, which is not scuffed, suggests that the early stages of wear proceeds first by the sinking-in and fracturing of exposed silicon particles (Figure 4-62(a)); similar observations were reported in laboratory tests by Chen et al. [23, 143]. Here, large silicon particles begin to fracture while smaller spherical particles and fragments become embedded into the matrix (Figure 4-62(c)). In this stage, silicon exposure is decreasing and the highest asperities, which now include some aluminum rich areas, come in contact with the counterface. Overall the original microstructure is intact with the exception of sunk-in fractured particles and flattened asperities.

As loads are increased, as in the major face, wear progresses to the next step which is more severe and delineated by two distinct regions pertaining to ring marks and scuff marks. Overall, the wear and appearance of the ring mark region is less severe than the scuff mark region. Both areas do not show any signs of the original microstructure. In the ring mark region, wear continues by completely fracturing all large silicon particles leaving only smaller fragments and cavities (Figure 4-57). Here, the bore surface continues to flatten but not completely due to silicon fragments which need to be further worked into the matrix. As asperities become flattened the ability of oil retention decreases and adhesion forces between the counterface and cylinder increase. With this in mind, the clearance between the piston rings and cylinder is also decreasing, thus, allowing for some of the sharp silicon fragments to become trapped between the two surfaces creating grooves parallel to sliding (Figure 4-57).

As asperities continue to flatten, adhesion and material transfer between the sliding surfaces increases to a point where scuffing can thrive; suggesting that the ring mark region could be a precursor to scuffing. By comparing the ring mark region (Figure 4-57) to the scuff mark region (Figure 4-53) it is obvious that the dominant wear mechanisms in each area are different. The fact that the scuffed surface is completely flattened with deformed aluminum covering fragmented silicon particles suggests that adhesive forces are high. Here, wear progresses by deformation of the aluminum which leads to spalling and most likely material transfer to the counterface (Figure 4-53). The transfer of highly deformed material to the piston rings could produce large hard asperities which scrape against the cylinder accounting for the large grooves observed in Figure 4-53. A

combination of this mechanism and spalling within the groove is also a viable alternative for large groove formation.

6   SUMMARY AND CONCLUSIONS

Wear Mechanism (Hot Testing)

After rigorous hot dynamometer testing, linerless Al-Si engines were shown to exhibit no evidence of excessive wear. Using an array of surface and subsurface techniques, comparisons of the engine cylinders before and after wear has yielded the following conclusions:

1) The evolution of the bore microstructure is explained in terms of fragmentation of silicon particles and subsequent "polishing" of the entire worn surface caused by sliding contact with the rings.

2) The overall wear resistance of linerless eutectic Al-Si engine bores is derived from the *combined* effects of oil deposits, silicon exposure, and the formation of reduced grain structures in the aluminum-matrix.

3) After engine break-in an equilibrium silicon exposure height of ~ 0.4 to 0.6 μm was established. Small silicon colonies were not distinguishable on the worn surface; in contrast, larger needle-like particles were intact with surfaces smooth and free from damage. The preservation of silicon exposure minimizes direct metal-to-metal contact between the piston rings and aluminum-matrix while at the same time maintaining a surface roughness that can retain the lubricant.

4) Oil deposits have formed during engine testing and were abundant on the worn surface. Oil deposits were shown to exist in various textures and sizes. These amorphous structures were found to consist primarily of P, S, Zn, Ca, C, and O; as well as nano-sized aluminum and silicon debris.

5) Wear induced ultra-fine grains and sub-grains were formed in the aluminum-matrix. Plastically deformed regions of aluminum residing beneath silicon particles suggest that the silicon particles do support a significant portion of the load and that the aluminum-matrix deforms to accommodate these pressures. The

same degree of deformation was not observed underneath oil deposits or at silicon free regions of the matrix.

Effect of Alloying

Two similar hot tested linerless Al-Si engines with variations in chemical composition (i.e. nickel and copper) have been examined in detail with respect to the effect of alloying on cylinder bore wear progression. Conclusions derived from this effort are presented below:

1) Both engines contained a mixed microstructure containing silicon needles and fine spherical silicon particles. Overall, the copper alloyed engine contained a finer silicon microstructure likely caused by the differences in chemical composition.

2) Overall, the variation in chemical composition did not lead to any significant differences in cylinder wear or engine performance. Both engines evolved to the same final surface microstructure, which consisted of exposed silicon particles, oil deposits, and a tribolayer that protected the underlying aluminum from further abrasion.

3) Both engines exhibited identical wear mechanisms and can be explained in terms of fragmented silicon particles that "polish" the entire worn surface, which help form an irregular tribolayer, and maintain silicon exposure.

Effect of Surface Preparation

To study the effect of cylinder bore surface preparation a two cylinder bores, one mechanically reduced and the other chemically etched, originating from the same tested engine block were analyzed with respect to cylinder bore microstructural evolution. Conclusions comparing these engines are presented here:

1) Both the chemically etched and mechanically reduced engine bores have shown no evidence of excessive wear such as scuffing, gross material transfer, delamination, or pitting after engine testing.

2) To the naked eye, the worn mechanically reduced bore showed faint signs of ring marks, while the chemically etched bore did not. Microscopically, both worn surfaces appeared to be the same. The presence of ring marks is partially explained by the fact that the mechanically prepared surface has some smeared aluminum, which causes ring marks during break-in, these marks persist (although diminished in severity) even in the equilibrium surface; etching removes all smeared aluminum. The ring marks are not detrimental to operation of the engine, there is no loss of power or torque, and there was no degradation of oil consumption or blow-by when ring marks are observed.

3) The initial chemically etched silicon exposure of 1.1 μm was reduced to 0.7 μm after 260 hrs of rigorous testing resulting in a stable surface virtually identical to a non-etched bore with initial silicon exposure of 0.2 μm and final exposure of ~0.6 μm. This suggests that silicon exposure can vary to a certain extent without compromising the development of a wear resistant surface. Once again, note that the silicon exposure of the etched bore was reduced by running the engine and that the non-etched bore increased, and that the equilibrium surfaces were virtually identical.

4) The equilibrium surfaces of both the chemically etched and mechanically reduced engine bores contain exposed silicon particles that are polished with rounded edges and a matrix covered by an irregular tribolayer comprised of a mixture of very fine silicon debris, aluminum debris, and oil deposits. It is this equilibrium surface, with the tribolayer, that is responsible for the low observed wear.

Cold Scuff Wear Progression and the Effect of Temperature

Microstructural characterization of a linerless Al-Si engine subjected to cold scuff dynamometer engine testing has been performed and compared to a similar engine subjected to hot scuff and durability testing. The main conclusions are as follows:

1) In comparison to the hot run engine, the lack of wear resistance exhibited in the cold scuffed engine was ultimately a consequence of the low operating

temperatures which prevented the formation of protective oil deposits on the cylinder surface.

2)   The unworn cold scuff surface contains silicon particles that were fractured and exposed from the matrix. A possibility of over-etching has occurred, leaving large voids around silicon particles making them more susceptible to root fracture, without increasing silicon exposure from the aluminum-matrix. However, compared to the large temperature difference between the two engines the slight difference between the unworn surfaces is negligible.

3)   Wear progressed in the cold scuff engine by the following sequence: i) silicon particles begin to fracture and sink-in, becoming level with the matrix; ii) high aluminum asperities begin to flatten/deform from contact with the counterface; iii) all large silicon particles on the surface completely fracture leaving only small fragments and cavities; iv) grooves form parallel to sliding; v) deformed aluminum completely covers silicon fragments leaving a flat surface; and vi) increased adhesion initiates scuffing which involves spalling, possible material transfer, and the formation of large grooves parallel to sliding.

Summary

The work presented in this thesis has shown that near-eutectic linerless Al-Si engines do not yet have the complete capability of replacing cast-iron cylinder liners in production vehicles. However, the product of this research has provided insight into the wear mechanisms of linerless eutectic Al-Si engines. Moreover, a design criterion specifically for linerless eutectic Al-Si engines has been developed, which states that low cylinder wear rates can be maintained by the combined effects of oil deposits, silicon exposure, and the formation of reduced grain structures in the aluminum-matrix.

Suggestions for Future Research

The current research suggests that the most advantageous linerless Al-Si cylinder design criteria involves one in which the long term wear resistance is derived from the combined results of oil deposits, silicon exposure, and the formation of reduced grain structures in the aluminum-matrix. However, due to the complicated tribosystem of a combustion chamber complete understanding of this system is far from absolute. Realization of the production of affordable robust linerless Al-Si engines can be achieved by future research in the following areas:

1)   In depth microstructural and chemical examination of the counterface; this includes the entire piston along with the ring pack. These results would coincide with the current research and provide more complete insight into the mechanisms of Al-Si cylinder wear.

2)   Determine the critical/lowest temperature, if any, at which a stable equilibrium surface can be attained. This can be accomplished by numerous separate dynamometer tests each set at different operating temperature ranges.

3)   Evaluate the performance of a fully developed equilibrium surface by subjecting it to cold scuff dynamometer testing. If the engine survives the testing procedure it will be certain that the development of an equilibrium surface is crucial for long term wear resistance in linerless Al-Si engines.

4)   Determine the optimal silicon exposure specifically for near-eutectic Al-Si engines that produces the least amount of wear and micro-abrasion. This can be accomplished by testing a single engine containing different silicon exposures in each cylinder.

REFERENCES

1. Tung, S.C. and M.L. McMillan, *Automotive tribology overview of current advances and challenges for the future.* Tribology International, 2004. **37**(7): p. 517-536.
2. Subramanian, C., *Some considerations towards the design of a wear resistant aluminium alloy.* Wear, 1992. **155**(1): p. 193-205.
3. Caceres, C.H., I.L. Svensson, and J.A. Taylor, *Strength-Ductility Behaviour of Al-Si-Cu-Mg Casting Alloys in T6 Temper.* International Journal of Cast Metals Research (UK), 2003. **15**(5): p. 531-543.
4. Moustafa, M.A., et al., *Metallographic observations on phase precipitation in strontium-modified Al-11.7% Si alloys: Role of alloying elements.* International Journal of Cast Metals Research (UK), 2003. **15**(6): p. 609-626.
5. Hwang, J.Y., H.W. Doty, and M.J. Kaufman, *The effects of Mn additions on the microstructure and mechanical properties of Al-Si-Cu casting alloys.* Materials Science and Engineering: A, 2008. **488**(1-2): p. 496-504.
6. Li, Z., et al., *Parameters controlling the performance of AA319-type alloys: Part I. Tensile properties.* Materials Science and Engineering A, 2004. **367**(1-2): p. 96-110.
7. Zhang, J. and A.T. Alpas, *Delamination wear in ductile materials containing second phase particles.* Materials Science and Engineering: A, 1993. **160**(1): p. 25-35.
8. Zhang, J. and A.T. Alpas, *Transition between mild and severe wear in aluminium alloys.* Acta Materialia, 1997. **45**(2): p. 513-528.
9. Sarkar, A.D., *Wear of aluminium-silicon alloys.* Wear, 1975. **31**(2): p. 331-343.
10. Clarke, J. and A.D. Sarkar, *Wear characteristics of as-cast binary aluminium-silicon alloys.* Wear, 1979. **54**(1): p. 7-16.
11. Bin, F. and G.S. Cole, *Scuffing Resistance of Selected Materials as Protection for Bores in Aluminum Engine Blocks.* SAE Int., 1992. **920285**.
12. Noorman, M.T., et al., *Overview of Techniques for Measuring Friction Using Bench Tests and Fired Engines.* SAE Int., 2000. **2000-01-1780**.
13. Bai, B.N.P., S.K. Biswas, and N.N. Kumtekar, *Scanning electron microscopy study of worn Al-Si alloy surfaces.* Wear, 1983. **87**(3): p. 237-249.
14. Elmadagli, M. and A.T. Alpas, *Progression of wear in the mild wear regime of an Al-18.5% Si (A390) alloy.* Wear, 2006. **261**(3-4): p. 367-381.
15. Shivanath, R., P.K. Sengupta, and T.S. Eyre, *Wear of aluminum--silicon alloys.* The British Foundryman, 1977. **70**: p. 349-356.
16. Dienwiebel, M., K. Pöhlmann, and M. Scherge, *Origins of the wear resistance of AlSi cylinder bore surfaces studies by surface analytical tools.* Tribology International, 2007. **40**(10-12): p. 1597-1602.
17. Kurita, H., et al., *Hypereutectic Al-20%Si Alloy Engine Block Using High-Pressure Die-Casting.* SAE Int., 2004. **2004-01-1028**.
18. Slattery, B.E., T. Perry, and A. Edrisy, *Microstructural evolution of a eutectic Al-Si engine subjected to severe running conditions.* Materials Science and Engineering: A, 2009. **512**(1-2): p. 76-81.
19. Tash, M., et al., *Effect of metallurgical parameters on the hardness and microstructural characterization of as-cast and heat-treated 356 and 319 aluminum alloys.* Materials Science and Engineering: A, 2007. **443**(1-2): p. 185-201.
20. Riahi, A.R., T. Perry, and A.T. Alpas, *Scuffing resistances of Al-Si alloys: effects of etching condition, surface roughness and particle morphology.* Materials Science and Engineering A, 2003. **343**(1-2): p. 76-81.
21. Chen, M. and A.T. Alpas, *Ultra-mild wear of a hypereutectic Al-18.5 wt.% Si alloy.* Wear, 2008. **265**(1-2): p. 186-195.

22. Chen, M., et al., *Micromechanisms and mechanics of ultra-mild wear in Al-Si alloys.* Acta Materialia. **In Press, Corrected Proof**.

23. Chen, M., T. Perry, and A.T. Alpas, *Ultra-mild wear in eutectic Al-Si alloys.* Wear, 2007. **263**(1-6): p. 552-561.

24. Green, R.E., *Die Casting the Vega Engine Block.* Die Casting Engineer, 1970. **14**: p. 12-26.

25. Jorstad, J.L., *The Hypereutectic Aluminum-Silicon Alloy Used to Cast the Vega Engine Block.* Modern Casting, 1971. **60**: p. 59-64.

26. Donahue, R. and P.A. Fabiyi, *Manufacturing Feasibility of All-Aluminum Automotive Engines Via Application of High Silicon Aluminum Alloy.* SAE Int., 2000. **00M-89**: p. 1-10.

27. Köhler, E. and J. Niehues, *Aluminum-matrix composite materials in combustion engines*, in *Metal Matrix Composites Custom-made Materials for Automotive and Aerospace Engineering*, K.U. Kainer, Editor. 2006, Wiley-VCH: Weinheim. p. 95-108.

28. Krug, P., M. Kennedy, and J. Foss, *New Aluminum Alloys for Cylinder Liner Applications* SAE Int., 2006. **2006-01-0983**.

29. Ye, H., *An overview of the development of Al-Si-Alloy based material for engine applications.* Journal of Materials Engineering and Performance, 2003. **12**(3): p. 288-297.

30. Schneider, E.W. and D.H. Blossfeld, *Effect of break-in and operating conditions on piston ring and cylinder bore wear in spark ignition engines.* SAE Int., 2004. **2004-01-2917**.

31. Stachowiak, G.W. and A.W. Batchelor, *Engineering Tribology*. 3 ed. 2005, Burlington, MA: Elsevier. 801.

32. Blau, P.J., *Friction and Wear Transitions of Materials: Break-in, Run-in, Wear-in*. 1 ed. 1989, Park Ridge, New Jersey, U.S.A.: Noyes Publications 476.

33. Dowson, D., *History of Tribology*. 1979, United Kingdom: Longman Group 700.

34. Ludema, K.C., *Introduction to Wear*, in *ASM Handbook Friction, Lubrication, and Wear Technology*, P.J. Blau, Editor. 1992, ASM International. p. 320.

35. Hutchings, I.M., *Surface topography and surfaces in contact*, in *Friction and Wear of Engineering Materials*. 1992, CRC Press: Florida, U.S.A. p. 5-21.

36. Zum Gahr, K.-H., *Microstructure and Wear of Materials*. Tribology Series. 1987: Elsevier Publishing Company. 560.

37. Bowden, F.P. and D. Tabor, *The Friction and Lubrication of Solids*. 1986, New York: Oxford University Press.

38. Hertz, H., *On the contact of elastic solids*, in *Miscellaneous Papers*, H. Hertz, Editor. 1896, Macmillan. p. 146–162.

39. Greenwood, J.A. and J.B.P. Williamson, *The contact of nominally flat surfaces.* Proceedings of the Royal Society of London 1966. **A295**: p. 300-319.

40. ASTM, *Standard Terminology Relating to Erosion and Wear*, S. G-40-83, Editor, ASTM: Philadephia, PA.

41. Amontons, G., *On the resistance originating in machines, [in French]*. Mem. Acad. Roy. Sci., 1699: p. 206–222.

42. Sethuramiah, A., *Lubricated Wear Science and Technology*. Tribology Series, ed. D. Dowson. 2003, Amsterdam: Elsevier.

43. Hutchings, I.M., *Friction*, in *Friction and Wear of Engineering Materials*. 1992, CRC Press: Florida, U.S.A. p. 22-57.

44. Rabinowicz, E., *Friction and Wear of Materials*. 1 ed. 1965, New York: John Wiley. 244.

45. Archard, J.F., *Wear Theory and Mechanisms*, in *Wear Control handbook*, M.B. Peterson and W.O. Winer, Editors. 1980, ASME: New York. p. 35-80.

201

46. Kimura, Y., *The Role of Fatigue on Sliding Wear*, in *Fundamentals of Friction and Wear of Materials*, D.A. Rigney, Editor. 1981, ASM: Ohio. p. 187-217.

47. Moore, M.A., *Abrasive Wear*, in *Fundamentals of Friction and Wear of Materials*, D.A. Rigney, Editor. 1981, ASM: Ohio. p. 73-111.

48. Rosenfield, A.R., *Wear and Fracture Mechanics*, in *Fundamentals of Friction and Wear of Materials*, D.A. Rigney, Editor. 1981, ASM: Ohio. p. 221-232.

49. Samuels, L.E., E.D. Doyle, and D.M. Turley, *Sliding Wear Mechanisms*, in *Fundamentals of Friction and Wear of Materials*, D.A. Rigney, Editor. 1981, ASM: Ohio. p. 13-41.

50. Suh, N.P., *Update on the Delamination Theory of Wear*, in *Fundamentals of Friction and Wear of Materials*, D.A. Rigney, Editor. 1981, ASM: Ohio. p. 43-68.

51. Eyre, T.S., *The mechanisms of wear.* Tribology International, 1978. **11**(2): p. 91-96.

52. Scherge, M., D. Shakhvorostov, and K. Pöhlmann, *Fundamental wear mechanism of metals.* Wear, 2003. **255**(1-6): p. 395-400.

53. Rigney, D.A., *Comments on the sliding wear of metals.* Tribology International, 1997. **30**(5): p. 361-367.

54. Quinn, T.F.J., *The Classifications, laws, Mechanisms and Theories of Wear*, in *Fundamentals of Tribology*, N.P. Suh and N. Saka, Editors. 1980, The MIT Press: Cambridge, Massachusetts. p. 477-492.

55. Rice, S.L., *A Review of Wear Mechanisms and Related Topics*, in *Fundamentals of Tribology*, N.P. Suh and N. Saka, Editors. 1980, The MIT Press: Cambridge, Massachusetts. p. 469-476.

56. Archard, J.F. and W. Hirst, *The Wear of Metals under Unlubricated Conditions.* The Royal Society, 1956. **236**(1206): p. 397-410.

57. Eyre, T.S., *Abrasive wear.* Tribology International, 1978. **11**(1): p. 4-5.

58. Hammitt, F., *Cavitation and Liquid Impact Erosion*, in *Wear Control handbook*, M.B. Peterson and W.O. Winer, Editors. 1980, ASME: New York. p. 161-230.

59. Lim, S.C. and M.F. Ashby, *Wear-Mechanism Maps.* Acta Materialia, 1987. **35**(1): p. 1-24.

60. Kato, K., *Classification of Wear Mechanisms/Models*, in *Wear: Materials, Mechanisms and Practice*, G.W. Stachowiak, Editor. 2005, John Wiley & Sons, Ltd: West Sussex, England. p. 9-20.

61. Sproles, E.S., D.J. Gaul, and D.J. Duquette, *A New Interpretation of the Mechanism of Fretting and Fretting Corrosion Damage*, in *Fundamentals of Tribology*, N.P. Suh and N. Saka, Editors. 1980, The MIT Press: Cambridge, Massachusetts. p. 585-596.

62. Hutchings, I.M., *Sliding Wear*, in *Friction and Wear of Engineering Materials*. 1992, CRC Press: Florida, U.S.A. p. 77-109.

63. Rigney, D.A. and J.P. Hirth, *Plastic deformation and sliding friction of metals.* Wear, 1979. **53**(2): p. 345-370.

64. Heilmann, P., et al., *Sliding wear and transfer.* Wear, 1983. **91**(2): p. 171-190.

65. Ludema, K.C., *Sliding and Adhesive Wear*, in *ASM Handbook Friction, Lubrication, and Wear Technology*, P.J. Blau, Editor. 1992, ASM International. p. 436-449.

66. Rigney, D.A., et al., *Wear processes in sliding systems.* Wear, 1984. **100**(1-3): p. 195-219.

67. Dautzenberg, J.H. and J.H. Zaat, *Quantitative determination of deformation by sliding wear.* Wear, 1973. **23**(1): p. 9-19.

68. Bayer, R.G., *Prediction of wear in a sliding system.* Wear, 1968. **11**(5): p. 319-332.

69. Lim, S.C., M.F. Ashby, and J.H. Brunton, *Wear-rate transitions and their relationship to wear mechanisms.* Acta Metallurgica, 1987. **35**(6): p. 1343-1348.

70. Blok, H., *The flash temperature concept.* Wear, 1963. **6**(6): p. 483-494.

71. Archard, J.F., *The temperature of rubbing surfaces.* Wear, 1959. **2**(6): p. 438-455.

72.   Abbott, E.J. and F.A. Firestone, *Specifying surface quality: a method based on accurate measurement and comparison.* Mechanical Engineering, 1933. **55**: p. 569-572.

73.   Blau, P.J., *On the nature of running-in.* Tribology International, 2006. **38**(11-12): p. 1007-1012.

74.   Sreenath, A.V. and N. Raman, *Mechanism of smoothing of cylinder liner surface during running-in.* Tribology International, 1976. **9**(2): p. 55-62.

75.   Rainforth, W.M., *Microstructural evolution at the worn surface: a comparison of metals and ceramics.* Wear, 2000. **245**(1-2): p. 162-177.

76.   Rainforth, W.M., et al., *Microstructural changes induced by wear*, in *Tribology Series*. 2002, Elsevier. p. 273-282.

77.   Rainforth, W.M., et al., *High resolution observations of friction-induced oxide and its interaction with the worn surface.* Tribology International, 2002. **35**(11): p. 731-748.

78.   Rigney, D.A., R. Divakar, and S.M. Kuo, *Deformation substructures associated with very large plastic strains.* Scripta Metallurgica et Materialia, 1992. **27**(8): p. 975-980.

79.   Rigney, D.A., et al., *Low energy dislocation structures caused by sliding and by particle impact.* Materials Science and Engineering, 1986. **81**: p. 409-425.

80.   Alpas, A.T., H. Hu, and J. Zhang, *Plastic deformation and damage accumulation below the worn surfaces.* Wear, 1993. **162-164**(Part 1): p. 188-195.

81.   Heilmann, P., W.A.T. Clark, and D.A. Rigney, *Orientation determination of subsurface cells generated by sliding.* Acta Metallurgica, 1983. **31**(8): p. 1293-1305.

82.   Bower, A.F. and K.L. Johnson, *The influence of strain hardening on cumulative plastic deformation in rolling and sliding line contact.* Journal of the Mechanics and Physics of Solids, 1989. **37**(4): p. 471-493.

83.   Kuhlmann-Wilsdorf, D., *Dislocation Concepts in Friction and Wear*, in *Fundamentals of Friction and Wear of Materials*, D.A. Rigney, Editor. 1981, ASM: Ohio. p. 119-186.

84.   Kuhlmann-Wilsdorf, D., *Fundamentals of cell and subgrain structures in historical perspective.* Scripta Metallurgica et Materialia, 1992. **27**(8): p. 951-956.

85.   Moore, M.A. and R.M. Douthwaite, *Plastic Deformation Below Worn Surfaces.* Metallurgical Transactions A, 1976. **7A**: p. 1833-1839.

86.   Wert, J.J., *The Role of Microstructure in Subsurface damage Induced by Sliding Contact*, in *Role of Subsurface Zones in the Wear of Materials*, R. Solecki, Editor. 1988, Trans Tech Publications. p. 101-134.

87.   Ruff, A.W., L.K. Ives, and W.A. Glaeser, *Characterization of Wear Surfaces and Wear Debris*, in *Fundamentals of Friction and Wear of Materials*, D.A. Rigney, Editor. 1981, ASM: Ohio. p. 235-284.

88.   Humphreys, F.J., et al., *Developing stable fine-grain microstructures by large strain deformation.* Philosophical Transactions of The Royal Society of London A, 1999. **357**(1756): p. 1663-1681.

89.   Rigney, D.A. and W.A. Glaeser, *The significance of near surface microstructure in the wear process.* Wear, 1978. **46**(1): p. 241-250.

90.   Ganapathi, S.K. and D.A. Rigney, *An HREM study of the nanocrystalline material produced by sliding wear processes.* Scripta Metallurgica et Materialia, 1990. **24**(9): p. 1675-1678.

91.   Shakhvorostov, D., et al., *Microstructure of tribologically induced nanolayers produced at ultra-low wear rates.* Wear, 2007. **263**(7-12): p. 1259-1265.

92.   Shakhvorostov, D., K. Pöhlmann, and M. Scherge, *Structure and mechanical properties of tribologically induced nanolayers.* Wear, 2006. **260**(4-5): p. 433-437.

93.   Kapoor, A. and F.J. Franklin, *Tribological layers and the wear of ductile materials.* Wear, 2000. **245**(1-2): p. 204-215.

94. Rice, S.L., H. Nowotny, and S.F. Wayne, *A Survey of the Development of Subsurface Zones in the Wear of Materials*, in *Role of Subsurface Zones in the Wear of Materials*, R. Solecki, Editor. 1988, Trans Tech Publications. p. 77-100.

95. Rigney, D.A., *Transfer, mixing and associated chemical and mechanical processes during the sliding of ductile materials.* Wear, 2000. **245**(1-2): p. 1-9.

96. Bay, B., N. Hansen, and D. Kuhlmann-Wilsdorf, *Deformation structures in lightly rolled pure aluminium.* Materials Science and Engineering: A, 1989. **113**: p. 385-397.

97. Hansen, N., *Cold deformation microstructures.* Materials Science and Technology, 1990. **6**: p. 1039–1047.

98. Hutchings, I.M., *Lubricants and Lubrication*, in *Friction and Wear of Engineering Materials*. 1992, CRC Press: Florida, U.S.A. p. 58-76.

99. Pawlak, Z., *Tribochemistry of Lubricating Oils*. Tribology and Interface Engineering Series, ed. B.J. Briscoe. 2003, Amsterdam: Elsevier B.V. 368.

100. Yu, H., *Tribological failure analyses of automotive engine blocks subjected to sliding wear damage*, in *Materials Engineering*. 2006, University of Windsor: Windsor, Canada.

101. Yamagata, H., *The science and technology of materials in automotive engines*. 2005, Boca Raton: CRC Press. 331.

102. Golloch, R., et al., *Functional Properties of Microstructured Cylinder Liner Surfaces for Internal Combustion Engines.* TriboTest, 2005. **11**(4): p. 307-324.

103. Taylor, B.J. and T.S. Eyre, *A review of piston ring and cylinder liner materials.* Tribology International, 1979. **12**(2): p. 79-89.

104. Wang, Y., et al., *Scuffing resistance of coated piston skirts run against cylinder bores.* Wear, 2005. **259**(7-12): p. 1041-1047.

105. Eyre, T.S., *Wear characteristics of castings used in internal-combustion engines.* Metals Technology, 1984. **11**(3): p. 81-90.

106. Schmid, J., *Metallic composite materials for cylinders surfaces of combustion engines and their finishing by honing*, in *Metal Matrix Composites Custom-made Materials for Automotive and Aerospace Engineering*, K.U. Kainer, Editor. 2006, Wiley-VCH: Weinheim. p. 215-229.

107. Elmadagli, M., *Microstructural studies of wear mechanisms in cast aluminum alloys*, in *Materials Engineering*. 2005, University of Windsor: Windsor, Canada. p. 1-23.

108. KS-Aluminium-Technologie-GmbH. *Low-pressure Die Cast Cylinder Blocks*. 2008 [cited 2008 Nov. 3, 08]; Available from: www.kolbenschmidt-pierburg.com.

109. Edrisy, A., T. Perry, and A.T. Alpas, *Investigation of scuffing damage in aluminum engines with thermal spray coatings.* Wear, 2005. **259**(7-12): p. 1056-1062.

110. KS-Aluminium-Technologie-GmbH. *High-pressure Die Cast Cylinder Blocks*. 2008 [cited 2008 Nov. 3, 08]; Available from: www.kolbenschmidt-pierburg.com.

111. Fursund, K., *Wear in cylinder liners.* Wear, 1957. **1**(2): p. 104-118.

112. Ye, Z., et al., *An experimental investigation of piston skirt scuffing: a piston scuffing apparatus, experiments, and scuffing mechanism analyses.* Wear, 2004. **257**(1-2): p. 8-31.

113. Eyre, T.S., K.K. Dutta, and F.A. Davis, *Characterization and simulation of wear occurring in the cylinder bore of the internal combustion engine.* Tribology International, 1990. **23**(1): p. 11-16.

114. Wang, H., *Wear and scuffing resistances of eutectic Al-Si alloys and Al-Si based composites*, in *Materials Engineering*. 2005, University of Windsor: Windsor, Canada.

115. Wang, Y. and S.C. Tung, *Scuffing and wear behavior of aluminum piston skirt coatings against aluminum cylinder bore.* Wear, 1999. **225-229**(Part 2): p. 1100-1108.

116. Sheiretov, T., H. Yoon, and C. Cusano, *Scuffing Under Dry Sliding Conditionsâ€"-Part II: Theoretical Studies*. Tribology Transactions, 1998. **41**(4): p. 447 - 458.

117.   Sheiretov, T., H. Yoon, and C. Cusano, *Scuffing Under Dry Sliding Conditionsâ€"Part I: Experimental Studies.* Tribology Transactions, 1998. **41**(4): p. 435 - 446.

118.   He, X., *Experimental and analytical investigation of the seizure process in aluminum-silicon alloy/steel tribocontacts*, in *Materials Engineering*. 1998, Northwestern University. p. 197.

119.   Ludema, K.C., *A review of scuffing and running-in of lubricated surfaces, with asperities and oxides in perspective.* Wear, 1984. **100**(1-3): p. 315-331.

120.   Ludema, K.C., et al., *Lubricated Sliding-A Review of Chemical and Physical Effects*, in *Tribology Series*. 1995, Elsevier. p. 383-398.

121.   Bäckerud, L., G. Chai, and J. Tammine, *Foundry Alloys*. 1 ed. Solidification Characteristics of Aluminum Alloys. Vol. 2. 1990, Sweden: AFS/Skan Aluminum. 1-99.

122.   Stefanescu, D.M. and R. Ruxanda, *Solidification Structures of Aluminum Alloys*. ASM Handbook Metallography and Microstructures, ed. G.F. Vander Voort. Vol. 9. 2004: ASM International. 107–115.

123.   Shabel, B.S., D.A. Granger, and W.G. Truckner, *Friction and Wear of Aluminum-Silicon Alloys*, in *ASM Handbook Friction, Lubrication, and Wear Technology*, P.J. Blau, Editor. 1992, ASM International. p. 1599-1617.

124.   Yuying, W., et al., *Modification effect of Ni-38 wt.%Si on Al-12 wt.%Si alloy.* Journal of Alloys and Compounds. **In Press, Corrected Proof**.

125.   Nafisi, S., R. Ghomashchi, and H. Vali, *Eutectic nucleation in hypoeutectic Al-Si alloys.* Materials Characterization, 2008. **59**(10): p. 1466-1473.

126.   Davis, F.A. and T.S. Eyre, *The effect of silicon content and morphology on the wear of aluminium-silicon alloys under dry and lubricated sliding conditions.* Tribology International, 1994. **27**(3): p. 171-181.

127.   Mahato, A., A.K. Sachdev, and S.K. Biswas, *Effect of particle morphology on resistance to permanent sinking by normal loading of silicon particle in aluminium matrix of a cast aluminium silicon alloy.* Wear, 2008. **265**(5-6): p. 849-855.

128.   Kori, S.A. and T.M. Chandrashekharaiah, *Studies on the dry sliding wear behaviour of hypoeutectic and eutectic Al-Si alloys.* Wear, 2007. **263**(1-6): p. 745-755.

129.   Basavakumar, K.G., P.G. Mukunda, and M. Chakraborty, *Influence of grain refinement and modification on dry sliding wear behaviour of Al-7Si and Al-7Si-2.5Cu cast alloys.* Journal of Materials Processing Technology, 2007. **186**(1-3): p. 236-245.

130.   Basavakumar, K.G., P.G. Mukunda, and M. Chakraborty, *Influence of grain refinement and modification on microstructure and mechanical properties of Al-7Si and Al-7Si-2.5Cu cast alloys.* Materials Characterization, 2008. **59**(3): p. 283-289.

131.   Basavakumar, K.G., P.G. Mukunda, and M. Chakraborty, *Dry sliding wear behaviour of Al-12Si and Al-12Si-3Cu cast alloys.* Materials & Design, 2009. **30**(4): p. 1258-1267.

132.   Gruzleski, J.E. and B.M. Closset, *The Treatment of Liquid Aluminum-Silicon Alloys*. 1990, Illinois, USA: American Foundrymen's Society. 12-51.

133.   Sebaie, O.E., et al., *The effects of mischmetal, cooling rate and heat treatment on the eutectic Si particle characteristics of A319.1, A356.2 and A413.1 Al-Si casting alloys.* Materials Science and Engineering: A, 2008. **480**(1-2): p. 342-355.

134.   Gruzleski, J.E., *Microstructure development during metalcasting*. 2000, Des Plaines, IL American Foundrymen's Society 82-124.

135.   Piwonka, T.S., *Sand Molding*, in *ASM Handbook: Casting*, D.M. Stefanescu, Editor. 1992, ASM International. p. 484-516.

136.   Byczynski, G.E., *Quantification of Solidification Characteristics of Al-Si Alloys by Thermal Analysis*, in *Materials Engineering*. 1997, University of Windsor: Windsor, Canada. p. 121.

137.   Tavitas-Medrano, F.J., et al., *Effect of Mg and Sr-modification on the mechanical properties of 319-type aluminum cast alloys subjected to artificial aging.* Materials Science and Engineering: A, 2008. **480**(1-2): p. 356-364.

138.   Gonzalez, N.A., *Aging Effects in 319-Type Alloys*, in *Materials Engineering.* 2006, McGill University: Canada.

139.   Callister, W.D., *Materials Science and Engineering: an introduction* 7ed. 2007, New York, USA: John Wiley & Sons Inc. 402-407.

140.   Anson, J.P. and J.E. Gruzleski, *Effect of hydrogen content on relative shrinkage and gas microporosity in Al-&% Si casting.* AFS Transactions, 1999. **26**: p. 135-142.

141.   Katgerman, L. and D. Eskin, *Hardening, Annealing, and Aging*, in *Handbook of Aluminum*, G.E. Totten and D.S. MacKenzie, Editors. 2003, Marcel Dekker, Inc.: New York. p. 259-304.

142.   Ashby, M.F. and D.R.H. Jones, *Engineering Materials 2: An Introduction to Microstructures, Processing and Design.* 3 ed. 2006, Great Britain: Elsevier. 108-120.

143.   Chen, M., et al., *Micromechanisms and mechanics of ultra-mild wear in Al-Si alloys.* Acta Materialia, 2008. **56**(19): p. 5605-5616.

144.   Elmadagli, M. and A.T. Alpas, *Sliding wear of an Al-18.5 wt.% Si alloy tested in an argon atmosphere and against DLC coated counterfaces.* Wear, 2006. **261**(7-8): p. 823-834.

145.   Deuis, R.L., C. Subramanian, and J.M. Yellup, *Dry sliding wear of aluminium composites--A review.* Composites Science and Technology, 1997. **57**(4): p. 415-435.

146.   Reddy, A.S., et al., *Wear and seizure of binary Al---Si alloys.* Wear, 1994. **171**(1-2): p. 115-127.

147.   Kanth, V.K., B.N. Pramila Bai, and S.K. Biswas, *Wear mechanisms in a hypereutectic aluminium silicon alloy sliding against steel.* Scripta Metallurgica et Materialia, 1990. **24**(2): p. 267-271.

148.   Shakhvorostov, D., K. Pöhlmann, and M. Scherge, *An energetic approach to friction, wear and temperature.* Wear, 2004. **257**(1-2): p. 124-130.

149.   Scherge, M., K. Pöhlmann, and A. Gervé, *Wear measurement using radionuclide-technique (RNT).* Wear, 2003. **254**(9): p. 801-817.

150.   Elmadagli, M., T. Perry, and A.T. Alpas, *A parametric study of the relationship between microstructure and wear resistance of Al-Si alloys.* Wear, 2007. **262**(1-2): p. 79-92.

151.   Liu, R., R. Asthana, and P. Rohatgi, *A map for wear mechanisms in aluminium alloys* Journal of Materials Science, 1991. **226**: p. 99-102.

152.   Suh, N.P., *An overview of the delamination theory of wear.* Wear, 1977. **44**(1): p. 1-16.

153.   Rice, J.R. and D.M. Tracey, *On the ductile enlargement of voids in triaxial stress fields.* Journal of the Mechanics and Physics of Solids, 1969. **17**: p. 201-217.

154.   Riahi, A.R. and A.T. Alpas, *Fracture of silicon-rich particles during sliding contact of Al-Si alloys.* Materials Science and Engineering: A, 2006. **441**(1-2): p. 326-330.

155.   Ghazali, M.J., W.M. Rainforth, and M.Z. Omar, *A comparative study of mechanically mixed layers (MMLs) characteristics of commercial aluminium alloys sliding against alumina and steel sliders.* Journal of Materials Processing Technology, 2008. **201**(1-3): p. 662-668.

156.   Biswas, S.K., *Some mechanisms of tribofilm formation in metal/metal and ceramic/metal sliding interactions.* Wear, 2000. **245**(1-2): p. 178-189.

157.   Li, X.Y. and K.N. Tandon, *Mechanical mixing induced by sliding wear of an Al-Si alloy against M2 steel.* Wear, 1999. **225-229**(Part 1): p. 640-648.

158.   Walker, J.C., et al., *TEM characterisation of near surface deformation resulting from lubricated sliding wear of aluminium alloy and composites.* Wear, 2007. **263**(1-6): p. 707-718.

159. Perrin, C. and W.M. Rainforth, *Work hardening behaviour at the worn surface of Al--- Cu and Al---Si alloys.* Wear, 1997. **203-204**: p. 171-179.

160. Li, J., et al., *FIB and TEM characterization of subsurfaces of an Al-Si alloy (A390) subjected to sliding wear.* Materials Science and Engineering: A, 2006. **421**(1-2): p. 317- 327.

161. Mohammed Jasim, K., *Nature of subsurface damage in Al-22wt.% si alloys sliding dry on steel discs at high sliding speeds.* Wear, 1984. **98**: p. 183-197.

162. Singh, J. and A.T. Alpas, *High-temperature wear and deformation processes in metal matrix composites.* Metallurgical and Materials Transactions A: Physical Metallurgy and Materials Science 1996. **27**(10): p. 3135-3148.

163. Barnes, A.M., K.D. Bartle, and V.R.A. Thibon, *A review of zinc dialkyldithiophosphates (ZDDPS): characterisation and role in the lubricating oil.* Tribology International, 2001. **34**(6): p. 389-395.

164. McQueen, J.S., et al., *Friction and wear of tribofilms formed by zinc dialkyl dithiophosphate antiwear additive in low viscosity engine oils.* Tribology International, 2005. **38**(3): p. 289-297.

165. Nicholls, M.A., et al., *Review of the lubrication of metallic surfaces by zinc dialkyl- dithiophosphates.* Tribology International, 2005. **38**(1): p. 15-39.

166. Fein, R.S., *CRC Handbook of Lubrication (Theory and Practice of Tribology)*, E.R. Booser, Editor. 1983, CRC Press LLC. p. 49-68.

167. Wan, Y., L. Cao, and Q. Xue, *Friction and wear characteristics of ZDDP in the sliding of steel against aluminum alloy.* Tribology International, 1997. **30**(10): p. 767-772.

168. Fuller, M., et al., *X-ray absorption spectroscopy of antiwear films on aluminum alloys generated from zinc dialkyldithiophosphate.* Tribology Letters, 1995. **1**: p. 367-378.

169. Nicholls, M.A., et al., *X-ray absorption spectroscopy of tribofilms produced from zinc dialkyl dithiophosphates on Al-Si alloys.* Wear, 2004. **257**(3-4): p. 311-328.

170. Hsu, S.M. and R.S. Gates, *Boundary lubricating films: formation and lubrication mechanism.* Tribology International, 2005. **38**(3): p. 305-312.

171. Wan, Y. and Q. Xue, *Effect of antiwear and extreme pressure additives on the wear of aluminium alloy in lubricated aluminium-on-steel contact.* Tribology International, 1995. **28**(8): p. 553-557.

172. Morina, A. and A. Neville, *Tribofilms: aspects of formation, stability and removal.* Journal of Physics D: Applied Physics, 2007. **40**: p. 5476-5487.

173. Neville, A., et al., *Compatibility between tribological surfaces and lubricant additives-- How friction and wear reduction can be controlled by surface/lube synergies.* Tribology International, 2007. **40**(10-12): p. 1680-1695.

174. Willermet, P.A., et al., *Mechanism of formation of antiwear films from zinc dialkyldithiophosphates.* Tribology International, 1995. **28**(3): p. 177-187.

175. Spikes, H., *The History and Mechanisms of ZDDP* Tribology Letters, 2004 **17**(3): p. 469- 489.

176. Pereira, G., et al., *A variable temperature mechanical analysis of ZDDP-derived antiwear films formed on 52100 steel.* Wear, 2007. **262**(3-4): p. 461-470.

177. Pereira, G., et al., *A multi-technique characterization of ZDDP antiwear films formed on Al (Si) alloy (A383) under various conditions.* Tribology Letters 2007. **26**(2): p. 103 -117

178. Pereira, G., et al., *Chemical characterization and nanomechanical properties of antiwear films fabricated from ZDDP on a near hypereutectic Al–Si alloy.* Tribology Letters, 2005. **18**(4): p. 411-427.

179. Nicholls, M.A., et al., *Spatially resolved nanoscale chemical and mechanical characterization of ZDDP antiwear films on aluminium–silicon alloys under cylinder/bore wear conditions.* Tribology Letters, 2005. **18**(3): p. 261-278.

180. Das, S., T. Perry, and S.K. Biswas, *Effect of surface etching on the lubricated sliding wear of an eutectic aluminum-silicon alloy.* Tribology Letters, 2006. **21**(3): p. 193-204.

181. Timmermans, G. and L. Froyen, *Fretting wear behaviour of hypereutectic P/M Al-Si in oil environment.* Wear, 1999. **230**(2): p. 105-117.

182. Walker, J.C., W.M. Rainforth, and H. Jones, *Lubricated sliding wear behaviour of aluminium alloy composites.* Wear, 2005. **259**(1-6): p. 577-589.

183. Legge, R.A., D.M. Smith, and G. Henkel, *Improved aluminum alloy for engine applications.* SAE Int., 1986. **860558**.

184. Tenekedjiev, N., et al., *Microstructures and Thermal Analysis of Strontium-Treated Aluminum-Silicon Alloys*. 1995: American Foundrymen's Society 82.

185. Watts, J.F. and J. Wolstenholme, *An Introduction to Surface Analysis by XPS and AES*. 2003, London: John Wiley & Sons.

186. Vickerman, J.C., *Surface analysis - the principle techniques*. 1997, New York: John Wiley & Sons.

187. Rizvi, S.Q.A., *Internal Combustion Engine Lubricants*, in *ASM Handbook Friction, Lubrication, and Wear Technology* P.J. Blau, Editor. 1992, ASM International. p. 301-319.

188. Martin, J.W., *Precipitation Hardening*. 1968, Great Britain: Pergamon Press Ltd.

189. Siddiqui, R.A., H.A. Abdullah, and A.-B.K. R., *Infuence of aging parameters on the mechanical properties of 6063 aluminium alloy.* Journal of Materials Processing Technology, 2000. **102**: p. 234-240.

190. Chakrabarti, D.J. and D.E. Laughlin, *Phase relations and precipitation in Al-Mg-Si alloys with Cu additions.* Progress in Materials Science, 2004. **49**(3-4): p. 389-410.

191. Marioara, C.D., et al., *The effect of Cu on precipitation in Al–Mg–Si alloys.* Philosophical Magazine, 2007. **87**(23): p. 3385 - 3413.

192. Li, Y.J., S. Brusethaug, and A. Olsen, *Influence of Cu on the mechanical properties and precipitation behavior of AlSi7Mg0.5 alloy during aging treatment.* Scripta Materialia, 2006. **54**(1): p. 99-103.

193. Li, X., et al., *Tribological behavior and phase transformation of single-crystal silicon in air.* Tribology International, 2008. **41**(3): p. 189-194.

194. Li, X., J. Lu, and S. Yang, *Effect of counterpart on the tribological behavior and tribo-induced phase transformation of Si.* Tribology International, 2009. **42**(5): p. 628-633.

195. Kovalchenko, A., et al., *Phase transformations in silicon under dry and lubricated sliding.* Tribology transactions, 2002. **45**(3): p. 372–380.

196. Kailer, A., Y.G. Gogotsi, and K.G. Nickel, *Phase transformations in silicon caused by contact loading.* Journal of Applied Physics, 1997. **81**(7): p. 3057-3063.

197. Talbot, D.E.J., *Hydrogen In Aluminum and Aluminum Alloys*, in *Solidification of Aluminum Alloys*, M.G. Chu, D.A. Granger, and Q. Han, Editors. 2004, The Minerals, Metals & Materials Society. p. 269-282.

PUBLICATIONS AND INDUSTRIAL REPORTS

Journal Publications

• Slattery, B.E., T. Perry, and A. Edrisy, Microstructural evolution of a eutectic Al-Si engine subjected to severe running conditions. Materials Science and Engineering: A, 2009. 512(1-2): p. 76-81.

• Slattery, B.E., T. Perry, and A. Edrisy, Investigation of wear induced surface and subsurface deformation in a linerless Al-Si engine, under GM approval for submission to Wear: An International Journal on the Science and Technology of Friction, Lubrication and Wear; Jun. 2009: p. 1-29.

Industrial Reports

• Slattery, B.E., T. Perry, and A. Edrisy, Microstructural Investigations of Mechanically Reduced GM 396-1 Aluminum Engine bore. Industrial report, distributed to GM Canada, United States, & India; Apr. 2008: p. 1-26.

• Slattery, B.E., T. Perry, and A. Edrisy, Microstructural Investigation of a Mechanically Reduced GM 396-3 Aluminum Engine bore. Industrial report, distributed to GM Canada, United States, & India; Dec. 2008: p. 1-28.

• Slattery, B.E., T. Perry, and A. Edrisy, Microstructural Comparison of a Mechanically Reduced and a Chemically Etched GM 396-1 Aluminum Engine Bore After Dynamometer Testing. Industrial report, distributed to GM Canada, United States, & India; Apr. 2009: p. 1-29.

• Slattery, B.E., T. Perry, and A. Edrisy, Microstructural Investigations of a Cold Scuffed GM 396-1 Aluminum Engine Bore After Dynamometer Testing. Industrial report, for submission to GM Canada, United States, & India; Sep. 2009: p. 1-30.

VITA AUCTORIS

NAME: Benjamin Everest Slattery

PLACE OF BIRTH: Windsor, Ontario

DATE OF BIRTH: 1985

EDUCATION: Ontario Secondary School Diploma
Vincent Massey Secondary School
Windsor, ON
1999– 2003

Bachelor of Applied Science
Honours Mechanical Engineering – Materials Option
University of Windsor
Windsor, ON
2003 – 2007

Master of Applied Science
Engineering Materials
University of Windsor
Windsor, ON
2007 – 2009